In vivo and *in vitro* analysis of RNases in *Bacillus subtilis*

Dissertation

„kumulativ“

zur Erlangung des Doktorgrades

der Naturwissenschaften

(Dr. rer. nat.)

dem

Fachbereich Chemie

der Philipps-Universität Marburg

vorgelegt von

Rebecca Hinrichs, M. Sc.

geboren in Westerstede, Deutschland

Marburg an der Lahn,

September 2022

Die vorliegende Dissertation wurde von Oktober/ 2019 bis August/ 2022 am Fachbereich Chemie/ SYNMIKRO der Philipps-Universität Marburg unter Leitung von Prof. Dr. Peter L. Graumann angefertigt.

Vom Fachbereich Chemie der Philipps-Universität Marburg (Hochschulkennziffer 1180) als Dissertation angenommen am _____

Erstgutachter(in): Prof. Dr. Peter L. Graumann

Zweitgutachter(in): Prof. Dr. Gert Bange

Tag der Disputation: _____

Eidesstattliche Erklärung

Ich erkläre, dass eine Promotion noch an keiner anderen Hochschule als der Philipps-Universität Marburg, Fachbereich Chemie, versucht wurde.

Hiermit versichere ich, dass ich die vorliegende Dissertation

In vivo and *in vitro* analysis of RNases in *Bacillus subtilis*

selbstständig, ohne unerlaubte Hilfe Dritter angefertigt und andere als die in der Dissertation angegebenen Hilfsmittel nicht benutzt habe. Alle Stellen, die wörtlich oder sinngemäß aus veröffentlichten oder unveröffentlichten Schriften entnommen sind, habe ich als solche kenntlich gemacht. Dritte waren an der inhaltlich-materiellen Erstellung der Dissertation nicht beteiligt; insbesondere habe ich hierfür nicht die Hilfe eines Promotionsberaters in Anspruch genommen. Kein Teil dieser Arbeit ist in einem anderen Promotions- oder Habilitationsverfahren verwendet worden. Mit dem Einsatz von Software zur Erkennung von Plagiaten bin ich einverstanden.

_____ _____

Ort/Datum Unterschrift (Vor- und Nachname)

Summary

RNA degradation is a key process in the control of gene expression in bacteria and is essential for the cell's homeostasis of nucleotide pools. A key player is the so-called RNA degradosome, proposed to be a membrane-associated complex containing endo- and exoribunucleases, as well as glycolytic enzymes and a DEAD-box RNA helicase. It is believed that endonuclease RNase Y is central to the formation of the RNA degradosome in *Bacillus subtilis*, leading to recruitment of RNases PnpA, RNase J1, and RNase J2, RNA helicase CshA, as well as glycolytic enzymes enolase and phosphofructokinase occurs. RNase Y has a transmembrane helix, and is "quasi" essential; it is also required for mRNA processing following transcription.

RNase Y also interacts with the so-called Y-complex, consisting of YaaT, YlbF, and, YmcA (RicT, RicF, RicA), which is important for RNase Y-mediated processing of mRNA. How RNase Y can operate in two different protein complexes and acts in RNA decay as well as transcription-associated processes, is unclear.

In this work, I show that the RNA degradosome is quite dynamic, having RNase Y, the glycolytic enzyme enolase, and the RNA helicase CshA and PnpA as central parts strongly reacting to a block in transcription, and thus to loss of mRNA substrate, while RNase J1 and J2 as well as the glycolytic enzyme phosphofructokinase show a much weaker response and are thus likely more peripheral components. The Y-complex clearly shows diffusion within the cytosol, but also the formation of membrane-associated accumulations, dissociating when transcription is blocked. Single molecule tracking (SMT) shows that the loss of one component of the Y-complex does not strongly affect the dynamics of the other proteins, suggesting that the complex forms a flexible association rather than a 1:1:1 stoichiometry. Biochemical analyses suggest that YaaT forms a membrane-anchor for the Y-complex, although it also has a cytosolic, freely diffusing fraction. A model will be presented that the Y-complex could function as an adaptor between nucleoid-associated mRNA synthesis and membrane-associated processing and degradation.

My thesis also presents a protocol for the successful purification of membrane-associated RNase Y, as a basis for further biochemical characterization of the protein, and interaction studies.

Another essential process in which RNases play a crucial role is DNA replication. In addition to the RNA primers, which are necessary for the placement of Okazaki fragments, DNA/RNA hybrids must be processed and RNA must be removed to ensure the stability of the DNA. A part of the thesis work shows that *B. subtilis* replication forks intimately employ two RNases of the „H“ family, DNA polymerase A and exonuclease ExoR *in vivo*. Recruitment appears to be based on substrate availability rather than on specific protein/protein interactions, involving redundant enzymatic activities.

Zusammenfassung

Der RNA-Abbau ist ein Schlüsselprozess bei der Steuerung der Genexpression in Bakterien und wesentlich für die Homöostase der Nukleotidpools in der Zelle. Eine Schlüsselrolle spielt das so genannte RNA-Degradosom, bei dem es sich um einen membranassoziierten Komplex handelt, der Endo- und Exoribunukleasen sowie glykolytische Enzyme und eine DEAD-Box-RNA-Helikase enthält. Es wird angenommen, dass die Endonuklease RNase Y eine zentrale Rolle bei der Bildung des RNA-Degradosoms in *Bacillus subtilis* spielt, was zur Rekrutierung der RNasen PnpA, RNase J1 und RNase J2, der RNA-Helikase CshA sowie der glykolytischen Enzyme Enolase und Phosphofructokinase führt. RNase Y hat eine Transmembranhelix und ist "quasi" essentiell; sie ist auch für die mRNA-Verarbeitung nach der Transkription erforderlich.

RNase Y interagiert auch mit dem so genannten Y-Komplex, bestehend aus YaaT, YlbF und YmcA (RicT, RicF, RicA), der für die RNase Y-vermittelte Verarbeitung von mRNA wichtig ist. Wie RNase Y in zwei verschiedenen Proteinkomplexen arbeiten kann und sowohl beim RNA-Zerfall als auch bei transkriptionsassoziierten Prozessen wirkt, ist unklar.

In dieser Arbeit zeige ich, dass das RNA-Degradosom recht dynamisch ist, mit RNase Y, dem glykolytischen Enzym Enolase und den RNA-Helikasen CshA und PnpA als zentralem Teil, der stark auf eine Blockade der Transkription und damit auf den Verlust von mRNA-Substrat reagiert, während RNase J1 und J2 sowie das glykolytische Enzym Phosphofructokinase eine viel schwächere Reaktion zeigen und daher wahrscheinlich eher periphere Komponenten sind. Der Y-Komplex zeigt eindeutig eine Diffusion innerhalb des Zytosols, aber auch die Bildung von membranassoziierten Ansammlungen, die dissoziieren, wenn die Transkription blockiert wird. Das “Single-molecule tracking” (SMT) zeigt, dass der Verlust einer Komponente des Y-Komplexes die Dynamik der anderen Proteine nicht stark beeinträchtigt, was darauf hindeutet, dass der Komplex eher eine flexible Assoziation als eine 1:1:1-Stöchiometrie bildet. Biochemische Analysen deuten darauf hin, dass YaaT eine Membranverankerung für den Y-Komplex bildet, obwohl es auch eine zytosolische, frei diffundierende Fraktion hat. Es wird ein Modell vorgestellt, wonach der Y-Komplex als Adaptor zwischen der nukleoid-assoziierten mRNA-Synthese und der membran-assoziierten Verarbeitung und Degradation fungieren könnte.

In meiner Dissertation wird auch ein Protokoll für die erfolgreiche Reinigung der membranassoziierten RNase Y vorgestellt, das die Grundlage für die weitere biochemische Charakterisierung des Proteins und für Interaktionsstudien bildet.

Ein weiterer wichtiger Prozess, bei dem RNasen eine entscheidende Rolle spielen, ist die DNA-Replikation. Zusätzlich zu den RNA-Primern, die für die Platzierung von Okazaki-Fragmenten notwendig sind, müssen DNA/RNA-Hybride prozessiert und RNA entfernt werden, um die Stabilität der DNA zu gewährleisten. Ein Teil der Arbeit zeigt, dass die Replikationsgabeln von *B. subtilis* zwei RNasen der "H"-Familie, die DNA-Polymerase A und die Exonuklease ExoR, *in vivo* eng miteinander verbinden. Die Rekrutierung scheint eher auf der Substratverfügbarkeit als auf spezifischen Protein/Protein-Interaktionen zu beruhen, wobei redundante enzymatische Aktivitäten beteiligt sind.

Contents

List of Figures

Introduction

Article I

Article II

List of Tables

Abbreviations

nm	nanometer
µm	micrometer
µl	microliter
ml	milliliter
l	liter
mM	milli Molar
M	Molar
µg	micro gram
mg	milli gram
g	gram
g/rcf	earth gravitational force /relative centrifugal force
ms	milli seconds
sec/ s	seconds
h	hour
°C	degree Celsius
%	percentage
bp	base pairs
kDa	kilo dalton
aa	amino acid
Amp	Ampicillin
BLAST	basic local alignment search tool
Cm/ cat	Chloramphenicol
DDM	Dodecyl-β-D-maltose
DNA	deoxyribonucleotide acid
dNTP	deoxynucleotide triphosphate
fw	forward/ upstream
IPTG	Isopropyl-β-D-thiogalactopyranosid
Kan	Kanamycin
LB	lysogeny broth
LMNG	Lauryl Maltose Neopentyl Glycol
mRNA	messenger RNA

mV	millivolt
mVenus	monomeric Venus
NMP	nucleoside mono-phosphates
OD	optical density
PBS	phosphate-buffered saline
PCR	polymerase chain reaction
pH	potential of hydrogen
rev	reverse/ downstream
RNA	ribonucleotide acid
SDS	sodium dodecyl sulfate
SDS-PAGE	sodium dodecyl sulfate polyacrylamide gel electrophoreses
SEC	size exclusion chromatography
sfGFP	super folder green fluorescent protein
SMALP	styrene maleic anhydride polymer
Tris	tris (hydroxymethyl) aminomethane
wt	wild type
xyl	Xylose

1. Introduction

1.1. RNA turnover in *Bacillus subtilis*

RNA turnover is an essential pathway for controlling gene expression. RNA molecules possess diverse structural and functional flexibility. This flexibility is occurring in their regulatory mechanisms, which often entail conformational changes due to an environmental trigger. These triggers can be, for example, the binding of metabolite and protein, or temperature changes (Mars, Nicolas *et al*. 2016). A common outcome of such binding events is modulation of translational efficiency, which can occur through occlusion or exposure of a ribosome binding site following small RNA (sRNA)-mediated remodeling of the local mRNA structure (Fig. 1.1) (Schroeder, Barta *et al*. 2004).

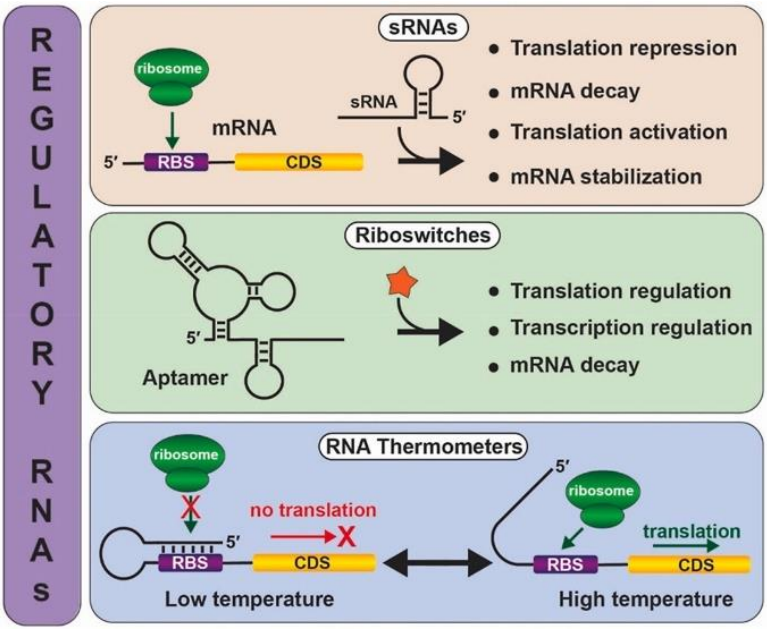

Figure 1.1: *Overview of regulatory RNAs in bacteria.* The regulatory RNAs are divided small RNAs (sRNAs), which include the processes of translation repression, mRNA decay, translation activation, and mRNA stabilization. Likewise, riboswitches for translation and transcription regulation as well as mRNA decay and RNA thermometers (RNAT) (Mahendran, Jayasinghe *et al*. 2022).

mRNAs transfer genetic information from DNA to proteins. In contrast to the high stability of tRNAs and rRNAs, bacterial mRNAs are slightly degraded. This crucial feature ensures that bacteria respond rapidly to changing environmental conditions by adding an additional layer of control that controls some of the transcription and enzymatic activities of proteins (Mahendran, Jayasinghe *et al.* 2022). The enzymes that process and degrade RNAs are called RNases (Mars, Nicolas *et al*. 2016).

Regulatory RNAs possess different ways of regulating cellular processes. A distinction is made between *cis*-acting and *trans*-acting RNAs (Georg, Hess *et al*. 2011).

sRNAs are among the most common regulatory RNAs (Waters and Storz 2009) and are often transcribed independently of each other and bound in *trans* to mRNA targets. This means that unlike *cis*-acting mRNA interactions where there is a perfect base pairing region and these genes overlap but are localized on different strands, in contrast, in *trans*-acting encoded sRNA-target mRNA interactions there is an imperfect base pairing region. These genes are separated from each other, so there is no overlap between them. This contributes to regulating the expression of genes (Mahendran, Jayasinghe *et al*. 2022). Furthermore, small transcripts can act as global regulators. In this process, they bind to their specific proteins and inhibit their function (Papenfort, Vogel *et al.* 2010). *Cis*-acting regulatory RNAs include riboswitches, RNA thermometers (RNAT), and T-boxes (Fig. 1.1.) (McCown, Corbino *et al.* 2017; Mahendran, Jayasinghe *et al*. 2022).

1.2. RNases in *Bacillus subtilis*

RNases (Ribonucleases) take an essential part in maturation, degradation, and turnover and are thus the essential part of RNA metabolism in the cell (Bechhofer, Deutscher *et al.* 2019). RNases represent enzymes that break phosphodiester bonds in the RNA chain and are thus key players in these processes. RNases are classified into Endoribonucleases and exoribonucleases. Exoribonucleases are characterized by the fact that they attack from the outside. There is some that attack RNA from 3' or also from 5'. In contrast, endoribonucleases can attack from the inside (Trinquier, Durand *et al*. 2020). Exoribonucleases in *Bacillus subtilis* include the polynucleotide phosphorylase (PNPase), RNase J1, and magnesium-dependent ExoR. The endoribonucleases are RNase Y, RNase J1 (which functions as both an endoribonuclease and an exonuclease), RNase J2, RNase HII, and RNase HIII (Dos Santos, Quendera *et al*. 2018).

1.2.1. RNase H family

A special characteristic of RNases are the RNases of the “H” family. RNases or endonucleases classified in the RNase H family are characterized as non-sequence-specific cleavers and hydrolyze RNA from RNA/DNA hybrids. The cleavage of DNA/RNA hybrids leads to 3' hydroxyl and 5' phosphate terminated products, which allows an intact DNA strand in the cell (Cerritelli and Crouch 2009). This functionality is not only used in DNA

replication (Okazaki fragments) and gene expression but also in DNA repair systems and is therefore essential for the cell (Crouch 1990). In eukaryotes, there are two classes of RNase H family, RNase 1 and RNase 2. In prokaryotes, especially *Bacillus subtilis*, RNase HII and RNase HIII are described (Crooke and Expression 1999). Endonucleases are divided into two types based on their amino acid sequence similarity. Type 1 includes RNase HI, which is found in bacteria, and RNase H1 from eukaryotic cells, as well as RNase H domains from reverse transcriptase. Type 2 includes RNases HII and HIII from bacteria, as well as archaeal RNases HII and eukaryotic RNases H2 (Haruki, Tsunaka *et al*. 2002).

The importance of RNase HII and HIII is reflected in the frequency processes in which RNA is covalently incorporated into duplex DNA. In addition to the necessary removal of RNA primers (10 to 15 consecutive ribonucleotides) during DNA replication (Ogawa, Okazaki *et al*. 1984), incorrect incorporation of individual ribonucleotides (single/ multiple rNMPs) by DNA polymerase occurs (Fig 1.2.). These must then be replaced with corresponding deoxyribonucleoside triphosphates (dNTPs) (Nick McElhinny, Watts *et al*. 2010; Nava, Grasso *et al*. 2020). Similarly, RNA transcripts may combine with DNA. This leads to the displacement of a single strand, resulting in a so-called R-loop (Fig 1.2.). These R-loops should be removed, as they reduce the integrity of the genome (Santos-Pereira and Aguilera 2015). The removal and processing of these RNA/DNA hybrids are carried out by RNase HII and HIII.

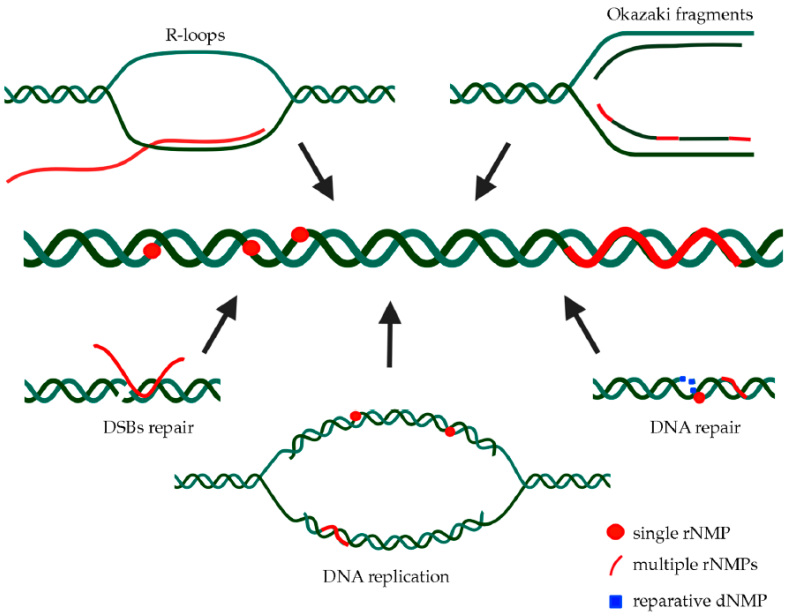

Figure 1.2: *Overview of the locus of DNA/RNA hybrids effects in the bacterial cell*. The ribonucleoside mono-phosphates (rNMPs) are incorporated in DNA replication, during double-strand breaks (DSBs), or in R-loops as single or multiple. The rNMPs can be

replaced by deoxynucleoside mono-phosphates (dNMPs) by RNase HII and RNase HIII in *Bacillus subtilis* (Nava, Grasso *et al*. 2020).

For RNases HII and HIII, it was shown in *Bacillus subtilis* that they are not essential individually, but double deletion leads to very poor growth in the cell (Yao, Schroeder *et al*. 2013). Interestingly, phenotypes associated with other exonucleases were also shown. Thus, deletion of the magnesium-dependent 5'->3' exonuclease ExoR with the deletion RNase HIII resulted in a temperature-sensitive phenotype leading to lethality at 25°C (Randall, Nye *et al*. 2019). ExoR, like RNase HIII, is described as an exonuclease involved in Okazaki fragment maturation. The DNA polymerase PolA was also shown in *in vitro* experiments to be involved in the maturation of Okazaki fragments together with RNase HIII and its exonuclease activity (Randall, Nye *et al.* 2019).

1.3. mRNA degradation in *Bacillus subtilis*

The control of messenger RNA (mRNA) stability is an important regulatory component in bacteria (Mohanty and Kushner 2016). While this regulation can occur at different levels, protein levels ultimately depend on the availability of mRNA. The amount of these RNAs is determined by the rate of transcription and degradation (RNA turnover) (Trinquier, Durand *et al.* 2020). mRNA processing and degradation are initiated by the endonucleolytic attack and the cleavage products are degraded by processes of exoribonucleases (Lehnik-Habrink, Newman *et al*. 2011). The RNA degradosome is responsible for this. In addition to the 5’ endoribonuclease RNase Y, other components of the RNA degradosome are known in *B. subtilis* (Trinquier, Durand *et al*. 2020). Probably involved in the degradation are the polynucleotide phosphorylase (PNPase) together with the DEAD-box RNA helicase (CshA), the exoribonuclease RNase J1, and the endoribonuclease RNase J2 as well as the glycolytic enzymes phosphofructokinase (PfkA) and the moonlight protein enolase (Eno) (Cascante-Estepa, Gunka *et al*. 2016).

In addition to the main activity of PNPase in RNA degradation, the protein can act as a synthetic enzyme leading to the polymerization of single-stranded RNA (ssRNA) from nucleoside diphosphates (dNDPs) (Andrade, Pobre *et al.* 2009) and is also involved in single-stranded DNA (ssDNA) degradation and DNA repair pathways (Cardenas, Carrasco *et al.* 2009).

CshA belongs to the family of DEAD-box RNA helicases, which means that it has a highly conserved DEAD motif consisting of the amino acid sequence aspartic acid (D), glutamic acid (E), alanine (A), and again aspartic acid (D) (Huen, Lin *et al.* 2017). These proteins are involved in the unwinding of RNA and break down of ds-RNA structures under ATP consumption, e.g. to enable the reading of the base sequence on the ribosome, by opening up stem loop structures, or the processing of the RNA by endo- and exoribonucleases (Lehnik-Habrink, Pförtner *et al.* 2010).

RNases J1 and J2 play a major role in the maturation and degradation of RNA in *B. subtilis* (Mathy, Hébert *et al.* 2010). In contrast to RNase J2, RNase J1 is essential for the organism, and RNase J1 and J2 are enzymes with dual exo- and endoribonucleolytic activity (Mathy, Bénard *et al*. 2007; Lebreton, Tomecki *et al.* 2008). The glycolytic enzymes enolase and phosphofructokinase have been shown in a variety of experiments to be involved in the RNA degradosome, but their role is not yet known (Commichau, Rothe *et al.* 2009).

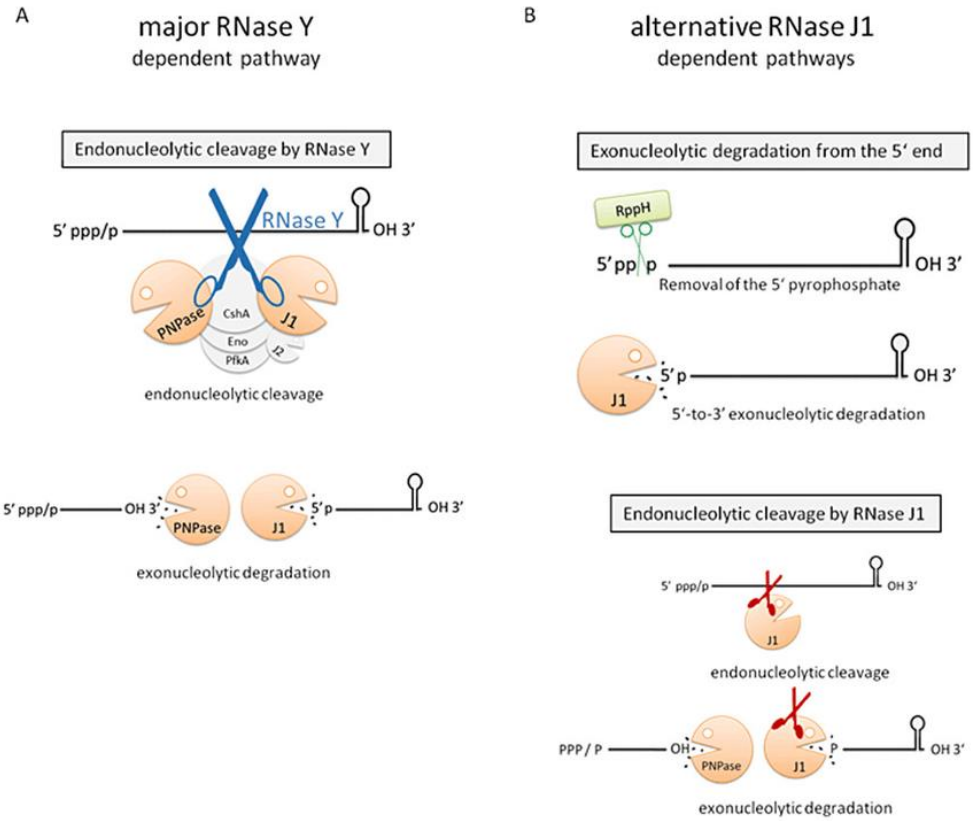

Figure 1.3: *Schematic representation of mRNA processing by PNPase and RNase J1, after initial cleavage by the endoribonuclease activity of RNase Y.* (A) The major pathway via endonucleolytic cleavage by RNase Y and exonucleolytic degradation of PNPase and RNase J1, contrasts with another possibility to degrade the mRNA (B) by exonucleolytic degradation from the 5' end or endonucleolytic cleavage by RNase J1 (Lehnik-Habrink, Lewis *et al*. 2012).

During mRNA degradation, first, the endoribonuclease activity of RNase Y cleaves single-stranded mRNA and the resulting mRNA fragments are subsequently degraded by the exoribonuclease activities of PNPase (3'→5') and RNase J1 (5'→3') (Fig. 1.3. A). An alternative pathway is discussed to be the 5' exonucleolytic degradation via RNase J1 or RNase J2. Because RNase J1 has a specific 5' to 3' exonucleolytic activity it is able to degrade the substrate directly at the 5' end. To ensure a preferential monophosphorylated transcript, RppH could be responsible for this modification of the triphosphate to a monophosphate. Or the dual activity of RNase J1 could be possible to start the mRNA degradation in *B. subtilis* together with the PNPase (Fig. 1.3. B) (Lehnik-Habrink, Lewis *et al*. 2012).

1.4. The endoribonuclease RNase Y

In *B. subtilis*, the RNA endonuclease RNase Y is known for global mRNA turnover and RNA processing (Mohanty, Kushner *et al*. 2016; Shahbabian, Jamalli *et al*. 2009). Thus, RNase Y plays an important role in the regulation of bacteria. The loss of RNase Y has been shown to lead to major defects in cell morphology, sporulation, and competence and is therefore described as quasi-essential (Benda, Woelfel *et al.* 2021). By regulating this process, cells can control gene expression and react quickly to changing growth conditions. In *B. subtilis* the quasi-essential endoribonuclease RNase Y is involved in the initiation of RNA degradation.

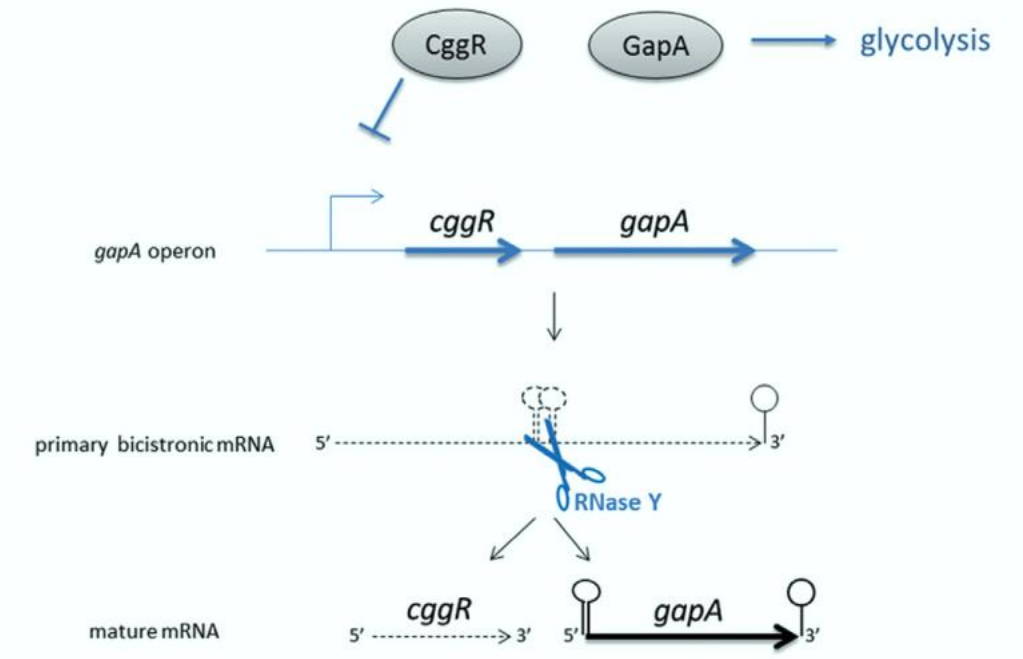

Figure 1.4: *Schematic representation of cggr-gapA operon cleavage in Bacillus subtilis.* The operon consists of *gapA, pgk, tpi, pgm* and *eno* and at the beginning the *cggR* operates as a transcriptional repressor of its own operon. The cleavage site by RNase Y is located upstream of *gapA* and regulated the control of the downstream gen of the glycolytic enzyme *gapA* (Lehnik-Habrink, Lewis *et al*. 2012).

It influences the intracellular levels of most transcripts (about 550 mRNAs) (Lehnik-Habrink, Schaffer *et al.* 2011) in *B. subtilis (*Lehnik-Habrink, Newman *et al.* 2011*;* Durand and Condon 2018).

RNase Y (*rny/ ymdA*) is a 5' end sensitive endoribonuclease that is involved in many mRNA maturation and degradation processes. An important function is the regulation of hexacistronic *cggR-gapA* operon. In the absence of, for example, glucose, the expression of the *gapA* operon is repressed by CggR, which is the product of the first gene (*cggR*) (Commichau, Rothe *et al.* 2009). To control the level of the glycolytic enzyme glyceraldehyde-3-phosphate dehydrogenase (*gapA*) it is important to regulate the co-transcribed regulator *cggR*. The CggR operates as a transcription repressor of its own operon, which consists of *gapA, pgk, tpi, pgm* and *eno*, to control the different protein levels of the glycolytic enzyme GapA (Fig. 1.4.). RNase Y is able to recognize the two stem-loops upstream of *gapA* and to cleave the operon in a short AU-rich single-stranded region which is located between two stable stem–loops structures (Ludwig, Homuth *et al*. 2001; Lehnik-Habrink, Lewis *et al*. 2012; Brantl, Licht *et al*. 2010; Doan and Aymerich 2003). In addition to RNase Y, it could be shown that proteins of the so-called Y-complex are also significantly involved in the processing of the *cggR-gapA* operon in *B. subtilis* (DeLoughery, Lalanne *et al*. 2018) (see chapter 1.7.).

1.5. Structural characteristics of RNase Y

The structure of RNase Y is not solved so far. To get an insight into the structure, *in silico* data can be used. The *in silico* analysis of the domain structure of RNase Y revealed a 25 amino acid long N-terminal transmembrane domain (TM) and a central K homology domain (KH) as RNA binding domains and a phosphohydrolase domain (HD). Also, a coiled-coil region is suggested for amino acids 30 to 150 (Fig. 1.5.) (Lehnik-Habrink *et al*. 2011a; Letunic, Khedkar *et al*. 2020). In general, KH domains are important for RNA binding and are necessary for posttranscriptional functions (Valverde, Edwards *et al*. 2008). The KH domain belongs to the Type I domains and is found in single copy in RNase Y. It is specific

because in general the Type II KH domains are found in prokaryotic proteins (Valverde, Edwards *et al.* 2008). It is known that the depletion of the RNase Y increases the half-life of mRNA so it is probable that the RNase Y seems to have a wide substrate specificity (Shahbabian, Jamalli *et al*. 2009). The RNase Y shows a conserved HD domain which is typical for proteins belonging to the superfamily of metal-dependent phosphorylases (Aravind and Koonin 1998).

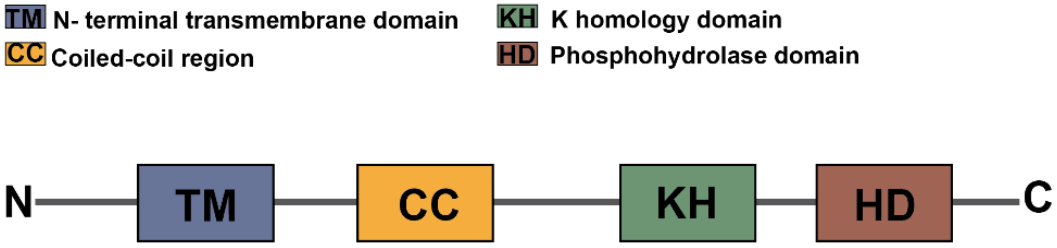

Figure 1.5: *Schematic illustration of the endoribonuclease* RNase Y *of Bacillus subtilis.* The illustration shows the transmembrane domain (1-25 amino acids, blue) and the coiled-coil domain (30-150 amino acids, orange) which is supposedly required for a dimer or multimer formation of RNase Y. The functional RNA-binding KH domain is described for the region of 208-275 amino acids, green, and the conserved metal-dependent phosphohydrolase domain (HD) for the region of 332-438 amino acids, pink (Shahbabian, Jamalli *et al.* 2009).

1.6. The three-protein complex (Y-complex)

The Y-complex consist of three proteins YaaT (RicT), YlbF (RicF) and YmcA (RicA). The complex is known for its involvement in sporulation, natural competence, biofilm formation, and mRNA cleavage events (DeLoughery, Lalanne *et al.* 2018; DeLoughery, Dengler *et al.* 2016). It has already been published with bacterial two-hybrid experiments that the Y-complex directly interacts directly with the membrane-anchored RNase Y in *B. subtilis* (DeLoughery, Dengler *et al.* 2016).

Endonucleolytic cleavage occurs within polycistronic mRNA, which leads to different stabilities of the obtained mRNA fragments. The different instability results for instance from different half-lives of the truncated mRNA resulting in transcripts of the operon and this results in an unequal frequency of these co-transcribed genes (Newbury, Smith *et al*. 1987).

In the case of the glycolytic operon *cggR-gapA*, the cleavage by RNase Y causes the first gene (*cggR*) to encode a transcriptional repressor of itself and the operon to become unstable. It was shown that the resulting pentacistronic mRNA *gapA-pgk tpi pgm eno* has a much higher half-life (3-4 min) whereas the *cggR* mRNA is extremely unstable (Meinken, Blencke *et al.* 2003). This results in a higher level of *gapA* and downstream genes in the operon and finally leads to a control of the amount of protein in the cell (Ludwig, Homuth *et al*. 2001). Using end-enrichment RNA sequencing (Rend-seq), DeLoughery *et al*. and other could show that the Y-complex, in addition to the RNase Y is necessary for the cleavage of *cggR-gapA* operon in *B. subtilis* (DeLoughery, Lalanne *et al*. 2018; DeLoughery, Dengler *et al*. 2016).

A key process in *B. subtilis* is the sporulation. The production of heat-resistant spores is initiated by the activation of the transcriptional regulator Spo0A via the phosphorelays. Spo0A is one of the master regulators of sporulation in *B. subtilis* (Piggot and Hilbert 2004). The sporulation can be achieved with the transformation to the active form of Spo0A (Spo0A-P) by phosphorylation. Spo0A is initially transcribed via a sigma H-dependent promoter. The Spo0A is converted into the active form (Spo0A-P) (Al-Hinai, Jones *et al*. 2015). Similarly, the cascade via the autophosphorylated KinA or KinB leads to a transfer of the phosphate to Spo0F. Spo0F then transfers a phosphate to Spo0B, which then phosphorylates Spo0A (Fig. 1.6.) (Siranosian and Grossman 1994). The active Spo0A-P acts as a requirement for different pathways in K-state, sporulation, and biofilm formation in *B. subtilis* (Carabetta, Tanner *et al*. 2013). The gene *abrB* encodes for the protein AbrB and acts as a transcriptional regulator and is necessary for the regulation of gene expression during the transition from growth to the stationary phase (Yamamoto, Chumsakul *et al.* 2022).

SinI is an antagonist of SinR (transcriptional regulator) and is responsible for the control of biofilm formation (Kearns, Chu *et al.* 2005). It could be shown that all Y-complex proteins are required to repress *abrB* transcription as well as for the activation of *sinI* transcription in the pathway of biofilm formation (Dubnau, Carabetta *et al.* 2016).

Hosoya *et al.* were able to show that in the mutant of *yaaT* as well as *ylbF* and *ymcA* could be shown that there is an inhibition of phosphorelay during sporulation in stage 0. The deletions of the Y-complex show a significant reduction in genetic competence due to the poor expression of *comK* (Hosoya, Asai *et al.* 2002; Carabetta, Tanner *et al.* 2013).

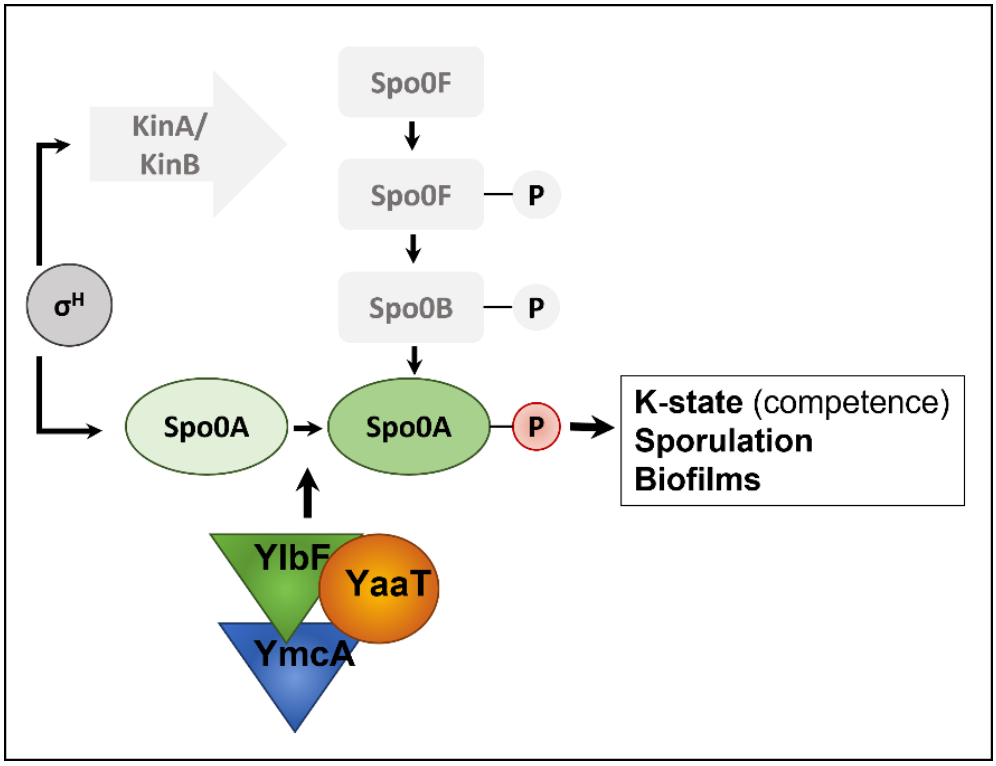

Figure 1.6: *Graphical representation of the proposed influence of the Y-complex proteins in phosphorylation of the master regulator Spo0A.* The phosphorylation of Spo0A into the active form Spo0A-P which is the requirement of genetic competence, sporulation, and biofilm formation in *B. subtilis* (Dubnau, Carabetta *et al.* 2016). Modified after (Al-Hinai, Jones *et al.* 2015).

YaaT shows up partly attached to the membrane as well as in the cytosol of the cell (DeLoughery, Lalanne *et al*. 2018; Hinrichs, Pozhydaieva *et al.* 2022). Its localization is revealed to be strongly dependent on RNase Y, as well as YlbF, since a deletion (delta *rny*, *ylbF*) leads to a loss of the membrane fraction. Interestingly a N-terminal fusion strain displays only a cytosolic protein (DeLoughery, Lalanne *et al*. 2018). In comparison, fractionation experiments show that YlbF prefers to be located in the cytosol, as is the case with YmcA (Hinrichs, Pozhydaieva *et al*. 2022).

In vitro experiments have shown that the Y-complex may exist in different conformations (Adusei-Danso, Khaja *et al*. 2019). The Y-complex was shown to carry two Fe-S clusters (Tanner, Carabetta *et al.* 2017). Using the purified Y-complex proteins, crystal structures of a heterotetramer (YmcA-YlbF) (Fig. 1.7. B) and a YmcA-dimer (Figure 1.7. A) were shown

besides they isolated a YaaT-monomer. Furthermore, Adusei-Danso *et al*. were able to show that the two $[_4Fe\text{-}_4S]^{2+}$ clusters are ligated via the cysteine residues of YaaT, YlbF and YmcA. More detailed, the first $[_4Fe\text{-}_4S]^{2+}$ cluster is coordinated by four conserved cysteine residues of YaaT (C161, C166, C198, C203). Whereas the second $[_4Fe\text{-}_4S]^{2+}$ cluster is coordinated by cysteine residues all proteins (YaaT C167, YlbF C134, C146 and by YmcA C141 They could clearly show that each monomer of YmcA consists of five α-helices. The dimerization of the protein occurs via intramolecular contacts between α1, α2, and α5. It could also be shown that despite a low agreement in sequence identity (20%), the structures of YmcA and Ymca-YlbF are almost identical and structurally resemble a c-shape.

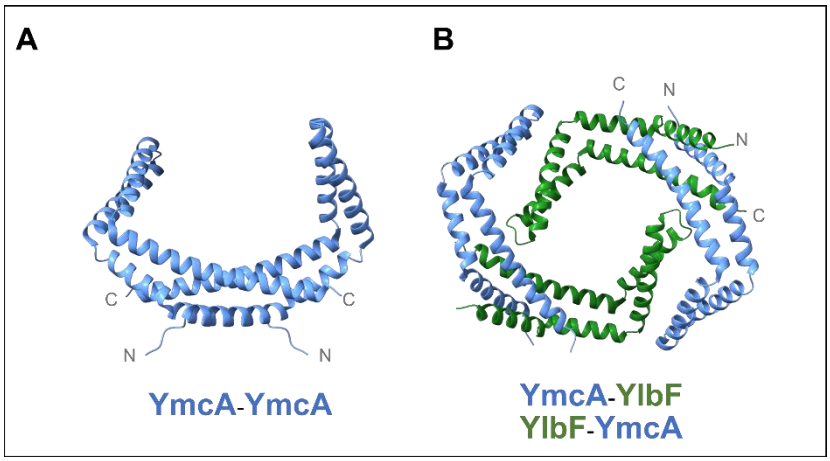

Figure 1.7: *The crystal structure of the homodimer YmcA and YmcA-YlbF heterodimer.* (A) Homodimer of YmcA is coloured in blue. PDB: 6PRH (B) YmcA-YlbF heterodimer, YmcA coloured in blue and YlbF in green (Adusei-Danso, Khaja *et al.* 2019). PDB: 6PRK

The authors were also able to make assumptions about the function of the Fe-S clusters and assign them to *cggR-gapA* mRNA maturation, among other things. Furthermore, the involvement in the transcript stability of *ylbF* as well as transformation, biofilm formation, and sporulation are reported (Adusei-Danso, Khaja *et al*. 2019).

1.7. Aim of research

RNases have a key function in organisms. The major endoribonuclease of *B. subtilis* RNase Y and also the three-protein complex (Y-complex) play a fundamental role in the maturation, processing, and degradation of mRNAs. On the other hand, in *B. subtilis*, it has not yet been clearly shown which and how many RNases are involved in Okazaki fragment maturation. *In vivo* analyses will reveal the RNases involved in the maturation of Okazaki fragments during DNA replication.

In this work, *in vivo* analyses will be used to determine the dynamics, localisations as well as potential interactions of proteins, which have RNA nuclease functions.

2. Articles

List of publications with collaborations

Wisniewska, Aleksandra; Wons, Ewa; Potrykus, Katarzyna; **Hinrichs, Rebecca**; Gucwa, Katarzyna; Graumann, Peter; Mruk, Iwona (accepted August 2022 by Nucleic Acids Research)

Molecular basis for lethal cross-talk between two unrelated bacterial transcription factors – The regulatory protein of a restriction-modification system and the repressor of a defective prophage

Alessandro Negri, Olesia Werbowy, Ewa Wons, Simon Dersch, **Rebecca Hinrichs**, Peter L Graumann, Iwona Mruk

Regulator-dependent temporal dynamics of a restriction-modification system's gene expression upon entering new host cells: single-cell and population studies

Nucleic Acids Research, Volume 49, Issue 7, 19 April 2021, Pages 3826–3840

Sonja Schibany, **Rebecca Hinrichs**, Rogelio Hernández-Tamayo, Peter L. Graumann

The Major Chromosome Condensation Factors Smc, HBsu, and Gyrase in *Bacillus subtilis* Operate via Strikingly Different Patterns of Motion

mSphere, Volume 5 Issue 5, 9 September 2020, S. e00817-00820.

2.1. Article I

Luis M. Oviedo-Bocanegra *, **Rebecca Hinrichs** *, Daniel Andreas Orlando Rotter, Simon Dersch, Peter L. Graumann, 2021

* The authors wish it to be known that, in their opinion, the first two authors should be regarded as Joint First Authors.

Single molecule/particle tracking analysis program SMTracker 2.0 reveals different dynamics of proteins within the RNA degradosome complex in *Bacillus subtilis*.

Nucleic Acids Res. 2021 Nov 8; 49(19): e112

I designed and carried out all experiments. Furthermore, I supported Luis M. Oviedo-Bocanegra and Prof. Dr. Peter L. Graumann in writing the manuscripts and revised the manuscripts during the publishing process. Daniel Andreas Orlando Rotter and Dr. Simon Dersch were involved in the conception and design of the SMTracker program.

2.2. Article II

Rebecca Hinrichs, Nadiia Pozhydaieva, Katharina Höfer, Peter L. Graumann, 2022

Y-Complex Proteins Show RNA-Dependent Binding Events at the Cell Membrane and Distinct Single-Molecule Dynamics

Cells MDPI. 2022 Mar 9;11(6):933

In this manuscript, I designed and carried out all experiments exept for Northern blot analysis. I wrote the manuscript together with Prof. Dr. Peter L. Graumann and created all figures and tables and revised the manuscripts during the publishing process.I would like to acknowledge helpful support from Dr. Katharina Höfer and Nadiia Pozhydaieva (*Northern blot analysis*), Alexandra Kilb (transformation assay), and Madita Viering (growth curve).

2.3. Article III

Rebecca Hinrichs and Peter L. Graumann, 2022

Visual evidence for the recruitment of four enzymes with RNase activity to the *Bacillus subtilis* replication forks

BIORXIV/2022/507877

In this manuscript, I designed and carried out all experiments. I wrote the manuscript together with Prof. Dr. Peter L. Graumann and created all figures and tables.

2.1. Article I

Single molecule/particle tracking analysis program SMTracker 2.0 reveals different dynamics of proteins within the RNA degradosome complex in *Bacillus subtilis*

Luis M. Oviedo-Bocanegra*, Rebecca Hinrichs*, Daniel Andreas Orlando Rotter, Simon Dersch and Peter L. Graumann[#]

August, 2021

Centre for Synthetic Microbiology (SYNMIKRO) and Fachbereich Chemie, Philipps-Universität Marburg, 35032 Marburg, Germany

*These authors contributed equally to this work

2.1.1. ABSTRACT

Single-molecule (particle) tracking is a powerful method to study dynamic processes in cells at highest possible spatial and temporal resolution. We have developed SMTracker, a graphical user interface for automatic quantifying, visualizing and managing of data. Version 2.0 determines distributions of positional displacements in *x*- and *y*-direction using multi-state diffusion models, discriminates between Brownian, sub- or superdiffusive behaviour, and locates slow or fast diffusing populations in a standardized cell. Using SMTracker, we show that the *Bacillus subtilis* RNA degradosome consists of a highly dynamic complex of RNase Y and binding partners. We found similar changes in molecule dynamics for RNase Y, CshA, PNPase and enolase, but not for phosphofructokinase, RNase J1 and J2, to inhibition of transcription. However, the absence of PfkA or of RNaseJ2 affected molecule dynamics of RNaseY-mVenus, indicating that these two proteins are indeed part of the degradosome. Molecule counting suggests that RNase Y is present as a dimer in cells, at an average copy number of about 500, of which 46% are present in a slow-diffusive state and thus likely engaged within degradosomes. Thus, RNase Y, CshA, PNPase and enolase likely play central roles, and RNase J1, J2 and PfkA more peripheral roles, in degradosome architecture.

2.1.2. INTRODUCTION

Degradation and processing of RNA is a central aspect within the central dogma in biology. The regulation of the lifetime of mRNAs, the specific cleavage of mRNAs to yield differentially regulated translation events, and the maturation of stable RNAs are essential for cellular life [1-3]. In many bacteria, RNase E plays a key role in RNA processing, and in the initiation of degradation events. RNase E contains an amphipathic helix at its N-terminus and thereby associates with the cell membrane, where it forms a complex with several additional proteins, the so called RNA degradosome [4]. Present within this complex are one exonuclease (PNPase) that after initial endonucleolytic cleavage by RNase E takes over processive degradation of mRNA, an RNA helicase that can open up secondary structures in RNA, as well as one enzymes thought to act as moonlighting protein: enolase is a glycolytic enzyme, and appears to help in complex formation, which is proposed to be centred around RNase E.

Many bacteria, including Gram positives lack RNase E, but contain an analogous enzyme, RNase Y, which associates with the membrane through a predicted transmembrane helix at its N-terminus [5]. Like RNase E, it is thought to be the central component of an RNA degradosome, containing RNases J1 and J2, PNPase, RNA helicase CshA, as well as enolase and phosphofructokinase I (PfkA), also a glycolytic enzyme [6, 7]. Evidence for this idea stems from two-hybrid experiments and interaction studies after chemical crosslinking. Interestingly, RNase Y has been proposed to act within a second complex, the so-called Y-complex (or RicAFT), which contains 3 additional soluble proteins, and has been shown to interact with RNase Y [8]. Lack of Y-complex proteins leads to loss of function of riboswitches as well as to dysregulation of global mRNA processing, analogous to loss of RNase Y [9]. Interestingly, RNase E as well as RNase Y have been shown to forms clusters underneath the cell membrane, which in case of RNase E are dynamic and short-lived [10-13].

We sought to further study the putative RNA degradosome by studying the dynamics of some of its proposed components at a single molecule level. While RNase Y has been shown to form membrane-associated foci under fluorescence microscopy experiments, other components of the putative RNA degradosome were homogeneously present within the cytosol, as investigated by epifluorescence microscopy [11]. These experiments suggest that the RNA degradosome may be dominated by transient interactions, which we wished to quantify by single molecule analyses.

For this task, we employed a highly evolved version of software SMTracker. The new version 2.0 now includes several distinct methods for obtaining diffusion coefficients, to automatically quantify molecule numbers in individual cells, to visualize populations of molecules with different diffusion coefficients within a standardized cell, and analyses of Brownian versus anomalous diffusion. SMTracker 2.0 contains several statistical tools and algorithms to find out if results are significant and are not dominated by overfitting. Importantly, SMTracker 2.0 is now compatible with any computer system and no longer requires additional programs to be operated. We will first introduce the new version 2.0, and then describe investigations of the RNA degradosome, which we interpret to show that together with enolase, RNase Y forms the central hub of the complex, which is highly dynamic and contains peripherally associated proteins such as PfkA and RNase J1. These appear to play minor roles as their dynamics are hardly affected by an inhibition of RNA synthesis, but whose absence affects single molecule dynamics of RNase Y.

2.1.3. Software

SMTracker is a graphical user interface (GUI), custom coded by our lab, that can be easily used by non-mathematicians or non-physicists. Previous versions have been used in several publications [14-18]. In this work, we have used the most versatile version of SMTracker, version 2.0, and all the dynamic and statistical analyses and graphs in this paper were generated exclusively by the software. For further information about the techniques applied, please also visit the Supplementary documentation. For specific details of the Software and the program for download can be found at https://sourceforge.net/projects/singlemoleculetracker/ where also a User Manual and sample data can be found and explored.

Construction of strains

Strains of bacteria used in this study were cultivated in LB medium and on solid agar plates at 30°C. Chloramphenicol 5 µg/ml, ampicillin 100 µg/ml, kanamycin 30 µg/ml, spectomycin 100 µg/ml and rifampicin 25 µg/ml were also added where necessary. For SMT experiments, minimal medium S_{750} was used (100 ml: 10 ml 10 x S_{750} salt solution [for 1 l, pH 7.0: 104.7 g of MOPS, 13.2 g of $(NH_4)_2SO_4$, 6.8 g of KH_2PO_4, 12 g of KOH], 1 ml 100 x metal solution [100 ml ddH_2O: 20 ml of $MgCl_2$ (1 M), 7 ml of $CaCl_2$ (1 M), 0.5 ml of $MnCl_2$ (1 M), 1 ml of $ZnCl_2$ (0.1 M), 1 ml of $FeCl_3$ (50 mM), 5 ml of Thiamine hydrochloride (2 mg /ml), 17 µl of HCl (2 M)], 2 ml 50% fructose (w/v), 1 ml of 10% L-glutamate (w/v), 40 µl of 1% Casamino acids (w/v)) [19]. For *Bacillus subtilis* BG214 it was necessary to add methionine (50 µg/ml) and tryptophane (50 µg/ml). The strain in which enolase-mV was induced at low level was treated with 0.01% xylose for 1 hour.

All proteins were visualized as mVenus (mV) fusions. *B. subtilis* mV-fusions of RNase Y, RNase J1, RNase J2 and PfkA were created with the use of plasmid pSG1164-mV, generating a C-terminal fusion at the original locus of the gene by a single-crossover event [20]. At least 500 bp of the 3`end of the desired gene (excluding the stop codon) were amplified by PCR cloned by Gibson Assembly [21] into the vector in frame with the linker and mV sequence. The necessary Gibson primers had an overhang of at least 20 bp (Table S1). For enolase we generated an ectopic fusion in order to express a low level of the enzyme that itself is present in the cell with a high copy number, to be able to rapidly reach single molecule level during SMT. For this purpose, pSG1193-mV was used. Full length *eno* gene (1293 bp) was cloned into the vector in frame with the linker and *mVenus*. Expression

of mRNA for the protein was mediated by the xylose promoter. The cloning of all vectors was done in DH5α *E. coli* cells. Deletion strains (*B. subtilis* 168 Δ*rnjB::kan trpC2*, Δ*pfkA::kan trpC2*) were obtained from the Bacillus Genetic Stock Center (Columbus, Ohio) [22]. Competent cells of strain RNase Y-mV were transformed with chromosomal DNA from deletion strains. Chromosomal DNA was obtained using innuPREP Bacteria DNA Kit (Analytik-Jena). Bacterial strains and plasmids used in this study are listed in Supplementary Table S2, primers in Supplementary Table S1.

Western blot

Strains were cultivated in LB medium (30°C) with the addition of the specific antibiotic until mid-exponential growth phase. The enolase-mV fusion was induced with 0.01% xylose for 1 hour. Pelleted cells were resuspended in buffer (100 mM NaCl, 50 mM EDTA, 2.5 mg/ml Lysozyme, 0.1 mg/ml RNase, 0.01 mg/ml DNAse). Samples were incubated at 37°C with SDS loading buffer, but were not boiled. Detection was performed with a primary antibody αGFP, polyclonal (1: 500, for 5 hours) [23] and secondary antibody goat-anti-Rabbit-IgG, peroxidase-conjugated (1 : 10000, for 1 hour) (Sigma-Aldrich). Protein marker Thermo Scientific™ PageRuler Prestained Protein Ladder was used.

Fluorescence microscopy and Single-molecule tracking

Epi-fluorescence microscopy was performed in S_{750} minimal medium at 25°C, using a Nikon Eclipse Ti-E, Nikon Instruments Inc with a CFI Apochromat objective (TIRF 100 x Oil, NA 1.49) and an EMCCD camera (ImagEM X2 EM-CCD, Hamamatsu Photonics KK). Data were evaluated using ImageJ [24].

For SMT, slim-field illumination was obtained using the central part of an expanded beam of a 514 nm laser diode (max. power 100 mW, TOPTICA Beam Smart) was focussed on the back focal plane of the objective. Up to 25% of the intensity was used via a YFP filter set (BrightLine 500/24, Beamsplitter 520 and BrightLine 542/27), generating a laser power density of about 160 W cm^{-2} in the object plane. We have previously shown that cells continue to grow following exposure to this intensity, following the 2 minute-long experiments [15]. NIS-elements was used for image acquisition. Videos were captured for 3000 frames, with integration time of 40 ms in the case of enolase-mV, RNase Y-mV, Δ*rnjB* RNaseY-mV, and Δ*pfkA* RNaseY-mV, or 30 ms for PfkA-mV, RNase J1-mV, and RNase J2-mV. The further processing was done with Oufti [25] to set the cell-meshes. Track generation was performed with a minimum track length of 5 steps u-track [26]. The reaching of a single

molecule level was tested by analysing bleaching curves in ImageJ. Analytical evaluation was carried out using the SMTracker 2.0, based on an earlier version [27].

Cross-Validation approach on the calculation of the diffusion coefficients.

Measurement errors on Diffusion coefficients and fraction sizes have been performed using a cross-validation approach, where the complete dataset has been split into 2 parts, train and test, in a proportion of 70%/30%. Given the size of our dataset, made more sense to divide the train set into 10 folds randomly and perform the fit on each fold, and showing as a final result the average, ± error, that comes from the standard error of the mean + the 95% confidence interval obtained from the fit procedure.

2.1.4. RESULTS

SMTracker 2.0 includes several new analytic tools that are highly useful for the analyses of single molecule dynamics

SMTracker 2.0 – built on its previous version 1.0 [27] – was completely revised and extended for this (and future) work. Now it is available as stand-alone version that can run independently of MATLAB. SMTracker 2.0 loads movies acquired from fluorescence microscopy and cell outlines obtained from bright field or phase contrast microscopy (Fig. 1). Data analysis is run on a graphical user interphase (GUI) containing 7 principle sections dealing with spatiotemporal analyses of single molecule/particle data (Fig. 1). In addition to updates on the Ensemble-Averaged Mean Squared displacement (MSD) setup, Gaussian Mixture modelling (GMM) and Squared displacement analyses (SQD) have been improved to detect up to 3 different Brownian-diffusive sub-populations. SMTracker 2.0 also contains Apparent Diffusion (AppD) analyses to determine diffusion constants using each track and Time-Averaged MSD. With the new tool “Clustering”, time-averaged MSD (TAMSD) data are used to classify trajectories using a machine-learning approach by an unsupervised K-means clustering algorithm. Spatial Localization (SLA) analysis, which comprehends Dwelling and Confinement events determination, have been completely reviewed and upgraded optimizing both the algorithm and the data visualization.

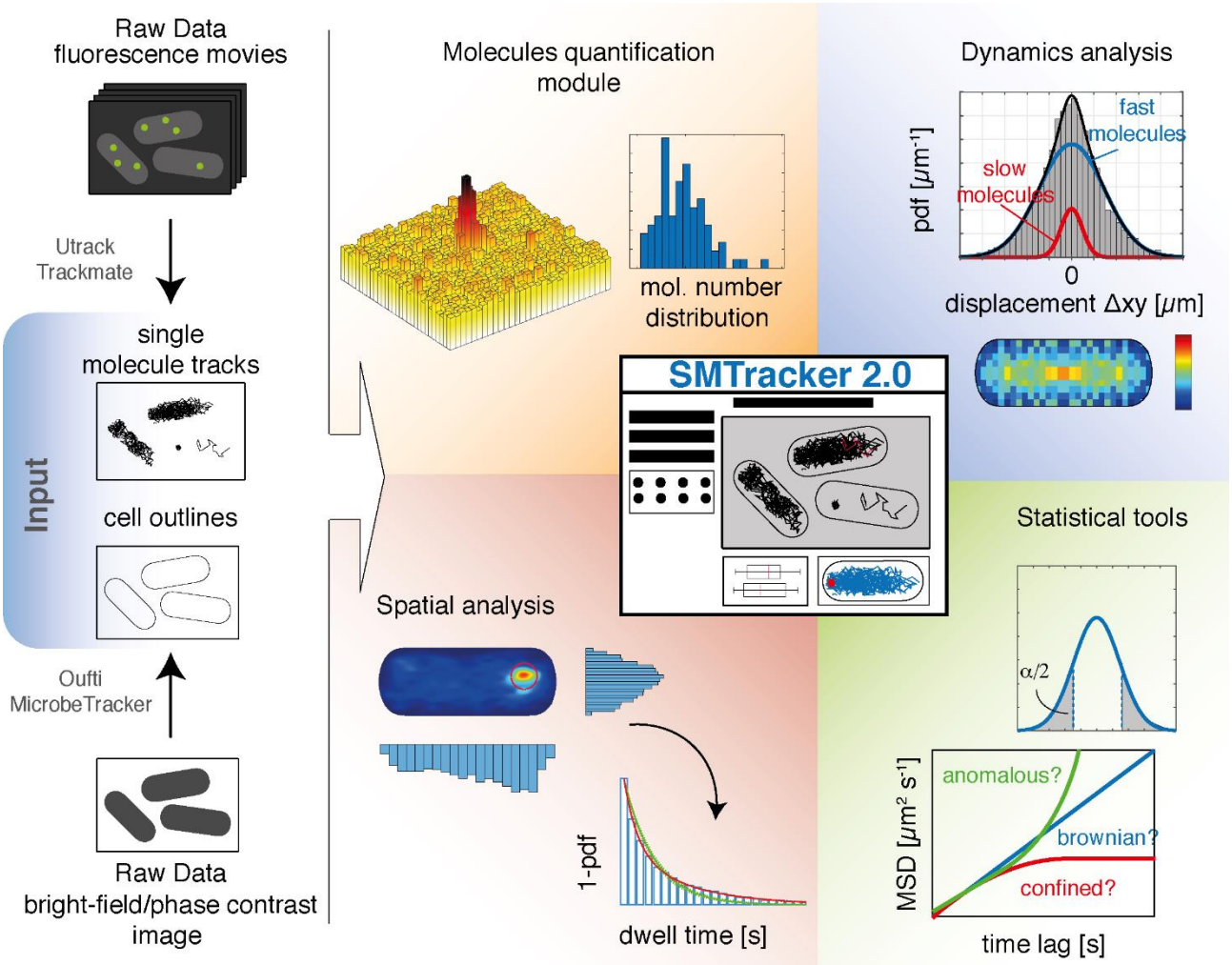

Figure 1. Graphical abstract of SMTracker 2.0 suite

Three new-fangled modules have been developed for a better understanding of the dynamic behaviour of proteins inside an organism, or *in vitro*. “Distance tool” is a user-driven module that provides information about the trend and the position of a protein with respect to defined points in the cell. A “Molecule quantification” tool takes advantage of the microscopy movies and the pattern of fluorescence emission that is inherent to the fluorescent protein (FP) to estimate the molecule copy number within a certain strain, and even within individual cells. Finally, the “Binned speed maps” tool has been devised that determines areas with varied protein diffusion coefficients within the cell. The latter tool is especially helpful in visualizing diffusive subpopulations in the cell, generating a 2D population diffusion map.

Please note that SMTracker 2.0 requires a certain arrangement of data within folders, explained in the manual. We have also created direct links to a program calculating dwell times in a way different from SMTracker, called “SMM Track” [28], and a link to the useful

tool vbSPT from the Elf laboratory, where changes of molecules between different diffusive populations can be predicted [29]. Instead of going through lengthy descriptions of SMTracker 2.0, we present experiments on the dynamics of the putative RNA degradosome in *Bacillus subtilis* cells, highlighting most powerful improvements in and additions to the program.

RNase Y and enolase, but not RNase J1, J2 and PfkA, show changes in protein dynamics in response to inhibition of transcription

We generated a fusion of mVenus to the last coding 500 base pairs of the *rny* gene; the plasmid was integrated into the *rny* gene locus via single crossover integration, generating a C-terminal RNase Y-mVenus fusion. This way, RNase Y-mVenus was the sole source of the protein expressed in the cell, under control of the original promotor, and expression of the downstream gene *ymdB* was ensured via addition of xylose driving the *pxyl* promoter present within the plasmid. Cells expressing this construct grew with a doubling time indistinguishable from wild type cells, suggesting that the fusion complemented the loss of the wild type protein, because an *rny* deletion leads to a severe growth defect [5, 30]. In an analogous manner, we generated mVenus fusions to enolase, RNase J1, RNase J2, PNPase, CshA and phosphofructokinase I (PfkA). All strains grew with wild type appearance and doubling times, suggesting that all fusions could functionally replace wild type copies. Using epifluorescence microscopy, RNase Y-mVenus showed a spotty pattern of localization, and likewise RNase J1 and RNase J2, in contrast to PfkA and enolase which revealed a more homogeneous fluorescence within the cytosol (Fig. S1A). Western blot analyses showed that all fusion were expressed as full-length proteins (Fig. S1B). Please note that the size of RNase J2-mV (83.57 kDa) and PfkA-mV (61 kDa) differs from the literature. The different running behaviour may be due to sample handling, as we avoided boiling of samples. The expression of free mVenus (26.9 kDa) that might occur due to proteolysis was not observed.

For single molecule tracking, we used a system in which the central part of a widened 514 nm laser is projected onto the back focal plane of the objective, generating a small homogeneous illumination at the center of the visible field (sometimes termed “slim-field” microscopy). Images were acquired with an EM-CCD camera at 20 (RNase J1, RNase J2, PfkA, PNPase and CshA and 40 ms (RNase Y and enolase) stream acquisition rate, such that movement of single point spread functions could be captured. Tracks were automatically recorded using u-track program. At the beginning of illumination, all molecules

in the cell fluoresce, and after few hundred frames, most molecules are bleached, leaving one or very few molecules per cell that can be tracked. Bleaching curves are evaluated in ImageJ to ensure that single molecule conditions applied at the beginning of the movies that were used for analyses. Because enolase is expressed at high copy number in *B. subtilis* cells, such that single molecule level was only obtained after several thousands of frames, we imaged a strain in which enolase-mVenus is expressed from a gene fusion at the ectopic *amyE* locus, using very low induction of the xylose promoter driving transcription. In this way, only very few molecules of enolase-mVenus are expressed together with many copies of the wild type protein, allowing single molecule level to be rapidly reached.

Molecule steps and trajectories were analysed using SMTracker 2.0. Fig. 2A shows an example of cells with recorded tracks. Only tracks of 5 steps or longer were used for analyses in order to avoid artefacts from very short events. Fig. 2B shows the jump distance distribution (as a probability density function) of RNase Y-mVenus, as determined from squared displacement analyses. The grey dotted line shows a single fit to the data, assuming one population of molecules that have a common diffusion coefficient. This single fit cannot explain the observed data, and the “residuals” panels (Fig. S2) indicate a great deviation of the fit (green line) from the measured values, which are represented by the horizontal line. Red and blue curves are Rayleigh fits assuming two or three populations, respectively, one with a low and one with a higher diffusion constant in case of two populations. Taken together (black solid line), two assumed populations can explain the observed distribution of steps rather well, which can also be seen in the corresponding residuals panel (Fig. S2). Likely, the fast-mobile fraction corresponds to freely diffusive RNase Y molecules, while the slow/static fraction is presumably composed of RNase Y molecules bound to mRNA and/or the putative degradosome. In fact, the diffusion constant determined for the static fraction with $D = 0.031 \pm 0.001$ $\mu m^2/s$ (Table 1) is similar to that determined for translating 70S ribosomes/polysomes with $D = 0.055$ $\mu m^2/s$ [31], suggesting that this fraction of RNase Y is within a large protein/RNA complex. The diffusion constant of the fast-mobile fraction with $D = 0.3 \pm 0.002$ $\mu m^2/s$ is quite low for a freely diffusive protein, compared with diffusion coefficients obtained before [18, 28] (free mVenus has a coefficient of 5 $\mu m^2/s$ within *B. subtilis* cells [27]). Possibly, the mobile fraction of RNase Y is composed of freely diffusing dimers (see further below for this point) as well as of molecules in transition towards binding to mRNA. Also, tracking of RNase Y at 40 ms integration time may miss out on some very rapidly diffusing molecules, leading to an underestimation of D. We will pick up this point further below.

According to tracks obtained for RNase Y, 48.2 ± 0.6 % of the molecules were in a slow-mobile state, and thus likely actively involved in mRNA degradation or RNA processing, while 51.8 ± 0.3% are in the mobile state (Table 1), illustrated by the size of the bubbles in Fig. 2C, blue panel. We further analysed RNase Y and the other four proteins using two population fits, which also explained data much better for the other RNases and glycolytic enzymes than single fits (Fig. S2). Thus, for RNase J1, RNase J2, PNPase, CshA, PfkA and enolase, we found a slow mobile/static fraction similar to that found for RNase Y (Fig. 2C, Table 1). The fact that these slow diffusion constants varied by a factor of more than two may indicate that e.g. RNase J1 or enolase may be present in additional complexes, because at the fast acquisition rates used, we cannot distinguish between different slow-mobile states of molecules. The fact that enolase, PfkA and RNase J molecules had different values for D_2 can be explained by their different sizes, although the D of 0.26 ± 0.004 $\mu m^2/s$ is very low for this 46 kDa protein. At present, we have no explanation for this unusually low mobility for enolase, with about 60% of molecules even being in the slow mobile/static state (Table 1).

Importantly, Fig. 2B shows that for RNase Y, there is a strong shift of step sizes towards larger steps after addition of rifampicin, which lowers transcription levels by blocking RNA polymerase (RNAP) activity. Note that the concentration of 25 µg/ml we used is more than 400 fold above the MIC [32], but less than a maximum of 100 µg/ml employed in a study to completely block RNA synthesis [33], because at the latter concentration we observed cell death 30 min after addition of rifampicin, as judged from cells becoming extremely fluorescent, during SMT acquisition. We did not observe this effect with 25 µg/ml, so we chose this lower concentration, where transcription may not be completely blocked, but where cells are alive, in order to avoid artefacts from dying cells in which molecules may move very differently than under physiological conditions.

The low-mobility fraction (red) strongly decreased in favour of the fast-mobile fraction (blue). The fraction of slow-mobile RNase Y molecules decreased from about 48 to 9.84 ± 0.6% (Table 1), while the fraction of mobile molecules increased concomitantly (Fig. 2C, blue panel). Thus, loss of substrate allows slow mobile RNase Y molecules to become mobile.

We also treated cells expressing the other putative RNA degradosome components with rifampicin to test if mobilities change similar to what was observed for RNase Y. Note that to better compare fraction sizes between conditions we kept D values for treated cells similar to those of non-treated cells, although when analysed separately, D values moderately differ

in addition to fraction sizes, between the two conditions. The size of the fractions found in untreated or treated cells is represented as bubbles in panels C. A strong shift in RNase Y mobility as well as of that of PNPase, CshA and enolase can easily be seen in Fig. 2C by the overlays of tracks from exponential growth (not filled) and those from rifampicin-treated cells (filled bars), but not to a considerable extent for RNase J1 and J2, or for PfkA. In contrast to RNase Y, RNase J2 molecules became even more static, the population increased from 37± 2% to 51.2 ± 2% in response to inhibition of transcription (Table 1). Thus, RNase Y becomes mobile due to a shortage in RNA substrates to bind to, as expected, and for enolase, apparently the same holds true, suggesting that many enolase molecules interact with mRNA (likely via RNase Y) as a component of the RNA degradosome. Conversely, our findings suggest that RNase J1, RNase J2 and PfkA molecules are not quantitatively part of the degradosome, as compared to RNase Y.

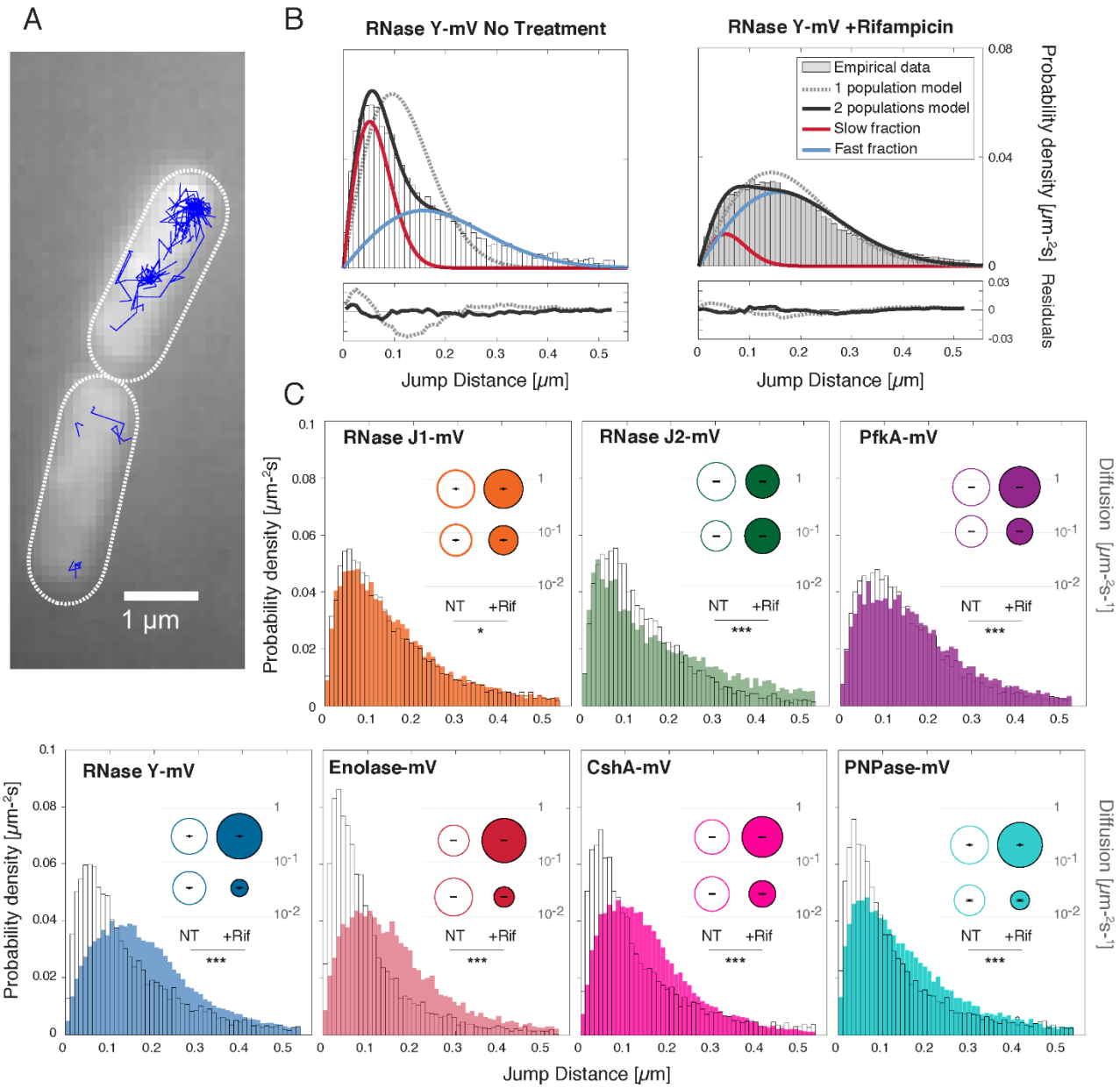

Figure 2. Acquisition and Diffusion analysis pipeline via SMTracker 2.0. **A** Examples of trajectories of RNase Y-mVenus. **B** Jump distance histograms overlaid with a 2-population model fit for RNase Y-mVenus before (left) and after Rifampicin (Rif) treatment (right). Fitting was performed by a non-linear least squares algorithm. Residuals are shown in the lower panels. **C** Jump distance histograms for the 4 RNases, RNA helicase and the 2 glycolytic enzymes before (no fill) and after Rif treatment (filled with solid color). Inlet: Bubble plots, the size of the bubbles is proportional to that of each diffusive subgroup, and short segments in black indicates the ± confidence interval at 95% of diffusion coefficients. Stars correspond to the result of a Kolmogorov-Smirnov 2-test to determine significant differences between the two distributions. As usual, *** ,**,* and ns when the p-values are lower than 0.001, 0.05, 0.01 and larger than 0.01 respectively.

RNase Y, PNPase, CshA and enolase change their pattern of localization in response to inhibition of transcription

We wished to obtain spatial information on changes occurring to putative RNA degradosome components in response to a reduction in cellular RNA levels. We therefore projected tracks obtained into a standardized cell of 1 x 3 µm size, an average size for growing *B. subtilis* cells. We sorted tracks into those that show an extended period of little to no movement, termed “confinement”, where molecules stop much longer than would be expected from stochastic slow-mobile events during free diffusion. Confined movement occurs when molecules become bound to larger structures; for RNase Y molecules, this would most likely correspond to mRNA binding, or binding to components of the putative degradosome. We chose 8 steps or more as indicative of confined motion, and a radius of 106 nm, corresponding to the pixel size of the camera, or about 2.5 times the localization error.

Fig. 3 shows that RNase Y moves throughout the cell (blue tracks), and shows confined motion mostly towards the periphery of the cell, i.e. close to the cell membrane. In the heat map, where localization probability increases from blue to red, RNase Y also shows a tendency towards the membrane. This pattern changes dramatically after addition of rifampicin. Under this condition, RNase Y relocates from the periphery to the cell center. This trend can also be seen for confined tracks, which are much more accumulated within the cell, away from the membrane, than during exponential growth. Thus, depletion of (m)RNA strongly affects the pattern of localization of RNase Y, and its preferred sites of confined motion, i.e. it is likely places of activity.

A comparable effect of relocation was observed for enolase, where rifampicin addition was accompanied by an accumulation towards the cell center (Fig. 3). This effect was visually less pronounced than for RNase Y, but still noticeable by eye; confined tracks of enolase also shifted away from the periphery towards the cell middle. An effect similarly striking as for RNase Y was seen for PNPase and for CshA (Fig. 3). However, neither RNase J1, nor J2, nor PfkA revealed considerable differences in the confinement maps or the heat maps between unperturbed growth and inhibition of transcription. RNase J1 showed a weak accumulation towards the membrane in the heat map, which appeared to be weakened after treatment, while RNase J2 showed a weak accumulation after treatment in the cell center, which was not apparent during exponential growth. Thus, RNase Y, CshA, PNPase and enolase show similar responses to an arrest in transcription in terms of single molecule

dynamics (Fig. 2) and spatial redistribution (Fig. 3), while the other proposed members of the degradosome show only mild to no changes.

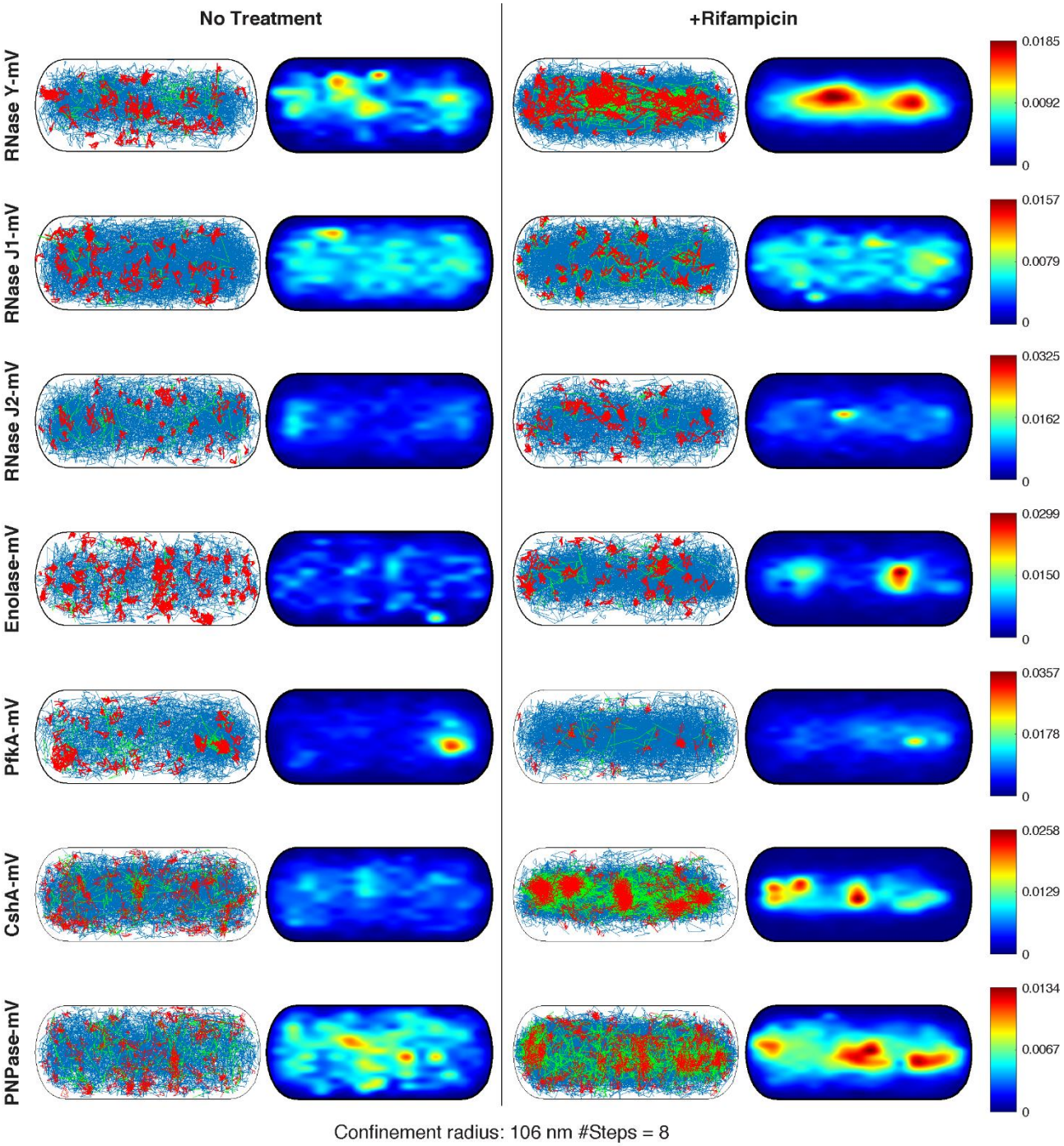

Figure 3. Confinement maps and heat maps. Confined tracks are shown in red, tracks showing no confined motion in blue, green tracks contain confined as well as non-confined motion. Colour codes on the right indicate low (“0” blue, to high, red, likeliness of presence). Cells have a width of 1 µm and a length of 3 µm, roughly the average of exponentially growing cells.

We also determined average dwell times for molecules. Here, the time spent within a radius that can be manually defined, or is determined to be three times the localization error (determined from the intercept of the MSD curve with the y-axis) is scored for x intervals. Representative curves showing dwell time determinations can be seen in Fig. S3. Exponential decay curves are fitted to the data, and an average dwell time “tau” is determined for all molecules, and in case two decay curves can better explain the obtained dwell time probabilities, tau 1 and tau 2 are calculated, together with corresponding sizes of populations, which one can interpret as molecules resting stochastically (tau 1), and molecules arresting because of e.g. binding events, which are much longer than stochastic “no-displacement” events (table 3). Fig. 4 illustrates that average dwell times for RNase Y decreased significantly following rifampicin treatment, and even more pronounced for enolase, while PNPase and CshA showed less pronounced, yet significant reductions in dwell times. This was not observed for RNase J1 and J2, nor for PfkA, which did not reveal significant changes in response to lowering of mRNA levels. Of note, while our analyses contain many long tracks that allow for a sufficiently reliable deduction of dwell times, actual dwell times *in vivo* will be longer, as our analyses involve bleaching of molecules, which leads to an underestimation of dwell times. Additionally, lack of changes may not mean absence of interaction with e.g. mRNA in this case: it has been shown that RNase J1 is responsible for the degradation of a considerable fraction of *B. subtilis* mRNAs [34]. Possibly, RNase J1 molecules undergo non-productive interactions with different, weakly binding proteins in the absence of high affinity binding substrates. Note that dwell times cannot be directly compared between protein fusions, because RNase Y and enolase were tracked using 40 ms integration time, and the other fusions with 20 ms.

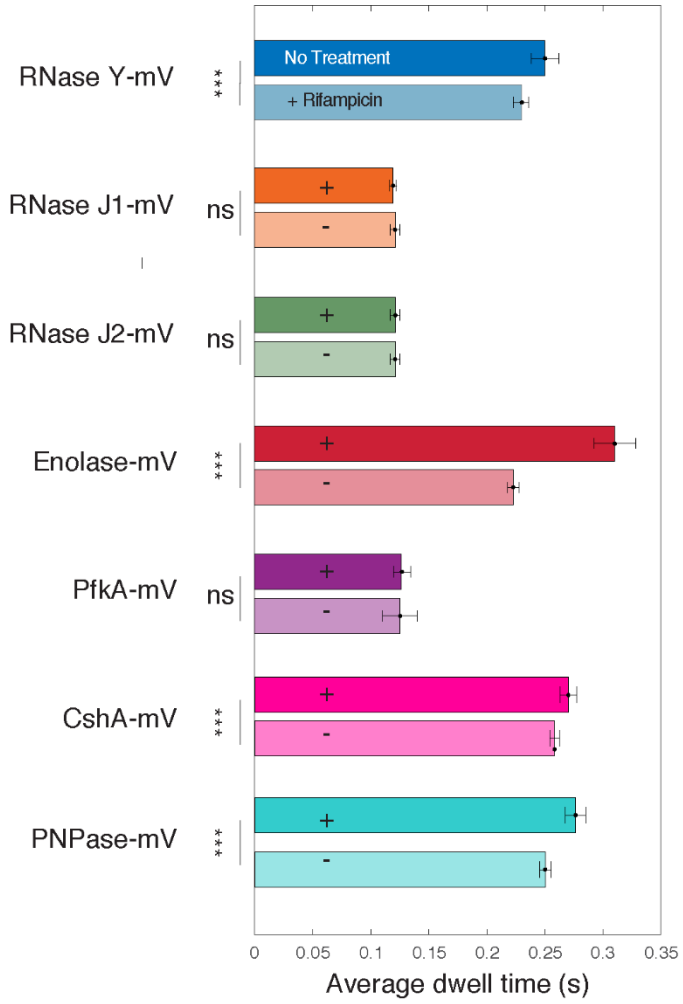

Figure 4. Dwell times for enzymes under investigation. As usual, *** indicates highly significant changes (p-value < 0.001), n.s. statistically not significant (p-value > 0.1). Note that while actual values for dwell times will be higher *in vivo* due to photobleaching effects, differences between individual proteins/conditions can be accurately determined.

SMTracker 2.0 provides a tool for automated counting of molecules in individual cells

We implemented a novel tool to obtain information on average molecule numbers, as well as numbers of molecules in individual cells. The approach calculates average signal intensity of single fluorophores and calculates molecule numbers from fluorescence intensity captured in the first frames. In order to account for background fluorescence, it is important to subtract fluorescence found in cells not expressing any fluorophore/fluorescent protein fusion. Fig. 5 illustrates our approach: from samples lacking any cells, uneven illumination is captured, and background fluorescence is scored from cells not expressing any fluorescent protein fusion. Having these values, initial fluorescence intensity of cells carrying fluorophores/FP fusions is captured, until after bleaching, signals from single molecules can

be quantified to yield an average number of intensity per single molecule. As opposed to YFP-tracking/photobleaching based SMT, in live cell PALM tracking, conditions would need to be established to photoactivate all molecules within the first few frames, in order to employ this approach.

For RNase Y, we determined an average molecule number of 485 per cell, and thus a medium copy number, as opposed to low copy numbers determined for e.g. DNA repair protein Ada [35] or cyclic di-GMP synthetases DgcK [14], which are not even present as single copy in all cells of a culture, or high copy numbers of several thousand for e.g. ribosomes or RNA polymerase [36]. This number lies in between that obtained in a report using mass spectrometry-based determination of protein copy numbers, of 222 copies in a richer and 716 molecules in a poorer growth medium [37]. Assuming a rounded number of 500 molecules per cell, our data suggest that based on our finding of about 46% of statically positioned RNase Y molecules (Fig. 2, Table 1), 230 molecules are engaged in RNase activity within the degradosome, while an average number of 270 molecules are diffusing through the cell in search of substrate and binding partners. Of interest, we also observed the existence of spots showing at least two discrete bleaching steps, indicating that a number of RNase Y molecules either form dimers, or that at least two molecules are in close proximity. This finding is in agreement with RNase Y forming dimers *in vitro* [38]. Fig. 5C shows that 32% of single spots contain two molecules, as the mean of the smaller population contains twice the integrated density of the mean of the larger (monomeric fraction). Because of stochastic bleaching of molecules, these findings do not mean that 68% of RNase Y molecules are monomers, but that clearly, a considerable fraction of molecules are accompanied by additional copies of RNase Y, implying that RNase Y clusters likely contain more than one RNase Y molecule. As a second example, we determined the copy number of enolase (in this case expressed from the original gene locus, as sole copy of the protein), shown to be present between 5000 and 10000 copies per cell [37], for which we determined an average number of 3900 ± 175 (Fig. S5). Likely, fluorescence signals will be close to saturation at this high level, wherefore the determined number may be an underestimate.

We benchmarked results obtained from the Molecule quantification tool with modelled data (table S3 and S4), in order to judge the capabilities of this method. Fig. S4 shows that for 10 molecules or less, the algorithm performs very well, while from 20 molecules up, a stable underestimation of 15% appears to take place. Thus, for 20 molecules or more, obtained numbers should be adjusted by addition of 15% (this was already done for the

RNase Y determination above). Note that also, not all fluorescent proteins may be in an excitable state within the cell (20% estimated for GFP [39], and likely much less for the fast maturing mVenus). Therefore, obtained numbers are also technically an underestimate of actual numbers within the cells.

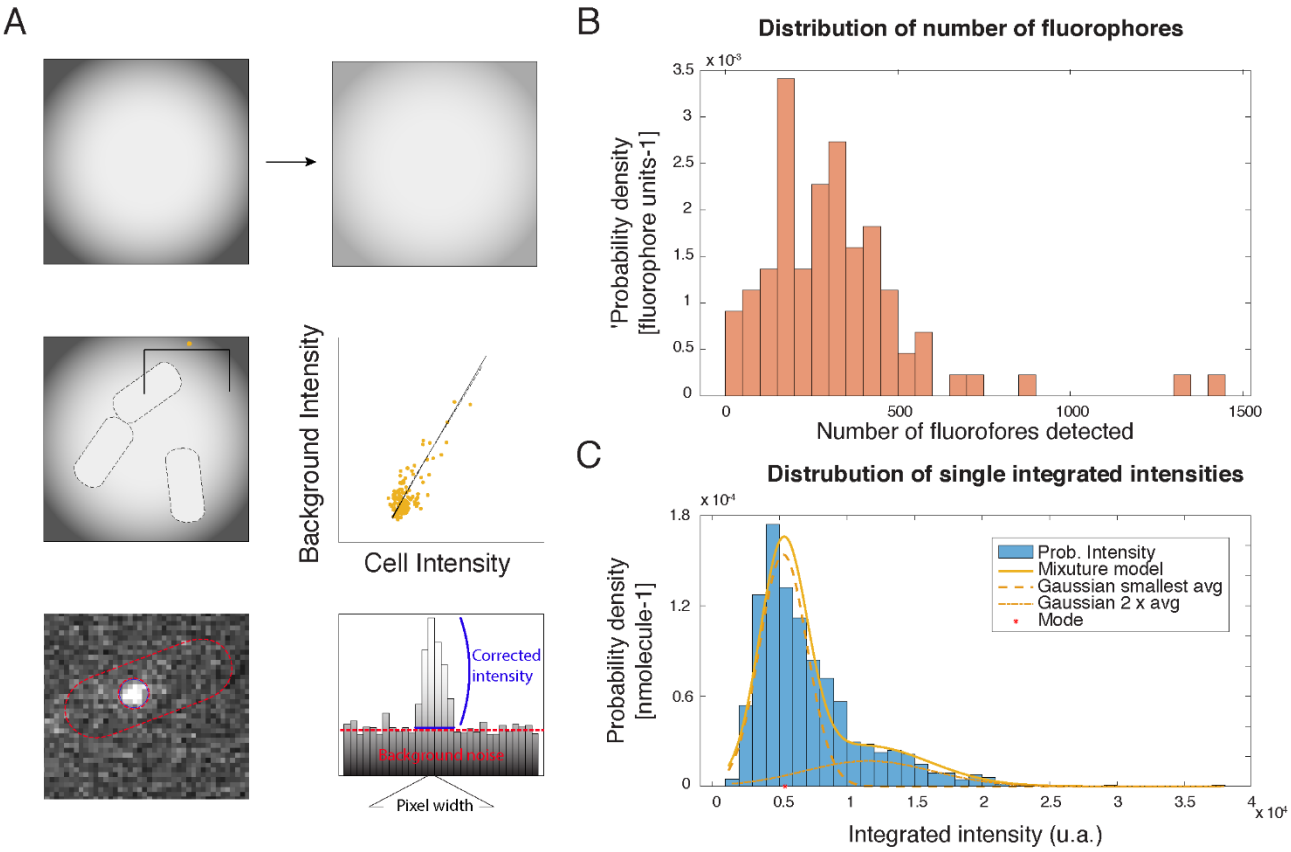

Figure 5. Automated fluorescence-based quantification of RNase Y molecule copy number. A) Scheme of the procedure to quantify the number of fluorophores in the movies, where first a correction of the irregular illumination is made (first row), then an estimation of the autofluorescence using the relationship between cells lacking any fluorescent protein fusion and background (second row) and finally, estimation of the fluorescent intensity of the spots using as center the detected position of the protein in the track detection algorithm inside a circle of radius 3 pixels. B) Distribution density function of the number of detected fluorophores in all cells. C) Distribution density function of 2004 integrated spot intensities. In the best estimation, there are two populations of average integrated intensity I_1 ~= 5284 and I_2 ~= 11326 u.a., with a proportion of 68% / 32%, suggesting dimerization of RNase Y. Estimation of number of fluorophores after accounting for dimer formation and simulation corrections = 485.

Active transcription affects subcellular diffusion of RNase Y

A tool we term “Binned speed map” can visualize average diffusion constants in the cell with 100 nm resolution. Fig. 6 reveals that diffusion of RNase Y is much slower close to the cell membrane than within the cell center. While this is likely based on the formation of RNA degradosome complexes containing RNase Y, leading to confined motion, we note that differences in diffusion constants span from close to zero to 0.65 $\mu m^2/s$. This considerable difference is largely lost upon inhibition of transcription (Fig. 6C), showing that RNA synthesis strongly affects the subcellular diffusion of RNase Y, and possibly of other proteins. We believe that this tool will be of high relevance for scientists studying subcellular movement of molecules within live cells.

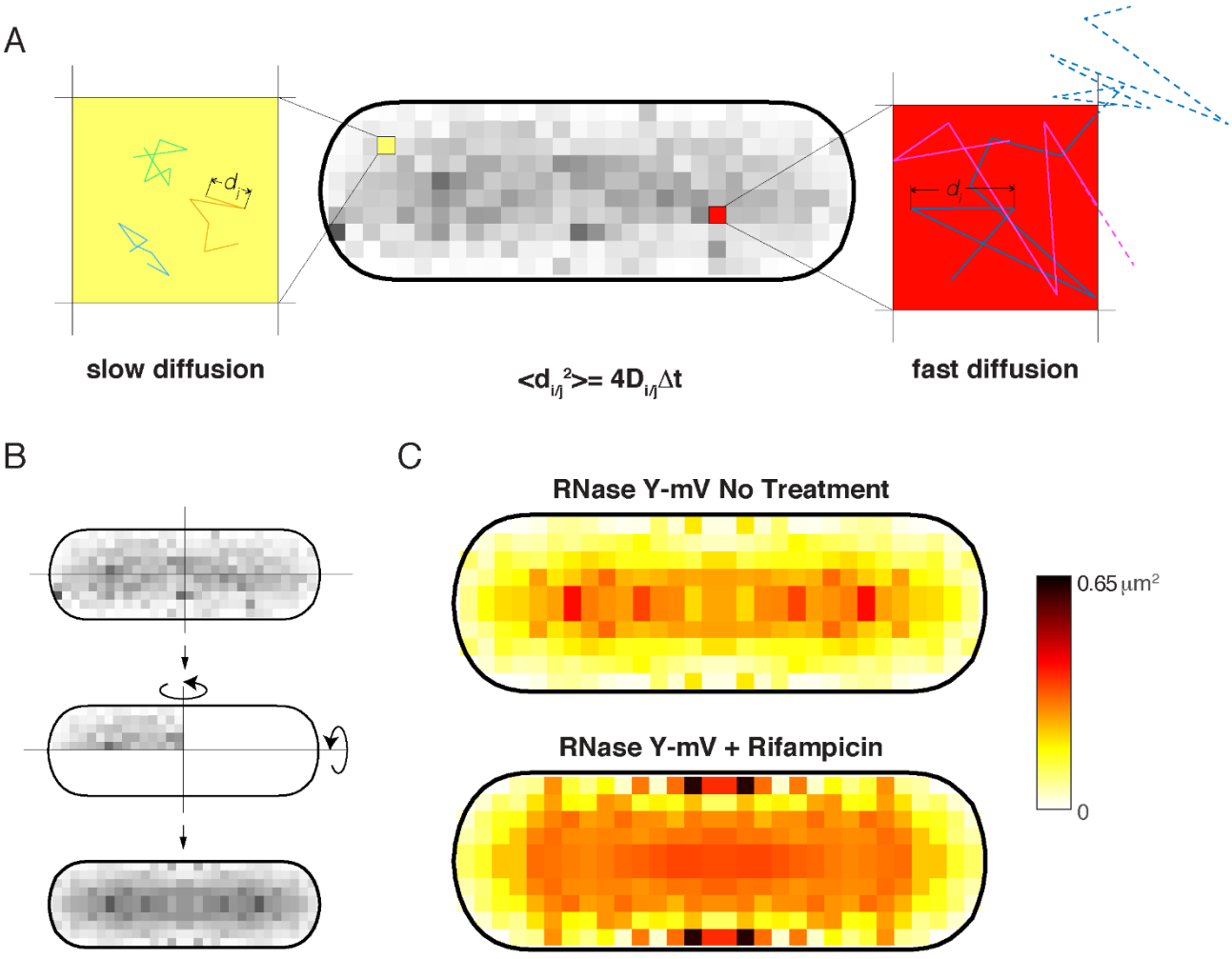

Figure 6. Binned speed maps. A) Average of the apparent diffusion from each two consecutives detections of all trajectories has been calculated and binned in a grid of 100 nm. B) Considering the absence of polarization, the map has been mirrored for a better visualization. C) Binned speed maps applied to RNase Y before and after Rifampicin treatment.

Absence of PfkA, and to a minor degree of RNase J2, leads to strong differences in RNase Y molecule dynamics

We did not observe strong changes in RNase J1, RNase J2 and PfkA molecules upon inhibition of transcription (Fig. 2 and 3). Because this does not necessarily mean that a small number of molecules may be implicated in the formation of the RNA degradosome, we used changes of RNase Y dynamics as an indicator of whether RNase J2 and PfkA may influence RNA degradosome motility by tracking RNase Y-mVenus in the corresponding deletion strains {note that a strain lacking RNase J1 is not viable [34]}. Fig. 7A shows that RNase Y single molecule dynamics were markedly altered in the absence of PfkA, and to a minor degree in cells lacking RNase J2. Please note that in order to better compare changes in dynamics, D values best-fitting for all three types of cells were determined and kept constant, such that only fraction sizes vary. Thus, in reality, D as well as population sizes are different, but in our analyses, we consider changes in molecule dynamics by solely projecting them into changes in fraction sizes. This is a further handy possibility of SMTracker 2.0. For this reason, numbers between Fig. 2 and Fig. 7 are slightly different. Clearly, in Δ*pfkA* cells, the size of the static/slow mobile of RNase Y molecules increased considerably, from about 40 to 56% (Fig. 7B, Table 2). Therefore, RNase Y became considerably more static in the absence of PfkA. A similar but smaller effect was seen in Δ*rnjB* cells (Fig. 7A and B). Possibly, RNase Y molecules become less efficient in the absence of PfkA or RNase J2, or can less efficiently change between bound and rebound states.

Interestingly, in mutant cells, the step size distribution of RNase Y could be better explained assuming three populations (Fig. 7A). The triple fit shown in blue describes observed data much better than the double fit shown in red. This finding is very valuable, because it reflects the importance of verifying single molecule tracking data by different types of analyses, and optimally under different conditions or mutant backgrounds. Assuming three populations for RNase Y does not violate the empirical probability density functions (pdfs) of the steps taken by molecules, but may be overfitting of data, while this is not the case for the data obtained from the two mutant strains. Assuming three populations could reflect RNase Y molecules being positioned in the membrane-associated RNA degradosome (static), molecules possibly being associated with the Y-complex (medium-mobile), and molecules freely diffusing along the membrane or through the cell (high mobile). Further experiments are required to reveal if RNase Y may have more than 2 mobility states. This question does not compromise our findings of changes between static/slow molecules after inhibition of transcription or in mutant backgrounds. Considering

three populations, RNase Y still becomes less mobile in the absence of PfkA, and to a smaller extent in cells devoid of RNase J2: while medium-mobile fractions remain relatively similar between wild type and mutant cells, fast-mobile fractions decrease in favour of static fractions (Fig. 7B, Table 2).

Figure 7. RNase Y-mV dynamics compared between wild type cells and two different mutant backgrounds, deletion of *pfkA* or of *rnjB* (encoding for RNase J2). A) Jump Distance histograms of RNase Y-mV in wild type, *pfkA* or *rnjB* mutant cells. B) Bubble plots comparing different estimation of the number of populations. For the deletions, 3 populations seem the best option.

Figure 7. RNase Y-mV dynamics compared between wild type cells and two different mutant backgrounds, deletion of *pfkA* or of *rnjB* (encoding for RNase J2). A) Jump Distance histograms of RNase Y-mV in wild type, *pfkA* or *rnjB* mutant cells. B) Bubble plots comparing different estimation of the number of populations. For the deletions, 3 populations seem the best option.

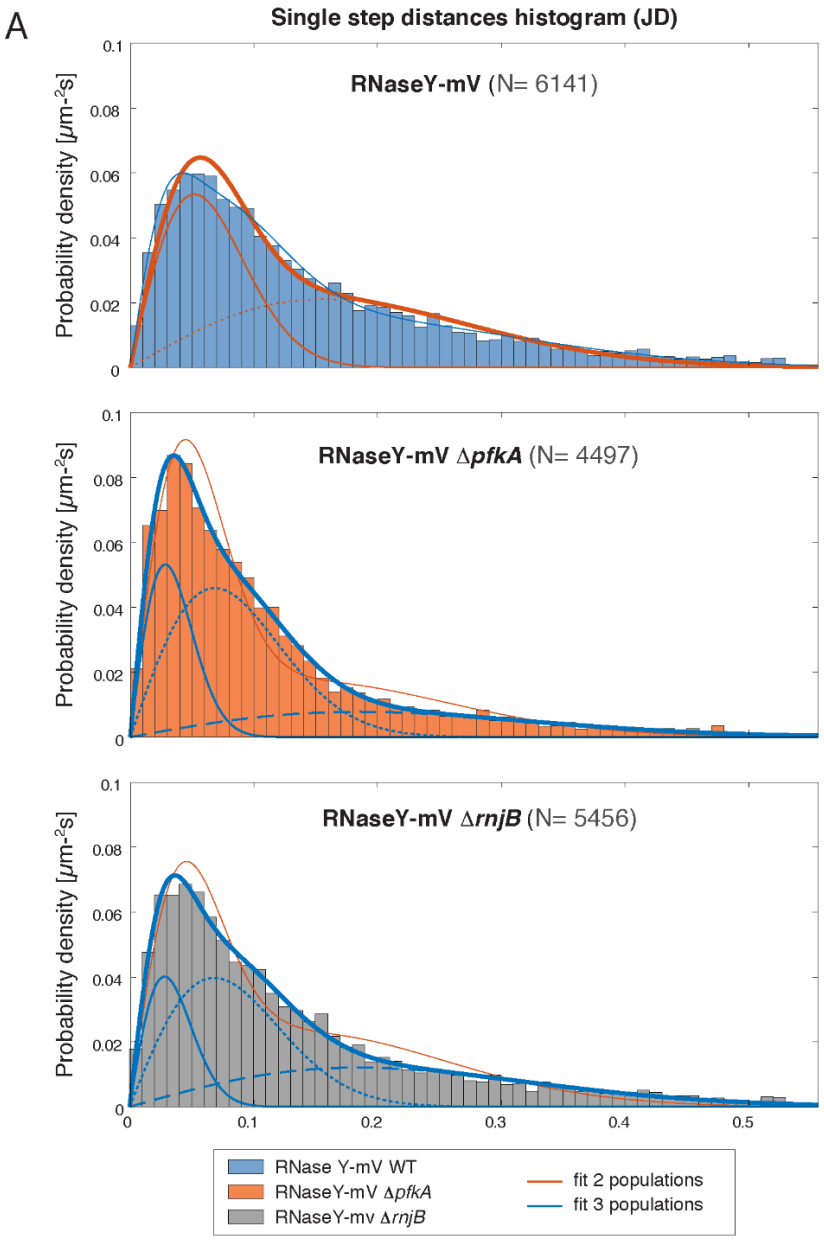
A
Single step distances histogram (JD)
RNaseY-mV (N= 6141)
RNaseY-mV ΔpfkA (N= 4497)
RNaseY-mV ΔrnjB (N= 5456)
Probability density [μm-2s]
RNase Y-mV WT
RNaseY-mV ΔpfkA
RNaseY-mv ΔrnjB
fit 2 populations
fit 3 populations

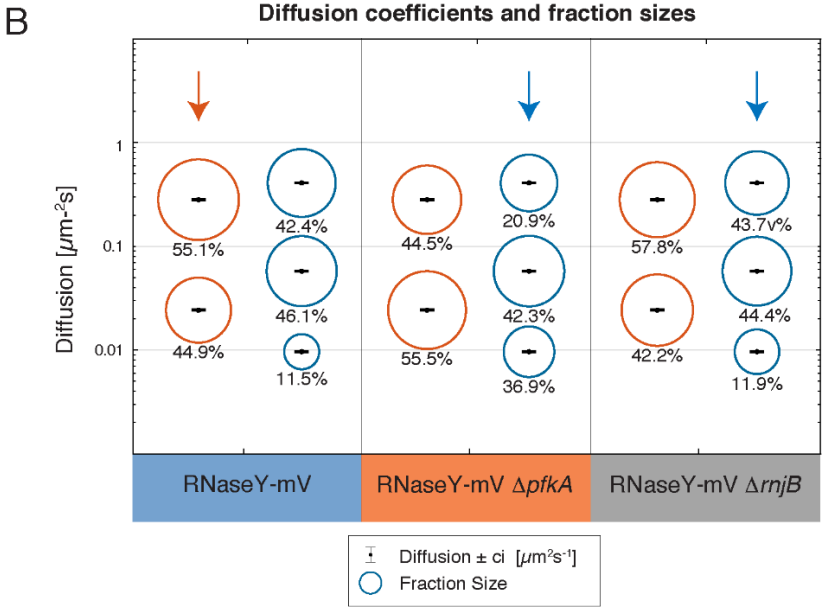
B
Diffusion coefficients and fraction sizes
Diffusion [μm-2s]
55.1%
42.4%
44.9%
46.1%
11.5%
44.5%
20.9%
55.5%
42.3%
36.9%
57.8%
43.7%
42.2%
44.4%
11.9%
RNaseY-mV
RNaseY-mV ΔpfkA
RNaseY-mV ΔrnjB
Diffusion ± ci [μm2s-1]
Fraction Size

Figure 7. RNase Y-mV dynamics compared between wild type cells and two different mutant backgrounds, deletion of *pfkA* or of *rnjB* (encoding for RNase J2). A) Jump Distance histograms of RNase Y-mV in wild type, *pfkA* or *rnjB* mutant cells. B) Bubble plots comparing different estimation of the number of populations. For the deletions, 3 populations seem the best option.

Consistent with these findings, we observed that cells expressing RNase Y-mVenus as sole source of the proteins grow with a doubling time indistinguishable from that of cells lacking the fusion (i.e. expressing wild type RNase Y), but show a growth defect in the absence of PfkA or of RNase J2 (Fig. S6), while *pfkA* or *rnjB* mutant cells grow with wild type-like doubling time. These data suggest that while the fusion of RNase Y and mVenus can complement the function of wild type RNase Y in wild type cells, absence of phosphofructokinase or of RNase J2 somewhat affects the activity of the fusion protein.

In summary, our data indicate that the absence of Phosphofructokinase has a noticeable effect on the motion of RNase Y, suggesting that PfkA does play a role in the formation of RNA degradosome, and likewise RNase J2, albeit not a pivotal role. We propose that both proteins are only peripherally associated with the degradosome and may optimize RNaseY activity, directly or indirectly.

2.1.5. DISCUSSION

Single molecule tracking is a highly powerful method. It has greatly increased the resolution scientists can employ to study protein localization, interaction and dynamics in live cells [40]. Biochemical experiments have put forward evidence suggesting that RNase Y from *B.-subtilis* forms a complex implicated in general mRNA decay at the cell membrane, involving different RNases, an RNA helicase as well as two glycolytic enzymes [38, 41, 42]. Cell biological evidence for this could not be obtained from conventional fluorescence microscopy [11]. Here, we provide evidence that PNPase, helicase CshA and enolase change their subcellular dynamics in a way similar to RNase Y upon depletion of mRNA, and also lose membrane-proximal confined motion similar to RNase Y, strongly indicating that many PNPase, CshA and enolase molecules are present within the membrane-associated RNA degradosome complexes. This agrees with a direct interaction of RNase Y and PNPase [43], and with interaction of CshA with RNase Y, PNPase, enolase and phosphofructokinase [41]. For phosphofructokinase and RNase J2, we obtained more indirect, nevertheless convincing evidence that they participate in RNase Y-associated activities, as suggested by two hybrid analyses [6], using SMT.

Several powerful programs exist that are helpful in analyzing and visualizing SMT data [44-46]. With SMTracker (version 1), we sought to establish a GUI that allows non-specialists to obtain information on single molecule dynamics. Here, we present SMTracker 2.0, a version that contains novel tools that greatly enhance the versatility of this analytic program. These features include determination of diffusion constants via mean squared displacement (MSD), squared displacement (SQD, which can be visually represented by jump distance – JD - analysis), apparent diffusion (AppD), as well as Gaussian mixture modelling (GMM). SQD/JD, AppD and GMM can be used to determine if molecule motion indicates one or several populations of molecules with distinct diffusion constants (up to 3 populations can be fitted), and several statistical tests and Bayesian information criterion (BIC) are employed to avoid overfitting of data. Abundance of tracks within a standardized cell can be visualized by “heat maps”, and “speed maps” visualize subcellular localization of populations having distinct diffusion constants. SMTracker 2.0 contains a tool for automated molecule counting, which we show performs well, especially for low-expressed proteins [14], and must be corrected because of underestimation of maximum 15% molecules per cell at high copy number (from 40 to 500). We have also developed a tool visualizing molecule tracks that remain confined by a certain number of steps within a chosen radius (which can be suggested by the program dependent on the localization error multiplied by a factor of

three), of molecules showing no confinement, and molecules showing transitions between confined and freely diffusive motion. All three patterns of movement can be quantified, such that percentage of e.g. transitions between bound and diffusive motion can be determined, for example for a given molecule under normal and stress conditions, or for a protein binding to and unbinding from a protein complex. To further investigate different modes of diffusion, we have included MSD-based analyses of tracks to determine if Brownian motion, sub – or superdiffusion may underlay molecule movement, which we have e.g. employed to analyse motion of actin-like MreB protein at a single molecule level [15]. A further handy tool we have developed is the ability to study proximity of proteins and defined subcellular sites. For example, we have used this tool to show that DNA polymerase A (analogue of DNA Pol I in *E. coli*) is rarely present at the replication fork, and is recruited to this multiprotein complex upon induction of DNA damage [17].

Using SMTracker 2.0, we show that the proposed RNA degradosome centered around RNase Y may consist of RNase Y and enolase, and helicase CshA that we have not investigated here, and may contain molecules of RNase J1 and J2, or of PfkA, but likely only in a substoichiometric amount and/or highly transient manner. The latter molecules might interact in a low-affinity manner, e.g. when they find substrate at the RNase Y/enolase structures, but based on a very different behaviour at a single molecule level are not stoichiometric complex partners. We show that RNase Y is present at an average copy number of about 500 (after correction by 15% for underperformance above 20 molecules per cell, and additionally for observed dimerization) molecules per cell, comparable to the number determined by mass spectrometry analyses [37]. We show that about 46% of RNase Y molecules are statically positioned, e.g. likely in a substrate/degradosome-bound state, and thus, about 223 molecules of RNase Y are in this state on average. Corroborating *in vitro* data [38], we provide evidence suggesting that RNase Y forms dimers *in vivo*, based on the detection of single particles containing twice the fluorescence intensity of single RNase Y molecules, which bleach in a single step. Assuming that RNase Y operates as a dimer within the RNA degradosome, our data suggest that there are about 112 of such structures on average in a growing cell, or fewer containing more than RNase Y dimers). Given the abundance of mRNA within growing cells, these structures must be highly efficient to ensure timely degradation of mRNA.

RNase Y shows at least two diffusive populations: a low mobile/static fraction and a mobile/diffusive fraction, which also holds true for the other degradosome components. RNase Y and enolase become much more mobile in response to tuning down of

transcription, suggesting that in the absence of substrate, they lose static motion within the degradosomes. This behaviour was not found for RNase J1 and J2, nor for PfkA. However, we observed that in the absence of PfkA or of RNase J2, the mobility of RNase Y molecules is considerably altered, in that they become more static. These data suggest that RNase J2 and PfkA may affect the efficiency of active RNase Y molecules, or may influence RNase Y turnover in terms of unbinding and rebinding to mRNA substrate, and suggest that they do play a role within the RNA degradosome. This was supported by genetic experiments, in which cells expressing an RNaseY-mVenus fusion as sole source of the protein grow indistinguishable from cells expressing wild type RNase Y, but grow slower in the absence of PfkA or of RNase J2. These findings support the idea that PfkA and RNase J2 increase the activity of RNase Y, which in case of the fusion protein is no longer optimal in cells lacking the degradosome components [42].

Interestingly, motion at the single molecule level of RNase Y can be better explained by assuming three different populations of molecules with distinct diffusion coefficients in case of mutant cells. We suggest that this is also true for wild type cells, but is difficult to see, possibly because of transition of RNase Y between different mobility states or present in different complexes. In case of three populations, we would like to suggest that besides degradosome-engaged (static) molecules and freely diffusive molecules, the intermediate mobility state may correspond to RNase Y present within the Y-complex, which may have distinct functions from those in the degradosome, or that RNase Y can bind to mRNA within the cytosol or at the cell membrane, and guide it to the nearest degradosome or initiate a new degradosome. These findings suggest that RNase Y may have a more complex role within the cell, rather than being bound to the degradosome or not, and indicate that future experiments using single molecule microscopy in different genetic backgrounds may shed further light onto the spatiotemporal mode of mRNA decay and its regulation in bacteria.

In *E. coli* and other bacteria, RNase E forms the central part of the RNA degradosome, which contains additional RNases, an RNA helicase, and enolase [4, 10, 47]. Our data strongly support the idea that enolase plays a similar role in *B. subtilis* and other bacteria that contain RNase Y instead of RNase E, and thus is also a moonlighting protein in *B. subtilis,* as has been proposed before based on interaction studies [6]. Proposed degradosome components RNase J1 and J2, and PfkA were identified from crosslinked cell extracts, and from two hybrid analyses. Our single molecule analyses support their involvement in RNase Y activity, but suggest that they are only peripherally associated with

RNase Y. It will be highly interesting how members of this obviously very dynamic machinery co-operate at a molecular level.

CONFLICT OF INTEREST

The authors declare that there is no conflict of interest.

FUNDING

This work has been supported by the Centre for Synthetic Microbiology (SYNMIKRO), funded by the LOEWE Program of the state of Hessen, and by consortium TRR 174 funded by the Deutsche Forschungsgemeinschaft (DFG).

SUPPLEMENTARY DATA

Supplementary Data are available at NAR online.

2.1.6. REFERENCES

1. Laalami, S. and Putzer, H. (2011) mRNA degradation and maturation in prokaryotes: the global players. *Biomol. Concepts*, **2**, 491-506.
2. Mohanty, B.K. and Kushner, S.R. (2016) Regulation of mRNA Decay in Bacteria. *Annu. Rev. Microbiol.*, **70**, 25-44.
3. Hui, M.P., Foley, P.L. and Belasco, J.G. (2014) Messenger RNA degradation in bacterial cells. *Annu. Rev. Genet.*, **48**, 537-559.
4. Bandyra, K.J., Bouvier, M., Carpousis, A.J. and Luisi, B.F. (2013) The social fabric of the RNA degradosome. *Biochim. Biophys. Acta*, **1829**, 514-522.
5. Shahbabian, K., Jamalli, A., Zig, L. and Putzer, H. (2009) RNase Y, a novel endoribonuclease, initiates riboswitch turnover in *Bacillus subtilis*. *EMBO J.*, **28**, 3523-3533.
6. Commichau, F.M., Rothe, F.M., Herzberg, C., Wagner, E., Hellwig, D., Lehnik-Habrink, M., Hammer, E., Volker, U. and Stülke, J. (2009) Novel activities of glycolytic enzymes in *Bacillus subtilis*: interactions with essential proteins involved in mRNA processing. *Mol. Cell. Proteomics*, **8**, 1350-1360.
7. Lehnik-Habrink, M., Schaffer, M., Mader, U., Diethmaier, C., Herzberg, C. and Stulke, J. (2011) RNA processing in *Bacillus subtilis*: identification of targets of the essential RNase Y. *Mol. Microbiol.*, **81**, 1459-1473.
8. DeLoughery, A., Dengler, V., Chai, Y. and Losick, R. (2016) Biofilm formation by *Bacillus subtilis* requires an endoribonuclease-containing multisubunit complex that controls mRNA levels for the matrix gene repressor SinR. *Mol. Microbiol.*, **99**, 425-437.
9. DeLoughery, A., Lalanne, J.B., Losick, R. and Li, G.W. (2018) Maturation of polycistronic mRNAs by the endoribonuclease RNase Y and its associated Y-complex in *Bacillus subtilis*. *Proc. Natl. Acad. Sci. U S A*, **115**, E5585-E5594.
10. Strahl, H., Turlan, C., Khalid, S., Bond, P.J., Kebalo, J.M., Peyron, P., Poljak, L., Bouvier, M., Hamoen, L., Luisi, B.F. *et al.* (2015) Membrane recognition and dynamics of the RNA degradosome. *PLoS Genet.*, **11**, e1004961.
11. Cascante-Estepa, N., Gunka, K. and Stulke, J. (2016) Localization of Components of the RNA-Degrading Machine in *Bacillus subtilis*. *Front. Microbiol.*, **7**, 1492.
12. Hamouche, L., Billaudeau, C., Rocca, A., Chastanet, A., Ngo, S., Laalami, S. and Putzer, H. (2020) Dynamic Membrane Localization of RNase Y in *Bacillus subtilis*. *mBio*, **11**.
13. Khemici, V., Poljak, L., Luisi, B.F. and Carpousis, A.J. (2008) The RNase E of *Escherichia coli* is a membrane-binding protein. *Mol. Microbiol.*, **70**, 799-813.

14. Kunz, S., Tribensky, A., Steinchen, W., Oviedo-Bocanegra, L., Bedrunka, P. and Graumann, P.L. (2020) Cyclic di-GMP Signaling in *Bacillus subtilis* Is Governed by Direct Interactions of Diguanylate Cyclases and Cognate Receptors. *mBio*, **11**.

15. Dersch, S., Mehl, J., Stuckenschneider, L., Mayer, B., Roth, J., Rohrbach, A. and Graumann, P.L. (2020) Super-Resolution Microscopy and Single-Molecule Tracking Reveal Distinct Adaptive Dynamics of MreB and of Cell Wall-Synthesis Enzymes. *Front. Microbiol.*, **11**, 1946.

16. Burghard-Schrod, M., Altenburger, S. and Graumann, P.L. (2020) The *Bacillus subtilis* dCMP deaminase ComEB acts as a dynamic polar localization factor for ComGA within the competence machinery. *Mol. Microbiol.*, **113**, 906-922.

17. Hernandez-Tamayo, R., Oviedo-Bocanegra, L.M., Fritz, G. and Graumann, P.L. (2019) Symmetric activity of DNA polymerases at and recruitment of exonuclease ExoR and of PolA to the *Bacillus subtilis* replication forks. *Nucleic Acids Res.*, **47**, 8521-8536.

18. Rosch, T.C., Altenburger, S., Oviedo-Bocanegra, L., Pediaditakis, M., Najjar, N.E., Fritz, G. and Graumann, P.L. (2018) Single molecule tracking reveals spatio-temporal dynamics of bacterial DNA repair centres. *Sci. Rep.*, **8**, 16450.

19. Jaacks, K., Healy, J., Losick, R. and Grossman, A.J.J.o.b. (1989) Identification and characterization of genes controlled by the sporulation-regulatory gene spo0H in *Bacillus subtilis*. **171**, 4121-4129.

20. Lucena, D., Mauri, M., Schmidt, F., Eckhardt, B. and Graumann, P.L.J.B.b. (2018) Microdomain formation is a general property of bacterial membrane proteins and induces heterogeneity of diffusion patterns. **16**, 1-17.

21. Gibson, D.J.P.E. (2009) One-step enzymatic assembly of DNA molecules up to several hundred kilobases in size. **6**, 343-345.

22. Koo, B.-M., Kritikos, G., Farelli, J.D., Todor, H., Tong, K., Kimsey, H., Wapinski, I., Galardini, M., Cabal, A. and Peters, J.M.J.C.s. (2017) Construction and analysis of two genome-scale deletion libraries for *Bacillus subtilis*. **4**, 291-305. e297.

23. Mascarenhas, J., Soppa, J., Strunnikov, A.V. and Graumann, P.L.J.T.E.j. (2002) Cell cycle-dependent localization of two novel prokaryotic chromosome segregation and condensation proteins in *Bacillus subtilis* that interact with SMC protein. **21**, 3108-3118.

24. Schindelin, J., Rueden, C., Hiner, M. and Eliceiri, K. (2015).

25. Paintdakhi, A., Parry, B., Campos, M., Irnov, I., Elf, J., Surovtsev, I. and Jacobs-Wagner, C.J.M.m. (2016) Oufti: an integrated software package for high-accuracy, high-throughput quantitative microscopy analysis. **99**, 767-777.

26. Jaqaman, K., Loerke, D., Mettlen, M., Kuwata, H., Grinstein, S., Schmid, S.L. and Danuser, G.J.N.m. (2008) Robust single-particle tracking in live-cell time-lapse sequences. **5**, 695.

27. Rösch, T.C., Oviedo-Bocanegra, L.M., Fritz, G. and Graumann, P.L.J.S.r. (2018) SMTracker: a tool for quantitative analysis, exploration and visualization of single-molecule tracking data reveals highly dynamic binding of *B. subtilis* global repressor AbrB throughout the genome. **8**, 1-12.

28. Schenk, K., Hervas, A.B., Rosch, T.C., Eisemann, M., Schmitt, B.A., Dahlke, S., Kleine-Borgmann, L., Murray, S.M. and Graumann, P.L. (2017) Rapid turnover of DnaA at replication origin regions contributes to initiation control of DNA replication. *PLoS Genet.*, **13**, e1006561.

29. Persson, F., Linden, M., Unoson, C. and Elf, J. (2013) Extracting intracellular diffusive states and transition rates from single-molecule tracking data. *Nat. Methods*, **10**, 265-269.

30. Figaro, S., Durand, S., Gilet, L., Cayet, N., Sachse, M. and Condon, C. (2013) *Bacillus subtilis* mutants with knockouts of the genes encoding ribonucleases RNase Y and RNase J1 are viable, with major defects in cell morphology, sporulation, and competence. *J. Bacteriol.*, **195**, 2340-2348.

31. Sanamrad, A., Persson, F., Lundius, E.G., Fange, D., Gynna, A.H. and Elf, J. (2014) Single-particle tracking reveals that free ribosomal subunits are not excluded from the *Escherichia coli* nucleoid. *Proceedings of the National Academy of Sciences of the United States of America*, **111**, 11413-11418.

32. Schibany, S., Kleine Borgmann, L.A.K., Rosch, T.C., Knust, T., Ulbrich, M.H. and Graumann, P.L. (2018) Single molecule tracking reveals that the bacterial SMC complex moves slowly relative to the diffusion of the chromosome. *Nucleic Acids Res.*, **46**, 7805-7819.

33. Bandow, J.E., Brotz, H. and Hecker, M. (2002) *Bacillus subtilis* tolerance of moderate concentrations of rifampin involves the sigma(B)-dependent general and multiple stress response. *J. Bacteriol.*, **184**, 459-467.

34. Price, A.R. and Frabotta, M. (1972) Resistance of bacteriophage PBS2 infection to rifampicin, an inhibitor of *Bacillus subtilis* RNA synthesis. *Biochem. Biophys. Res. Commun.*, **48**, 1578-1585.

35. Durand, S., Gilet, L., Bessieres, P., Nicolas, P. and Condon, C. (2012) Three essential ribonucleases-RNase Y, J1, and III-control the abundance of a majority of *Bacillus subtilis* mRNAs. *PLoS Genet.*, **8**, e1002520.

36. Uphoff, S., Lord, N.D., Okumus, B., Potvin-Trottier, L., Sherratt, D.J. and Paulsson, J. (2016) Stochastic activation of a DNA damage response causes cell-to-cell mutation rate variation. *Science*, **351**, 1094-1097.

37. Bremer, H. and Dennis, P.P. (2008) Modulation of Chemical Composition and Other Parameters of the Cell at Different Exponential Growth Rates. *EcoSal Plus*, **3**.

38. Muntel, J., Fromion, V., Goelzer, A., Maabeta, S., Mader, U., Buttner, K., Hecker, M. and Becher, D. (2014) Comprehensive absolute quantification of the cytosolic proteome of *Bacillus subtilis* by data independent, parallel fragmentation in liquid chromatography/mass spectrometry (LC/MS(E)). *Mol. Cell Proteomics*, **13**, 1008-1019.

39. Lehnik-Habrink, M., Newman, J., Rothe, F.M., Solovyova, A.S., Rodrigues, C., Herzberg, C., Commichau, F.M., Lewis, R.J. and Stulke, J. (2011) RNase Y in *Bacillus subtilis*: a Natively disordered protein that is the functional equivalent of RNase E from *Escherichia coli*. *J. Bacteriol.*, **193**, 5431-5441.

40. Ulbrich, M.H. and Isacoff, E.Y. (2007) Subunit counting in membrane-bound proteins. *Nat. Methods*, **4**, 319-321.

41. Dersch, S. and Graumann, P.L. (2018) The ultimate picture-the combination of live cell superresolution microscopy and single molecule tracking yields highest spatio-temporal resolution. *Curr. Opin. Microbiol.*, **43**, 55-61.

42. Lehnik-Habrink, M., Pfortner, H., Rempeters, L., Pietack, N., Herzberg, C. and Stulke, J. (2010) The RNA degradosome in *Bacillus subtilis*: identification of CshA as the major RNA helicase in the multiprotein. complex. *Mol. Microbiol.*, **77**, 958-971.

43. Lehnik-Habrink, M., Lewis, R.J., Mader, U. and Stulke, J. (2012) RNA degradation in *Bacillus subtilis*: an interplay of essential endo- and exoribonucleases. *Mol. Microbiol.*, **84**, 1005-1017.

44. Salvo, E., Alabi, S., Liu, B., Schlessinger, A. and Bechhofer, D.H. (2016) Interaction of *Bacillus subtilis* Polynucleotide Phosphorylase and RNase Y: STRUCTURAL MAPPING AND EFFECT ON mRNA TURNOVER. *J. Biol. Chem.*, **291**, 6655-6663.

45. Lee, B.H. and Park, H.Y. (2018) HybTrack: A hybrid single particle tracking software using manual and automatic detection of dim signals. *Sci. Rep.*, **8**, 212.

46. Hansen, A.S., Woringer, M., Grimm, J.B., Lavis, L.D., Tjian, R. and Darzacq, X. (2018) Robust model-based analysis of single-particle tracking experiments with Spot-On. *Elife*, **7**.

47. Sage, D., Kirshner, H., Pengo, T., Stuurman, N., Min, J., Manley, S. and Unser, M. (2015) Quantitative evaluation of software packages for single-molecule localization microscopy. *Nat. Methods*, **12**, 717-724.

48. Carpousis, A.J., Khemici, V. and Poljak, L. (2008) Assaying DEAD-box RNA helicases and their role in mRNA degradation in *Escherichia coli*. *Methods Enzymol.*, **447**, 183-197.

Table 1. Diffusion coefficients and fraction sizes

	RNase Y	RNase Y *with Rif*
pop1 [%]	48.2 ± 0.6	9.84 ± 0.6
pop2 [%]	51.8 ± 0.3	90.2 ± 0.3
D1 [µm² s⁻¹]	0.031 ± 0.0008	
D2 [µm² s⁻¹]	0.3 ± 0.002	
	RNase J1	*RNase J1 with Rif*
pop1 [%]	38.5 ± 0.8	35.3 ± 0.8
pop2 [%]	61.5 ± 0.7	64.7 ± 0.7
D1 [µm² s⁻¹]	0.072 ± 0.002	
D2 [µm² s⁻¹]	0.69 ± 0.01	
	RNase J2	*RNase J2 with Rif*
pop1 [%]	37 ± 2	51.2 ± 2
pop2 [%]	63 ± 2	48.8 ± 2
D1 [µm² s⁻¹]	0.084 ± 0.004	
D2 [µm² s⁻¹]	0.85 ± 0.03	
	enolase	*enolase with Rif*
pop1 [%]	59.3 ± 1	14.5 ± 1
pop2 [%]	40.7 ± 0.7	85.5 ± 0.7
D1 [µm² s⁻¹]	0.022 ± 0.0007	
D2 [µm² s⁻¹]	0.26 ± 0.004	
	PfkA	*PfkA with Rif*
pop1 [%]	38.5 ± 1	28.1 ± 1
pop2 [%]	61.5 ± 1	71.9 ± 1
D1 [µm² s⁻¹]	0.087 ± 0.004	
D2 [µm² s⁻¹]	0.67 ± 0.01	
	CshA	*CshA with Rif*
pop1 [%]	39.3 ± 0.7	15.1 ± 0.7
pop2 [%]	60.7 ± 0.6	84.9 ± 0.6
D1 [µm² s⁻¹]	0.02 ± 0.0008	
D2 [µm² s⁻¹]	0.21 ± 0.003	

ε in this context means $<10^{-6}$. The low confident interval amplitude is due to the high number of data

	PNPase	*PNPase with Rif*
pop1 [%]	50 ± 0.7	30.1 ± 0.7

pop2 [%]	50 ± 0.6	69.9 ± 0.6
D1 [µm² s⁻¹]	0.026 ± 0.0006	
D2 [µm² s⁻¹]	0.3 ± 0.004	

Table 2. Diffusion coefficients and fraction sizes RNase Y upon deletion of *pfkA* or of *rnjB*

	RNase Y	RNase Y *ΔpfkA*	RNase Y *ΔrnjB*
pop1 [%]	44.9 ± 1	55.5 ± 1	42.2 ± 1
pop2 [%]	55.1 ± 1	44.5 ± 1	57.8 ± 1
D1 [µm² s⁻¹]		0.025 ± 0.001	
D2 [µm² s⁻¹]		0.29 ± 0.01	
pop1 [%]	11.5 ± 0.7	20.9 ± 0.7	11.9 ± 0.7
pop2 [%]	46.1 ± 0.9	42.3 ± 0.9	44.4 ± 0.9
pop3 [%]	42.4 ± 5	36.9 ± 5	43.7 ± 5
D1 [µm² s⁻¹]		0.0081 ± ε	
D2 [µm² s⁻¹]		0.16 ± 0.2	
D3 [µm² s⁻¹]		0.3 ± 0.2	

ε in this context means $<10^{-3}$. The low confident interval amplitude is due to the high number of data

Table 3. Dwell time estimation (min 4 steps)

	No Treatment	***+ Rifampicin***
		RNase Y
average residence time [s]	0.25 ± 0.008	0.23 ± 0.005
τ (1-comp.) [s]	0.21 ± 0.006	0.19 ± 0.004
τ_1 (2-comp.) [s]	0.18 ± 0.004	0.17 ± 0.002
Fraction τ_1 [%]	82.4 ± 3.78	86.8 ± 2.15
τ_2 (2-comp.) [s]	0.43 ± 0.048	0.43 ± 0.041
Fraction τ_2 [%]	17.6 ± 3.78	13.2 ± 2.15
		RNase J1
average residence time [s]	0.119 ± 0.003	0.121 ± 0.004
τ (1-comp.) [s]	0.1 ± 0.0025	0.099 ± 0.002
τ_1 (2-comp.) [s]	0.086 ± 0.005	0.089 ± 0.001
Fraction τ_1 [%]	62.7 ± 15	84.4 ± 2.18
τ_2 (2-comp.) [s]	0.14 ± 0.018	0.22 ± 0.017
Fraction τ_2 [%]	37.3 ± 15	15.6 ± 2.18
		RNase J2
average residence time [s]	0.121 ± 0.004	0.121 ± 0.004
τ (1-comp.) [s]	0.1 ± 0.002	0.1 ± 0.0028
τ_1 (2-comp.) [s]	0.087 ± 0.005	0.087 ± 0.001
Fraction τ_1 [%]	61.4 ± 14.2	82.4 ± 2.8
τ_2 (2-comp.) [s]	0.14 ± 0.02	0.21 ± 0.02
Fraction τ_2 [%]	38.6 ± 14.2	17.6 ± 2.8
		Enolase
average residence time [s]	0.310 ± 0.012	0.223 ± 0.005
τ (1-comp.) [s]	0.27 ± 0.008	0.19 ± 0.007
τ_1 (2-comp.) [s]	0.19 ± 0.004	0.15 ± 0.006
Fraction τ_1 [%]	56.8 ± 3.09	57.5 ± 8.56
τ_2 (2-comp.) [s]	0.42 ± 0.02	0.26 ± 0.02
Fraction τ_2 [%]	43.2 ± 3.09	42.5 ± 8.56
		PfkA
average residence time [s]	0.126 ± 0.005	0.125 ± 0.010
τ (1-comp.) [s]	0.11 ± 0.004	0.094 ± 0.002
τ_1 (2-comp.) [s]	0.078 ± 0.004	0.088 ± 0.001
Fraction τ_1 [%]	53.9 ± 7.51	92.8 ± 1.07
τ_2 (2-comp.) [s]	0.15 ± 0.01	0.41 ± 0.05
Fraction τ_2 [%]	46.1 ± 7.51	7.23 ± 1.07 %
CshA		
average residence time [s]	0.270 ± 0.007 s	0.258 ± 0.004 s
τ (1-comp.) [s]	0.23 ± 0.0063 s	0.23 ± 0.0035 s
τ_1 (2-comp.) [s]	0.2 ± 0.0059 s	0.2 ± 0.0056 s
Fraction τ_1 [%]	81.6 ± 5.29 %	76.9 ± 7.45 %
τ_2 (2-comp.) [s]	0.47 ± 0.071 s	0.36 ± 0.039 s
Fraction τ_2 [%]	18.4 ± 5.29 %	23.1 ± 7.45 %
PNPase		
average residence time [s]	0.276 ± 0.009 s	0.250 ± 0.005 s
τ (1-comp.) [s]	0.23 ± 0.005 s	0.22 ± 0.0025 s

τ_1 *(2-comp.) [s]*	0.2 ± 0.0042 s	0.18 ± 0.0056 s
Fraction τ_1 *[%]*	83.8 ± 3.53 %	58.4 ± 8 %
τ_2 *(2-comp.) [s]*	0.5 ± 0.058 s	0.29 ± 0.016 s
Fraction τ_2 *[%]*	16.2 ± 3.53 %	41.6 ± 8 %

2.1.7. Supplementary Material

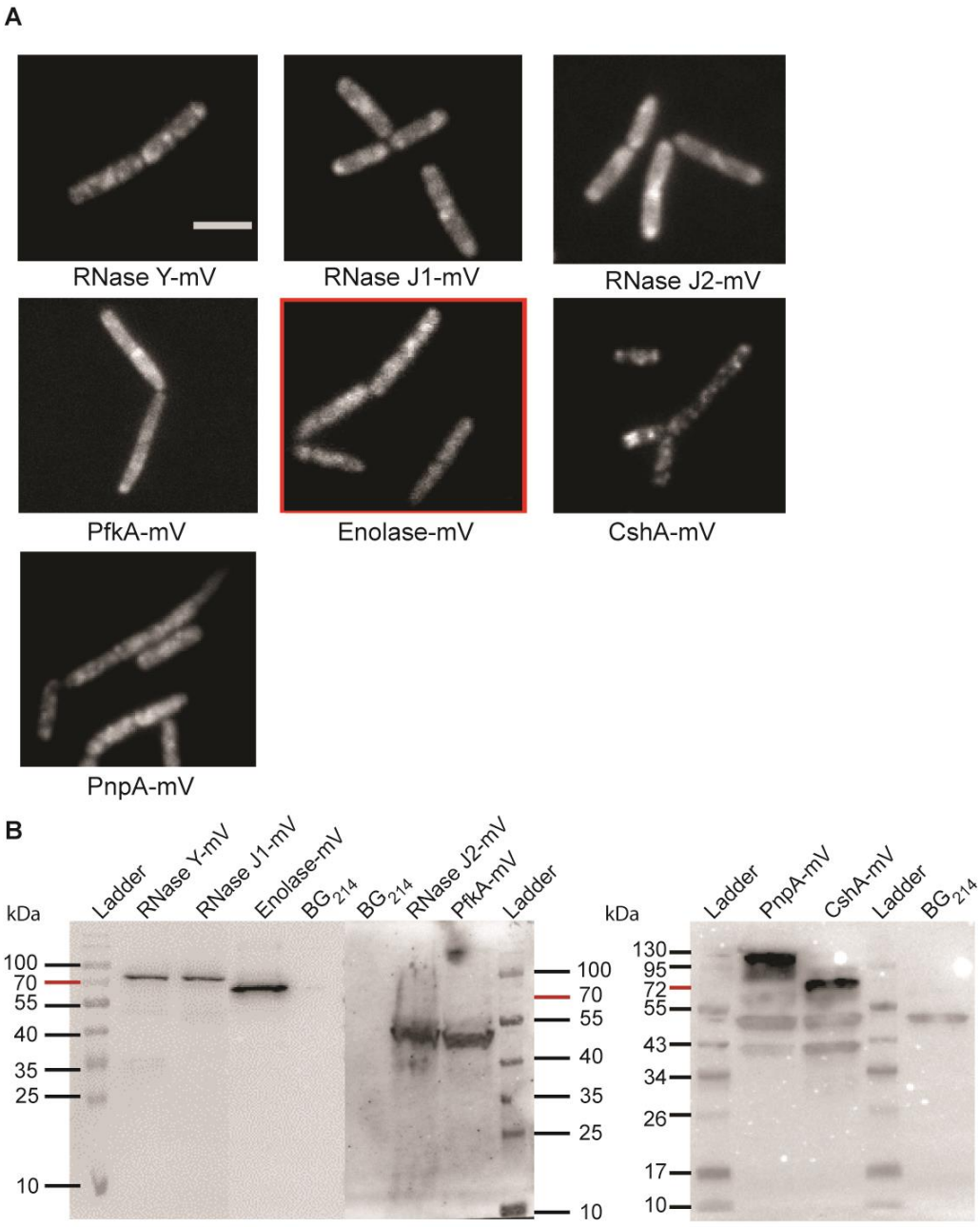

Figure S1. Localization of degradasome proteins by epifluorescence (A) RNase Y-mV, RNase J1-mV, RNase J2-mV, PfkA-mV, CshA-mV, PnpA-mV were expressed from the native locus. Enolase-mV (red frame) was ectopically induced (low expression) under a xylose promoter. Cells were incubated until mid-exponential phase. White bars 2 µm. (B) Western blots of the mVenus-fusions. Among the protein sizes, 26.9 kDa are calculated for the fluorescent protein (mVenus). RNase Y-mV (85.65 kDa), RNase J1 (88.24 kDa), RNase J2 (83.57 kDa), PfkA (61 kDa), Enolase (73.32 kDa), CshA (57.11 kDa), PnpA (77.28 kDa), BG214 wild type cells as negative control.

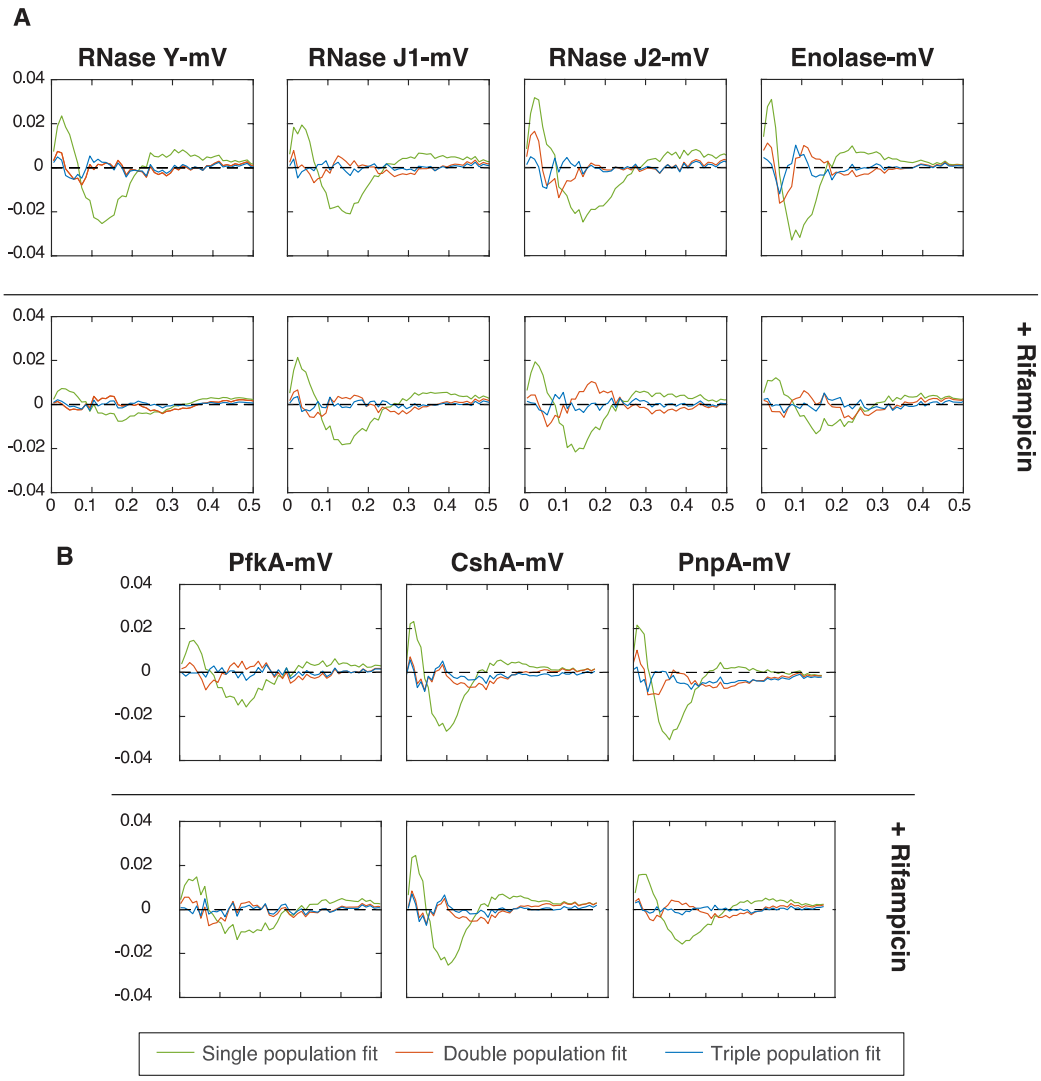

Figure S2. Residuals (difference between empirical data and the fitted model) obtained on the test dataset from the Squared Distance Analysis, for one (green), two (red) and three (blue) different diffusive populations.

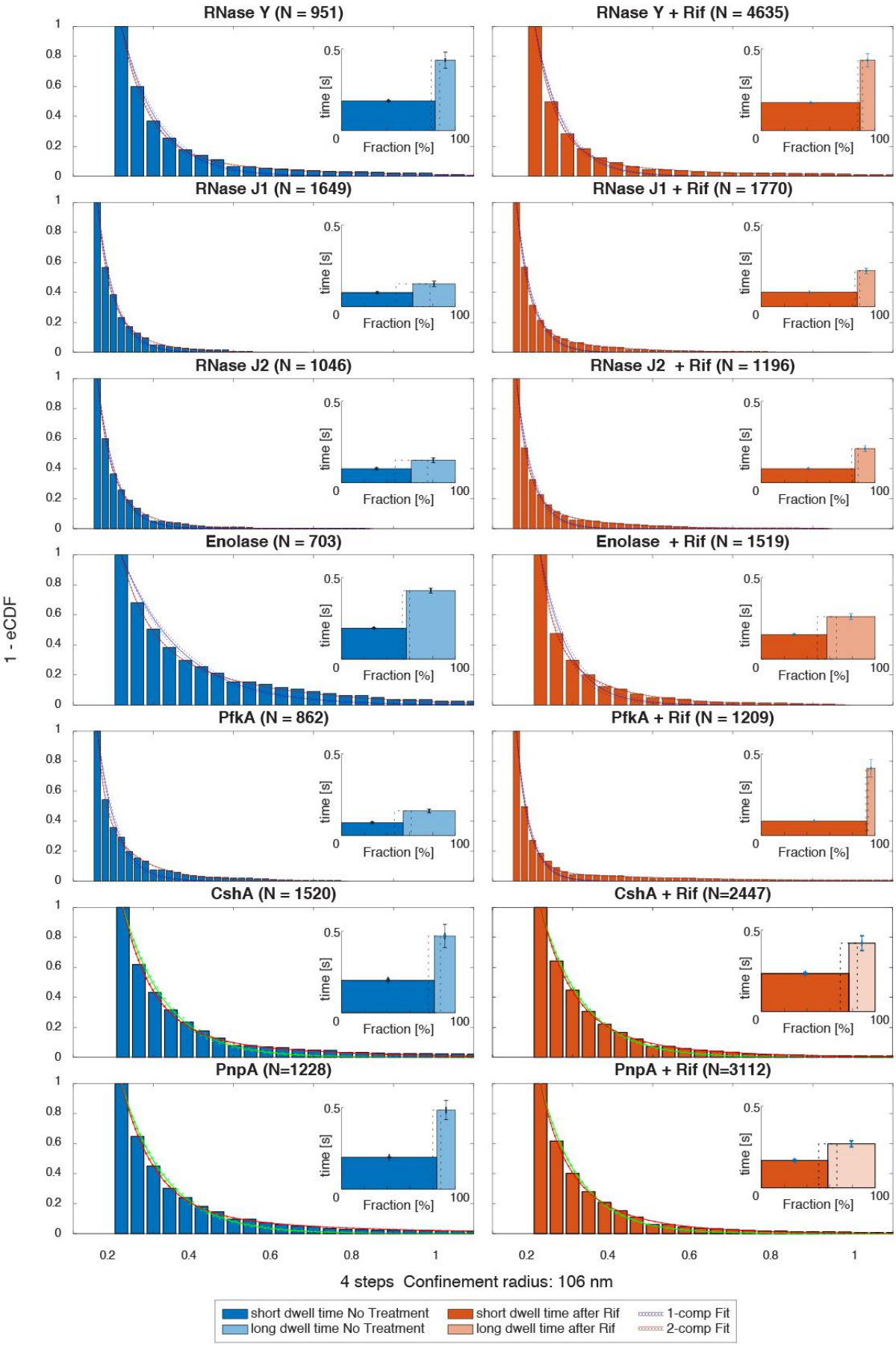
RNase Y (N = 951)
RNase Y + Rif (N = 4635)
RNase J1 (N = 1649)
RNase J1 + Rif (N = 1770)
RNase J2 (N = 1046)
RNase J2 + Rif (N = 1196)
Enolase (N = 703)
Enolase + Rif (N = 1519)
PfkA (N = 862)
PfkA + Rif (N = 1209)
CshA (N = 1520)
CshA + Rif (N=2447)
PnpA (N=1228)
PnpA + Rif (N=3112)
1 - eCDF
time [s]
Fraction [%]
4 steps Confinement radius: 106 nm
short dwell time No Treatment
long dwell time No Treatment
short dwell time after Rif
long dwell time after Rif
1-comp Fit
2-comp Fit

Figure S3 Determination of dwell times, for each protein as indicated within the panels, without and after Rifampicin treatment (in columns). Inlets show mean dwell times and proportion as a result of a double exponential decay fit to the survival function (probability of molecules confined at least a certain amount of time). Dotted areas and error bars indicate uncertainty of the parameter estimation via confidence intervals at 95%.

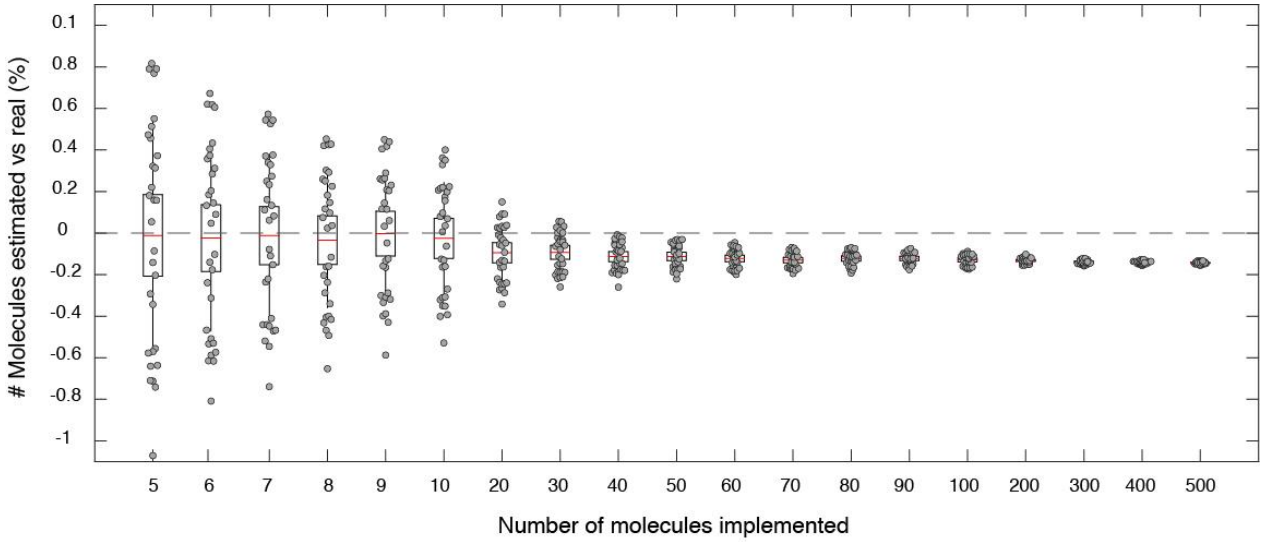

Figure S4. Simulation results for benchmarking the capabilities of the Molecule quantification tool. Shown are simulated versus estimated results and a boxplot, for which the median is marked as a red solid line. For 30 different synthetic cells, a varied number of fluorophores from 5 to 500 have been randomly inserted. The closer to 0, the better the algorithm performs. With less than 20 copies of the protein, the median remains close to 0, while a constant underfitting of 15% appears from 20 copies of the molecules, which can be used as a stable correction factor in SMTracker.

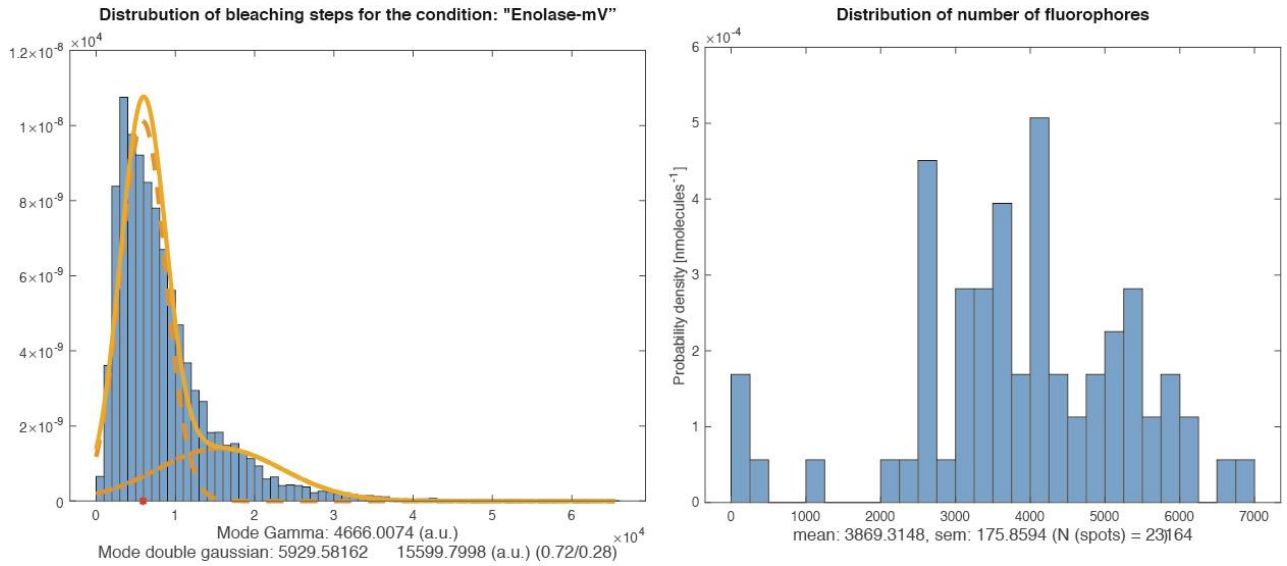

Figure S5. Automated fluorescence-based quantification of enolase molecule copy number. Left panel: distribution density function of integrated spot intensity. Distribution density function of the number of detected fluorophores in all cells. Note that a strain expressing enolase-mVenus from the original gene locus, as sole source of the protein, was used for these analyses, rather than the *amy* site-expressed fusion used for single molecule tracking experiments.

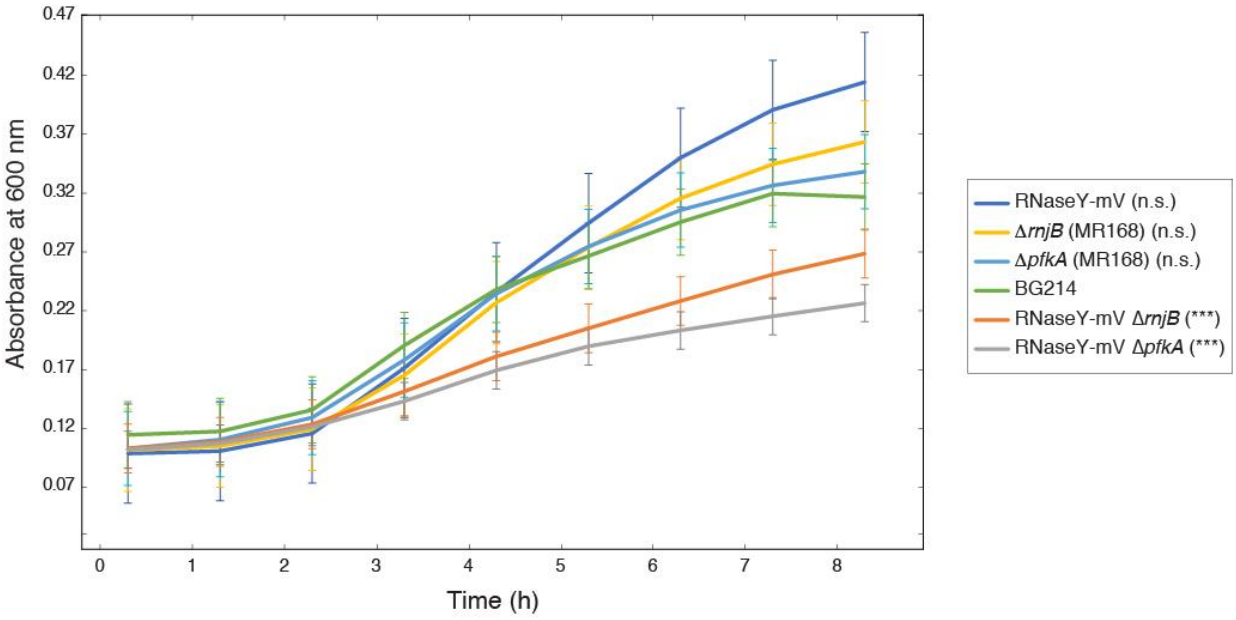

Figure S6. Growth curves for strains containing the following strains: RNase Y-mV (dark blue), RNase Y-mV Δ*rnjB* (orange, cells are lacking RNAse J2), RNase Y-mV Δ*pfkA* (grey), Δ*rnjB* (yellow), Δ*pfkA* (light blue), BG214 (green). Measurements were performed in 96-well plates with a volume of 150 µl, using a microplate reader. Differences in growth compared with the strain BG214 were statistically analysed. value: The symbols *, ** and *** represent *P*-values lower than 0.1, 0.05 and 0.01, respectively, “n.s.” statistically not significant.

Table S1 Primers used in this study

Primer	*Sequence 5´→ 3´*
PG385 1 fw	AAGGAGATTCCTAGGATGGGTACCGCTTGGTGAAGACGCAA AGCT
PG385 1 rev	CCTCCCAGGCCAGATAGGCCGGGCCCTTTTGCATACTCTAC GGCTCG
PG385 5 fw	AAGGAGATTCCTAGGATGGGTACCGATTCACGGTGAGTACAGAATGC
PG385 5 rev	CCTCCCAGGCCAGATAGGCCGGGCCCAACCTCCATAATGATCGGCA
PG385 6 fw	AAGGAGATTCCTAGGATGGGTACCGGTAAACGGCGAATACAGAAT
PG385 6 rev	CCTCCCAGGCCAGATAGGCCGGGCCCTACTTCCATAATAATTGGGATGA TC
PG404 1 fw	AAGGAGATTCCTAGGATGGGTACCGATTCGCGATACAGCGACTT
PG404 1 rev	CCTCCCAGGCCAGATAGGCCGGGCCCGATAGACAGTTCTTTTGAAAGC
PG385 7 fw	CTAGAAAGGAGATTCCTAGGATGCCATACATTGTTGATGT
PG385 5 rev	AGGCCAGATAGGCCGGGCCCCTTGTTTAAGTTGTAGAAAG

Table S2 Strains used in this study

Strain or Plasmid	*Relevant features*	*Reference or source*
B. subtilis		
BG214	Wild type	
PG3844	*rny*-mVenus^{cmR}	This study
PG3845	*rnjA*-mVenus^{cmR}	This study
PG3846	*rnjB*-mVenus^{cmR}	This study
PG3847	amyE::Pxyl-*eno*-mV	This study
PG3848	pfkA-mVenus^{cmR}	This study
PG3920	*ΔrnjB*::kan trpC2 *rny*-mVenus^{cmR}	This study
PG4040	*ΔpfkA*::kan trpC2 *rny*-mVenus^{cmR}	This study
E. coli		
DH5α	*sup*E44 Δ*lac*U169 φ80d*lac*ZΔM15 *hsd*R171 *rec*A1 *end*A1 *gyr*A96 *thi*-1 *rel*A1	New England Biolabs (NEB)
PG3730	DH5α pSG1164-mVenus, expression Vektor, Amp^R, Cm^R	(Lucena *et al*. 2018)
PG332	DH5α pSG1193-mVenus, expression Vektor, amy-locus Pxyl, Amp^R, Spec^R	(Feucht A & Lewis PJ 2001)
PG3851	DH5α pSG1164 *rny*-mVenus, expression Vektor, Amp^R, CM^R	This study
PG3855	DH5α pSG1164 *rnjA*-mVenus, expression Vektor, AmpR, CmR	This study
PG3856	DH5α pSG1164 *rnjB*-mVenus, expression Vektor, Amp^R, Cm^R	This study
PG4041	DH5α pSG1164 *pfkA*-mVenus, expression Vektor, Amp^R, Cm^R	This study
PG3857	DH5α pSG1193 eno-mVenus, expression Vektor, amy-locus Pxyl, Amp^R, Spec^R	This study

Table S3 Single molecule tracking setup parameters

Description	*Value*
Number of tracks	2000
Max number of points/track	20
Simulation time lag τ (ms)	0.02
Observation time lag (ms)	20
Number of simulation runs	30
Diffusion constant D_1 ($\mu m^2 s^{-1}$)	[0.01 0.05 0.1]
Diffusion constant D_2 ($\mu m^2 s^{-1}$)	[0.1 0.5 1]
Fraction size α (% molecules at diffusion rate D_1)	[20 40 60 80]
Localization error ξ (nm)	30

Table S4 Configuration of the synthetic trajectories

Description	*Value*
#Empirical movies with wt cells	10
#Empirical movies with wt cells to simulate autofluorescence	40
#Empirical movies with wt cells to simulate wild-type cells with FP	30
Sigma noise of spot fluorescence	50 a.u.
Typical fluorescent spot intensity	2500 ± 200 a.u.
#molecules per cell, Nmol	[5:9 10:10:100 200:100:1000]
Localization error	30 nm
#molecules added to simulate initial fluorescence	$n_1=0.9 \cdot n_{tot}$.

Supplementary Methods

1. SMTracker software updates

1.1. Stationary Localization Analysis (SLA) panel

Residence or dwell time is defined as the average duration that a particle stays inside a certain region. Observing the trajectories in this manner could give insights, for example, on how long the degradosome is bound before disassembling mRNA. For that matter, dwell times calculations need as parameters the region, in this case a circle is the type chosen, and the minimum number of steps that should remain inside the circle (1 step = 1 interval time).

The procedure operates in such a way that searches for the longest dwell events of the protein in each trajectory (a “dwell event” occurs when a trajectory has at least one consecutive subset of nodes that fulfills the conditions of minimum number and spread). Being $T = \{C_1, \dots, C_n\}$ a trajectory defined as a set of nodes $C_i = (x_i, y_i)$, and x_i, y_i the nodes coordinates in a cartesian axis, the circle $C(C_k, R)$ is chosen, -with R being the radius- that contains the maximum number of consecutive points of the trajectory. Then, the amount of time the molecule stays is stored, and the same track T excluding that segment of trajectory , $T/\{C_k, \dots, C_{k+p}\}$, is again searched for more dwell events. The procedure finishes when no more dwell events can be found. In our procedure, one gap (point absent for one frame) or one point outside the circle that goes and comes back are also considered to have remained inside the circle (for quantification purposes). The number of dwell events and their frequency is plotted in a pdf-histogram, and this data is fitted to a multi-exponential decay

$$d(t) = \sum_{i=1}^{2} \alpha_i \cdot e^{-\frac{t-t_0}{\tau_i - t_0}} \qquad (1)$$

in order to distinguish up to two different populations of dwell times events. In another plot, it is shown the average number of dwell events per length of the track + standard error.

The results of this quantification are displayed in the table as follows:

- average dwell time (s)
- The estimated dwell time for 1 pop

- Estimated dwell times for 2 populations and their percentage.

Additionally, the result of the Kolmogorov-Smirnov hypothesis test that checks whether the dwell times distributions are different compared to other conditions would be displayed in the table.

The concept of confinement or confined event happens when a protein has restricted movement for a certain amount of time, which is important to locate areas where it is interacting or to detect possible binding partners. To this end, a confinement map has been developed using the information given by the dwell times calculation algorithm. In the same way, a trajectory is considered to present confinement when it has at least one dwell event. This confinement can be total (confined track), partial (mixed behaviour), or absent (freely diffusive). Along with the confinement map, another graph is shown that holds information about the number and probability of a track of a certain length do “transitions” (transitions are defined if a protein changes its state from confined to free and vice versa). It is considered that a track has transitioned from one state to the other if the trajectory, while not in a confined state, travelled an average step distance longer than the confinement radius for at least 3 steps (3*interval time).

1.2. Mean-square displacement (MSD) analysis panel (updated)

In order to gain a better understanding of the type of motion of a protein, an individual fitting procedure to the time-averaged MSD (TAMSD) curves has been added. Given the coordinates of a trajectory with a minimum number of time lags, the TAMSD curve is obtained and fitted via non-least squares algorithm to the equation $\mathrm{MSD(t)} \sim 2\mathrm{d} \cdot \mathrm{D}_{\alpha}\, \mathrm{t}_{\alpha}$, where α is a value between 0 and 2. The results are shown in an auxiliary panel, highlighting the frequency of Brownian, super-diffusive or sub-diffusive trajectories, depending on the values of α. The decision is supported by a Statistical F-test for nested model to determine the type of motion.

1.3. Cluster Algorithms (Clustering) analysis panel (new)

To compare the overall behaviour of every diffusive group without any previous considerations, we implemented k-means into SMTracker, an unsupervised Machine Learning method to classify all trajectories via their TAMSD, and group them into subsets

(or *clusters*) depending on their distance to the centroid of each cluster. The number of clusters is set to a maximum of 6, while the optimal number of clusters is finally set using the Calinski-Harabasz criterion. This panel would be easily expandable to different types of clustering algorithms e.g., hierarchical, DBSCAN or nearest-neighbours.

1.4. Squared displacement (SQD) analysis panel (updated)

In search of more intuitive representation of the data, SQD panel has been updated with a new way of visualizing the Square-Displacement fit. Jump-Distance histograms (Weimann *et al*., 2013) have been added, along with F-test to choose the optimal number of diffusive populations.

1.5. Apparent Diffusion (APPD) analysis panel (new)

From the equation MSD(t) ~ 2·d·D_{app} t, being *d* the dimensionality of the data and D_{app} the apparent diffusion obtained from the linear fit of the MSD curve, the theoretical random variable D_{app} can be explained by a Gamma Distribution

$$f(D,n) = \frac{\left(\frac{n}{D}\right)^n x^{n-1} e^{-\frac{nx}{D}}}{(n-1)!} \tag{2}$$

(Stracy *et al*, 2015,) and similarly by a Gaussian Distribution

$$g(x|D,\sigma) := \frac{1}{\sigma\sqrt{2\pi}}\, e^{-\frac{1}{2\left(\frac{x-D}{\sigma}\right)^2}} \tag{3}$$

(Xu, M. *et al*, 2019, Zhang, M. *et al*, 2017).

Accordingly, for multiple diffusive species with diffusion constants D_i $(i = 1, \dots, q)$ and relative fractions α_i the probability density function reads

$$P(r^2,t) = \sum_{i=1}^{q} \alpha_i \cdot h(x) \tag{4}$$

where $\sum_{i=1}^{q} \alpha_i = 1$, and $h(x) = f(x|D,n)\ or\ g(x|D,\sigma)$, in the Gamma or Gaussian Distribution case respectively. For a given number of diffusive states q, the algorithm implemented in the SQD panel performs a nonlinear least-square fit of Eq. (3) to the experimental pdfs therefore estimating the α_i and D_i. On user's request, D_i could be fixed, for each $i = 1, \dots, q$, being $q = 3$ in our setup.

1.6. Spatial distribution (SDA) panel (updated)

The spatial distribution panel summarizes the localization distributions for the detections of the fluorescent protein into a cell-centric coordinate system and then scaled to a standardized cell This tool has been improved by the inclusion of new filters according to the cell size or the type of diffusion a certain trajectory has. In addition, binned heat maps to show the dynamics of a molecule related to the local position in the cell have been included.

1.7. Distance calculator tool (new)

Determining co-localization of two interacting proteins is an interesting property that can be laborious when freely diffusive proteins is the subject of study. SMTracker includes a tool that permits visualization of such events and provides a histogram to characterize the movement of a freely diffusive protein relatively to a fixed focus. For each cell, one or more foci can be selected, and it is displayed the histogram of distances from the detected trajectories to them. If several foci are marked, the distance to the closer focus is considered.

1.8. Molecule quantification tool (new)

Knowing the copy number of a protein is extremely useful to understand the function and mechanisms of it. For this purpose, we have developed a tool that estimates the number of copies of a protein based on the Single Molecule Tracking pipeline. In short, the quantification of fluorophores has two steps: The estimation of the bleaching step of a single fluorophore (A) and the measurement of the integrated intensity of the cell right after the laser illuminates the sample (B). Dividing the latter by the former will give us a good estimation of the number of fluorophores presented inside a cell. A more detailed explanation can be found below.

A. Estimation of a single bleaching step
    a) First, after having done a regular tracking procedure with minimum length of the track of 3 frames, for every frame that holds a track, the intensity would be calculated as follows:
    b) Apply illumination correction and background subtraction to the frame.

i) Set two masks, one circled mask centred on the spot exact location with diameter 6 pixels, and the other mask with the cell contour extended in 2 pixels. The median of the pixels outside the inner circle but inside the cell will be considered the whole contribution of background and subtracted to the intensity inside the inner circle.
ii) The integrated intensity of the spot is the sum of intensity per pixel inside of the inner circle.
iii) Move forward to the next frame and back to step i)
iv) Once the last frame of this track is reached, a median filter to the intensity data vs time is applied to clean noisy data. Every resulting intensity is stored.
v) A multiple Gaussian fit to the histogram of “spot intensities” is used to infer the intensity of a single fluorophore. The mean of the gaussian component with the lower order peak is considered as the best estimate for the unitary step size (like proposed by Badrinarayanan *et al*., 2012). Coffman & Wu, 2012 suggest using the mode of a Gamma Distribution.

B. Initial Integrated intensity

After background subtraction and corrected by uneven illumination and autofluorescence contribution, the average of the first two frames after the laser is on is considered.

C. Uneven Illumination correction (ratio)

In order to correct uneven illumination along the focused field, a ratio matrix has been constructed. Using movies without any cells previously corrected by instrumental background, the mean of the intensities for every pixel after the laser is on is calculated and divided by the maximum intensity. This would give for every pixel a ratio with values between 0 and 1. This matrix must divide the intensity of every frame.

D. Instrumental background subtraction (offset)

The median of the first 20 frames before the laser is on is subtracted to each frame. (offset like in Coffman *et al*, 2011)

E. Autofluorescence contribution

To estimate the amount of fluorescence that comes from cell autofluorescence, a quadratic regression model to the background signal and autofluorescence signal in wild type cells using several movies (typically 10) has been applied. Then implementing the

same model to the movies containing cells with tagged proteins we recover the autofluorescence contribution at the moment that the laser is switched on.

F. Considering both types of correction, the measured intensity is resulting from the equation: Intensity = (Observed_intensity - offset) / ratio.

1.9. Statistical tests

Statistical tests

To validate each result, Kolmogorov-Smirnov Goodness of fit tests were performed to assess the fitting procedure. PP-plots have been used to point out graphically the goodness of fit as well. Also, Kolmogorov-Smirnov 2-test was used to stand significant differences between 2 empirical distributions of steps distances, or squared ones, dwell times distributions and Apparent Diffusion empirical probability density values. F-test for nested models were used to avoid overfitting in the identification of anomalous tracks.

2. Benchmarking SMTracker performance with synthetic SMT microscopy movies

To validate the performance of SMTracker, we used computational simulations to generate sets of synthetic SMT movies. Applying the molecule quantification tool allows benchmarking the performance of this method, as detailed in the following.

2.1. *Simulation of synthetic single molecule images*

Synthetic movies were produced using a 16x38x2000 matrix representing a stack of images of 2000 frames, and each cell of the matrix corresponding to the fluorescent intensity, simulating the pixels. These pixel values have been randomly sampled from the empirical distribution of intensities taken from real microscopy movies, both containing no cells (only instrumental and experimental noise) and adding *Bacillus subtilis* 3610 wild-type cells. In addition, we worked with the idea that if a molecule bound to a fluorescent protein (FP) is hit by the laser, it will produce a trajectory at least for 3 frames. Therefore, molecules were simulated with synthetic trajectories in a 1 to 1 ratio, which were inserted into a standard wild-type cell like in previous work (Roesch *et al*, 2018), incorporating the illumination contribution of a fluorescent spot + some noise, and convolving the signal with a Gaussian illumination profile (Zhang, B. *et al*, 2006).

Finally, being $n_{tot} = n_1 + n_2$ the total number of molecules simulated, the illumination coming from excited fluorescent proteins when the laser beam is emitted was reproduced; n_1 molecules were located starting in the 30^{th} frame and the resting n_2 were located in a random frame (beyond the 500^{th}) in the movie. The fluorophore lifetime typically follows an exponential decay distribution, which makes the behaviour of bleaching-down in a Single Particle Tracking Slim-field microscopy experiment to be reproduced.

2.2. *Benchmarking molecule quantification*

For each value N_{mol} of number of molecules, 30 synthetic cells were created to replicate a regular experiment in our lab (of 10 movies with an average of 3 cells per movie). N_{mol} is the average number of molecules simulated per cell.

After inserting our package of synthetic movies into the SMTracker pipeline, estimated vs simulated number of molecules were compared (Figure S4). The median has been chosen as the estimator of the average number of fluorophores per cell. There is a maximum of 15% of deviation from the gold truth that stays constant from approximately 20 molecules.

References

1. Stracy M., Lesterlin C, Federico Garza de Leon, Stephan Uphoff, Pawel Zawadzki, and Achillefs N. Kapanidis (2015) Live-cell superresolution microscopy reveals the organization of RNA polymerase in the bacterial nucleoid. *PNAS* **112** (32): E4390-E4399.
2. Haas, B.L., Matson, J.S., DiRita, V.J., and Biteen, J.S. (2014) Imaging live cells at the nanometer-scale with single-molecule microscopy: obstacles and achievements in experiment optimization for microbiology. *Molecules* **19**: 12116–12149.
3. Kass, R.E., and Raftery, A.E. (1995) Bayes Factors. *J. Am. Stat. Assoc.* **90**: 773-795
4. Schütz, G.J., Schindler, H., Schmidt, T. (1997) Single-molecule microscopy on model membranes reveals anomalous diffusion. *Biophys. J.* **73**:1073–80.
5. Borgmann, L.A.K., Ries, J., Ewers, H., Ulbrich, M.H., and Graumann, P.L. (2013) The bacterial SMC complex displays two distinct modes of interaction with the chromosome. *Cell Rep.* **3**: 1483–1492.

6. Jaqaman, K., Loerke, D., Mettlen, M., Kuwata, H., Grinstein, S., Schmid, S.L., and Danuser, G. (2008) Robust single-particle tracking in live-cell time-lapse sequences. *Nat. Meth.* **5**: 695–702.

7. Manzo, C., and Garcia-Parajo, M.F. (2015) A review of progress in single particle tracking: from methods to biophysical insights. *Rep. Prog. Phys.* **78**: 124601

8. Michalet, X. (2010) Mean square displacement analysis of single-particle trajectories with localization error: Brownian motion in an isotropic medium. *Phys. Rev. E* **82**: 041914

9. Paintdakhi, A., Parry, B., Campos, M., Irnov, I., Elf, J., Surovtsev, I., and Jacobs-Wagner, C. (2016) Oufti: an integrated software package for high-accuracy, high-throughput quantitative microscopy analysis. *Mol. Microbiol.* **99**: 767–777.

10. Xu M, Ross JL, Valdez L, Sen A. Direct Single Molecule Imaging of Enhanced Enzyme Diffusion. *Phys Rev Lett*. 2019;123(12):128101.

11. Zhang, M., He, K., Wu, J. *et al.* Single-molecule imaging reveals the stoichiometry change of epidermal growth factor receptor during transactivation by β_2-adrenergic receptor. *Sci. China Chem.* **60,** 1310–1317 (2017).

12. Sliusarenko, O., Heinritz, J., Emonet, T., and Jacobs-Wagner, C. (2011) High-throughput, subpixel precision analysis of bacterial morphogenesis and intracellular spatio-temporal dynamics. *Mol. Microbiol.* **80**: 612–627.

13. Tinevez, J.-Y., Perry, N., Schindelin, J., Hoopes, G.M., Reynolds, G.D., Laplantine, E., *et al.* (2017) TrackMate: An open and extensible platform for single-particle tracking. *Methods* **115**: 80–90.

14. Badrinarayanan, A. *et al*. In vivo Architecture and Action of Bacterial Structural Maintenance of Chromosome Proteins. Science 338, 528 (2012)

15. Coffman & Wu. Counting protein molecules using quantitative fluorescence microscopy. Cell Press. Volume 37, Issue 11, November 2012, Pages 499-506

16. Coffman VC, Wu P, Parthun MR, Wu JQ. CENP-A exceeds microtubule attachment sites in centromere clusters of both budding and fission yeast. *J Cell Biol*. 2011;195(4):563-572.

17. Zhang B, Zerubia J, Olivo-Marin JC. Gaussian approximations of fluorescence microscope point-spread function models. *Appl Opt*. 2007;46(10):1819-1829.

18. Weimann L, Ganzinger KA, McColl J, Irvine KL, Davis SJ, Gay NJ, *et al*. (2013) A Quantitative Comparison of Single-Dye Tracking Analysis Tools Using Monte Carlo Simulations. PLoS ONE 8(5): e64287. https://doi.org/10.1371/journal.pone.0064287

2.2. Article II

Y-complex proteins show RNA-dependent binding events at the cell membrane and distinct single molecule dynamics

Rebecca Hinrichs[1,2], Nadiia Pozhydaieva[1,3], Katharina Höfer[1,3] and Peter L. Graumann[1,2]*

[1] SYNMIKRO, Zentrum für Synthetische Mikrobiologie, Karl-von-Frisch-Str. 14, 35043 Marburg

[2] Fachbereich Chemie, Hans-Meerwein-Straße 4, 35032 Marburg, Germany

[3] Max-Planck Institut für terrestrische Mikrobiologie, Max-von Frisch Straße, Marburg, Germany

* Correspondence: graumanp@uni-marburg.de; Tel.: +4964212822210

2.2.1. Abstract: Bacteria are dependent on rapid alterations in gene expression. A prerequisite for rapid adaptations is efficient RNA turnover, with endonuclease RNase Y playing a crucial role in mRNA stability as well as in maturation. In *Bacillus subtilis,* RNase Y in turn interacts with the so-called “Y-complex” consisting of three proteins, which play important functions in sporulation, natural transformation and biofilm formation. It is thought that the Y-complex acts as an accessory factor in RNase Y regulation but might also have independent functions. Using single molecule tracking we show that all three Y-complex proteins exhibit three distinct mobilities, including movement through the cytosol, and confined motion, predominantly at membrane-proximal sites, but also within the cell centre. A transcriptional arrest leads to a strong change in localization and dynamics of YmcA, YlbF and YaaT, supporting their involvement in global RNA degradation. However, Y-complex proteins show distinguishable protein dynamics, and the deletion of *yaaT* or of *ylbF* shows a minor effect on the dynamics of YmcA. Cell-fractionation shows that YaaT displays a mixture of membrane association and presence in the cytosol, while YlbF and YmcA do not show direct membrane-attachment. Taken together, our experiments reveal membrane-associated and membrane-independent activities of Y-complex proteins, and a dynamic interplay between them, with indirect membrane association of YmcA and YlbF via YaaT.

Keywords: RNA degradation; Riboswitch; *Bacillus subtilis*; Y-complex; RNase; single molecule tracking

Importance

Regulation of RNA half-life and processing of mRNAs to yield products with different translational efficiency are central to protein homeostasis in all cells. RNase Y has been shown to be a key player in global RNA degradation as well as in specific processing of transcripts. It has been proposed that its activity is affected by the so-called Y (or Ric)-complex. Using single molecule tracking we show that Y-complex proteins arrest at membrane-proximal sites in the cell, but also within the cytosol, strongly suggesting that they also find substrate-binding sites within the cytosol, likely on the nucleoids where transcription takes place. Arresting at membrane-proximal sites is reduced when transcription is blocked, implicating the Y-complex in activities towards general RNA degradation. Y-complex proteins show dissimilar membrane affinity and molecule dynamics, showing that the complex has a highly dynamic setup and could affect a variety of interaction partners besides the RNA degradosome.

2.2.2 Introduction

Control of messenger RNA (mRNA) stability is a central part of gene regulation in all cells. Extending or shortening the life time of an mRNA has a profound effect on protein expression. Generally, most mRNAs have a short life-time, their instability is fundamental for the control of protein levels [2, 48, 49]. The processing and degradation of mRNAs is usually initiated by an endonucleolytic attack [50], so the most efficient way to regulate mRNA decay is to control the steps that initiate degradation.

In *Escherichia coli* and *Bacillus subtilis*, endonucleases RNase E and RNase Y, respectively, are known for a global effect on mRNA turnover, as well as for specific RNA processing [2, 5, 49]. For example, the RNase Y is able to produce endonucleolytic cleavages in the 5'-untranslated regions (UTRs) of genes to produce alternative transcript isoforms with shortened leader sequences from their precursor mRNAs [51, 52]. Thus, RNase Y plays an important role in the regulation of *B. subtilis*. Especially for bacteria, the regulation of mRNA turnover allows cells to control gene expression at a post-transcriptional level and thus react quickly to changing growth conditions [50]. In *B. subtilis,* RNase Y is not essential, but deletion of the corresponding *rny* gene leads to severely retarded growth [53]. RNase Y influences the intracellular levels of most transcripts [34, 38], and affects turnover of riboswitches [5].

Two RNase Y-containing complexes have been proposed to exist in *B. subtilis:* a "degradosome" containing three other RNases, an RNA helicase as well as glycolytic

enzymes [6], comparable to the RNase E-based degradosome in *Escherichia coli* [54-56]. In contrast to *E. coli*, the degradosome in *B. subtilis* could only be isolated with cross-linking agents [6]. Thus, the nature of the putative mRNA degradosome is still rather unclear. Recently, it was reported that the so-called Y-complex (YlbF, YmcA, YaaT) physically interacts with RNase Y, possibly setting up a second RNase Y-containing complex [8, 57]. In addition to biofilm formation, competence and sporulation (here the complex acts on the phosphorelay, although this is currently under debate), it was shown that the Y-complex plays a role global in mRNA stability and is necessary for the processing of the *cggR-gapA* transcript in *B. subtilis* [9]. Interestingly, RNase Y is also essential for this posttranscriptional regulation [6]. Thus, the complex is necessary for the efficient maturation of operon-mRNAs and influences the frequency of distinct riboswitches [9]. Because of its crucial role in mRNA cleavage *in vivo*, Y-complex proteins have been proposed to act as accessory factors that regulate RNase Y activity [9]. An additional function for the Y-complex (apparently consisting of a 1:2:1 stoichiometry of YaaT/YmcA/YlbF) has been proposed based on its two (4 FeS_4) clusters [58], and its FAD binding capability, in that the complex may be involved in redox regulation.

Interestingly, a functional RNase Y-GFP fusion forms distinct foci at the cell membrane [11], and the dynamics of these foci have recently been shown to be influenced by Y-complex proteins, to a different extent dependent on the individual proteins [12]. Of these, YmcA could be purified as a soluble protein, in contrast to YaaT and YlbF, such that the complex can only be obtained by co-expression of all three proteins. Thus, YaaT and YlbF appear to be insoluble and interestingly, YaaT has also been shown to localize as foci at the cell membrane [9], similar to RNase Y.

In our work, we addressed the question of how Y-complex proteins can affect processes such as mRNA maturation, which we would expect to take place on the nucleoids, where mRNA is synthesized [59], unless non-matured mRNAs move from the nucleoids into the membrane-attached RNase Y foci. To obtain a spatial and temporal resolution as high as possible, we studied dynamics of the three members of the Y-complex during exponential growth using single molecule tracking (SMT). We show that the localization and dynamics of all three proteins changes during a transcriptional arrest, which suggests an active participation of membrane-structures in mRNA decay. We show that Y-complex proteins also arrest at sites in the cell away from the cell membrane, strongly suggesting that it also acts on the nucleoids, and not solely at the cell membrane. Our data considerably revise

and refine our understanding of Y-complex dynamics in cells and reveal distinct biophysical properties of the three proteins.

2.2.3. Materials and Methods

2.1. Growth conditions

Bacterial strains, plasmids and oligonucleotides used in this study are listed in Supplementary Table S1. LB (Lysogenic Broth) medium was used for the cultivation of *E. coli* strains. LB medium was also used for protein production, *B. subtilis* cultivation (overnight) and for solid agar plates. To study the used *B. subtilis* BG214 strain in the exponential phase, the culture was incubated at 30°C and 200 rpm. For SMT the culture was cultivated in S_{750} minimal medium (100 ml: 10 ml 10 x S_{750} salt solution [1 l ddH_2O; pH 7.0: 104.7 g MOPS, 13.2 g of $(NH_4)_2SO_4$, 6.8 g of KH_2PO_4, 12 g of KOH], 1 ml 100 x metal solution [100 ml bdH_2O: 20 ml of $MgCl_2$ (1 M), 7 ml of $CaCl_2$ (1 M), 0.5 ml of $MnCl_2$ (1 M), 1 ml of $ZnCl_2$ (0.1 M), 1 ml of $FeCl_3$ (50 mM), 5 ml of Thiamine hydrochloride (2 mg /ml), 17 µl of HCl (2 M)], 2 ml 50 % fructose (w/v), 1 ml of 10% L-glutamate (w/v), 40 µl of 1% Casamino acids (w/v)) [60]. When needed, antibiotics were added at the following concentrations: ampicillin 100 µg/ml, chloramphenicol 5 µg/ml, kanamycin 30 µg/ml, rifampicin 25 µg/ml. 0.5% of xylose was added from a 50% sterile filtrated stock solution in ddH_2O. For *B. subtilis* BG214, methionine (50 µg/ml) and tryptophan (50 µg/ml) were added to the medium.

2.2. Construction of strains

To create mV-fusions of *B. subtilis* we used plasmid pSG1164-mV. Plasmid pSG1164-mV, which encodes the corresponding fluorophore mV, creates a single-crossover of the desired gene with the introduced plasmid sequence, thereby generating a C-terminal fusion of the sequence to the fluorophore at the original locus of the gene [61]. To insert a homologous region required for plasmid integration, at least 500 bp of the C-terminus of the desired gene was cloned by Gibson Assembly [62] into the vector next to the linker and mV sequence. The Gibson primers used had a homologous overhang of at least 20 bp Supplementary Table 3. The transformed plasmids were extracted using a kit (Sigma-Aldrich). The deletion strains are based on *B. subtilis* BG214 containing YmcA-mV constructs and were generated by transformation of cells with chromosomal DNA from *B. subtilis* 168 *ΔyaaT::kan trpC2*, *ΔylbF::kan trpC2*, or *ΔymcA::ery trpC2*, obtained from the

Bacillus Genetic Stock Center (Columbus, Ohio) [63]. The chromosomal DNA was extracted using a kit (innuPREP Bacteria DNA Kit, Analytik-Jena).

2.3. Protein fractionation

50 ml of lysogenic broth supplied with 5 µg/ml of chloramphenicol were inoculated from a 2 ml overnight culture. Cells were grown to mid-exponential phase (OD600 of 0.6) at 30°C, and were harvested. The resulting pellet was resuspended in 1 ml lysis buffer F (50 mM EDTA, 100 mM NaCl, pH 7.5, and Protease Inhibitor Cocktail cOmplete™: EDTA-free Protease Inhibitor Cocktail, Roche). Cells were enzymatically lysed by incubation with 2.5 mg/ml lysozyme for 30 min at 37°C. The subsequent protein fractionation of parts of the samples is described down below. For the SDS-PAGE, SDS loading buffer was added and the samples were incubated for 1 h at room temperature. All samples were loaded using 16 µl thereof onto a 12% mini-PROTEAN TGX Stain-Free SDS gel by Bio-Rad. Prior to western blotting, the total protein load of the gel was controlled via stain-free imaging using UV exposure.

For protein fractionation of the cell lysate, first, a 50 µl sample was withdrawn for SDS-PAGE analysis. The remaining cell lysate was transferred to a centrifugation tube with a volume capacity of 4 ml (Beckman coulter ®) Samples were centrifuged in 4 ml, Quick-Seal, g-Max Polypropylene tubes (Beckman Coulter) and were filled up with lysis buffer F to ¾ of the total tube volume (dilution about three-fold). We used an ultracentrifuge (Optima XPN 80, Beckman Coulter), and a 70 Ti fixed-angle rotor. After centrifugation at 100,000 g for 1 h in the ultra-centrifuge a 50 µl sample of the cytosol containing supernatant was taken. The remaining supernatant was discarded. The remaining pellet was resuspended in 1 ml lysis buffer. Again a 50 µl sample (which is about three-fold concentrated relative to the cytosolic fraction) was taken for SDS-PAGE analysis. Resulting fractions were termed “lysate”, and after ultra-centrifugation, the supernatant (cytosolic proteins) “cytosol”, and the pellet containing membrane proteins “membrane”. As a control, wild type strain BG214 was used.

2.4. Northern blot analysis

Total RNA isolated from *B. subtilis* was analyzed by Northern blotting with target-specific RNA riboprobes for *cggR* and *gapA* transcripts. Probes for detection of *cggR, gapA* and 5S rRNA transcripts were generated from DNA oligonucleotides listed in supplementary table S1. The partially complement primers pairs were converted to dsDNA by PCR reaction with 2.5 U of JumpStart™ Taq DNA Polymerase (Sigma Aldrich). Following DNA was

precipitated with isopropanol, the pellet was dissolved in 100 µl Millipore water. Northern Blot probes were transcribed in 100 µl scale in the presence of 40 mM Tris-HCl pH 8.1, 1 mM spermidine, 22 mM $MgCl_2$, 0.01% Triton-X-100, 10 mM DTT, 5% DMSO, 3 µM DNA template, 0.1 mg/ml T7 RNA polymerase (lab-prepared stock), 20 µCi α-^{32}P-ATP (Hartmann Analytik), 4 mM of CTP, GTP and UTP and 2 mM of ATP at 37°C for 3.5 h. Afterwards, residual DNA template was removed by DNase I digest (0.02 U/µL, Roche) at 37°C for 30 min. Samples were phenol/chloroform extracted, isopropanol precipitated and the pellet resuspended in 50 µl Millipore water.

For Northern blot analysis, RNA samples were mixed with 2x PAGE loading dye (1x TBE in formamide containing xylene cyanol and bromphenol blue). ^{32}P-labelled HR RiboRuler Ladder (Thermo Scientific) was prepared using 20 µl HR RiboRuler Ladder, 40 µCi of γ-^{32}P-ATP (Hartmann Analytik), 1x Buffer A (Thermo Fisher) and 20 U PNK (Thermo Fisher) at 37°C for 1 h. Total RNA was fractionated by agarose gel electrophoresis (1.2% agarose, 0.6% formaldehyde v/v, 1x MOPS buffer, pH 7) at 110 V. Using a capillary transfer, RNA was transferred from the agarose gel to Whatman Nytran SuPerCharge nylon blotting membrane (GE Healthcare) in 10x SSC buffer, pH 7 overnight. The membrane was UV crosslinked and prehybridized in 20 ml ROTI® Hybri-Quick (Carl Roth) for 30 min at 45°C. 10 µl of previously radiolabeled RNA riboprobes were added to the prehybridized membrane and incubated for 3 h at 45°C. The blots were washed twice for 20 min with wash solution 1 (2x SSC, 0.1% SDS w/v) and twice for 20 min with wash solution 2 (0.1x SSC, 0.1% SDS w/v) at 45°C. Results were visualized using storage phosphor screens (GE Healthcare) and Typhoon™ biomolecular imager (GE Healthcare).

2.5. Western blot

The samples of protein fractionation were separated by SDS-PAGE and visualized by western-blotting. The detection was performed with a primary polyclonal α GFP antibody (1:5000), and secondary antibody goat-anti-Rabbit-IgG, peroxidase-conjugated (1:100,000) (Sigma-Aldrich).

2.6. Fluorescence microscopy

Fluorescence microscopy was performed with S_{750} medium cultivated cells. *B. subtilis* cells were grown at 30°C and 200 rpm until exponential phase. For wide-field epifluorescence microscopy a Zeiss Observer A1 microscope (Carl Zeiss) with an oil

immersion objective (100 x magnification, 1.45 numerical aperture, alpha PlanFLUAR; Carl Zeiss) was used. The images were recorded with a charge-coupled-device (CCD) camera (CoolSNAP EZ; Photometrics) and an HXP 120 metal halide fluorescence illumination with intensity control. Sample preparation was performed using round coverslips (25 mm, Marienfeld) and covering 5 µl cell culture with a 1% agarose pad. The agarose pads were made with S_{750} medium by sandwiching 100 µl of the melted agarose between two smaller coverslips (12 mm, Menzel). Images were processed using ImageJ [64].

2.7. Single-molecule tracking

The individual molecules were tracked using custom-made slim-field setup on an inverted fluorescence microscope (Nikon Eclipse Ti-E, Nikon Instruments Inc.). An EMCCD camera (ImagEM X2 EM-CCD, Hamamatsu Photonics KK) was used to ensure high-resolution detection of the emission signal, resulting in a calculated resolution of the position of the molecule down to 20 nm. The central part of a 514 nm laser diode (max power 100 mW, TOPTICA Beam Smart) was used with up to 20% of the intensity (about 160 W cm^{-2}) in the image plane) to excite samples fused to mVenus (using a laser filter set with BrightLine 500/24, dichroic mirror 520 and BrightLine 542/27), by focusing the beam onto the back focal plane of the objective. A CFI Apochromat objective (TIRF 100 x Oil, NA 1.49) was used in the setup. The videos were recorded with 3000 frames and 40 ms stream acquisition, using the camera program NIS-Elements. The software Oufti [65] was used to set the necessary cell meshes. Utrack [66] was used for signal detection and track generation, with a minimum track length of six steps selected. A strong fluorescence signal from the sample would lead to incorrectly connected tracks. To be sure that the motion is only analysed at the single molecule level, a bleaching curve of each movie was calculated in ImageJ. The bleaching curve can be modeled as an exponential decay, and a threshold on the slope of less than 10% is used as a cut off. On this basis, the first 500 to 1000 frames were cut out for all movies (dependent on signal intensity of the strains) to insure imaging at a single molecule level. All cells were incubated in S_{750} medium to the exponential phase at 30°C and 200 rpm. The statistical data analysis was carried out according to already established methods [14, 67].

2.2.4. Results

3.1. Localization of the Y-complex in live B. subtilis cells

RNase Y has been shown to form discrete fluorescent foci at the cell membrane in exponentially growing cells [12], and similarly YaaT [9]. In order to obtain further knowledge on the role of the Y-complex in *B. subtilis,* we created C-terminal mVenus fusions (termed “mV” from here on) to each protein of the three proteins of the complex, which were integrated via single crossover integration into the respective gene locus. To ensure the functionality of the Y-complex proteins with fusions, we performed sporulation assays and transformability tests. Both experiments showed that all fusions retained close to wild type-like function: cells carrying single fusions showed even slightly higher sporulation efficiency for YaaT and YmcA, and normal activity for YlbF (Fig. S1A), and transformability was normal, except for the YmcA-mV fusion that showed slightly reduced activity, compared with wild type cells devoid of any fusion (Fig. S1B). As an additional control, we assayed for the processing of the *cggR-gapA* mRNA, which depends on the activity of RNase Y as well as that of the Y-complex proteins [9]. Figure S2 shows that while the *cggR-gapA* transcript fails to be cleaved in each strain lacking a component of the Y-complex, all the mVenus fusion strains are proficient in this activity, except for a minute accumulation of non-matured transcripts. Lastly, growth of fusion strains was very similar to that of cells not carrying any fusion construct (Fig. S1C). These assays indicate that all proteins retained their functionality as protein fusions, and showed only a minimal reduction in functioning, as is often seen in fusion proteins.

Using epifluorescence (Figure 1) revealed that YaaT-mVenus forms fluorescent foci, mostly close to the cell membrane, similar to what was reported before for YaaT [68]. For YlbF-mV and YmcA-mV we also observed foci, however seemingly fewer per cell than for YaaT-mV. In order to obtain a better view on the spot-like assemblies of Y-complex proteins, we used slim-field microscopy, where the central part of a laser diode is focused on the back focal plane of the objective, resulting in high light intensity and slightly divergent illumination of the image plane. This technique allows to track single molecule at a time scale of milliseconds; adding up images from a whole movie of 3000 frames blurs out diffusing molecules and reveals the presence of molecules at similar positions, forming discrete foci. Using this approach yielded more clearly defined foci (Figure 2) and revealed the existence of many foci in a majority of cells, mostly but not always close to the cell membrane.

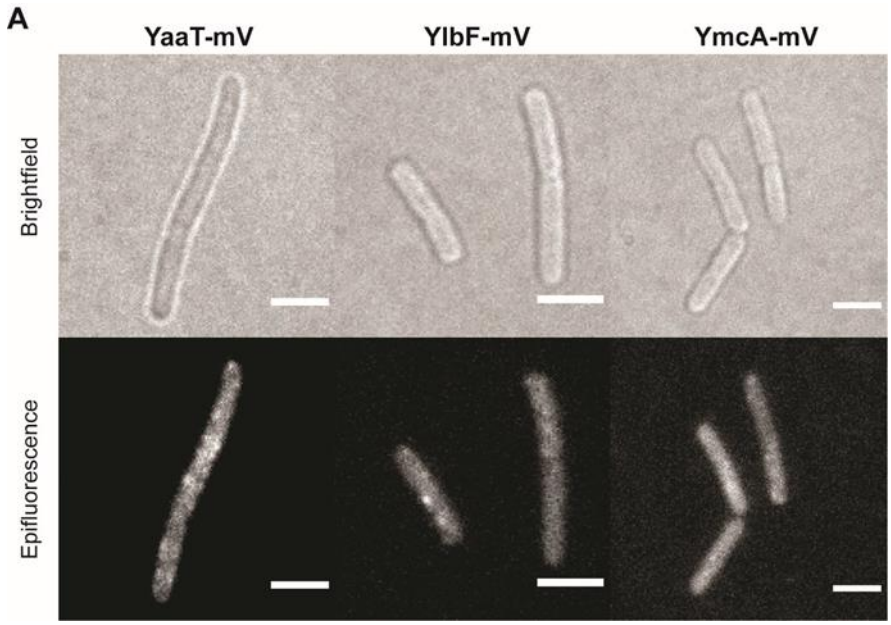

Figure 1. Localization of the Y-complex proteins expressed from native locus by epifluorescence in *Bacillus subtilis* (BG214). Scale bars 2 µm.

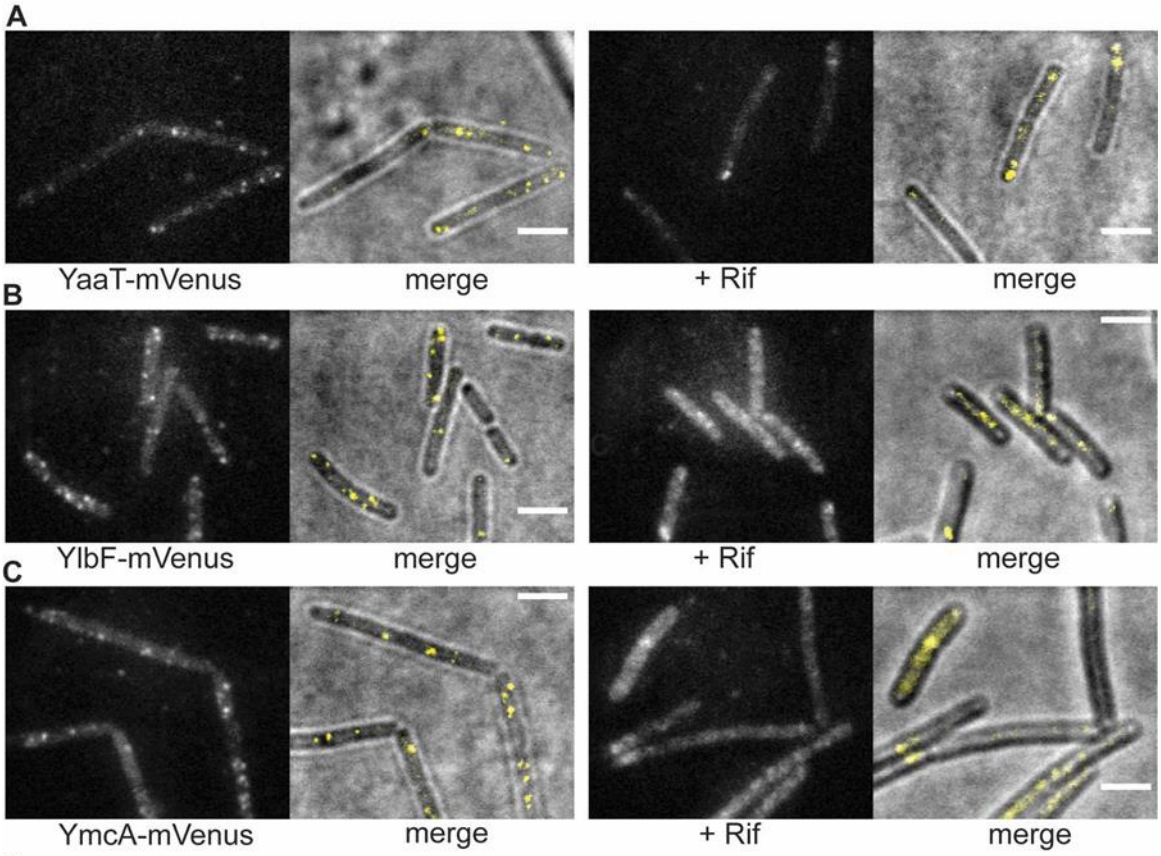

D

	YaaT-mV		YlbF-mV		YmcA-mV	
	-Rif	+ Rif	- Rif	+ Rif	- Rif	+ Rif
0 focus/cell [%]	11	25	4	37	24	50
1 focus/cell [%]	37	62	31	56	35	47
2 foci/cell [%]	25	12	31	7	22	3
3 foci/cell [%]	21	1	20	0	14	0
4 foci/cell [%]	4	0	12	0	4	0
5 foci/cell [%]	2	0	1	0	1	0
6 foci/cell [%]	0	0	1	0	0	0

Figure 2. Changes in the localization patterns of Y-complex proteins during exponential growth phase and in phase response to transcription arrest, by treatment with rifampicin for 30 minutes ("+ Rif"). A to C: Localization by slim-field illumination. (A-C) Panels show the localization of the three different Y-complex proteins (expressed from native locus. Merge displays overlay of bright field and fluorescence. Scale bars 2 µm. D: Percentage of the number of foci in cells with fluorescent signal before and after treatment with rifampicin.

Counting the number of foci in about 200 cells for each strain, from a biological triplicate, showed that few cells did not contain any foci, and most cells showed between one and two visible foci (Figure 2D). The number of foci contains an error based on subjective counting of fluorescent signals. Interestingly, when cells were incubated with rifampicin, inhibiting the activity of RNA polymerase, the number of foci per cell dropped, and the number of cells

lacking foci increased (Figure 2). Thus, the components of the Y-complex behave similarly towards rifampicin treatment, corresponding to the finding of complex formation by the three proteins [58]. It has been shown that RNase Y still forms foci at the cell membrane after inhibition of transcription [12], but that RNase Y relocalizes from the membrane towards to cytosol [69]. Because there is a dispute over whether SMT data on RNase Y are valid, we will perform additional control experiments before further proceeding with a comparison between RNase Y and Y-complex protein dynamics in a future study.

3.2. Dynamics of Y-complex proteins at a single molecule level reveals rapid binding and unbinding events

In order to better quantify changes in molecule dynamics of Y-complex proteins in response to transcription inhibition, we employed SMT microscopy [18, 27]. With this method we were able to detect the localization of the Y-complex fusion proteins with a higher spatiotemporal sensitivity than with epifluorescence or TIRF microscopy. Briefly, the beam of a 514 nm laser diode was widened 20-fold, and the central part was focused on the back focal plane of the 100 x A = 1.49 objective. Images were captured in stream acquisition using an EM-CCD camera. With SMT we are able to visualize events of molecules resting at a defined subcellular site with a precision of 40 nm and less [15], and can detect freely diffusive molecules in living cells (21). The generated fusion proteins were tracked using 40 ms stream acquisition, because at this integration time, we obtained the highest number of tracks. After initial bleaching of most molecules, single molecule tracks are captured for a total of 3000 frames (120 s). Cell meshes were determined using the software Oufti [65] and trajectories were determined by u-track [66]. Only consecutive tracks of 5 steps and longer were used for evaluation. Final analysis was performed using SMTracker 2.0, a custom-made graphical user interphase program [69]. Data for each represented experiment were collected from three independent biological replicates.

Figure 3A shows an example of a single molecule/particle track, in this case travelling along the cell pole. The 2D distance travelled can be seen in the standardized cell, and in the coordinate system (Figure 3A). Fluorescence of the focus is bleached in one step in the final frame, which can be seen in the fluorescence plot. The latter also reveals that the intensity of the fluorescent focus roughly doubled at least once (more likely twice) during the life time of the particle trajectory, suggesting that at least one molecule attached to the structure containing YaaT within the observation time. Figure 3B shows the bleaching curve, from which the trajectory was taken. Interestingly, events of binding of new molecules to

existing YaaT-mV assemblies was frequently observed for YaaT (Figure 3C, note that formally, maturation of newly attached YaaT-mV molecules is observed, which is stochastic). Average background fluorescence was 2100 a.u., and that is single YaaT-mV molecules about 2150 a.u. Interestingly, events of 100 or 150 a.u. increase during a single frame was observed (Figure 3C), showing that two or three molecules can associate with YaaT-mV molecules within 40 ms intervals. These observations suggest exchange rates of 20 ms and less for YaaT from the Y-complex, faster than e.g. 40 ms reported for exchange of MotB from the rotating flagellum [70]. Expecting that there are fewer than 22 copies of YaaT within a mobile Y-complex (as opposed to MotB within the flagellar machinery), exchange rate of YaaT is much faster than that of MotB. Similar events of at least two molecules adding to existing structures within one frame could be observed for YmcA (Figure 3E), but more rarely than for YaaT, and very rarely for YlbF (Figure 3D), indicating different exchange rates of YaaT, YlbF and YmcA from the Y-complex.

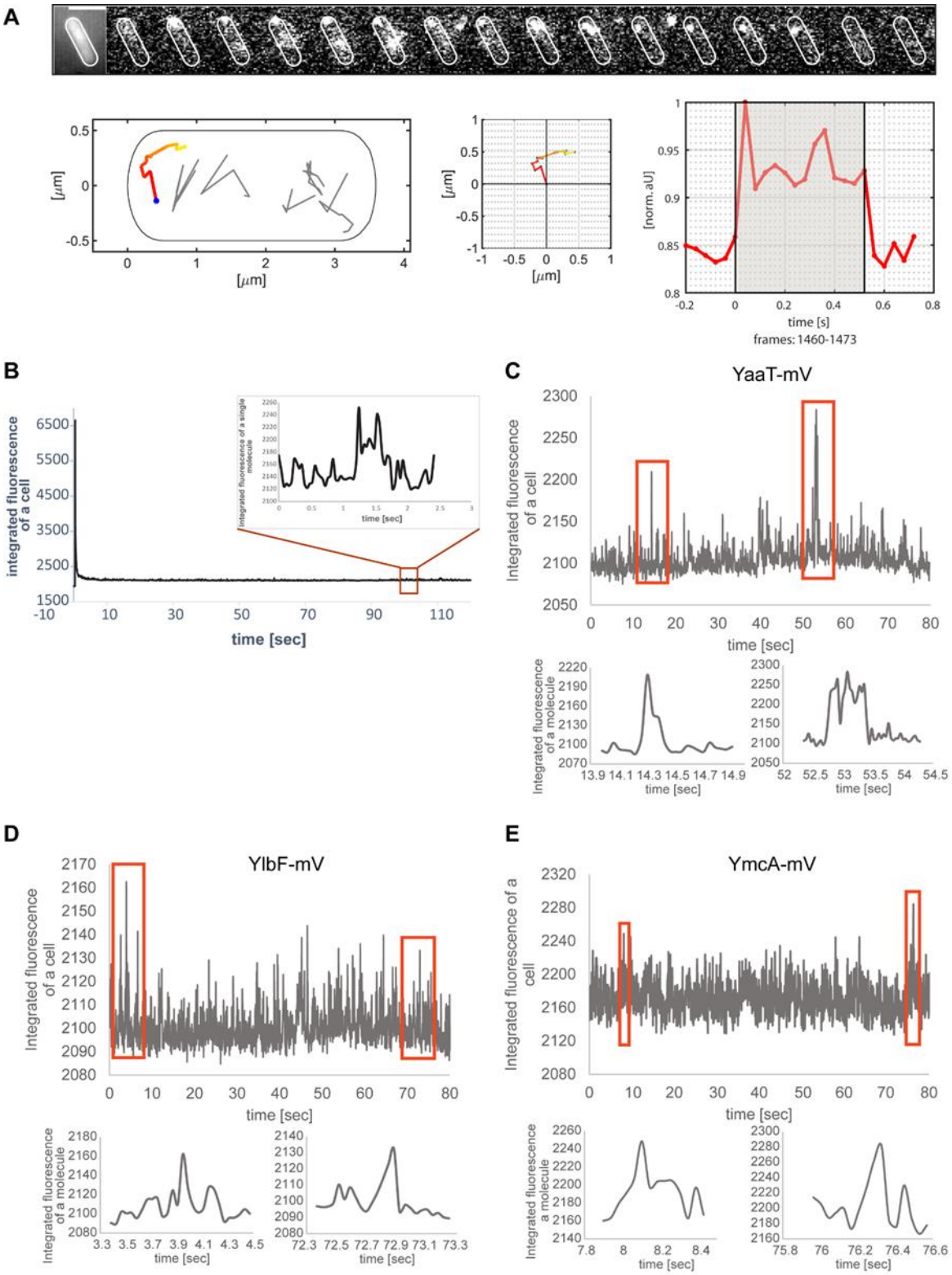

Figure 3. Single molecule/particle tracking of the Y-complex proteins. A) Exemplary track of YaaT-mV. Montage shows images captured by 40 ms stream acquisition. Middle panels show motion of the focus within 2D, and fluorescence in arbitrary units. B) Bleaching curve of the movie from panel A, inset shows track from panel A. C) Examples of fluorescence for

two or three molecules adding to a YaaT assembly within single frames, D) and E) track events for YlbF-mV or for YmcA-mV.

3.3. Single molecule dynamics can be best explained by assuming three distinct populations with distinct mobilities

Jump-distance is defined as the Euclidean distance between consecutive detections. A shift of movement of molecules towards larger displacement after addition of rifampicin is clearly visible in Figure 4A, showing that YaaT molecules become more dynamic after rifampicin treatment. Squared displacement (SQD) analysis was employed to quantify obtained displacements, which uses the cumulative probability distribution of the quadratic shifts to estimate the diffusion constants, and to determine if the distribution of displacements can be explained by a single population of molecules, or if more populations have to be assumed in order to explain the data. The number of populations is determined via a non-linear least-square fitting procedure [69]. When the distribution of jump distances was fitted with two Rayleigh distributions, deviations were well visible (Figure S3A), using three distributions explained the observed data much better (Figure S3B). Residuals that did not agree with the predicted fit (based on Brownian motion) were smaller for 3 distributions (Figure S3B, compare with A), and quantile-quantile (Q-Q) plots showed that the observed data (red line Figure S3) showed a higher deviation from the modelled data (black dotted line, Figure S3 for two than for three Rayleigh fits. These analyses strongly suggest that three populations with distinct diffusion coefficients exist for YaaT *in vivo,* which was also found for YmcA and YlbF. Figure 4B visualizes the data shown in Figure 4C: the size of the bubbles corresponds to the relative size of the population, the height along the Y-axis the diffusion constant. Note that errors reported are fitting errors (see material and methods for details of error determination), all data are from three independent biological replicates. It is apparent that diffusion constants of the slowest population (from here on called the “static” fraction) are very close to each other, with D = 0.01 $\mu m^2 s^{-1}$ for YaaT-mV, D = 0.01 $\mu m^2 s^{-1}$ for YlbF-mV, and D = 0.01 $\mu m^2 s^{-1}$ for YmcA-mV, suggesting that about 20% of the proteins form one complex of very large size, based on minimal diffusion.

The medium-mobile populations of all three proteins had similar diffusion constants as well, varying between 0.05 and 0.06 $\mu m^2 s^{-1}$. This value is similar to that reported for translating 70S ribosomes [71, 72], indicating that this population of Y-complex proteins is also part of a complex of a considerable size. Because it is unlikely that the Y-complex is

associated with active translation, we propose that this fraction might be Y-complex proteins bound to mRNA, directly or indirectly (see further below). The high mobile fractions of about 0.5 $\mu m^2 s^{-1}$, quite low for molecules we would expect to be freely diffusive. To test if using 40 ms stream acquisition might lead to an underestimation of the diffusion constant of freely diffusing molecules, whose motion may be blurred out at this acquisition speed, we tracked the three proteins using 20 ms integration time. Diffusion constants of the fast-mobile fractions rose to 1.1 ± 0.01 $\mu m^2 s^{-1}$ for YaaT-mV, 0.97 ± 0.02 $\mu m^2 s^{-1}$ for YlbF-mV, and 1.3 ± 0.02 $\mu m^2 s^{-1}$ for YmcA-mV, which is in the range of diffusion constants obtained for other freely diffusive proteins in *B. subtilis* [18, 28]. Taken together, we interpret these findings as support of the presence of three different mobilities for Y-complex proteins, with an underestimation of the diffusion constants of the medium and fast mobile fractions at 40 ms, which has to be kept in mind, but does not generally compromise further results obtained.

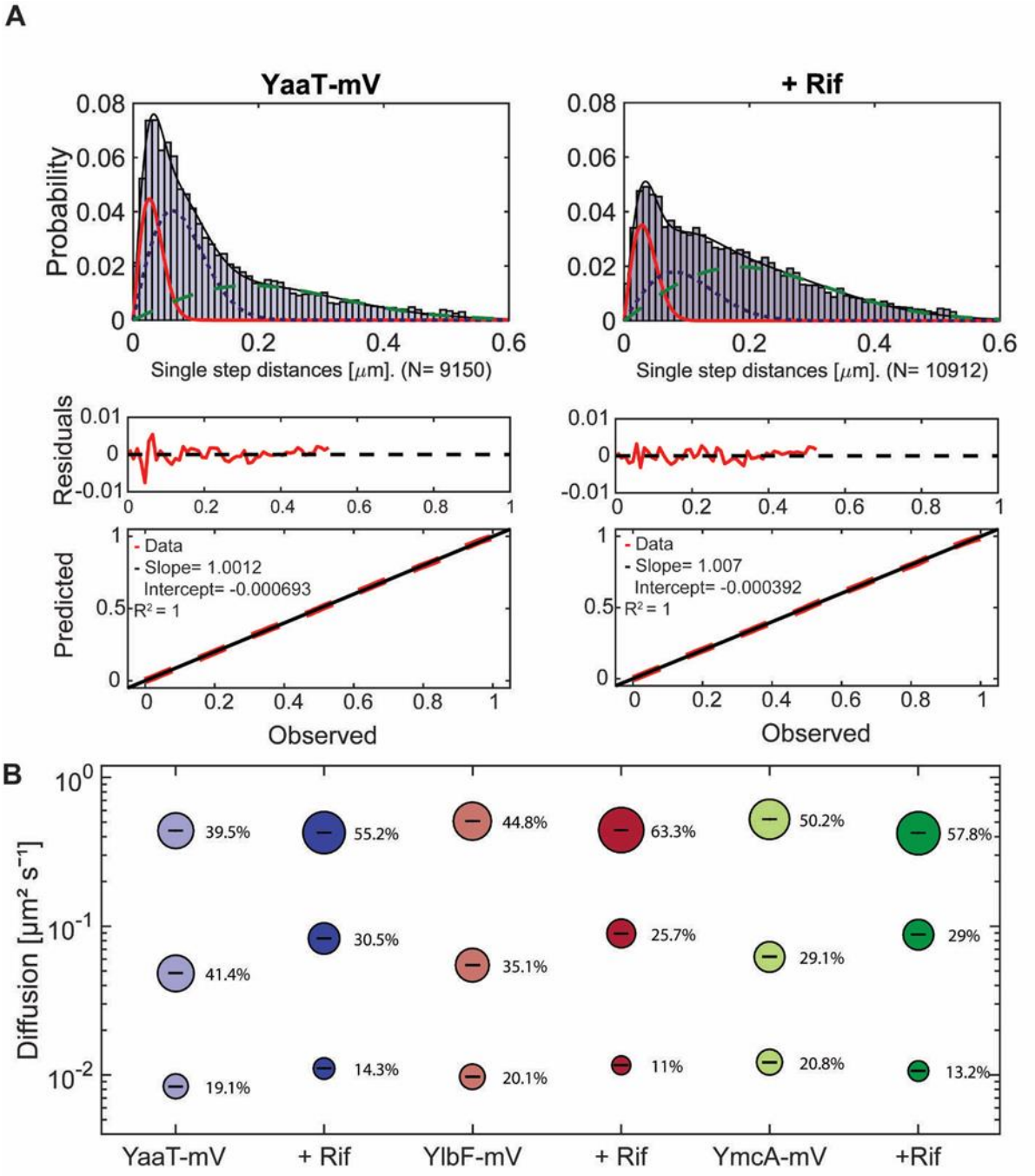

C

	YaaT-mV	YaaT-mV + Rif	YlbF-mV	YlbF-mV + Rif	YmcA-mV	YmcA-mV + Rif
$D1_{(static)}$ μm² s⁻¹	0.01 ± 0.0	0.01 ± 0.0	0.01 ± 0.0	0.01 ± 0.0	0.01 ± 0.0	0.01 ± 0.0
$D2_{(slow)}$ μm² s⁻¹	0.05 ± 0.0	0.08 ± 0.0	0.06± 0.0	0.09 ± 0.0	0.06 ± 0.0	0.09 ± 0.0
$D3_{(fast)}$ μm² s⁻¹	0.44 ± 0.001	0.43 ± 0.001	0.51 ± 0.001	0.44 ± 0.001	0.53 ± 0.001	0.42 ± 0.001
Static %	19.1 ± 0.001	14.3 ± 0.001	20.1 ± 0.001	11 ± 0.001	20.8 ± 0.001	13.2 ± 0.0
Slow-mobile %	41.4 ± 0.001	30.5 ± 0.001	35.1 ± 0.001	25.7 ± 0.001	29.1 ± 0.001	29 ± 0.002
Fast-mobile %	39.5 ± 0.001	55.2 ± 0.001	44.8 ± 0.001	63.3 ± 0.001	50.2 ± 0.001	57.8 ± 0.002
P-values		***		***		***
R^2	1	1	1	1	1	1

Figure 4. Squared displacement (SQD) analysis of Y-complex-mV fusion proteins under different conditions in cells growing in mid-exponential phase. (A) Three Rayleigh

distributions were used to fit the observed data and to calculate diffusion coefficients for individual diffusive populations (YaaT-mV: N (number of trajectories) = 6141, YaaT-mV + Rifampicin: N = 14339). Values show diffusion coefficients and their fraction sizes calculated by a nonlinear least-squared fitting method by the native MATLAB function. The frequency of the diffusion constants (probability density) was plotted against the specific diffusion coefficient of each track in a histogram. R^2 value is annotated for each histogram. Diffusion of Y-complex proteins can be described best with a three populations fit representing a static (red solid line), slow-diffusive (blue dotted line) and one fast diffusive (green dashed line) population. The lower two panels show quantile-quantile plots, where the difference between measured data and modelled data (indicated by straight red dotted line) is shown by the blue curve (see Fig. S3 for the corresponding JD analyses for two populations). (B) Bubble plot shows diffusion constants [$\mu m^2\ s^{-1}$] of mVenus fusions and fraction size of populations [%]. (C) Diffusion constants and percentages of static, slow-mobile and fast-mobile molecule fractions. The errors correspond to the 95% confidence intervals given by the MATLAB function “confint”, which uses for its calculation the values that result from the fit. Low confidence intervals are due to the large data sets. *P*-value: Symbols *, ** and *** indicate for *P*-values lower than 0.05, 0.01 and 0.001, respectively, n.s. statistically not significant. The R^2 value of each fit is annotated.

3.4. Inhibition of transcription leads to large changes in the dynamics and of the location of confined motion

We wished to analyse the behaviour of Y-complex proteins during the depletion of mRNA at the single molecule level, to investigate changes in dynamics in the absence of substrate. For this we incubated the cell culture for 30 min with rifampicin, after it had reached exponential phase. Rather than using 200 µg/ml as in standard protocols, we treated cells with 25 µg/ml, because we found that even with 100 µg/ml treatment, some cells started to show cell lysis after 30 minutes. We chose a reduced concentration of rifampicin to be able to investigate cells that are still alive, with the caveat that possibly overall transcription was not completely blocked, but considerably reduced. SQD analysis after treatment with rifampicin revealed a shift in population sizes towards a higher diffusion constants. The diffusion constant of the static population of YaaT-mV remained similar at 0.01 $\mu m^2\ s^{-1}$ and the size of this population decreased from 19 to 14%. The medium-mobile population strongly increased almost two-fold in mobility, from 0.05 to 0.08 $\mu m^2\ s^{-1}$, but decreased in size, while the fast-mobile population showed an increase from 40 to 55%

(Figure 4C). For comparison, we also tracked glycolytic enzyme PfkA, suggested to be a part of the RNA degradosome [6]. Although obtained tracks could be well explained by the existence of two populations, we chose three populations for comparison with Y-complex proteins. Figure S5B and S5C show a mild decrease in the static fraction of PfkA following rifampicin treatment, and a less than two-fold increase in the diffusion constant of the putative medium mobility fraction. Thus, even though some PfkA molecules may be involved in RNA degradation via the degradosome [6, 69], it shows much less pronounced increases in mobility during RNA depletion. This control experiment shows that the significant shift of the diffusion constant of the medium-mobile fraction of YaaT-mV after transcription arrest, and the strong reduction of the static population, reflects a strong involvement of YaaT in mRNA binding, directly or indirectly, in accordance with its participation in global mRNA stability [5, 38]. For YlbF-mV and YmcA-mV, we found a similar strong reduction of the static fraction, and a shift in diffusion constant of the medium-mobile fraction, with a concurrent increase in the fast mobile/freely diffusing population.

As an important control, we tested if the increase in overall mobility for molecules of the Y-complex observed after rifampicin treatment could be an effect on the viscosity within the cells, as addition of rifampicin has been shown to decreased the mobility of a very large protein complex in *E. coli* cells [73]. Using YmcA as a representative of the complex, we treated cells with an increased dose of rifampicin (100 µg/ml) for 15 minutes (still trying to avoid too many dying cells), we observed an even stronger decrease of the static fraction to below 3% (compared with 13% using the lower concentration), and an even stronger increase in the diffusion constant of the medium-mobile fraction to 0.16 $\mu m^2 s^{-1}$, as opposed to 0.06 $\mu m^2 s^{-1}$ in non-stressed cells or 0.09 $\mu m^2 s^{-1}$ in cells after the lower rifampicin dose (Figure 5). While the population sizes changed in favour of the medium-mobile population (likely reflecting a loss of sharpness between the distinction between medium – and freely mobile molecules), no drastic effect was seen after osmotic upshift by the addition of 1 M sorbitol to the medium, which only slightly increased the size of the medium-mobile fraction, and lowered its diffusion constant. Of note, it has recently been shown that translating ribosome (polysome)-induced crowding at sites surrounding the nucleoids (i.e. predominantly at the cell poles) is accompanied by lowered diffusion of large enzymes, but not of smaller proteins [74]. This is in agreement with our observation of the shift in mobility of the medium-mobile YmcA molecules, but not of the freely diffusive ones (Figure 5), supporting the view that increased crowding via osmotic stress affects the mobility of larger protein complexes, but not of small proteins such as YmcA. These experiments support the

idea that the medium-mobile population of Y-complex proteins is associated with mRNA, either directly or indirectly.

A

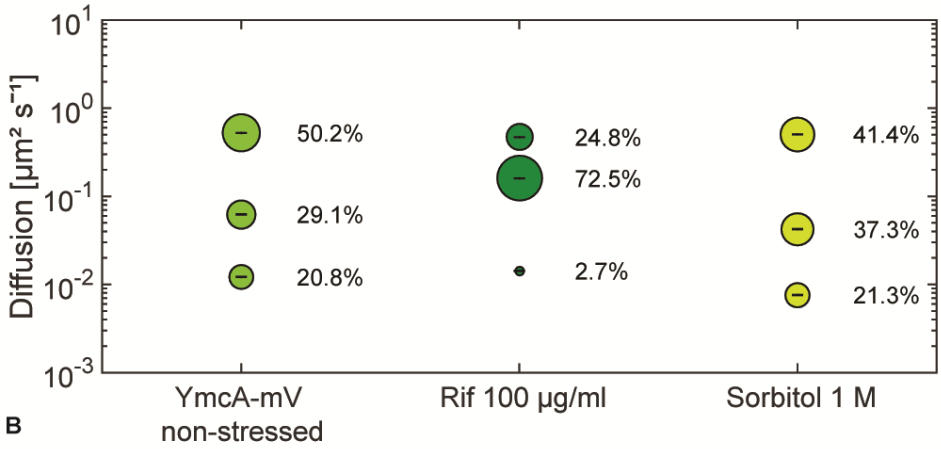

B

	YmcA-mV non-stressed	Rif 100 µg/ml	Sorbitol 1 M
$D1_{(static)}$ µm^2 s^{-1}	0.01 ± 0.0	0.01 ± 0.0	0.01 ± 0.0
$D2_{(slow)}$ µm^2 s^{-1}	0.06 ± 0.0	0.16 ± 0.0	0.04± 0.0
$D3_{(fast)}$ µm^2 s^{-1}	0.53 ± 0.001	0.47 ± 0.001	0.51 ± 0.001
Static %	20.8 ± 0.001	2.71 ± 0	21.3 ± 0.001
Slow-mobile %	29.1 ± 0.001	72.5 ± 0.001	37.3 ± 0.001
Fast-mobile %	50.2 ± 0.001	24.8 ± 0.001	41.4 ± 0.001
R^2	1	1	1

Figure 5. Squared displacement analyses of YmcA single molecule dynamics. A) bubble plot showing fractions sizes and their corresponding diffusion constants, “Rif” indicates cells treated with 100 µg/ml of rifampicin for 15 min, “Sorbitol” indicates cells incubeáted with 1 M sorbitol for 30 min. C) Data from SQD analyses.

We next projected all tracks from the three biological replicates into an average size cell of 3 x 1 µm size (“confinement heat map”, *B. subtilis* cells are on average 0.75 µm wide and 2 to 4 µm long). Tracks were sorted into those that stay within a radius of 120 nm, determined as three times our localization error (deduced from the intercept of MSD graphs), for at least 5 consecutive steps (confined motion), and into those that show large displacements, indicative of free diffusion. Figure 6 shows that during exponential growth, confined motion was largely biased towards the cell membrane/the cell periphery, for all three proteins. However, especially for YaaT and YlbF, confined motion also occurred away from the cell membrane (Figure 6A and B). Of note, confined motion of Y-complex proteins was different from that of the – mostly polarly localized – ribosomes showing confined motion, as

represented by L1-mV (Figure S4) [75], indicating that Y-complex proteins are not associated with translating ribosomes.

In response to RNA depletion, all three Y-complex proteins showed a lower degree of confined motion, and absence of membrane-oriented confinement (Figure 6A, B, D). About 12% of YaaT-mV tracks were static (i.e. showing purely confined motion) during growth, and only about 4% following rifampicin treatment (Figure 6G). A similar effect was found for YlbF and for YmcA (Figure 6G). To further quantify the effect of mRNA depletion of Y-complex dynamics, mobile tracks were sorted into those that are non-confined for the entire length of the track (“free”) and those that show a period of confined motion, representing molecule that undergo a transition between free diffusion and confined motion (“mixed behavior”). Transition events accounted for about 22% of YaaT molecules, and 16 or 15% for YlbF and YmcA, revealing a somewhat higher degree of binding and unbinding events to larger structures/complexes for YaaT. After rifampicin treatment, the number of transitions was lower for YaaT, but remained similar for YlbF, and was only mildly increased for YmcA, showing slightly different changes in dynamics of the three proteins.

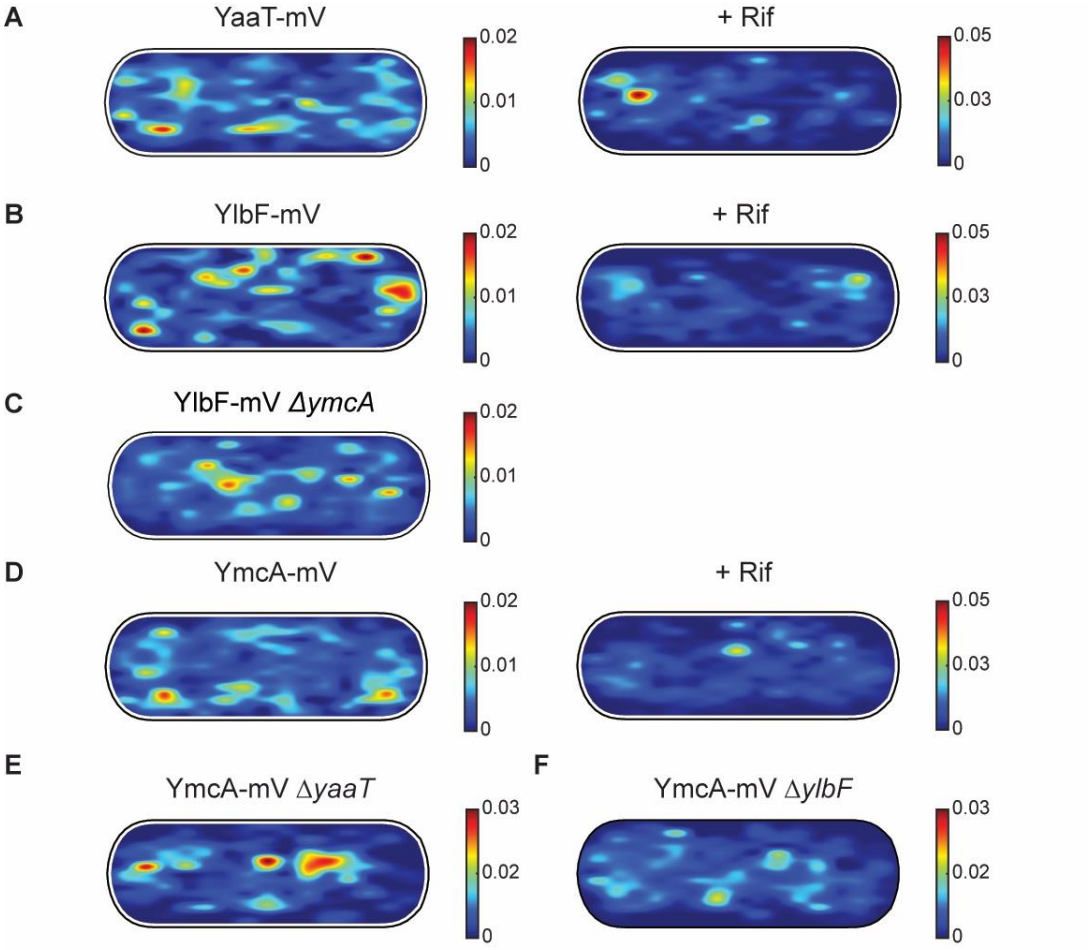

G

	YaaT-mV	YaaT-mV + Rif	YlbF-mV	YlbF-mV + Rif	YlbF-mV Δ*ylbF*	YmcA-mV	YmcA-mV + Rif	YmcA-mV Δ*yaaT*	YmcA-mV Δ*ylbF*
Static tracks [%]	11.8	4.4	10.5	2.7	9.4	8.7	3.2	8.8	9.8
Mobile tracks [%]	88.2	95.6	89.5	97.3	90.6	91.3	96.8	91.2	90.2
Free [%]	66.6	78.1	73.6	82.8	75.1	76.8	79.0	85.3	83.8
Mixed behaviour	21.7	17.4	15.9	14.5	15.5	14.5	17.7	5.9	6.3

Figure 6. Confinement maps of Y-complex proteins with and without Rifampicin, and of YmcA-mV in the absence of YaaT or YlbF. (A-E) Plots of heat map of confined tracks, projected into a standardized *B. subtilis* cell. Constructs as indicated above the panels. G: Overview of ratios between static and mobile tracks.

Figure S5A shows all tracks, confined, freely diffusing, and transitions, in a standardized cell for YaaT. Rifampicin treatment leads to a strong relocalization of all kinds of tracks away from the cell membrane towards to cell centre for YaaT, but not for PfkA. Additionally, mobility of PfkA-mV only moderately increased after rifampicin treatment (Figure S5B and C), in agreement with an earlier report [69], and different from the strong changes seen for Y-complex proteins (Figure 4B and C). Please note that molecules showing confined motion

will largely overlap, but are not necessarily identical, with those that showed static motion in SQD analyses.

Relocalization of molecules away from the periphery towards the cell centre following treatment with rifampicin was also found in heat maps, in which all tracks were projected into a standardized cell (Figure S6). These experiments support findings made with wide field fluorescence microscopy that peripheral accumulation of molecules, which corresponds to confined motion, depends on transcription (Figure 1) and thus on the availability of mRNA as a substrate for the Y-complex.

3.5. Deletion of yaaT or of ylbF has a moderate influence on the dynamics of YmcA-mV

We wished to investigate if the absence of Y-complex proteins has a profound effect on the motion of another protein from the complex. We therefore investigated the localization and dynamics of the most mobile fusion, of YmcA-mV, after deletion of *yaaT* or of *ylbF*. For this purpose we transformed the fusion strain YmcA-mV with DNA from *yaaT* or *ylbF* deletion strains (Koo *et al*. 2017). In addition to the transformation ability we were able to test the function of the strains with a sporulation assay (Figure S1A). YmcA-mV/ *ΔyaaT* cells showed a reduced sporulation capacity of 24.6% compared to the wild type (set to 100%) or 57.5% for the YmcA-mV *ΔylbF* strain.

Interestingly, the deletion of *yaaT* led to a strong shift of confined YmcA-mV tracks away from the periphery towards the cell centre (Figure 6E). These experiments suggest that YaaT may be a membrane anchor for the Y-complex. The deletion of *ylbF* also led to noticeable but less pronounced changes in the localization of YmcA-mV tracks (Figure 6F).

In SQD analyses, we observed considerable changes in YmcA dynamics, but surprisingly, in a counterintuitive manner. For the purpose of this analysis, a common average diffusion constant was determined for populations for all three strains, such that changes in dynamics are represented by changes in population sizes only. Although we would have expected YmcA to lose binding to the putative complex with RNase Y, YmcA-mV became more static in the absence of YaaT, and more so in cells lacking YlbF (Figure 6). Also, in both *ΔyaaT* or *ΔylbF* cells, the medium-mobile fraction of YmcA-mV increased considerably, from about 30 to 36 or over 40% (Figure 6A), and the fast-mobile fraction decreased. Whatever the nature of the complex containing medium-mobile YmcA molecules (and likewise medium-mobile YaaT and YlbF molecules), its steady state-composition during exponential growth depends on the presence of all Y-complex proteins. On the other

hand, lack of YaaT or of YlbF does not abolish the ability of YmcA to become statically positioned, likely representing its binding to the very slow-moving RNA degradosome or at least a complex containing RNase Y, based on its dependence of the availability of (m)RNA. To determine expression levels, we performed western Blot analyses of YmcA-mV, using anti GFP antiserum, in wild type and in *yaaT* or *ylbF* deletion strains. Figure S7A shows that YmcA-mV was about two-fold more abundant in both mutant strains than in wild type cells. Possibly, absence of YaaT or of YlbF reduces overall RNA degradation, leading to increased YmcA levels. For higher than normal levels of YmcA, an increase in freely diffusive molecules would have been expected, due to a possible lack of binding sites on partner proteins, but the opposite was observed in the SQD analyses. Also, higher levels of YmcA cannot explain a complete relocation of confined tracks from the cell membrane towards the cell centre. Poised by this finding, we tested for YlbF abundance in the absence of YmcA, and found a strong, roughly 8-fold reduction in YlbF levels (Figure S7B). This unexpected observation suggests that YmcA might affect the stability of YlbF in cells. Remaining YlbF-mV lost predominantly membrane-associated confined motion in Δ*ymcA* cells, and was mostly found within the cytosol at the centre of cells (Figure 6C). Thus, lack of Y-complex components affects intracellular protein levels as well as protein mobility of other components.

These experiments suggest that the Y-complex is a highly dynamic entity, where on and off-binding events are affected by the presence of all three proteins, rather than a complete loss of complex formation.

A

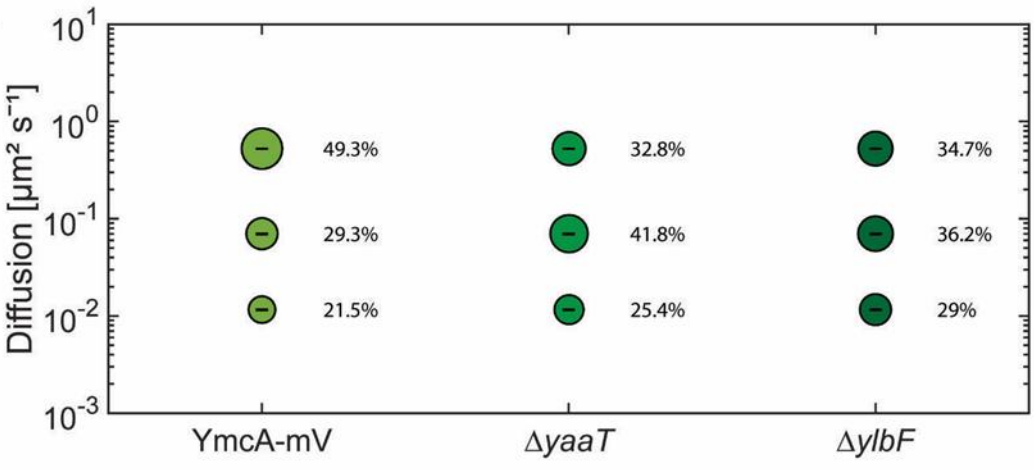

B

	YmcA-mV	*ΔyaaT*	*ΔylbF*
$D1_{(static)}$ µm² s⁻¹	0.01 ± 0.0	0.01 ± 0.0	0.01 ± 0.0
$D2_{(slow)}$ µm² s⁻¹	0.07 ± 0.0	0.07± 0.001	0.07 ± 0.0
$D3_{(fast)}$ µm² s⁻¹	0.53 ± 0.002	0.53 ± 0.002	0.53 ± 0.002
Static %	21.5 ± 0.001	25.4 ± 0.002	29.0 ± 0.001
Slow-mobile %	29.3 ± 0.001	41.8 ± 0.002	36.2 ± 0.001
Fast-mobile %	49.3 ± 0.002	32.8 ± 0.002	34.7 ± 0.002
P-values		***	***
R^2	1	1	1

Figure 7. Squared displacement analysis of YmcA-mV under different conditions in cells grown to mid-exponential phase. Bubble blot shows diffusion constants [µm^2 s^{-1}] of YmcA-mV, YmcA-mV Δ*yaaT* and YmcA-mV Δ*ylbF* cells and comparison of fast-mobile, slow-mobile and static fraction sizes [%]. (B) Diffusion constants and percentages of static, slow-mobile and fast-mobile molecule fractions. P-value: The symbols *, ** and *** represent P-values lower than 0.1, 0.05 or 0.01, respectively, n.s. statistically not significant.

3.6. Y-complex proteins show different degrees of association with the membrane

Heat maps generated from SMT experiments suggested that YmcA loses membrane-association in the absence of YaaT (Figure 6E). We therefore performed cell fractionation and subsequent western blot analyses of exponentially growing cells. As a control for successful fractionation, the integral membrane protein SpoIIIE-YFP (86.96 kDa + 27 kDa mVenus) was analysed, which was exclusively present within the membrane fraction (Figure 8B) [76]. YaaT was found in the membrane fraction and in the cytosolic fraction (Figure 8A). Figure S8 shows a fractionation in which the amount of membrane proteins is loaded such that cytosol plus membrane proteins equal the amount of protein from the lysate, showing that YaaT is present in each fraction to roughly equal parts. This finding is in agreement with the difficulty of obtaining soluble YaaT protein [58], but also agrees with our observation of

diffusive as well as confined motion of YaaT within the cytosol. Different from YaaT, YlbF and YmcA were only present within the cytosolic fraction (Figure 7A). Please note that the faint bands seen in the YmcA western blot are crossreactions that run at different heights than YmcA-mVenus. These data show that YlbF and YmcA have different physical properties than YaaT *in vivo*, and suggest that YaaT serves as an anchor for the Y-complex at the cell membrane. We can not distinguish at present if YaaT has membrane-association via strong binding to RNase Y, or via an intrinsic membrane-binding activity.

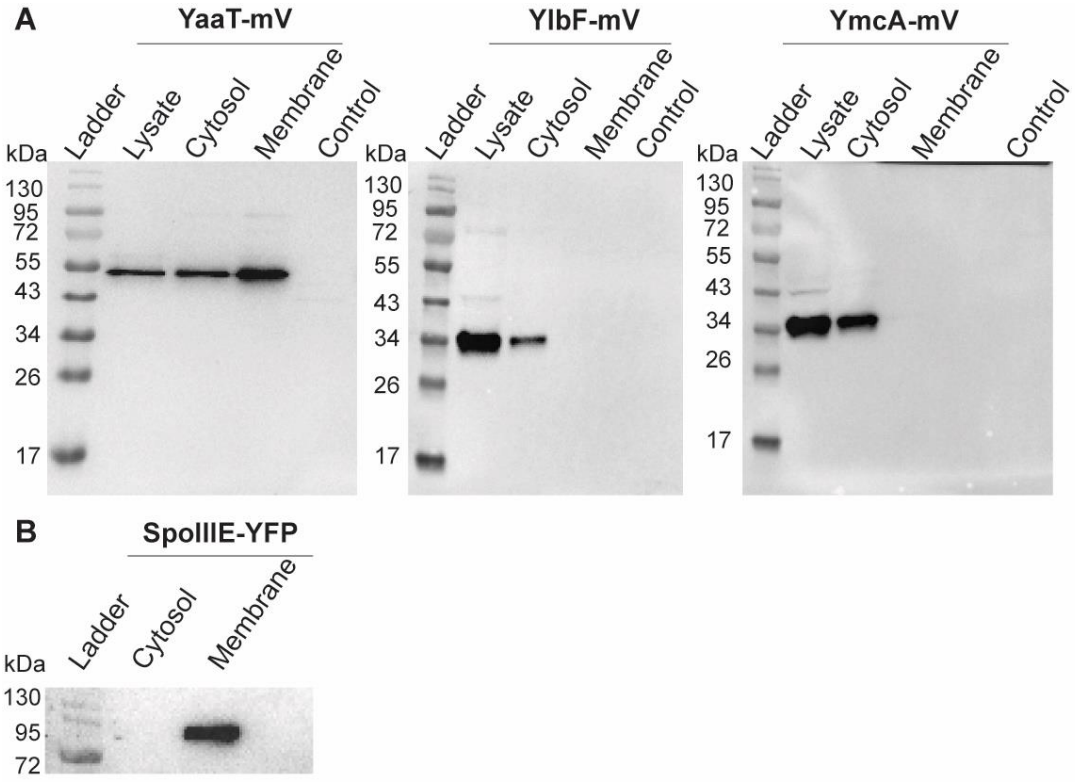

Figure 8. Western blots showing cell fractionation. Total cell extracts from exponentially growing cultures (LB) were used. The YaaT-mV fusion (57.9 kDa), YlbF-mV (43.7 kDa), YmcA (42.9 kDa) contains the mVenus polypeptide (26.9 kDa). Note that YlbF runs erroneously low, possibly because samples have not been heated before loading to the gel, which yields clearer bands. All strains were detected via GFP-antiserum. The fractionation was carried out by ultracentrifugation (100,000 x g). The displayed fractions shown are full lysate, supernatant (Cytosol) and pellet (Membrane). “Control” BG214 wild type cells without mVenus fusion.

2.2.5. Discussion

RNA turnover is an important way of controlling gene expression, an essential trait for bacteria to rapidly adapt to changing environmental conditions. In *E. coli* and many other bacterial species, RNase E plays a key role in global mRNA decay, and does so in conjunction with several other proteins, including other RNases, an RNA helicase, and a glycolytic enzyme, enolase [1]. Interestingly, bacterial species from many different phyla possess RNase Y, which appears to play an analogous function as RNase E, in initiating RNA decay through endonucleolytic attacks [38]. RNase Y also appears to be part of an RNA degradosome [6, 41]. Intriguingly, RNase Y has also been implicated in being part of a second complex, the so-called Y-complex (or RicAFT, for regulatory iron-sulfur containing): YaaT, YlbF and YmcA form a soluble complex [58], and are involved in RNA turnover as well as in specific RNA maturation events that also include RNase Y [8, 9, 34, 77]. However, many features of the Y-complex are unclear. While YlbF can be purified separately, YaaT can not, and only becomes soluble when all three proteins are present. RNase Y membrane assemblies are affected in their mobility by Y-complex proteins in *B. subtilis* [12], but in an unknown manner. It is also curious to note that RNase Y and the Y-complex play a role in gene regulation, occurring on the nucleoids, e.g. in riboswitch activities [9]. There are precedents of membrane-localized transcription factors [78, 79], so obviously, Y-complex regulated operons might translocate to the cell membrane, analogous to the *lac* operon moving to the cell membrane when transcription of the lactose permease is induced [80], whose transcription is thought to be directly coupled to its membrane insertion.

We addressed some of these intriguing questions by studying the dynamics of all three proteins of the Y-complex at a single molecule level. We reasoned that binding to different protein complexes or RNA substrates might lead to Y-complex proteins being present in different states of mobility, which would change upon loss of interaction partners or substrate. We found that three fractions with distinct average diffusion constants could well account for all molecule dynamics. They could make sense because YmcA, YlbF and YaaT might be associated with differently sized protein/RNA complexes.

RNA endonuclease activity for RNase Y toward operon mRNA maturation and degradation requires the Y-complex [9]. We show that very similar to RNase Y, YaaT, YlbF and YmcA also show considerable events of confined motion within the cell, indicating that they participate in RNase Y activity taking place on the nucleoids. Further key findings of our work are: a) Y complex proteins not only show confined motion close to the cell

membrane (which likely correspond to the foci observed by epifluorescence microscopy), but also within the cytosol. Because confined motion can most easily be explained by binding to a larger structure showing little movement, it is likely that YmcA, YlbF and YaaT arrest at sites of transcription where mRNA substrates for RNase Y and the Y-complex are synthesized (e.g. riboswitches); b) we also find freely diffusive tracks within the cytosol. This is in complete agreement with cell fractionation experiments showing that about half of YaaT molecules are strongly attached to the cell membrane, and 50% are cytosolic, while YlbF and YmcA are only found in the cytosolic fraction. These findings imply that YaaT serves as a membrane anchor for the other two Y-complex proteins. This idea is supported by our finding that the absence of YaaT in the cell leads to a shift of confined motion for YlbF away from the cell membrane, towards the cell centre, and vice versa. Interestingly, YmcA levels in the cell about double in the absence of YaaT or of YlbF, while YlbF is present in highly reduced amount in □*ymcA* cells. The most straight forward explanations for these observation are a reduction in *ymcA* mRNA turnover in the absence of YaaT or of YlbF, while YlbF may require YmcA for protection against proteolysis. However, several other alternative scenarios could be the case. Cell fractionation also shows that the components of the Y-complex have different biophysical properties with regard to membrane-association, and that the complex might be highly dynamic in terms of its composition. This is underlined by our finding that overall dynamics of YlbF do not change drastically in the absence of YaaT or of YlbF, which we would have expected would the proteins form a defined stoichiometric complex that falls apart in the absence of components.

Our findings also reveal that d) inhibition of transcription leads to a loss of confined motion at the cell membrane, and thus to a decrease in membrane recruitment for all three Y-complex proteins. This strongly suggests that Y-complex membrane assemblies are active structures, forming in a substrate-dependent manner. It will be of importance to study whether the foci correspond to RNA degradosome assemblies, or to independent structures.

SQD analysis of obtained tracks strongly suggested that all three Y-complex proteins are present in at least three distinct populations showing different mobilities. We observed a fraction of about 20% of molecules that showed extremely low mobility, lower than that described for translating ribosomes. This fraction could be part of the RNA degradosome, also containing RNase Y and several other RNases, an RNA helicase and two glycolytic enzymes. Such a large complex bound to possible multiple RNAs could indeed show observed low mobility. A second, largest fraction, of molecules showed mobility similar to that of translating ribosomes. We speculate that this population could be a cytosolic complex

bound to mRNA, which is then transported to the membrane-localized RNA degradosome. The Fast-moving fraction of molecules likely correspond to freely diffusing YaaT, YmcA and YlbF proteins, or a small, soluble subcomplex of e.g. YmcA and YlbF: these proteins showed most similar single molecule dynamics and solubility, and are quite small, compared with YaaT, which showed membrane-association for a large portion of molecules. Our finding that the diffusion constant of the medium-mobile fraction became much faster, while the fast-moving fraction remained largely unaffected after rifampicin treatment suggests that the fast-mobile fraction indeed consists of freely diffusive Y-complex molecules, while the medium-mobile fraction is apparently involved in RNA binding.

The differential effects of loss of individual Y-complex proteins suggests that *in vivo,* there could well be different associative forms of the Y-complex, which might explain the different effects of the individual mutants observed: the Y-complex has been reported to accelerate the phosphorylation of the transcription factor Spo0A, contribute to genetic competence, sporulation and biofilm formation and to be essential for the correct maturation of multiple protein- coding and riboswitch RNAs in *B. subtilis* [8, 9, 58]. Our analyses suggest that Y-complex proteins associate in a highly dynamic manner, and do not form a single defined complex. For example, the SMC chromosome segregation complex shows complete loss of the static, DNA bound fraction upon loss of one of its three subunits, and the diffusion constant of ScpA subunits increases drastically when the ScpB protein, which ScpA forms a subcomplex with, is absent from cells [27, 81]. Such clear-cut changes in molecule dynamics were not observed for Y complex proteins in cells lacking a component of the putative complex.

Pioneering work from the Dubnau group has shown that the Y-complex can only be purified by coexpression of all three proteins, and has a complex structure [77]. We found that the localization of YmcA-mV and single molecule dynamics are affected by the loss of *yaaT*, as well as *ylbF*. However, we still found YmcA being mobile within cells, indicating that *in vivo*, at least YmcA can remain soluble in the absence of its complex partners. Collectively, our data support the idea that the Y-complex can exist in different forms in *B. subtlilis*, and reveal that the Y-complex is intimately associated with RNA dynamics, at the cell membrane and within the cytosol. It remains an intriguing question how the four proteins can associate so dynamically assuming such different functions.

Supplementary Materials: The following are available online at www.mdpi.com/xxx/s1, Figure S1: title, Table S1: title.

Acknowledgments: We would like to thank Alexandra Kilb and Madita Viering for technical help, and Hannah Schmitz for advice on the manuscript. This work was supported by the Deutsche Forschungsgemeinschaft, and by the state of Hessen (MOSLA group, funded by the LOEWE program).

2.2.6. References

1. Laalami, S. and H. Putzer, *mRNA degradation and maturation in prokaryotes: the global players.* Biomol. Concepts, 2011. **2**(6): p. 491-506.
2. Mohanty, B.K. and S.R. Kushner, *Regulation of mRNA Decay in Bacteria.* Annu. Rev. Microbiol., 2016. **70**: p. 25-44.
3. Hui, M.P., P.L. Foley, and J.G. Belasco, *Messenger RNA degradation in bacterial cells.* Annu. Rev. Genet., 2014. **48**: p. 537-559.
4. Bandyra, K.J., *et al*., *The social fabric of the RNA degradosome.* Biochim. Biophys. Acta, 2013. **1829**(6-7): p. 514-522.
5. Shahbabian, K., *et al*., RNase Y*, a novel endoribonuclease, initiates riboswitch turnover in Bacillus subtilis.* EMBO J., 2009. **28**(22): p. 3523-3533.
6. Commichau, F.M., *et al*., *Novel activities of glycolytic enzymes in Bacillus subtilis: interactions with essential proteins involved in mRNA processing.* Mol. Cell. Proteomics, 2009. **8**(6): p. 1350-1360.
7. Lehnik-Habrink, M., *et al*., *RNA processing in Bacillus subtilis: identification of targets of the essential* RNase Y*.* Mol. Microbiol., 2011. **81**(6): p. 1459-1473.
8. DeLoughery, A., *et al*., *Biofilm formation by Bacillus subtilis requires an endoribonuclease-containing multisubunit complex that controls mRNA levels for the matrix gene repressor SinR.* Mol. Microbiol., 2016. **99**(2): p. 425-437.
9. DeLoughery, A., *et al*., *Maturation of polycistronic mRNAs by the endoribonuclease* RNase Y *and its associated Y-complex in Bacillus subtilis.* Proc. Natl. Acad. Sci. U S A, 2018. **115**(24): p. E5585-E5594.
10. Strahl, H., *et al*., *Membrane recognition and dynamics of the RNA degradosome.* PLoS Genet., 2015. **11**(2): p. e1004961.
11. Cascante-Estepa, N., K. Gunka, and J. Stulke, *Localization of Components of the RNA-Degrading Machine in Bacillus subtilis.* Front. Microbiol., 2016. **7**: p. 1492.
12. Hamouche, L., *et al*., *Dynamic Membrane Localization of* RNase Y *in Bacillus subtilis.* mBio, 2020. **11**(1).
13. Khemici, V., *et al*., *The RNase E of Escherichia coli is a membrane-binding protein.* Mol. Microbiol., 2008. **70**(4): p. 799-813.
14. Kunz, S., *et al*., *Cyclic di-GMP Signaling in Bacillus subtilis Is Governed by Direct Interactions of Diguanylate Cyclases and Cognate Receptors.* mBio, 2020. **11**(2).

15. Dersch, S., *et al*., *Super-Resolution Microscopy and Single-Molecule Tracking Reveal Distinct Adaptive Dynamics of MreB and of Cell Wall-Synthesis Enzymes.* Front. Microbiol., 2020. **11**: p. 1946.

16. Burghard-Schrod, M., S. Altenburger, and P.L. Graumann, *The Bacillus subtilis dCMP deaminase ComEB acts as a dynamic polar localization factor for ComGA within the competence machinery.* Mol. Microbiol., 2020. **113**(5): p. 906-922.

17. Hernandez-Tamayo, R., *et al*., *Symmetric activity of DNA polymerases at and recruitment of exonuclease ExoR and of PolA to the Bacillus subtilis replication forks.* Nucleic Acids Res., 2019. **47**(16): p. 8521-8536.

18. Rosch, T.C., *et al*., *Single molecule tracking reveals spatio-temporal dynamics of bacterial DNA repair centres.* Sci. Rep., 2018. **8**(1): p. 16450.

19. Jaacks, K., *et al*., *Identification and characterization of genes controlled by the sporulation-regulatory gene spo0H in Bacillus subtilis.* 1989. **171**(8): p. 4121-4129.

20. Lucena, D., *et al*., *Microdomain formation is a general property of bacterial membrane proteins and induces heterogeneity of diffusion patterns.* 2018. **16**(1): p. 1-17.

21. Gibson, D.J.P.E., *One-step enzymatic assembly of DNA molecules up to several hundred kilobases in size.* 2009. **6**: p. 343-345.

22. Koo, B.-M., *et al*., *Construction and analysis of two genome-scale deletion libraries for Bacillus subtilis.* 2017. **4**(3): p. 291-305. e7.

23. Mascarenhas, J., *et al*., *Cell cycle-dependent localization of two novel prokaryotic chromosome segregation and condensation proteins in Bacillus subtilis that interact with SMC protein.* 2002. **21**(12): p. 3108-3118.

24. Schindelin, J., *et al*., *The ImageJ ecosystem: an open platform for biomedical image analysis. ResearchGate 82: 518–529*. 2015.

25. Paintdakhi, A., *et al*., *Oufti: an integrated software package for high-accuracy, high-throughput quantitative microscopy analysis.* 2016. **99**(4): p. 767-777.

26. Jaqaman, K., *et al*., *Robust single-particle tracking in live-cell time-lapse sequences.* 2008. **5**(8): p. 695.

27. Schibany, S., *et al*., *Single molecule tracking reveals that the bacterial SMC complex moves slowly relative to the diffusion of the chromosome.* Nucleic Acids Res., 2018. **46**(15): p. 7805-7819.

28. Schenk, K., *et al*., *Rapid turnover of DnaA at replication origin regions contributes to initiation control of DNA replication.* PLoS Genet., 2017. **13**(2): p. e1006561.

29. Persson, F., *et al*., *Extracting intracellular diffusive states and transition rates from single-molecule tracking data.* Nat. Methods, 2013. **10**(3): p. 265-269.

30. Figaro, S., *et al*., *Bacillus subtilis mutants with knockouts of the genes encoding ribonucleases* RNase Y *and RNase J1 are viable, with major defects in cell morphology, sporulation, and competence.* J. Bacteriol., 2013. **195**(10): p. 2340-2348.

31. Sanamrad, A., *et al*., *Single-particle tracking reveals that free ribosomal subunits are not excluded from the Escherichia coli nucleoid.* Proc. Natl. Acad. Sci. U S A, 2014. **111**(31): p. 11413-11418.

32. Bandow, J.E., H. Brotz, and M. Hecker, *Bacillus subtilis tolerance of moderate concentrations of rifampin involves the sigma(B)-dependent general and multiple stress response.* J. Bacteriol., 2002. **184**(2): p. 459-467.

33. Price, A.R. and M. Frabotta, *Resistance of bacteriophage PBS2 infection to rifampicin, an inhibitor of Bacillus subtilis RNA synthesis.* Biochem. Biophys. Res. Commun., 1972. **48**(6): p. 1578-1585.

34. Durand, S., *et al*., *Three essential ribonucleases*-RNase Y*, J1, and III-control the abundance of a majority of Bacillus subtilis mRNAs.* PLoS Genet., 2012. **8**(3): p. e1002520.

35. Uphoff, S., *et al*., *Stochastic activation of a DNA damage response causes cell-to-cell mutation rate variation.* Science, 2016. **351**(6277): p. 1094-1097.

36. Bremer, H. and P.P. Dennis, *Modulation of Chemical Composition and Other Parameters of the Cell at Different Exponential Growth Rates.* EcoSal Plus, 2008. **3**(1).

37. Muntel, J., *et al*., *Comprehensive absolute quantification of the cytosolic proteome of Bacillus subtilis by data independent, parallel fragmentation in liquid chromatography/mass spectrometry (LC/MS(E)).* Mol. Cell Proteomics, 2014. **13**(4): p. 1008-1019.

38. Lehnik-Habrink, M., *et al*., RNase Y *in Bacillus subtilis: a Natively disordered protein that is the functional equivalent of RNase E from Escherichia coli.* J. Bacteriol., 2011. **193**(19): p. 5431-5441.

39. Ulbrich, M.H. and E.Y. Isacoff, *Subunit counting in membrane-bound proteins.* Nat. Methods, 2007. **4**(4): p. 319-321.

40. Dersch, S. and P.L. Graumann, *The ultimate picture-the combination of live cell superresolution microscopy and single molecule tracking yields highest spatio-temporal resolution.* Curr. Opin. Microbiol., 2018. **43**: p. 55-61.

41. Lehnik-Habrink, M., *et al*., *The RNA degradosome in Bacillus subtilis: identification of CshA as the major RNA helicase in the multiprotein. complex.* Mol. Microbiol., 2010. **77**(4): p. 958-971.

42. Lehnik-Habrink, M., *et al*., *RNA degradation in Bacillus subtilis: an interplay of essential endo- and exoribonucleases.* Mol. Microbiol., 2012. **84**(6): p. 1005-1017.

43. Salvo, E., *et al*., *Interaction of Bacillus subtilis Polynucleotide Phosphorylase and* RNase Y*: STRUCTURAL MAPPING AND EFFECT ON mRNA TURNOVER.* J. Biol. Chem., 2016. **291**(13): p. 6655-6663.

44. Lee, B.H. and H.Y. Park, *HybTrack: A hybrid single particle tracking software using manual and automatic detection of dim signals.* Sci. Rep., 2018. **8**(1): p. 212.

45. Hansen, A.S., *et al*., *Robust model-based analysis of single-particle tracking experiments with Spot-On.* Elife, 2018. **7**.

46. Sage, D., *et al*., *Quantitative evaluation of software packages for single-molecule localization microscopy.* Nat. Methods, 2015. **12**(8): p. 717-724.

47. Carpousis, A.J., V. Khemici, and L. Poljak, *Assaying DEAD-box RNA helicases and their role in mRNA degradation in Escherichia coli.* Methods Enzymol., 2008. **447**: p. 183-197.

48. Trinquier, A., *et al*., *Regulation of RNA processing and degradation in bacteria.* Biochim. Biophys. Acta Gene Regul. Mech., 2020. **1863**(5): p. 194505.

49. Hui, M.P., P.L. Foley, and J.G. Belasco, *Messenger RNA degradation in bacterial cells.* Annu. Rev. Genet., 2014. **48**: p. 537-559.

50. Arraiano, C.M., *et al*., *The critical role of RNA processing and degradation in the control of gene expression.* FEMS Microbiol. Rev., 2010. **34**(5): p. 883-923.

51. Bruscella, P., *et al*., RNase Y *is responsible for uncoupling the expression of translation factor IF3 from that of the ribosomal proteins L35 and L20 in Bacillus subtilis.* Mol. Microbiol., 2011. **81**(6): p. 1526-1541.

52. Braun, F., S. Durand, and C. Condon, *Initiating ribosomes and a 5′/3′-UTR interaction control ribonuclease action to tightly couple B. subtilis hbs mRNA stability with translation.* Nucleic Acids Res., 2017. **45**(19): p. 11386-11400.

53. Benda, M., *et al*., *Quasi-essentiality of* RNase Y *in Bacillus subtilis is caused by its critical role in the control of mRNA homeostasis.* Nucleic Acids Res., 2021. **49**(12): p. 7088-7102.

54. Carpousis, A.J., *et al*., *Co-immunopurification of multiprotein complexes containing RNA-degrading enzymes.* Methods Enzymol., 2008. **447**: p. 65-82.

55. Carpousis, A.J., *et al*., *Copurification of E. coli RNAase E and PNPase: evidence for a specific association between two enzymes important in RNA processing and degradation.* Cell, 1994. **76**(5): p. 889-900.

56. Py, B., *et al*., *A protein complex mediating mRNA degradation in Escherichia coli.* Mol. Microbiol., 1994. **14**(4): p. 717-729.

57. Carabetta, V.J., *et al*., *A complex of YlbF, YmcA and YaaT regulates sporulation, competence and biofilm formation by accelerating the phosphorylation of Spo0A.* Mol. Microbiol., 2013. **88**(2): p. 283-300.

58. Adusei-Danso, F., *et al*., *Structure-Function Studies of the Bacillus subtilis Ric Proteins Identify the Fe-S Cluster-Ligating Residues and Their Roles in Development and RNA Processing.* mBio, 2019. **10**(5).

59. Lewis, P.J., S.D. Thaker, and J. Errington, *Compartmentalization of transcription and translation in Bacillus subtilis.* EMBO J., 2000. **19**(4): p. 710-718.

60. Jaacks, K.J., *et al*., *Identification and characterization of genes controlled by the sporulation regulatory gene spo0H in Bacillus subtilis.* J. Bacteriol., 1989. **171**: p. 4121-4129.

61. Lucena, D., *et al*., *Microdomain formation is a general property of bacterial membrane proteins and induces heterogeneity of diffusion patterns.* BMC Biol., 2018. **16**(1): p. 97.

62. Gibson, D.G., *et al*., *Enzymatic assembly of DNA molecules up to several hundred kilobases.* Nat. Methods, 2009. **6**(5): p. 343-345.

63. Koo, B.M., *et al*., *Construction and Analysis of Two Genome-Scale Deletion Libraries for Bacillus subtilis.* Cell Syst., 2017. **4**(3): p. 291-305 e7.

64. Schindelin, J., *et al*., *Fiji: an open-source platform for biological-image analysis.* Nat. Methods, 2012. **9**(7): p. 676-682.

65. Paintdakhi, A., *et al*., *Oufti: an integrated software package for high-accuracy, high-throughput quantitative microscopy analysis.* Mol. Microbiol., 2016. **99**(4): p. 767-777.

66. Jaqaman, K., *et al*., *Robust single-particle tracking in live-cell time-lapse sequences.* Nat. Methods, 2008. **5**(8): p. 695-702.

67. Rosch, T.C., *et al*., *SMTracker: a tool for quantitative analysis, exploration and visualization of single-molecule tracking data reveals highly dynamic binding of B. subtilis global repressor AbrB throughout the genome.* Sci. Rep., 2018. **8**(1): p. 15747.

68. Hosoya, S., *et al*., *Mutation in yaaT leads to significant inhibition of phosphorelay during sporulation in Bacillus subtilis.* J. Bacteriol., 2002. **184**(20): p. 5545-5553.

69. Oviedo-Bocanegra, L.M., *et al*., *Single molecule/particle tracking analysis program SMTracker 2.0 reveals different dynamics of proteins within the RNA degradosome complex in Bacillus subtilis.* Nucleic Acids Res., 2021.

70. Leake, M.C., *et al*., *Stoichiometry and turnover in single, functioning membrane protein complexes.* Nature, 2006. **443**(7109): p. 355-358.

71. Bakshi, S., *et al*., *Superresolution imaging of ribosomes and RNA polymerase in live Escherichia coli cells.* Mol. Microbiol., 2012. **85**(1): p. 21-38.
72. Sanamrad, A., *et al*., *Single-particle tracking reveals that free ribosomal subunits are not excluded from the Escherichia coli nucleoid.* Proceedings of the National Academy of Sciences, 2014. **111**(31): p. 11413-11418.
73. Wlodarski, M., *et al*., *Cytosolic Crowding Drives the Dynamics of Both Genome and Cytosol in Escherichia coli Challenged with Sub-lethal Antibiotic Treatments.* iScience, 2020. **23**(10): p. 101560.
74. Rotter, D.A.O., *et al*., *Transcription-dependent confined diffusion of enzymes within subcellular spaces of the bacterial cytoplasm.* BMC Biol., 2021. **19**(1): p. 183.
75. Sattler, L. and P.L. Graumann, *Real-Time Messenger RNA Dynamics in Bacillus subtilis.* Front. Microbiol., 2021. **12**: p. 760857.
76. El Najjar, N., *et al*., *Single-Molecule Tracking of DNA Translocases in Bacillus subtilis Reveals Strikingly Different Dynamics of SftA, SpoIIIE, and FtsA.* Appl. Environ. Microbiol., 2018. **84**(8): p. e02610-17.
77. Tanner, A.W., *et al*., *The RicAFT (YmcA-YlbF-YaaT) complex carries two [4Fe-4S](2+) clusters and may respond to redox changes.* Mol. Microbiol., 2017. **104**(5): p. 837-850.
78. Gorke, B. and B. Rak, *Efficient transcriptional antitermination from the Escherichia coli cytoplasmic membrane.* J. Mol. Biol., 2001. **308**(2): p. 131-145.
79. Brameyer, S., *et al*., *DNA-binding directs the localization of a membrane-integrated receptor of the ToxR family.* Commun. Biol., 2019. **2**: p. 4.
80. Libby, E.A., M. Roggiani, and M. Goulian, *Membrane protein expression triggers chromosomal locus repositioning in bacteria.* Proc. Natl. Acad. Sci. U S A, 2012. **109**(19): p. 7445-7450.
81. Kleine Borgmann, L.A., *et al*., *The bacterial SMC complex displays two distinct modes of interaction with the chromosome.* Cell Rep., 2013. **3**(5): p. 1483-1492.

2.2.7. Supplementary Material

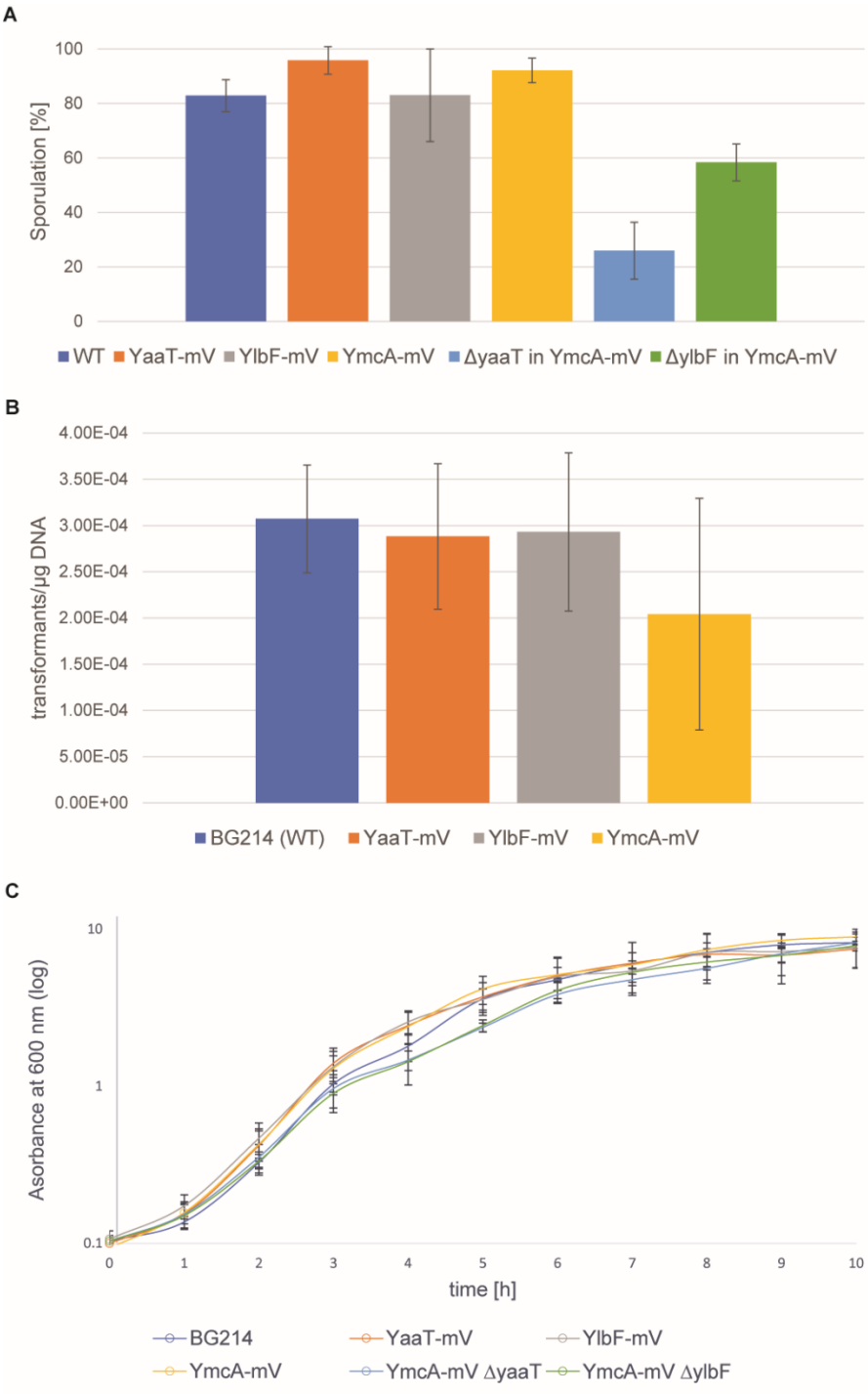

Fig. S1 Figure S1. Test for functionality of the Y-complex protein fusions in *Bacillus subtilis* cells. **A)** Bar plot with error bars shows the percentage of sporulation after incubation in DSM-culture medium in comparison to the wild type. The wild-type represents a sporulation of 82.5%. The mVenus fusions showed no compromise in the function of the sporulation

(YaaT-mV 95.5%, YlbF-mV 81.7%, YmcA-mV 92.1%). The deletions of *yaaT* and *ylbF* in YmcA-mV clarify a reduced function of the sporulation. P-value: The symbols *, ** and *** indicate P-values lower than 0.1, 0.05 and 0.01, respectively, n.s. statistically not significant. **B)** Transformation assay. Bar plot with error bars shows the percentage of transformants/µg DNA in comparison to the wild type strain. Assays were performed in technical triplicates and in biological duplicates. Error bars indicate standard deviation. **C)** Growth curves for strains containing the following strains: BG214 (darkblue), YaaT-V (orange), YlbF-mV (grey), YmcA-mV (yellow), YmcA-mV *ΔyaaT* (light blue), YmcA-mV *ΔylbF* (green). Measurements were performed in 300 ml flasks with a volume of 50 ml.

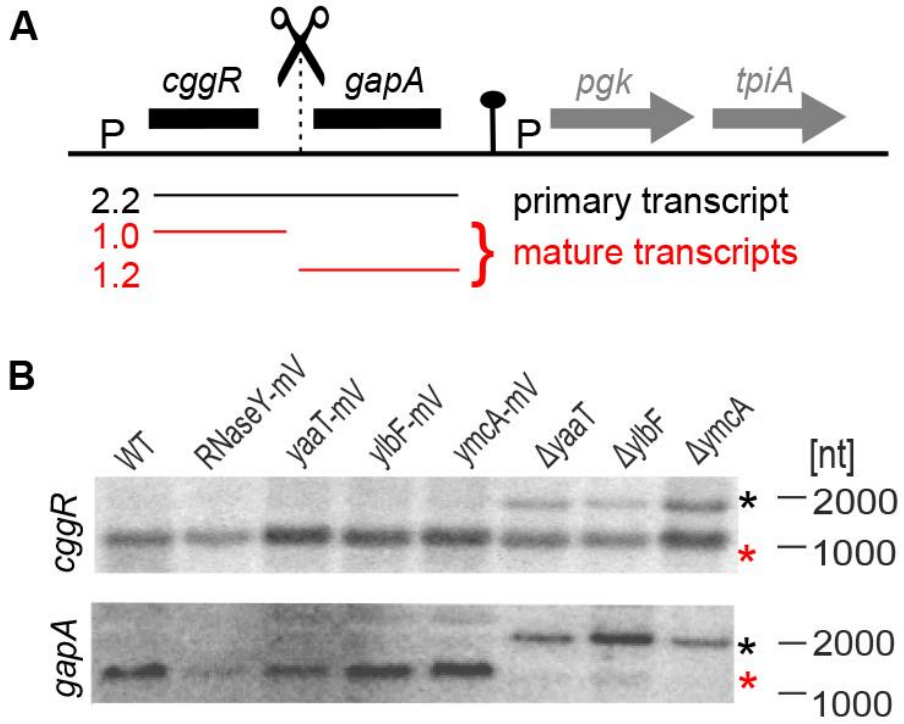

Fig. S2 Maturation of the *gapA* operon mRNA by RNase Y degradosome. **A)** Schematic illustration of the *gapA* operon primary transcripts processed by RNase Y. The maturation of the RNA results in two transcripts *cggR* (1.0 kb) and *gapA* (1.2 kb). **B)** Analysis of the processing of *cggR* and *gapA* transcripts in different *B. subtilis* strains. Processed *cggR* or

gapA transcripts are visualized by Northern blot. Primary (black asterisk) and mature transcripts (red asterisk) of the *gapA* operon are detected by specific riboprobes.

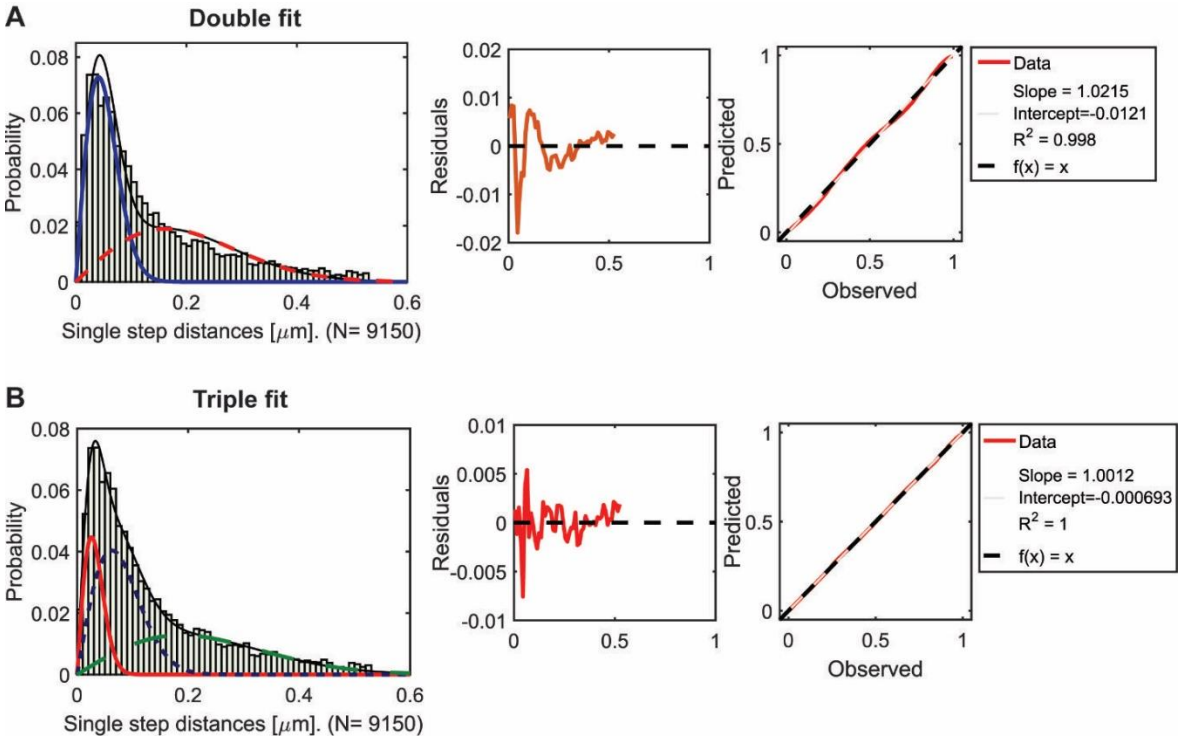

Fig. S3 Jump-distance histograms to compare a double **A)** or triple population **B)** Rayleigh fit for YaaT-mV. Histograms of jump-distance values overlaid with each individual group model, static (green solid line in **A)**, red solid line in **B)**), slow-diffusive (blue dotted line in (B), and diffusive (green dotted or dashed line)), and their sum (black solid line). Lower panels are quantile-quantile plots, showing the difference (blue curve) between measured data and modelled data (represented by the dashed red line), and the resulting R^2 determined the goodness-of-fit.

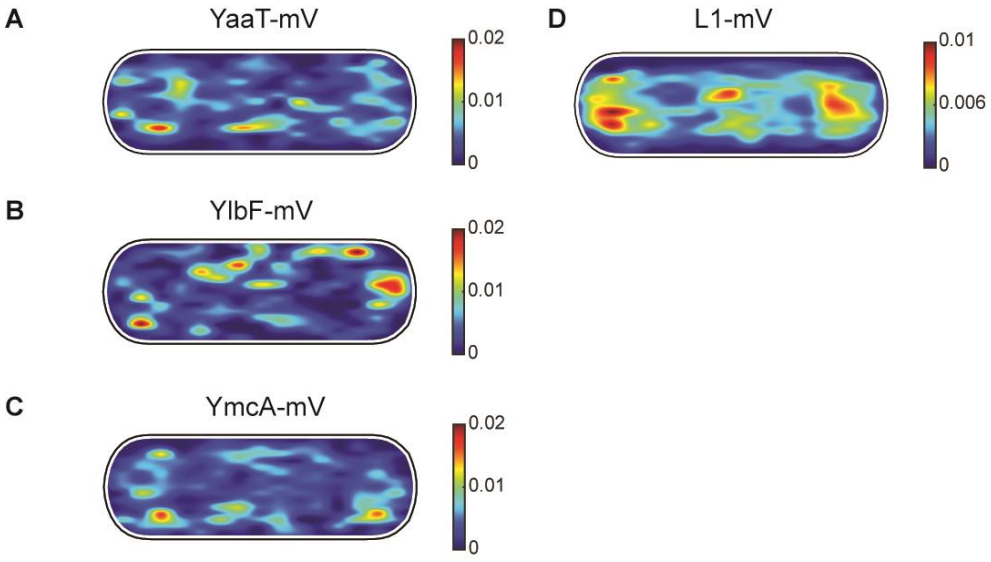

Fig. S4 Confinement maps of Y-complex proteins compared with that of L1-mV representing ribosomes ribosomes, projected into standardized (medium-size) *B. subtilis* cells. Strains in panels **A-D** as indicated above the maps.

A

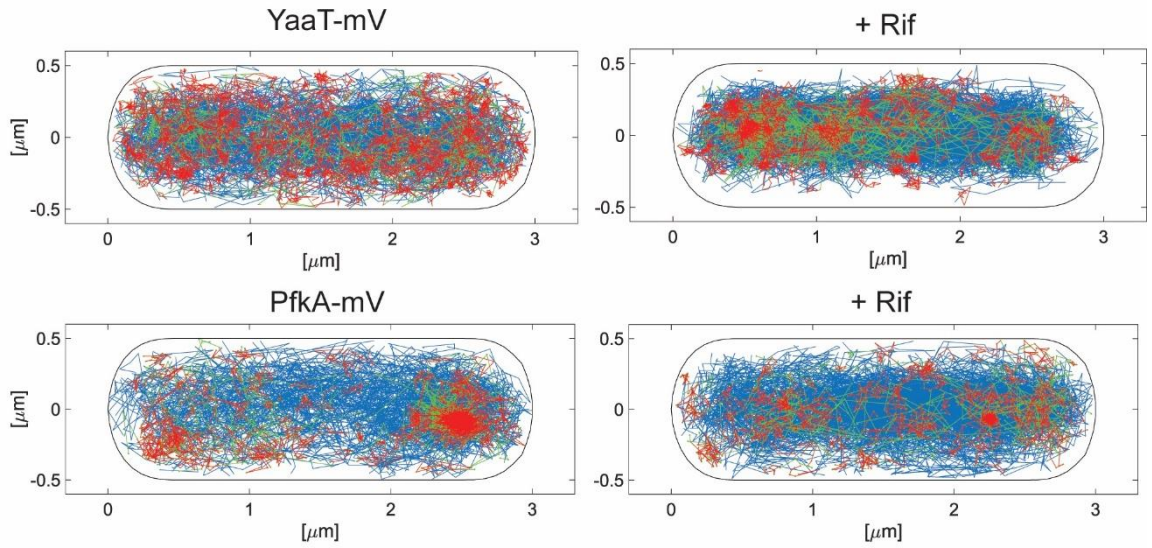

B

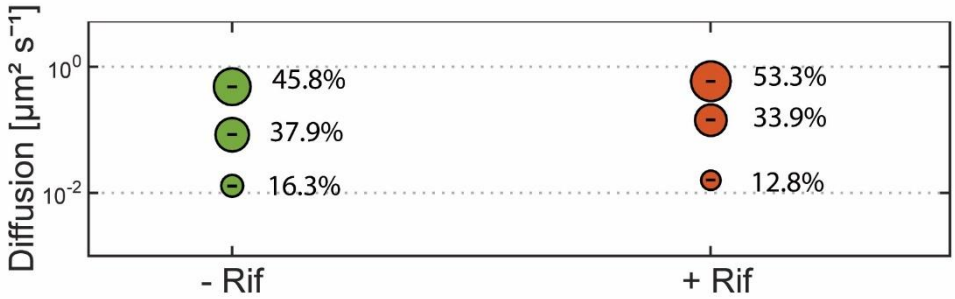

C

	PfkA-mV (-Rif)	PfkA-mV (+Rif)
$D1_{(static)}$ $\mu m^2/s^{-1}$	0.01 ± 0.0	0.02 ± 0.0
$D2_{(slow)}$ $\mu m^2/s^{-1}$	0.08 ± 0.001	0.14± 0.001
$D3_{(fast)}$ $\mu m^2/s^{-1}$	0.49 ± 0.002	0.58 ± 0.002
Static %	16.3 ± 0.002	12.8 ± 0.001
Slow-mobile %	37.9 ± 0.002	33.9± 0.001
Fast-mobile %	45.8 ± 0.002	53.3 ± 0.001
R^2	0.99997	0.99998

Fig. S5 A) Confinement maps of YaaT-mV and of PfkA-mV during exponential growth and after rifampicin treatment. Plots of tracks classified into confined (red, staying within a radius of 120 nm for at least 6 steps), mobile (blue) and tracks performing transitions (green), in a standardized *B. subtilis* cell. **B)** Bubble blots show diffusion constants of PfkA-mV without and with treatment of Rifampicin and fractions sizes for fast-mobile, slow-mobile and static molecules. **C)** Diffusion constants and percentages of static, slow-mobile and fast-mobile molecule fractions. Values were fitted using non-linear least-square fitting, R^2 values for each condition are stated.

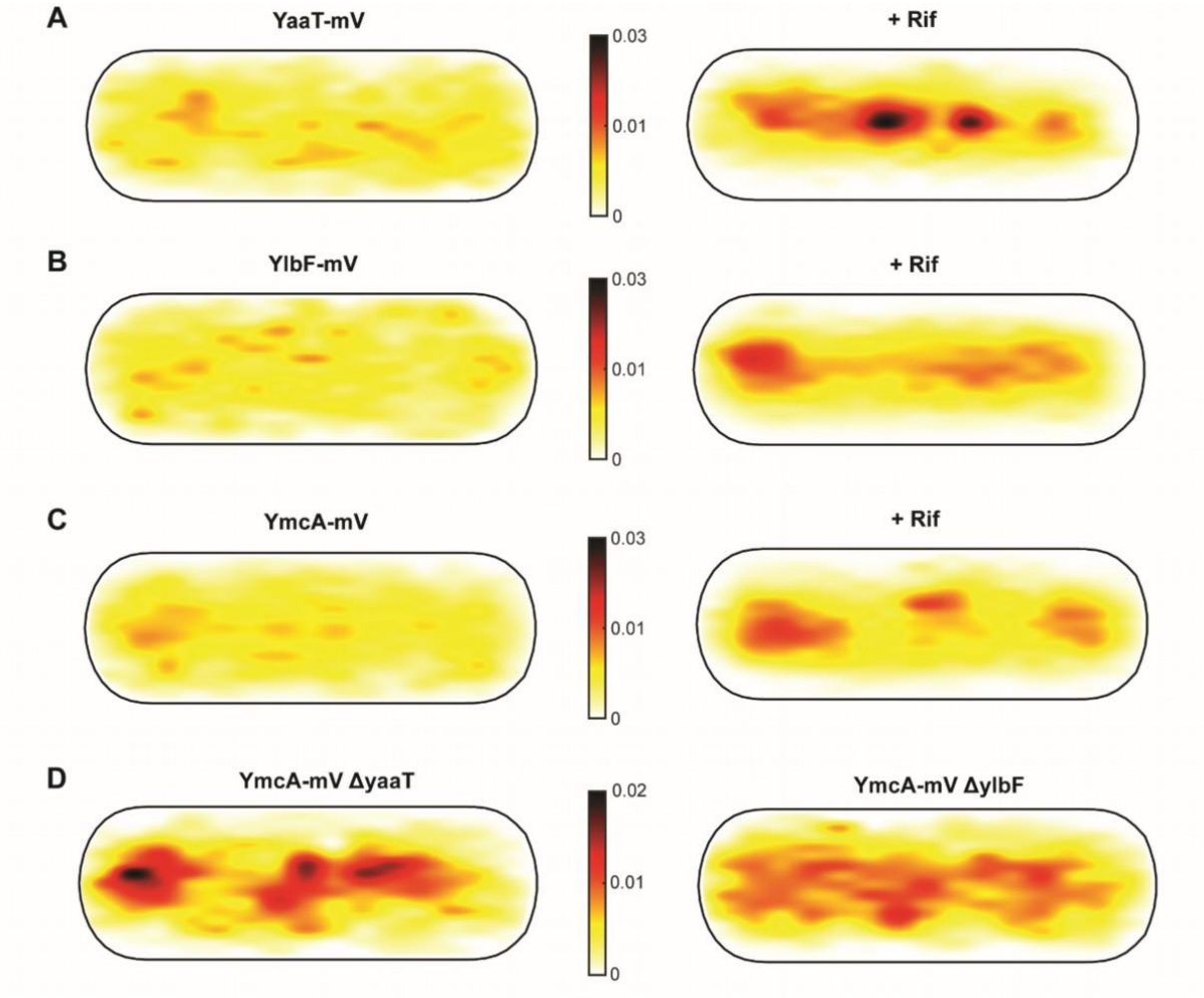

Fig. S6 Heat maps of single-molecule localization of Y-complex proteins in a medium-size *Bacillus subtilis* cell. The distribution of tracks is indicated by a color shift from yellow (low probability) to black (highest probability). **A)** A YaaT-mV fusion localized throughout the cells. “+Rif” YaaT-mV fusion after treatment with rifampicin for 30 min, revealing a relocation away from the membrane towards the cell center. **B)** YlbF-mV as in panel A, **C)** YmcA-mV fusion as in panel A. **D)** YmcA-mV fusion in the absence of YaaT or of YlbF.

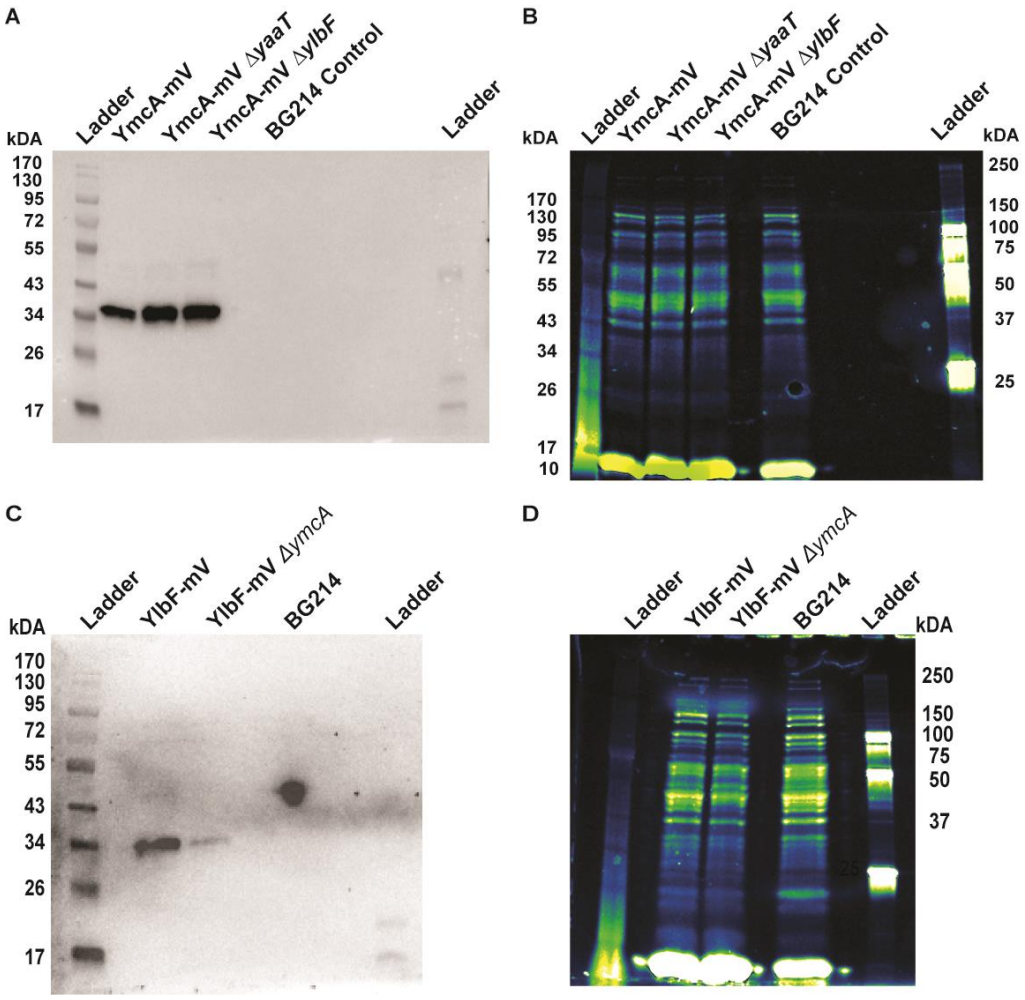

Fig. S7 Western Blot analyses of YmcA-mV expression levels in the absence of YaaT or of YlbF. **A**) Western blot analysis of YmcA-mV and the deletion strains *ΔyaaT* and *ΔylbF*. **C**) Western blot analysis of YlbF-mV in comparison to the deletion *ΔymcA.* The wild type strain BG214 was used as a control. All strains were detected via GFPtag- antiserum. **B**, **D**) Prior to western blotting, the total protein load of the gel was controlled by stain-free imaging, using Bio-Rad PROTEAN TGX Stain-Free SDS gels that allow for UV-activated quantitative imaging using UV exposure, before the gels are blotted onto a membrane.

Table S1 Strains and primers used in this study

Strain or Plasmids	Relevant features	Reference or source
B. subtilis		
BG214	Wild type	
PG3741	BKK14990 Δ*yaaT*::kan trpC2	(Koo *et al*. 2017)
PG3740	BKK00320 Δ*ylbF*::kan trpC2	(Koo *et al*. 2017)
PG3742	BKK17020 Δ*ymcA*::kan trpC2	(Koo *et al*. 2017)
PG3811	*yaaT*-mVenus^{cmR}	This study
PG3812	*ylbF*-mVenus^{cmR}	This study
PG3813	*ymcA*-mVenus^{cmR}	This study
PG3838	Δ*yaaT*::kan trpC2 *ymcA*-mVenus^{cmR}	This study
PG3839	Δ*ylbF*::kan trpC2 ymcA-mVenus^{cmR}	This study
E. coli		
DH5α	*sup*E44 Δ*lac*U169 φ80d*lac*ZΔM15 *hsd*R171 *rec*A1 *end*A1 *gyr*A96 *thi*-1 *rel*A1	New England Biolabs (NEB)
PG3730	DH5α pSG1164-mVenus, expression Vektor, Amp^R, Cm^R	(Lucena *et al*. 2018)
PG3852	DH5α pSG1164 *yaaT*-mVenus, expression Vektor, Amp^R, Cm^R	This study
PG3853	DH5α pSG1164 *ylbF*-mVenus, expression Vektor, Amp^R, Cm^R	This study
PG3854	DH5α pSG1164 *ymcA*-mVenus, expression Vektor, Amp^R, Cm^R	This study

Primer	Sequence 5´→ 3´
PG3811 fw	CCTAGGATGGGTACCGAATTCCGTTTGATCGCAATAAAGT
PG3811 rv	AGGCCAGATAGGCCGGGCCCATCTGTGGTTTGTGCGG
PG3812 fw	CTAGGATGGGTACCGAATTCATGTATGCGACGATGGAATC
PG3812 rv	AGGCCAGATAGGCCGGGCCCGGACACTTTACATCC GC
PG3813 fw	CTAGGATGGGTACCGAATTCGAAAATCCAGCAAGCGAAAA
PG3813 rv	AGGCCAGATAGGCCGGGCCCGAGAGAACAGCTGTTAT
Sequencing primer	
mVenus/yfp rev	TGCGCTCCTGGACG
kan^R fw	CGCTCTACTCAAAAAAAGAC
kan^R rv	CTGTAAAGGCACCGTGTTTA
Northern Blot	

cggR_fw	TAATACGACTCACTATAGGCAATAATATCGGGGATGGCGTCTATGTCATC CAGCTGCATT
cggR_rev	CGGACGGCGAAGTGGTTCACAAAGTGCATTCTGTCGGAATGCAGCTGGATGA CATAGACG
gapA_fw	TAATACGACTCACTATAGGCTGCAAGGTCAACAACGCGGTTAGAGTAGCCGC TTTCGTTA
gapA_rev	GGCAGCATGGTAAAAGTAATCTCTTGGTACGATAACGAAAGCGGCTACTCTAA CCGCG

2.3. Article III

Visual evidence for the recruitment of four enzymes with RNase activity to the *Bacillus subtilis* replication forks

Rebecca Hinrichs and Peter L. Graumann

Centre for Synthetic Microbiology (SYNMIKRO) and Fachbereich Chemie, Philipps-Universität Marburg, 35032 Marburg, Germany

for correspondence graumanp@uni-marburg.de

Phone number: +49-6421 28 22210

Key words: DNA replication, RNases, Okazaki fragment maturation, *Bacillus subtilis*, DNA Polymerase 1, Exonuclease

2.3.1. Abstract

Removal of RNA/DNA hybrids for the maturation of Okazaki fragments on the lagging strand, or due to misincorporation of ribonucleotides by DNA polymerases, is essential for all types of cells. In prokaryotic cells such as *Escherichia coli*, DNA polymerase 1 and RNase HI are supposed to remove RNA from Okazaki fragments, but many bacteria lack HI-type RNases, such as *Bacillus subtilis.* Here, four proteins have been shown to be able to remove RNA from RNA/DNA hybrids *in vitro*, but their actual contribution to DNA replication is unclear. We have studied the dynamics of DNA polymerase A (similar to Pol 1), 5'->3' exonuclease ExoR, and the two endoribonucleases RNase HII and HIII in *B. subtilis* using single molecule tracking. We found that all four enzymes show a localization pattern similar to that of replicative DNA helicase. By scoring the distance of tracks to replication forks, we found that all four enzymes are enriched at DNA replication centers. After inducing UV damage, RNase HIII was even more strongly recruited to the replication forks, and PolA showed a more static behavior, indicative of longer binding events, whereas RNase HII and ExoR showed no response. Inhibition of replication by HPUra clearly demonstrated that both RNase HII and RNase HIII are directly involved in replication, with RNase HIII playing a major role. We found that the absence of ExoR increases the likelihood of RNase HIII at the forks, indicating that substrate availability rather than direct protein

interactions may be a major driver for the recruitment of RNases to the lagging strands. Thus, *B. subtilis* replication forks appear to be an intermediate between *E. coli* type and eukaryotic replication forks and employ a multitude of RNases, rather than any dedicated enzyme for RNA/DNA hybrid removal.

2.3.2. Introduction

RNA maturation, RNA degradation, and RNA turnover are essential processes for all kinds of cells. Enzymes known as ribonucleases (RNases) are crucial for these processes (Williams & Kunkel, 2014), and are usually present in many different versions per cell. During DNA replication, RNases play a major role in the maturation of Okazaki fragments on the discontinuous, lagging strand, by removing the arising DNA/RNA hybrids made by DNA primase (Li & Breaker, 1999). In addition, even though DNA polymerases have a much higher affinity for desoxy ribonucleotides (dNTPs) than ribonucleotides, the RTP pools are in large excess of those of dNTPs, wherefore ribonucleo-monophosphates (rNMPs) are incorporated about every 2.3 kb in *E. coli* cells (Yao *et al*, 2013). Loss of removal of for rNMPs leads to an increase in mutation frequency.

A general differentiation can be made between endoribonucleases and exoribonucleases. RNase E or RNase Y are major endoribonucleases that initiate RNA turnover, which is then taken over by exonucleases (Bechhofer & Deutscher, 2019). The latter process RNA molecules that result in 3’ or 5’ terminal release of nucleotide residues. A 3' to 5' exoribonuclease in *Bacillus subtilis* is exemplified by polynucleotide phosphorylase (PNPase), while magnesium-dependent ExoR or RNase J1 are 5' to 3' exonucleases (Bechhofer & Deutscher, 2019; Li & Deutscher, 2004). In addition to the classical ribonucleases, several other enzymes also exhibit exonucleolytic functions on RNA/DNA hybrids, like the DNA polymerase Pol I or PolA, which exhibit 5'->3' exonuclease activity in *E. coli* or *B. subtilis*, respectively (Duigou *et al*, 2005). Pol I and PolA are thought to contribute to RNA removal at replication forks in bacteria, in conjunction with or in addition to different RNases. During DNA replication in eukaryotes, two RNases were discovered, which belong to the RNase H family: RNase H1 and RNase H2 hydrolyze RNA from RNA/DNA hybrids (Cerritelli & Crouch, 2009). Prokaryotes possess one or two of three H-type RNases, RNase HI, HII, and RNase HIII. In *E. coli*, RNase HI hydrolyzes RNA-DNA hybrids, which contain polymers of four or more ribonucleotides (Ohtani *et al*, 1999b). RNase HII is characterized by hydrolyzing at the 5′ to a single ribonucleotide, i.e. it acts as

an endonuclease, unlike RNase HI. Also, it hydrolyzes at the 5′ to the ribonucleoside monophosphate (Yao *et al.*, 2013). Thus, it is important to initiate removal of incorporated rNMPs from the genome, to ensure genomic integrity (Clark & Kunkel, 2010). RNase HIII has a high enzymatic similarity to RNase HI (Ohtani *et al*, 1999a). Bacteria are considered to generally have two RNase H enzymes, which in *Bacillus subtilis* are RNase HII and RNase HIII (Kochiwa *et al*, 2007). Most endoribonucleases cleave RNA in the presence of divalent cations, resulting in fragments containing 3′-hydroxyl and 5′-phosphate termini (Li & Deutscher, 2004), including RNase HII and RNase HIII.

During DNA replication in *B. subtilis*, continuous synthesis of the leading strand occurs by polymerase PolC. For lagging strand synthesis, primase DnaG synthesizes RNA primers, which are extended by DNA polymerase DnaE (Dervyn *et al*, 2001; Sanders *et al*, 2010). DnaE is thought to only extend by few bases, and then hand over to PolC (Seco & Ayora, 2017), which finishes the 1-2 kb Okazaki fragments (Ogawa & Okazaki, 1980). Indeed, 2000-4000 fragments per 4.6 Mb chromosome could be identified in *E. coli* for whole chromosome replication (Su'etsugu & Errington, 2011). Removal of RNA primers is important for DNA stability (Williams & Kunkel, 2014), and lagging strand synthesis is terminated by ligase LigA sealing remaining single strand gaps. As pointed out above, DNA polymerase PolA shows 5'-3' exonuclease activity and could be detected together with RNase HIII and ExoR in *in vitro* studies for the maturation of Okazaki fragments in *B. subtilis* (Randall *et al*, 2019). Also, as stated above, RNase HII appears to be responsible for the removal of individual rNMPs that are incorporated into DNA by DNA polymerase during DNA replication (Schroeder *et al*, 2017; Yao *et al.*, 2013). Similarly, PolA, as well as ExoR could be determined to be involved in the repair of DNA damage due to UV (Hernández-Tamayo *et al*, 2019). Interestingly, temperature-sensitive phenotypes were discovered in different deletions combinations. It was shown that the deletion of *rnhC* and *polA*, as well as the deletion of *rnhC* and *exoR*, lead to lethality under 25°C growth conditions (Randall *et al.*, 2019), while a double mutation (*rnhB*, *rnhC*) leads to poor growth (Yao *et al.*, 2013). These findings point to a possible role of these proteins at *B. subtilis* replication forks, but other explanations for synthetic phenotypes are possible. In order to obtain definite proof for enzymatic activity of the four mentioned proteins at replication forks, or at sites all over the chromosome distinct from replication events, we monitored single molecule dynamics, to test if replication forks represent sites of frequent stops for different enzymes having RNase activity.

2.3.3. Materials and Methods

Strain construction

For the construction of the mV /mNeo fusions in *B. subtilis*, the integration plasmid pSG1164 was used. Using pSG1164, the corresponding fluorophore is integrated through a single crossover c-terminal to the original locus (Lucena *et al*, 2018). For integration, a 500 bp homolog of the C-terminus of the gene of interest must be cloned using Gibson Assembly (Gibson *et al*, 2009) into the vector next to the linker and mV/ mNeo sequence. Used primers have a homologue 25 bp overhang and are listed in Table 1. The transformed plasmids were extracted using a kit (New England BioLabs). The deletion strains are based on *B. subtilis* BG214 and containing RNase HIII-mV or ExoR-mV constructs and were generated by transformation of cells with chromosomal DNA from *B. subtilis* 168 *ΔrnhC::kan trpC2*, *ΔexoR::kan trpC2*, obtained from the *Bacillus* Genetic Stock Center (Columbus, Ohio) (Koo *et al*, 2017). The chromosomal DNA was extracted using a kit (innuPREP Bacteria DNA Kit, Analytik-Jena).

Growth conditions

All plasmids, strains and oligonucleotides used are listed in tables in the Supplement. *E. coli* strains were cultured in LB (lysogenic broth) medium at 37°C. Likewise, LB medium was used for microscopy (SMT). For this experiment, the *B. subtilis* strains were cultured in LB at 30°C. When needed, antibiotics were added at the following concentrations: ampicillin 100 µg/ml, chloramphenicol 5 µg/ml, kanamycin 30 µg/ml, 6(p-hydroxyphenylazo)-uracil (HPUra) 15 mg/ml. 0.5% of xylose was added from a 50% sterile filtrated stock solution in ddH_2O.

Western blot

The samples were harvested from the exponential growth phase and digested by lysozyme (proceed according to (Hinrichs *et al*, 2022)). The detection was performed with a primary polyclonal α GFP-tag antibody (1:5000)/ mNeonGreen-tag (1:4000), and secondary antibody goat-anti-Rabbit-IgG, peroxidase-conjugated (1:100,000) (Sigma-Aldrich).

Fluorescence microscopy

Microscopy was performed in LB medium with a prior cultivation of 30°C, 200 rpm. Cells were analized in the exponential growth phase. For wide-field epifluorescence microscopy,

a Zeiss Observer A1 microscope (Carl Zeiss) with an oil immersion objective (100 x magnification, 1.45 numerical aperture, alpha PlanFLUAR; Carl Zeiss) was used. The images were recorded with a charge-coupled-device (CCD) camera (CoolSNAP EZ; Photometrics) and an HXP 120 metal halide fluorescence illumination with intensity control (Hinrichs *et al.*, 2022). For the sample preparation a round coverslips (25 mm, Marienfeld) was used and covering 5 µl cell culture with a 1.5 % agarose pad. The agarose pads were made with water by sandwiching 100 µl of the melted agarose between two smaller coverslips (12 mm, Menzel). Images were processed using ImageJ (Schindelin *et al*, 2012).

Single-molecule tracking (SMT)

Individual molecules were tracked using custom-made slim-field setup on an inverted fluorescence microscope (Nikon Eclipse Ti-E, Nikon Instruments Inc.). An EMCCD camera (ImagEM X2 EM-CCD, Hamamatsu Photonics KK) was used to ensure high-resolution detection of the emission signal, resulting in a calculated resolution of the position of the molecule down to 20 nm. The central part of a 514 nm laser diode (max power 100 mW, TOPTICA Beam Smart) was used with up to 20% of the intensity (about 160 W cm^{-2} in the image plane) to excite samples, fused to mNeonGreen (using laser filter set BrightLine 500/24, dichroic mirror 520 and BrightLine 542/27), by focusing the beam onto the back focal plane of the objective. A CFI Apochromat objective (TIRF 100 x Oil, NA 1.49) was used in the setup (Oviedo-Bocanegra *et al*, 2021). For the analysis, a video of 3000 frames at 20 ms was recorded, of which 1000 starting after 200 to 300 frames, dependent on the time point when single molecule levels was reached due to bleaching, were used for the analysis. Software Oufti (Paintdakhi *et al*, 2016) was used to set the necessary cell meshes. Utrack (Jaqaman *et al*, 2008) was employed for automatic determination of molecule trajectories. Data analysis was carried out using software SMTracker 2.0 (Dersch *et al*, 2020; Oviedo-Bocanegra *et al.*, 2021).

2.3.4. Results

PolA, ExoR and RNase HII show nucleoid localization

To investigate the localization of PolA, ExoR, RNase HII, and RNase HIII *in vivo*, C-terminal mVenus or mNeonGreen fusions were created and integrated at the original locus. The localization of the replication forks was visualized using a DnaX-CFP (DNA polymerase III, part of the clamp-loader complex) allele in the same strain. To ensure that the fused proteins are expressed in full length, a western blot was made against the corresponding fluorophore (Fig. S1/S2). The experiments showed full-length expression in all cases.

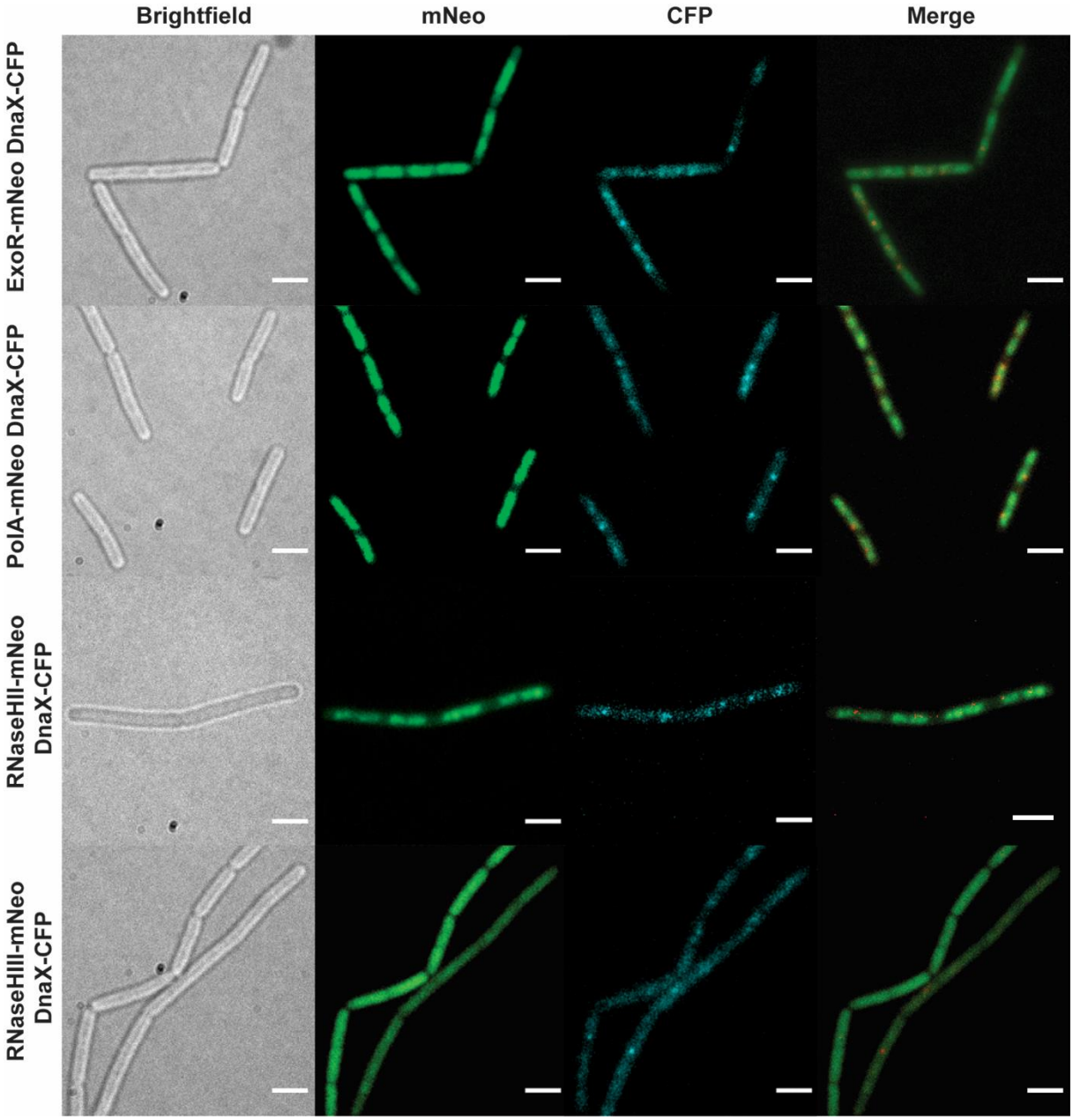

Figure 1: Epifluorescence microscopy of fusion strains. The image shows the brightfield image, the mNeonGreen of the fusions, DnaX-CFP for replication fork localization, and a

corresponding merge. PolA-mNeo, ExoR-mNeo, RNase HII-mNeo and, RNase HIII-mNeo were colocalized with DnaX-CFP. Scale bar 2 µm.

Using epifluorescence microscopy (Fig. 1), we found that ExoR-mNeo, PolA-mNeo and RNase HII-mNeo show a clear staining pattern comparable to a DAPI stain of the nucleoids in the cell (Pediaditakis *et al*, 2012). The fusion of RNase HIII showed a diffuse localization throughout the cells (Fig. 1). The CFP channel provides information about the localization of the replication forks: the DnaX-CFP fusion showed distinct foci in the cell (1-2 per cell). The merge of both channels shows the colocalization of the proteins relative to DnaX, showing clear overlap of signals.

Single molecule tracking reveals distinctive patterns of motion for RNases

Epifluorescence experiments could not reveal an association of any RNase or of PolA with replication forks. To obtain a better understanding of protein dynamics and increased spatiotemporal resolution, we used single-molecule tracking (SMT) (Oviedo-Bocanegra *et al.*, 2021). The method employs a beam of a 514-nm laser diode is expanded by a factor of 20, and the central part is focused on the rear focal plane of the 100 x A = 1.49 objective. SMT allows visualization of events of molecules located at a defined subcellular location with an accuracy of 40 nm or less (Dersch *et al.*, 2020). SMT was performed with 20 ms stream acquisition. To determine the area of the cell to be detected, cell-meshes are set by using Oufti (Paintdakhi *et al.*, 2016) and trajectories were determined by u-track (Jaqaman *et al.*, 2008). Tracks of only 5 steps and more were used. Analysis of the resulting data, all from biological triplicates, was done with the SMTracker 2.0 (Oviedo-Bocanegra *et al.*, 2021).

Figure 2A shows the heat maps of the given proteins to visualize the localization of molecule tracks in the cell. For this, we projected all tracks from the biological replicates into a cell with an average size of 3 x 1 µm. The distribution of tracks is indicated by a color shift from yellow (low probability) to black (highest probability). The intensity of the maps created is adapted to each other. To be able to compare localization patterns with already known replication proteins, a fusion of DnaC (DNA helicase) was included (Bin *et al*, 2013). Similar to the epifluorescence images (Fig 1), the localization of PolA, ExoR, and RNase HII fusions are clearly seen on the nucleotides, with a concentration to the central parts of the nucleoids, very similar to DnaC. The localization of RNase HIII is very similar, but with a lower intensity gradient from central parts to sites surrounding the nucleoids. RNase HIII most strongly

resembled the heat map of DnaC (Fig 2A). Contrarily, RNase J2, component of the RNA degradosome, which is mostly membrane-associated, showed strong accumulation towards the cell periphery and was depleted from many central positions. These data support the notion that RNase HII and HIII are associated with removal of RNA/DNA hybrids from the DNA, and may be associated with replication.

We next determined diffusion constants of the proteins using squared displacement analyses (SQD), shown in Figures 2B and 2C. SQD analysis can be used to determine the average diffusion constant of a molecule, as well as to analyse if a single or several populations with different diffusion constants exist; if several, the size of the populations can be determined. For PolA, ExoR and RNases, a two-population Rayleigh fit was used, which explained the observed distribution of tracks very well. This analysis suggests the existence of a slow mobile/static and a high mobile population, most likely freely diffusive molecules. The bubble blot (Fig. 2C) visualizes diffusion constants and sizes of the two assumed populations, revealing that all proteins have slow-mobile fractions whose diffusion constants are in a similar range, one that has been described for tight DNA-binding events. In case of DnaC, this is tight hexamer formation ahead of replication forks. ExoR, RNase HII and, DnaC have the largest slow mobile/static fractions, RNase HIII has the largest diffusive population (Fig 2B). Thus, a quarter to a third of molecules appears to be engaged in a substrate-bound form. For detailed numbers, please also consult table 1. Although informative, these data still do not provide an answer if RNase activity of the studied proteins is associated with replication forks *in vivo*, other than for PolA and ExoR, where spatial connection to replication has been shown before (Hernández-Tamayo *et al.*, 2019).

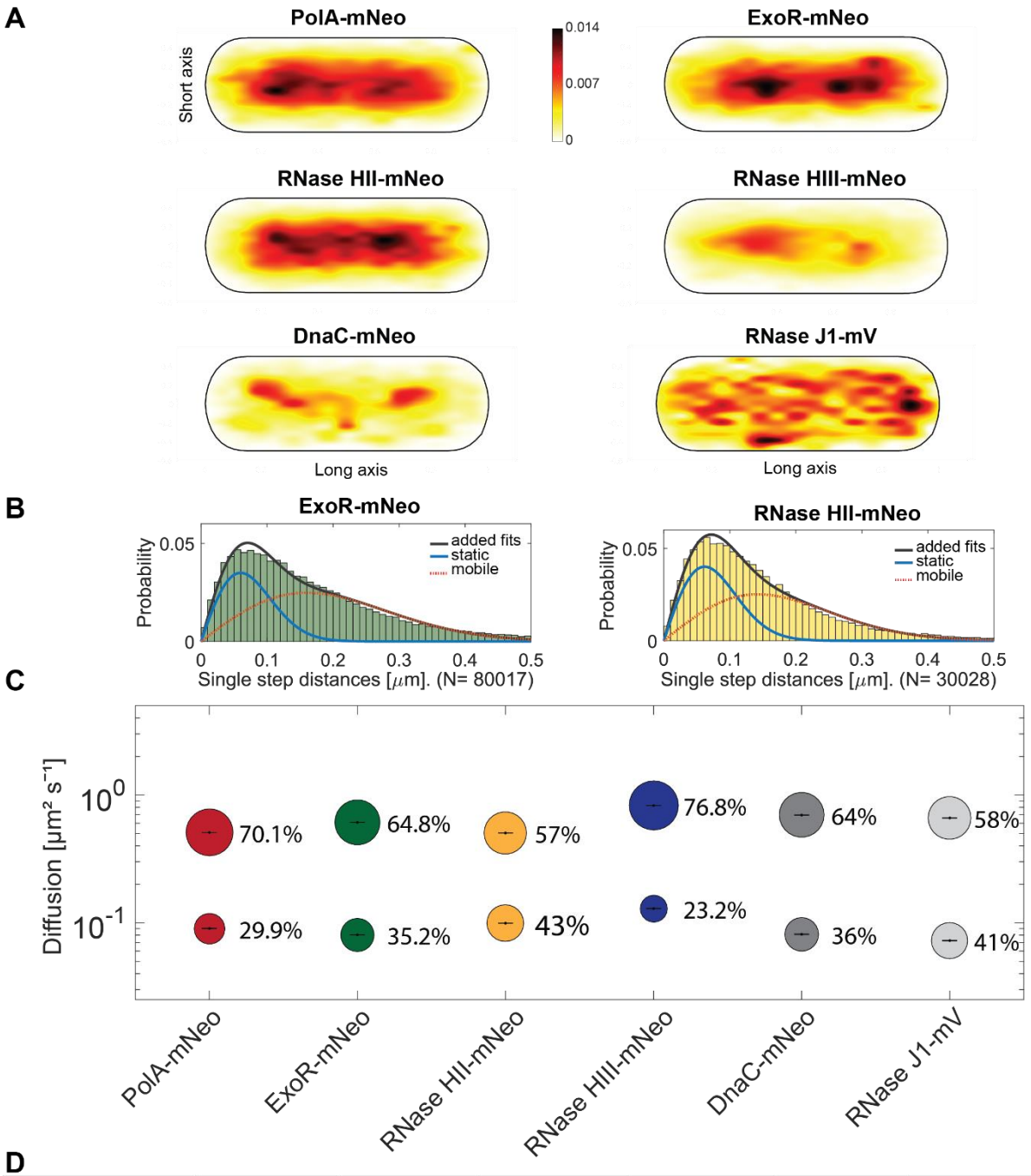

D

	PolA-mNeo	ExoR-mNeo	RNase HII-mNeo	RNase HIII-mNeo	DnaC-mNeo	RNase J1-mV
$D1_{(static)}$ $\mu m^2 s^{-1}$	0.09 ± 0.0	0.09 ± 0.0	0.10 ± 0.0	0.13 ± 0.001	0.08 ± 0.001	0.07 ± 0.001
$D3_{(mobile)}$ $\mu m^2 s^{-1}$	0.51 ± 0.001	0.63 ± 0.001	0.50 ± 0.001	0.82 ± 0.001	0.70 ± 0.002	0.66 ± 0.002
Static %	29.9 ± 0.001	35.2 ± 0.001	43.0 ± 0.001	23.2 ± 0.001	36.0 ± 0.001	41.6 ± 0.001
Mobile %	70.1 ± 0.001	64.8 ± 0.001	57.0 ± 0.001	76.8 ± 0.001	64.0 ± 0.001	58.4 ± 0.001
R^2	1	0.999	1	1	0.999	0.999

Figure 2: Single molecule analyses of PolA-mNeo, ExoR-mNeo, RNase HII-mNeo, RNase HIII-mNeo and, DnaC-mNeo. (A) Heat maps of single-molecule localization of replication proteins in a medium-size *Bacillus subtilis* cell. The distribution of tracks is

indicated by a color shift from yellow (low probability) to black (highest probability). (B) Jump distance analyzes of ExoR-mNeo and RNase HII-mNeo. The two rayleigh fits display a two-population fit (static in blue, mobile in red and, added fits in black). (C) Bubble blots show diffusion constants of replication Proteins and fractions sizes for static and mobile molecules. (D) Diffusion constants and percentages of static and mobile molecule fractions. Values were fitted using non-linear least-square fitting, R^2 values for each condition are stated.

All four enzymes showing RNase activity feature close spatial proximity of motion to are frequent arrests at replication forks

A convincing argument that an enzyme takes place in a reaction at a defined subcellular space in proximity of motion at or close to that site. We used a tool in SMTracker 2.0 that allows to score proximity of molecule trajectories close to sites in the cell that can be defined e.g. by localizing a protein complex using a protein fusion having a different fluorescent colour. Fig. 3A shows an example of two cells in which the position of replication forks has been determined by acquiring an image in the CFP channel, detecting DnaX-CFP, a component of the clamp loading complex. Blue tracks reveal freely diffusive trajectories, red tracks trajectories staying within a radius of 106 nm for at least 5 time points, i.e. molecules showing confined diffusion, likely due to binding events. These are close to DnaX-CFP signals, and thus at replication forks.

Green trajectories reveal events of transition between free diffusion and confined motion, logically being close to events of confined motion. Thus, our analyses can capture events of transitions from free diffusion to DNA binding, and release from DNA binding. The lower right cell in Fig. 3A likely contains a second replication fork close to the two events of confined motion for RNase HII, which was not captured in the CFP channel. As a definition of what “close to replication forks” means, we tracked DnaC-mNeo relative to DnaX-CFP. Fig. 3B shows a roughly Gaussian distribution of tracks with a centre at about 400 nm. The relatively large deviation from “0” is partially due to a change in filters and illumination between taking the CFP image by epifluorescence and by tracking DnaC-mNeo molecules by SMT, because replication forks are quite mobile (Monahan *et al*, 2014). In addition, replication forks can only be located with a resolution of 250 nm, while SMT has a localization error of less than 40 nm. Fig. 3B contains a second peak at about 1.4 µm, likely

DnaC-mNeo moving close to replication forks that have not been identified in epifluorescence.

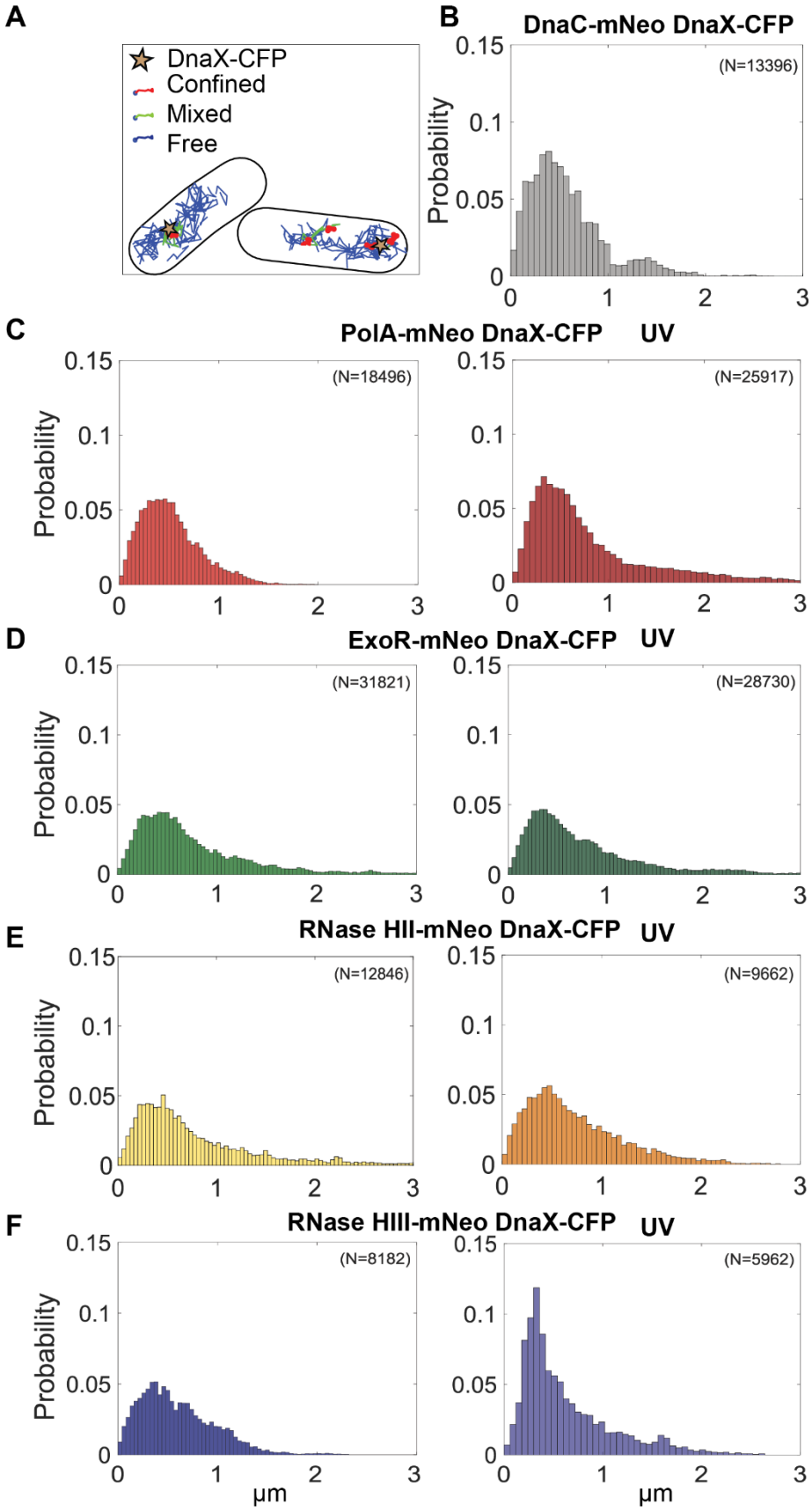

Figure 3: Distance measurement of potential replication proteins to DnaX-CFP (replication fork). Panel A shows an example for the confinement analyses of RNase HII-mNeo. The marker for the replication fork is DnaX-CFP, expressed from the original gene locus. At least 50 cells were measured. The number of tracks measured is indicated (N). The probability of detection close to DnaX-CFP foci is shown in relation to the distance in micrometers (µm). The above proteins are described in A-E.

For PolA-mNeo, the distribution is between 0 µm and 2 µm distance to the DnaX-CFP signal is centered at a distance of about 0.4 µm, and thus similar to DnaC-mNeo. The same is true for all three other enzymes investigated, indicating that all frequently arrest at replication forks in their search for DNA/RNA hybrids.

The above data revealed that PolA, ExoR, RNase HII and HIII show high probability of motion close to sites of DNA replication. These analyses do not quantify the extent of motion, or rather arrest, at replication forks. We searched for further evidence for the presence of four enzymes with RNase activity by confinement analysis in relation to the replication forks (Fig 4). For this, scored for confined tracks, i.e. tracks that stay within three times the localization precision of this work, for 5 or more time points. We analyzed only cells with distinct DnaX-CFP signals and counted how many cells had confined tracks immediately at a replication fork (Fig. 4A). As we used a tracking time of 1000 frames, confinement analyses shows percentage of cells having molecules arresting at DnaX-CFP foci within a 20 seconds time frame. Interestingly, all enzymes (PolA (71.4%), ExoR (72.7%), RNase HII (76%), and RNase HIII (72.1%) showed confined tracks at replication forks in more than 70% of cells (Fig. 4C). As reference, for DNA helicase reference, a similar percentage of more than 78% could be determined.

These data strongly suggest that Okazaki fragment maturation involves the recruitment of at least four enzymes to the replication forks in *B. subtilis*. Because we wished to obtain additional evidence for this idea, we tested if enzymes would be more strongly engaged as replication forks become stalled, e.g. in the response to UV irradiation, which of course also induced DNA repair events at many other sites on the chromosome.

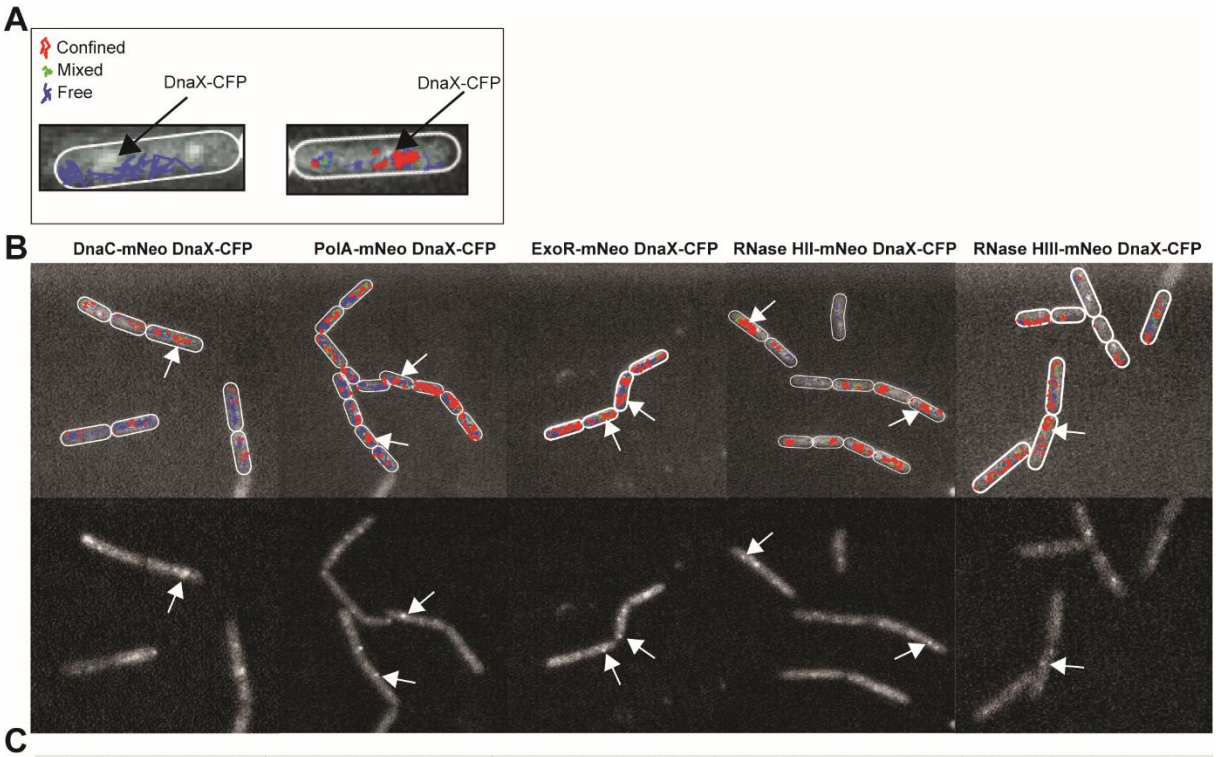

C

DnaC-Neo DnaX-CFP		PolA-mNeo DnaX-CFP		ExoR-mNeo DnaX-CFP		RNase HII-mNeo DnaX-CFP		RNaseHIII-mNeo DnaX-CFP	
Cells with DnaX-CFP [N]	Tracks confined on DnaX [%]	Cells with DnaX-CFP [N]	Tracks confined on DnaX [%]	Cells with DnaX-CFP [N]	Tracks confined on DnaX [%]	Cells with DnaX-CFP [N]	Tracks confined on DnaX [%]	Cells with DnaX-CFP [N]	Tracks confined on DnaX [%]
56.0	**78.6**	63.0	**71.4**	55.0	**72.7**	50.0	**76.0**	61.0	**72.1**

Figure 4 Confinement analyses of replication-associated proteins relative to DnaX-CFP foci. A) example of two cells, one in which freely diffusing tracks are shown in blue, and one where confined tracks overlapping with a DnaX-CFP focus are shown. B) upper panels show an overlay of confinement analyses of DnaC-mNeo, PolA-mNeo, ExoR-mNeo, RNase HII-mNeo, and RNase HIII-mNeo, in relation to the foci of replication forks (DnaX-CFP, lower part). More than 50 cells per strain were analysed. C) Table of percentage counts. The cells with visible DnaX-CFP signal are indicated (N). Cells with confined tracks at the replication fork are indicated in percent [%]. The tracks are divided into confined (red), in transition (green) and free (blue).

PolA and RNase HIII show a change in mobility in response to UV light-induced DNA damage

To test the influence of DNA damage on the dynamics of RNases HII and HIII and to identify a possible involvement in the UV repair system, the dynamics of the proteins under UV-damage of DNA was determined. Therefore we induced DNA damage *via* crosslinks using UV light (Duigou *et al.*, 2005), using a treatment of 60 J m^{-2}. Please note that for this

analysis, diffusion constants for each protein were determined by a simultaneous fit, in order to better compare changes in population size. Interestingly, only the population sizes of PolA-mNeo change significantly. After UV treatment, there was an increase in the static population from 30.2% to 43.2%, with a concomitant decrease of the high-mobile fraction (Fig 5A and B). ExoR-mNeo, RNase HII-mNeo and RNase HIII-mNeo did not show any significant changes in their dynamics in response to UV treatment. This is somewhat contradictory to earlier reports of our group, in which significant changes were also detected for ExoR (Hernández-Tamayo *et al.*, 2019). We will come to this point later.

A

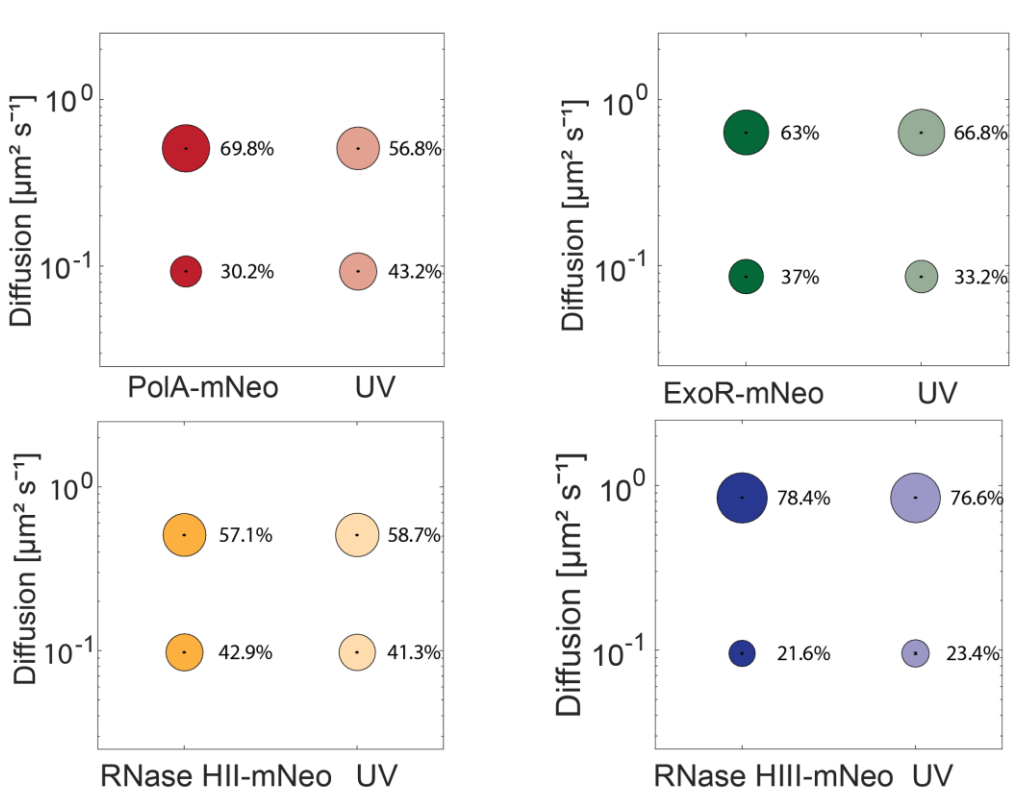

B

	PolA-mNeo	UV	ExoR-mNeo	UV	RNase HII-mNeo	UV	RNase HIII-mNeo	UV
$D1_{(static)}$ µm² s⁻¹	0.09 ± 0.0	0.09 ± 0.0	0.09 ± 0.0	0.09 ± 0.0	0.10 ± 0.0	0.10 ± 0.001	0.10 ± 0.003	0.10 ± 0.003
$D3_{(mobile)}$ µm² s⁻¹	0.51 ± 0.001	0.51 ± 0.001	0.63 ± 0.001	0.63 ± 0.001	0.51 ± 0.002	0.51 ± 0.002	0.84 ± 0.004	0.84 ± 0.004
Static %	30.2 ± 0.001	43.2 ± 0.001	37.0 ± 0.001	33.2 ± 0.001	42.9 ± 0.002	41.3 ± 0.002	21.6 ± 0.003	23.4 ± 0.003
Mobile %	69.8 ± 0.001	56.8 ± 0.001	63.0 ± 0.001	66.8 ± 0.001	57.1 ± 0.002	58.7 ± 0.002	78.4 ± 0.003	76.6 ± 0.003
R^2	1	0.999	1	1	1	1	0.999	0.996

Figure 5: Analyses of protein dynamics via Single molecule tracking with or without UV-treatment. (A) Bubble blots show diffusion constants of replication Proteins and fractions sizes for static and mobile molecules with and without treatment with UV-light. (C) Diffusion constants and percentages of static and mobile molecule fractions. Values were fitted using non-linear least-square fitting, R^2.

We employed proximity determination as a second means to detect changes in protein dynamics/localization after induction of DNA damage. Following UV treatment, PolA-mNeo showed a shift of the probability of tracks towards the “0” position (Fig 3C), indicating even stronger association with DnaX and thus replication forks. For ExoR-mNeo of RNase HII-mNeo, there was no noticeable change of distance to DnaX-CFP foci with and without UV light treatment (Fig 3D and E). However a considerable change was seen for RNase HIII-mNeo. Without treatment, the distribution showed a peak at about 0.4 µm, and a maximum probability of occurrence of 0.05. After UV treatment, there was an almost threefold increase in abundance at a distance of 0.4 µm from 0.05 to about 0.14 (Fig 3F). This finding argues for a higher accumulation of RNase HIII-mNeo at the replication forks during DNA damage by UV. For reference, DnaC-mNeo showed a peak at about 0.4 µm with a probability frequency of 0.075 (Fig. 3B).

Inhibiting PolC activity leads to a strong effect on the localization of RNase HII and HIII

Because there were no detectable changes for single molecule dynamics of RNase HII-mNeo or RNase HIII-mNeo during UV stress, we employed a third treatment, to arrest DNA replication via inhibition of DNA polymerase PolC, using 6(p-hydroxyphenylazo)-uracil (HPUra), which reversibly binds to and inhibits DNA polymerase PolC, thereby completely blocking progression of replication (Brown, 1970), as opposed to slowing down replication due to the necessity to repair based dimers in response to UV irradiation. In this case, we used mVenus fusion strains, for which we did not observe any differences with respect to single molecule dynamics. Fig. 5 shows corresponding heat maps for RNase HII-mV and RNase HIII-mV, which display a visually clear difference in the preferred localization of RNase HII-mV in the cell (Fig 6 A): during exponential growth, a high concentration of tracks is found in the central area of nucleoids, where replication takes place, which is lost during replication arrest. With regard to population size, RNase HII-mV shows a considerable decrease in the static population from 49.5% to 40.2% in response to HP Ura treatment, indicating that a large pool of substrate-binding sites is abolished. Interestingly, although RNase HIII did not show a strong visual alteration in the heat maps of tracks (Fig. 6A), the RNase showed a pronounced decrease in the static population, from 53% to 29.7%. The mobile populations increased accordingly (Fig 6 B, C).

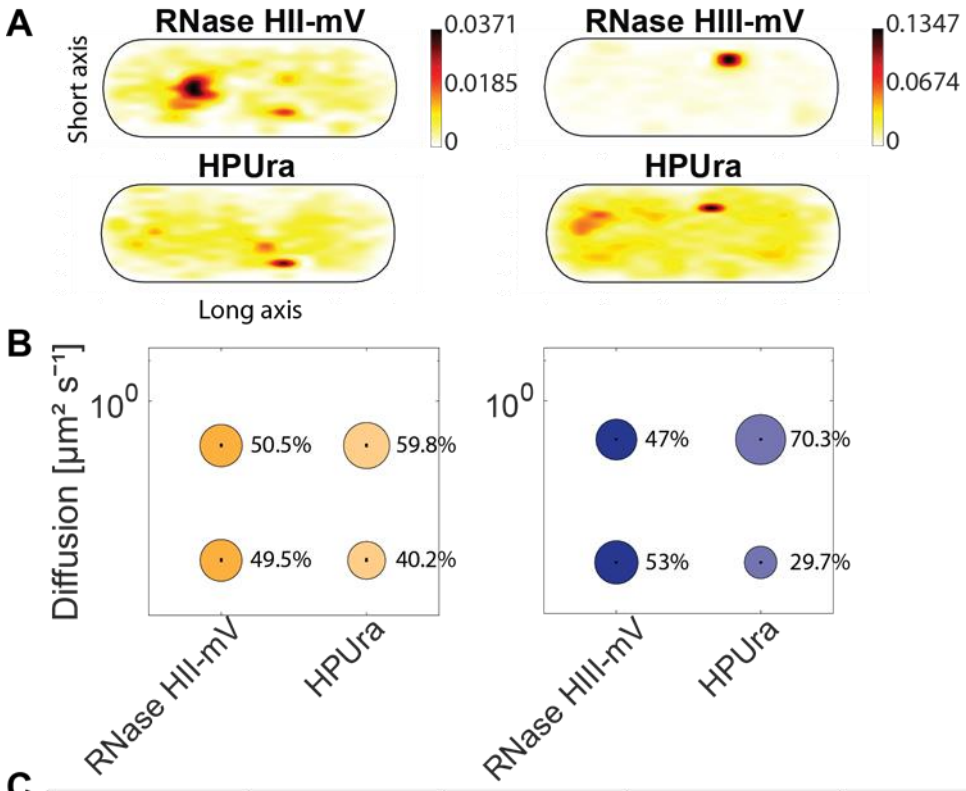

C

	RNase HII-mV	HPUra	RNase HIII-mV	HPUra
$D1_{(static)}$ µm² s⁻¹	0.06 ± 0.002	0.06 ± 0.002	0.06 ± 0.001	0.06 ± 0.0
$D3_{(mobile)}$ µm² s⁻¹	0.47 ± 0.011	0.47 ± 0.001	0.51 ± 0.005	0.51 ± 0.005
Static %	49.5 ± 0.011	40.2 ± 0.011	53.0 ± 0.004	29.7 ± 0.004
Mobile %	50.5 ± 0.011	59.8 ± 0.011	47.0 ± 0.004	70.3 ± 0.004
R^2	0.999	0.997	0.999	0.999

Figure 6: Analyses of protein dynamics under treatment of HPUra via single molecule tracking. (A) Heat maps of single-molecule localization of RNase HII and HIII with and without HPUra (15mg/ml) in a medium-size *Bacillus subtilis* cell. The distribution of tracks is indicated by a color shift from yellow (low probability) to black (highest probability). (B) Bubble blots show diffusion constants of RNase HII/HIII and fractions sizes for static and mobile molecules under the treatment of HPUra. (C) Diffusion constants and percentages of static and mobile molecule fractions. Values were fitted using non-linear least-square fitting, R2 values for each condition are stated.

Thus, a block in replication fork progression alters dynamics of both type H RNases, strongly supporting the idea that they are intimately involved in the processing of Okazaki fragments.

Lack of ExoR affects RNase HIII dynamics

Previous work has shown that double mutation of *rnhC* and *exoR* results in a phenotype that is lethal at 25°C (Randall *et al.*, 2019). We investigated a possible influence of the proteins on each other's activity by analyzing the dynamics of each in strains carrying the respective deletion of the other gene (ExoR-mVenus *ΔrnhC*, RNase HIII-mV *ΔexoR*). In case both proteins are recruited to replication forks via specific protein/protein interaction with proteins present at the forks at all times, we would not expect strong alterations in e.g. static populations representing DNA-bound molecules, while independent recruitment due to substrate availability might lead to detectable changes in DNA-bound, slow mobile/static, states.

For these analyses, we projected all tracks showing confined motion from the three biological replicates into an average size cell of 3 x 1 µm size ("confinement heat map", *B. subtilis* cells are on average 0.75 µm wide and 2 to 4 µm long). To achieve this, tracks were sorted into those that stay within a radius of 120 nm, determined as three times our localization error, for at least 6 consecutive steps (confined motion), and into those that show large displacements, indicative of free diffusion (Hinrichs *et al.*, 2022).

For ExoR-mV, as well as RNase HIII-mV with and without deletions, there were inconsiderable difference in the pattern of confined tracks at 30°C (Fig. 7A). Incubation at 37°C, where DNA replication occurs at maximum speed, led to an increase in the degree of confined motion relative to 30°C (Fig 7A). While deletions of *rnhC* or *exoR* did not result in clear changes in the heat maps, considerable changes were observed in the dynamics of the proteins. For ExoR-mV, the static fraction decreased from 47.7% to 36% in the deletion background of *rnhC,* compared to wild type cells (Fig. 6B). Conversely, RNase HIII-mV *ΔexoR* cells showed an increase in the static population during incubation at 37 degrees (43.3% to 51.3%) (Fig. 7B and C). Western blotting was performed to determine the expression levels of the proteins (Fig S2). No significant changes were found, showing that changes in population sizes are due to changed binding behavior (i.e. engagement in slow diffusion) of existing molecules.

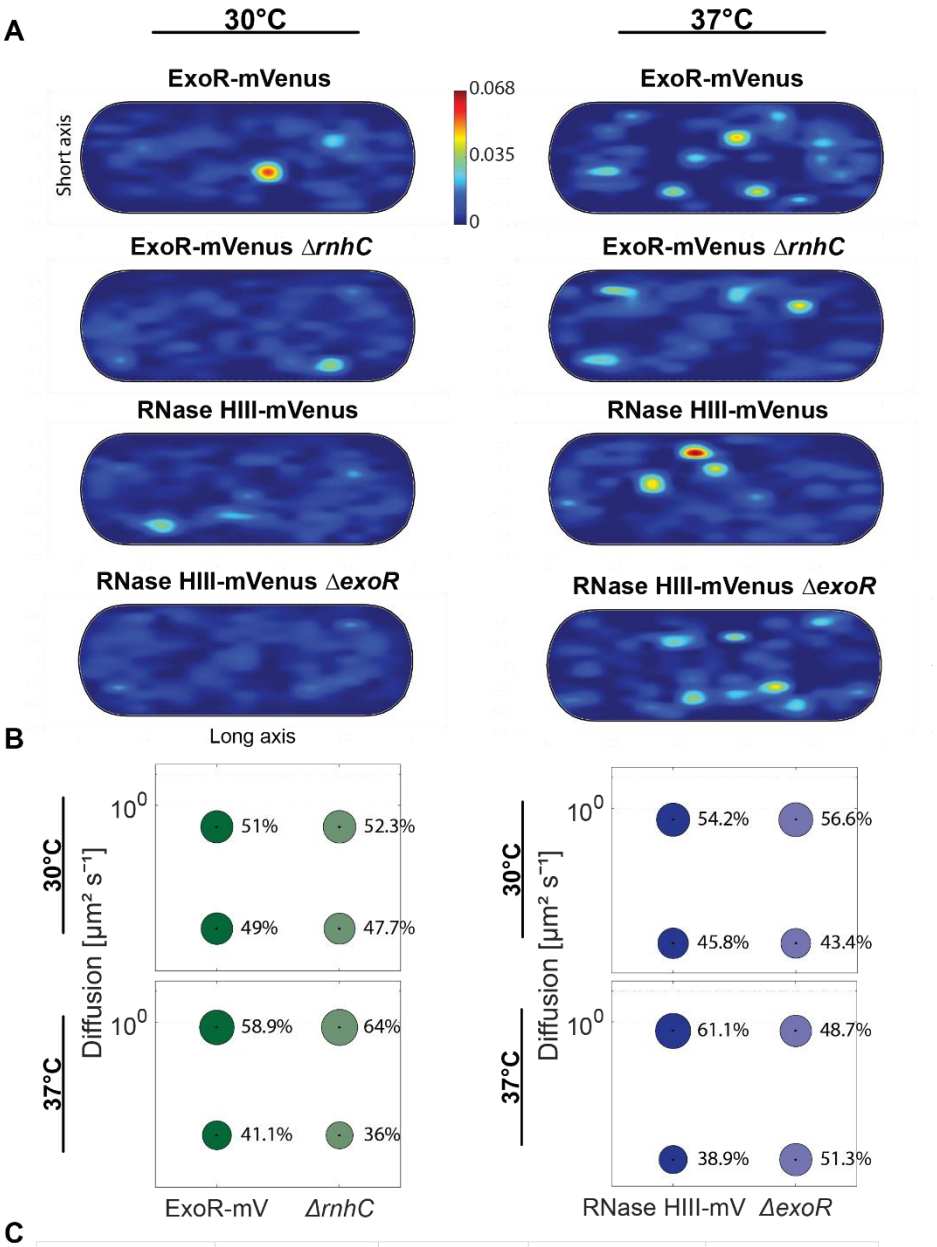

C

		ExoR-mV	ExoR-mV Δ *rnhC*	RNase HIII-mV	RNase HIII-mV Δ *exoR*
30°C	$D1_{(static)}$ µm² s⁻¹	0.06 ± 0.001	0.06 ± 0.001	0.05 ± 0.0	0.05 ± 0.0
	$D3_{(mobile)}$ µm² s⁻¹	0.62 ± 0.011	0.62 ± 0.011	0.78 ± 0.009	0.78 ± 0.009
	Static %	49.0 ± 0.006	47.7 ± 0.006	45.8 ± 0.004	43.4 ± 0.004
	Mobile %	51.0 ± 0.006	52.3 ± 0.006	54.2 ± 0.004	56.6 ± 0.004
	R^2	0.999	0.999	0.998	0.998
37°C	$D1_{(static)}$ µm² s⁻¹	0.08 ± 0.003	0.08 ± 0.003	0.05 ± 0.001	0.05 ± 0.001
	$D3_{(mobile)}$ µm² s⁻¹	0.89 ± 0.006	0.89 ± 0.006	0.82 ± 0.007	0.82 ± 0.007
	Static %	41.1 ± 0.003	36.0 ± 0.003	38.9 ± 0.003	51.3 ± 0.003
	Mobile %	58.9 ± 0.003	64.0 ± 0.003	61.1 ± 0.003	48.7 ± 0.003
	R^2	0.998	0.998	0.998	0.997

Figure 7: Analyses of protein dynamics via Single molecule tracking at 30°C and 37°C

(A) Confinement maps of potential replication proteins by 30°C and 37°C. Plots of heat map of confined tracks, projected into a standardized *B. subtilis cell*. (B) Bubble blots show diffusion constants of replication Proteins and fractions sizes for static and mobile molecules

at different temperatures (30°C and 37°C). (C) Diffusion constants and percentages of static and mobile molecule fractions. Values were fitted using non-linear least-square fitting, R2 values for each condition are stated.

While we can not show where changes in slow mobility occur in a decisive manner, we favour the view that for RNase HIII, lack of ExoR provides more substrate sites, suggesting that RNase HIII is recruited based on the occurrence of DNA/RNA hybrids rather than via specific protein interactions. For ExoR, changes are more difficult to interpret. A reduction of slow mobile/static molecules from 41 to 36% represents a change of 12.2%, which is close to what we would regard as noise in biological systems, and may thus rather be a “no-change” phenotype.

2.3.5. Discussion

Incorporation of short stretches of RNA as primers for lagging strand synthesis requires the activity of enzymes that remove RNA from DNA/RNA hybrids in all organisms. In eukaryotic cells, RNase H2 and Exo1 together with the flap endonucleases Fen1 and Dna2 have been reported to be involved in Okazaki fragment maturation (Liu *et al*, 2017), while in *E. coli*, it is believed that DNA Pol 1 and RNase HI take over this task. In the Gram positive model organism *B. subtilis,* RNase HIII, exonuclease ExoR and DNA polymerase PolA have been proposed to be involved in replication, based on biochemical and genetic data (Randall *et al.*, 2019). It has also been suggested that RNase HIII acts as an important supporter of PolA in the maturation of Okazaki fragments (Randall *et al.*, 2019): it has been shown that RNase HIII influences endonucleolytic cleavage of RNA in RNA-DNA hybrid molecules in the processing of R-loops and maturation of Okazaki fragments. Additionally, the absence of both H-type RNases, HII and HIII leads to a synthetic slow-growth phenotype (Yao *et al.*, 2013), indicating that also RNase HII may be involved. However, the exact *in vivo* function of RNase HII is not known except for the possible removal of single rNMPs incorporated into DNA by DNA polymerases (DNA replication (Randall *et al*, 2018; Yao *et al.*, 2013). We sought to provide *in vivo* evidence to answer the question, which enzymes are truly involved in RNA removal from replication forks. Using single molecule tracking, we could show that RNase HII, RNase HIII, as well as ExoR and PolA arrest at replication forks with a frequency

that is close to that of molecules of replicative helicase DnaC**.** In response to DNA damage induced via UV stress, we found increased activity of RNase HIII and Pol A at the forks.

Single molecule trajectories for all four enzymes could be explained by assuming two populations having distinct diffusion constants. Based on the idea that DNA polymerases or RNases detecting DNA/RNA hybrids would be in a bound state, where there is little diffusion (basically that displayed by DNA strands), the slow mobile population should represent enzymatically active enzymes bound to DNA, while the high-mobile fraction should represent diffusing molecules. Diffusion constants for all proteins were quite low in comparison to freely diffusing enzymes (Rotter *et al*, 2021), and PolA, ExoR and RNase HII showed clear nucleoid staining in epifluorescence microscopy. Heat maps of all single molecule trajectories showed a clear enrichment of tracks at central places, even within nucleoid areas, similar to those of DNA polymerase C, and very different from the more peripheral pattern of RNase J1, which is involved in RNA degradation within the membrane-associated RNA degradosome. These data show that like DNA transcription factors (Stracy *et al*, 2021), or sequence-specific DNA methylases (Negri *et al*, 2021), H-type RNases and ExoR mostly employ constrained motion through the nucleoids, diffusing between DNA strands to find binding targets, which would explain the rather low mobility of the high-mobile fraction.

RNase HII and HIII belong to the RNase H enzyme family, which are responsible for the identification and cleavage of RNA-DNA hybrids (Cerritelli & Crouch, 2009; Ohtani *et al.*, 1999b). The formation of R-loops and the resulting DNA-RNA hybrids is a known stress response. This stress can be caused by cell wall damage, osmotic stress, oxidative damage, but also DNA damage, and can lead to genomic instability and replication arrest (Gan *et al*, 2011; Lin & Pasero, 2012). Using confinement analysis relative to the replication forks, we were able to clearly show that all four analysed enzymes have a very similar percentage of confined tracks in the direct proximity of the replication fork, similar to DNA helicase (DnaC). Confined tracks show dwell events for at least 100 ms, likely reflecting enzymatic activity in the DNA-bound form. Based on distance determination between molecule trajectories and replication forks, we could clearly see an abundance of RNase HIII at the replication forks. Interestingly, during the influence of DNA damage (UV), RNase HIII became more enriched at sites close to the forks, possibly reflecting its published involvement in R-loop processing in *Bacillus subtilis* (Lang *et al*, 2017). Interestingly, RNase HII also showed a high degree of spatial proximity to sites of DNA replication, strongly suggesting it is likewise involved in Okazaki fragment maturation (based on the notion that incorporation if RNA nucleotides by

DNA polymerases is a very rare event). In contrast to RNase HIII, HII did not show any stronger shift to the forks after inducing DNA damage by UV. PolA showed a stronger engagement with forks following UV irradiation, as was reported before (Hernández-Tamayo *et al.*, 2019). In contrast to this study, we found PolA even strongly associated with DNA replication sites even before induction of DNA damage, and similarly for ExoR. We believe that these differences are due to larger sample sizes in this work, showing significant localization even during normal growth. Likewise, the mNeo fluorophore used can lead to lower artifacts, as it has a higher lifetime, higher brightness, with a shorter maturation time in contrast to mVenus (Shaner *et al*, 2013). The improvement of the fluorophore in combination with the higher sample size can lead to deviations.

In order to use a third means to show involvement of RNase HII and HIII, we tracked the fusion proteins during a replication block by HPUra, where the activity of PolC is inhibited. We observed strong differences in mobilities and localization pattern. Both RNases became more dynamic, with RNase HIII showing the largest change from static to mobile diffusion. For RNase HII, we observed a strong relocalization of molecules from central places on the nucleoids towards more peripheral sites. Overall, our *in vivo* analysis provide evidence that both proteins are actively involved at replication forks, With RNase HIII playing a more pronounced role than RNase HII. Similarly, only RNase HIII together with DNA polymerase I (PolA) seems to show significant responses to UV stress, underlining the already assumed interdependence of the two proteins. It could be shown that RNase HIII supports PolA in the maturation of Okazaki fragments (Randall *et al.*, 2019). Interestingly, RNase HII as well as ExoR show very similar dynamics and localizations in the cell. RNase HII is known to remove single ribonucleoside monophosphates (rNMPs) during DNA replication (Yao *et al.*, 2013) The function is important for the cell because DNA is more stable than RNA. Resulting rNMP residues in DNA could lead to spontaneous strand breaks. ExoR and endoribunclease RNase HII showed very similar dynamics and localization, but it is unclear if they may have similar functions, in line of their synthetic lethality with PolA or RNase HIII, respectively (Thomaides *et al*, 2007). However, RNase HII and HIII treated with HPUra demonstrated a response to replication blockage. So, the single molecule tracking of these treated strains has revealed although that RNase HII and RNase HIII appear to have distinct functions *in vivo*, the analysis suggests that RNase HII may have a supporting effect in the maturation of Okazaki fragments and might be a RNase involved in this process.

We addressed the question whether enzymes may be specifically recruited to forks in order to remove RNA primers, or whether these sites are found by a diffusion/capture mode.

We therefore analysed the dynamics of ExoR and RNase HIII in the corresponding deletion backgrounds, as a cold-sensitive phenotype for double mutations of *exoR* and *rnhC* were observed (Randall *et al.*, 2019). The dynamics of the proteins did not show notable changes at 30°C, but at 37°C, RNaseH III-mV revealed a remarkable increase in the static population in the absence of *exoR*. ExoR-mV showed a slight decrease in the static population in the deletion background of *rnhC*. Clearly the lack of ExoR leads to mode binding events of RNase HIII, based on its higher abundance in the low mobility state, apparently leading to a takeover of RNA nucleotide removal by RNase HIII. These data suggest that RNAse HIII shows a diffusion/capture mode of recruitment at replication forks, besides possible, unknown direct protein/protein interactions.

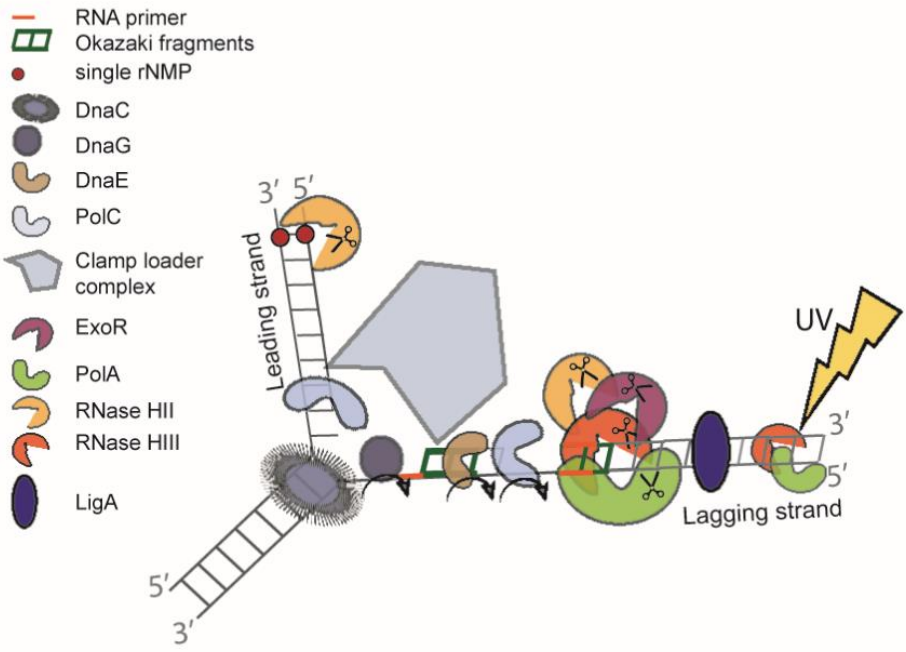

Figure 8: Graphical illustration of replication in *Bacillus subtilis* during UV stress. At the replication fork, a DNA helicase (DnaC) precedes the DNA synthesis machinery and unwinds the exist duplex parental DNA in cooperation with the single stranded binding proteins (SSB). On the leading strand (5 to 3 direction), replication proceeds continuously via the replisome. In contrast, on the lagging strand, DNA replication is performed discontinuously by synthesizing and assembling short Okazaki fragments. DNA primase (DnaG) is required for the formation of RNA primers. During DNA template replication, an RNA primer is removed either by the 5-bis-3 exonuclease activity of ExoR and Okazaki

fragments are matured via PolA, RNase HII and RNase HIII. Afterwards DNA ligase LigA fuses matured Okazaki fragments.

With the help of previous work (Jameson & Wilkinson, 2017; Patlán *et al*, 2019; Randall *et al.*, 2018; Randall *et al.*, 2019; Yao *et al.*, 2013) and our *in vivo* analyses, we conclude that *B. subtilis* has replication forks that strongly deviate from textbook knowledge on bacterial replication forks (Fig 7). Initiation of replication leads to loading and ensuing unwinding activity of the double-stranded DNA by the DNA helicase DnaC. The leading strand (5 to 3 direction) is then continuously processed by DNA polymerase C holoenzyme. For the replication of the lagging strand (3 to 5 direction), discontinuous processing occurs. Small RNA primers start each Okazaki fragment, which is synthesized by the primase (DnaG). DNA polymerase E, extends RNA primers by some DNA bases, and hands over synthesis of the lagging strand to DNA PolC. DNA ligase (LigA) ligates all fragments of the lagging strand at the 3' end. At least four specific exo- or endonucleases are used to remove RNA primers from the lagging strand. A known one is DNA polymerase I (PolA), which removes these primers with its exonuclease function (5'-3' exonuclease activity) together with the endoribonuclease RNase HIII (Randall *et al.*, 2019). In a likely redundant manner, RNaseH II and ExoR also remove RNA primers, while only RNase HIII and PolA show increased recruitment are suitable for UV damage and could be a part of the SOS response in *B. subtilis (Lenhart et al, 2012)*. However, it can be assumed that RNase HIII has functions outside of replication forks, because it shows areas of constrained motion at many sites on the nucleoids (Fig. 6A).

Altogether, our work clarifies functions for four enzymes removing DNA/RNA hybrids from replication forks, which may be a unique multitude of proteins for *B. subtilis*. It will be interesting to investigate if some or many other bacterial species also distribute RNA removal during replication onto many enzyme's shoulders.

Acknowledgments

This work has been supported by the LOEWE funded consortium MOSLA (state of Hessen).

Author contribution

RH has performed all experiments, and co-wrote the manuscript. PLG supervised experiments, conceived of the study, and co—wrote the manuscript.

2.3.6. Supplementary Material

Table 1: Strains or plasmids used in this study

Strain or Plasmids	**Relevant features**	**Reference or source**
Bacillus subtilis		
BG214	Wild type	gift from Juan C. Alonso
PG3977	BKK40880 (*ΔexoA*::kan trpC2)	(Koo *et al.* 2017)
PG3777	BKK28620 (*ΔrnhC*::kan trpC2)	(Koo *et al.* 2017)
PG4345	*rnhB*-mV ^{cmR}	This study
PG4346	*rnhB*-mNeo ^{cmR} *dnaX*-CFP ^{specR}	This study
PG4347	*rnhC*-mV ^{cmR}	This study
PG4348	*rnhC*-mNeo ^{cmR} *dnaX*-CFP ^{specR}	This study
PG4349	*ΔexoR*::kan trpC2 *rnhC*-mV ^{cmR}	This study
PG4350	*exoR*-mV ^{cmR}	This study
PG4351	*exoR*-mNeo ^{cmR} *dnaX*-CFP^{specR}	This study
PG4352	*ΔrnhC*::kan trpC2 *exoR*-mV ^{cmR}	This study
PG4353	*polA*-mNeo ^{cmR} *dnaX*-CFP^{specR}	This study
PG4374	*polC*-mNeo ^{cmR} *dnaX*-CFP^{specR}	This study
PG3173	*dnaX*-CFP ^{specR}	(Lindow *et al.* 2002)
PG3730	DH5α pSG1164-mVenus, expression Vektor, Amp^R, Cm^R	(Lucena *et al.* 2018)
131	pSG1164 *rnhB*-mVenus, integration Vector, Amp^R, Cm^R	This study
132	pSG1164 *rnhB*-mNeonGreen, integration Vector, Amp^R, Cm^R	This study
133	pSG1164 *rnhC*-mVenus, integration Vector, Amp^R, Cm^R	This study
134	pSG1164 *rnhC*-mNeonGreen, integration Vector, Amp^R, Cm^R	This study
135	pSG1164 *polA*-mNeonGreen, integration Vector, Amp^R, Cm^R	This study
136	pSG1164 *exoR*-mNeonGreen, integration Vector, Amp^R, Cm^R	This study
137	pSG1164 *exoR*-mVenus, integration Vector, Amp^R, Cm^R	This study

Table 2: List of Oligonucleotides

Primer	Sequence 5'→ 3'
rnhB-mNeo fw	GATTCCTAGGATGGGTACCGAATTCTTGTCGCCAGCGCAGTCATCCTTCC
rnhB-mNeo rev	CTCCCAGGCCAGATAGGCCGGGCCCTCTGAAAGATTGAACAGGAGCGAAA
rnhB_fw_full length	GTGAATACATTAACCGTAAA
rnhC-mNeo fw	GATTCCTAGGATGGGTACCGAATTCGAAACCTGATTAAAACCATTCCGTA
rnhC-mNeo rev	CTCCCAGGCCAGATAGGCCGGGCCCTGAACGTTTTTTATCAGCAAGGCGC
rnhC_fw_full length	CACCGACAATCGTGAAGTGC
exoR-mNeo fw	GATTCCTAGGATGGGTACCGAATTCCGGACATTACGGTGGTAACAGGGGA
exoR-mNeo rev	CTCCCAGGCCAGATAGGCCGGGCCCAACGATCTCTCTAGCGTTCAGCTTT
exoR-fw_full length	ATGAATAATAATAAACTATTGCTGGTTGAC
PolA-mNeo fw	GATTCCTAGGATGGGTACCGAATTCTTGGCATTGTTTACGGGATCAGCGA
PolA-mNeo rev	CTCCCAGGCCAGATAGGCCGGGCCCTTTCGCATCGTACCAAGATGGGCCT
PolA_fw_full length	CGAAAAAAATTAGTGCTTGT
DnaC-mNeo fw	GATTCCTAGGATGGGTACCGAATTCTTTACATCGATGATACACCGGGTAT
DnaC-mNeo rev	CTCCCAGGCCAGATAGGCCGGGCCCTGCGCCGGGCGGAACGCCTGCGTCA
DnaC_fw_full length	ATGACAGACCTTCTGAATGA
mNeonGreen rev	TTACTTGTACAGCTCGTCCA

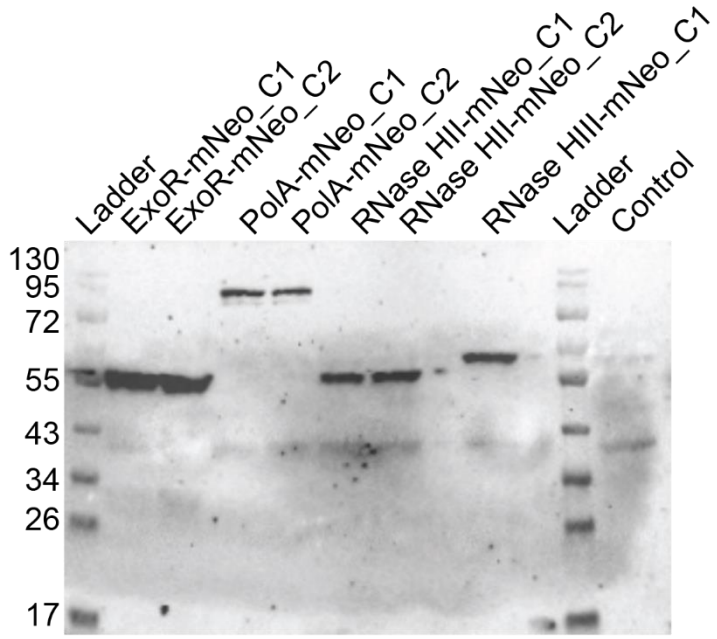

Figure S1: Western blot of potential replication proteins. Western blots showing mNeo fusion expressed from native locus. Total cell extracts from exponentially growing cultures (LB) were used. Two different clones are shown in each case (C1/C2). The ExoR-mNeo fusion (59.7 kDa), PolA-mNeo (125.8 kDa), RNaseHII-mNeo (55.1 kDa) and RNaseHIII-mNeo (60.8 kDa) contains the mNeongreen polypeptide (26.9 kDa). All strains were detected via mNeongreen-antiserum. As a control strain, the *Bacillus subtilis* BG214 was used.

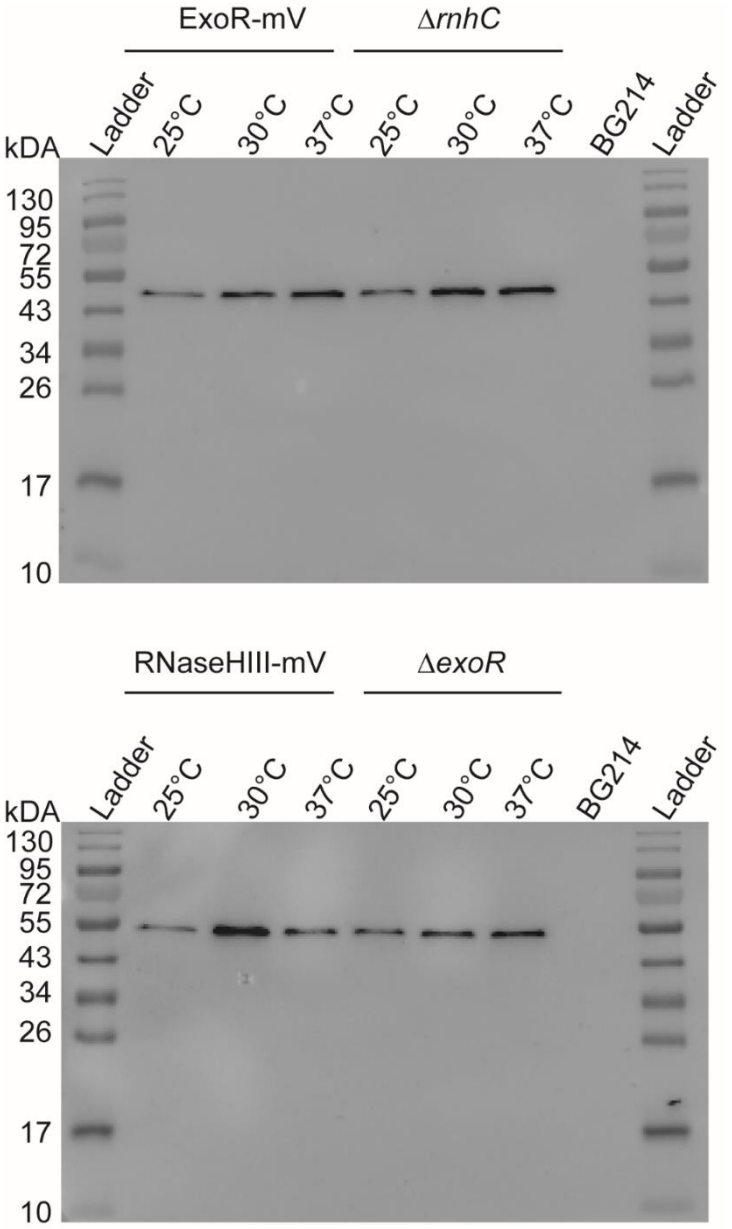

Figure S2: Comparison of expression level under deletion conditions and different temperatures. Western blots showing mVenus fusion expressed from native locus. Total cell extracts from exponentially growing cultures (LB), incubated at different temperatures (25°C, 30°C, 37°C) were used. The ExoR-mV fusion as well as the deletion of rnhC (59.7 kDa), RNaseHIII-mV (60.8 kDa) and the delition of exoR contains the mVenus polypeptide (26.9 kDa). All strains were detected via mVenus-antiserum. As a control strain, the *Bacillus subtilis* BG214 was used.

2.3.7. References

Bechhofer DH, Deutscher MP (2019) Bacterial ribonucleases and their roles in RNA metabolism. *Crit Rev Biochem Mol* 54: 242-300

Bin L, Eliason WK, Steitz TA (2013) Structure of a helicase-helicase loader complex reveals insights into the mechanism of bacterial primosome assembly. *Nature Communications* 4: 1-8

Brown NC (1970) 6-(p-hydroxyphenylazo)-uracil: a selective inhibitor of host DNA replication in phage-infected *Bacillus subtilis*. *Proc Natl Acad Sci U S A* 67: 1454-1461

Cerritelli SM, Crouch RJ (2009) Ribonuclease H: the enzymes in eukaryotes. *FEBS J* 276: 1494-1505

Clark AB, Kunkel TA (2010) The importance of being DNA. *Cell Cycle* 9: 4422-4424

Dersch S, Mehl J, Stuckenschneider L, Mayer B, Roth J, Rohrbach A, Graumann PL (2020) Super-Resolution Microscopy and Single-Molecule Tracking Reveal Distinct Adaptive Dynamics of MreB and of Cell Wall-Synthesis Enzymes. *Front Microbiol* 11: 1946

Dervyn E, Suski C, Daniel R, Bruand C, Chapuis J, Errington J, Janniere L, Ehrlich SD (2001) Two essential DNA polymerases at the bacterial replication fork. *Science* 294: 1716-1719

Duigou S, Ehrlich SD, Noirot P, Noirot-Gros MF (2005) DNA polymerase I acts in translesion synthesis mediated by the Y-polymerases in *Bacillus subtilis*. *Mol Microbiol* 57: 678-690

Gan WJ, Guan ZS, Liu J, Gui T, Shen K, Manley JL, Li XL (2011) R-loop-mediated genomic instability is caused by impairment of replication fork progression. *Genes & Development* 25: 2041-2056

Gibson DG, Young L, Chuang RY, Venter JC, Hutchison CA, Smith HO (2009) Enzymatic assembly of DNA molecules up to several hundred kilobases. *Nature Methods* 6: 343-U341

Hernández-Tamayo R, Oviedo-Bocanegra LM, Fritz G, Graumann PLJNar (2019) Symmetric activity of DNA polymerases at and recruitment of exonuclease ExoR and of PolA to the *Bacillus subtilis* replication forks. 47: 8521-8536

Hinrichs R, Pozhydaieva N, Hofer K, Graumann PL (2022) Y-Complex Proteins Show RNA-Dependent Binding Events at the Cell Membrane and Distinct Single-Molecule Dynamics. *Cells* 11: 933

Jameson KH, Wilkinson AJ (2017) Control of Initiation of DNA Replication in *Bacillus subtilis* and Escherichia coli. *Genes (Basel)* 8: 22

Jaqaman K, Loerke D, Mettlen M, Kuwata H, Grinstein S, Schmid SL, Danuser G (2008) Robust single-particle tracking in live-cell time-lapse sequences. *Nat Methods* 5: 695-702

Kochiwa H, Tomita M, Kanai A (2007) Evolution of ribonuclease H genes in prokaryotes to avoid inheritance of redundant genes. *BMC Evol Biol* 7: 128

Koo BM, Kritikos G, Farelli JD, Todor H, Tong K, Kimsey H, Wapinski I, Galardini M, Cabal A, Peters JM *et al* (2017) Construction and Analysis of Two Genome-Scale Deletion Libraries for *Bacillus subtilis*. *Cell Syst* 4: 291-305 e297

Lang KS, Hall AN, Merrikh CN, Ragheb M, Tabakh H, Pollock AJ, Woodward JJ, Dreifus JE, Merrikh H (2017) Replication-Transcription Conflicts Generate R-Loops that Orchestrate Bacterial Stress Survival and Pathogenesis. *Cell* 170: 787-+

Lenhart JS, Schroeder JW, Walsh BW, Simmons LA (2012) DNA repair and genome maintenance in *Bacillus subtilis*. *Microbiol Mol Biol Rev* 76: 530-564

Li YF, Breaker RR (1999) Kinetics of RNA degradation by specific base catalysis of transesterification involving the 2 '-hydroxyl group. *Journal of the American Chemical Society* 121: 5364-5372

Li Z, Deutscher MP (2004) Exoribonucleases and Endoribonucleases. *EcoSal Plus* 1

Lin YL, Pasero P (2012) Interference Between DNA Replication and Transcription as a Cause of Genomic Instability. *Current Genomics* 13: 65-73

Liu B, Hu J, Wang J, Kong D (2017) Direct Visualization of RNA-DNA Primer Removal from Okazaki Fragments Provides Support for Flap Cleavage and Exonucleolytic Pathways in Eukaryotic Cells. *J Biol Chem* 292: 4777-4788

Lucena D, Mauri M, Schmidt F, Eckhardt B, Graumann PL (2018) Microdomain formation is a general property of bacterial membrane proteins and induces heterogeneity of diffusion patterns. *Bmc Biology* 16: 1-17

Monahan LG, Liew AT, Bottomley AL, Harry EJJFim (2014) Division site positioning in bacteria: one size does not fit all. 5: 19

Negri A, Werbowy O, Wons E, Dersch S, Hinrichs R, Graumann PL, Mruk I (2021) Regulator-dependent temporal dynamics of a restriction-modification system's gene expression upon entering new host cells: single-cell and population studies. *Nucleic Acids Res* 49: 3826-3840

Ogawa T, Okazaki T (1980) Discontinuous DNA replication. *Annu Rev Biochem* 49: 421-457

Ohtani N, Haruki M, Morikawa M, Crouch RJ, Itaya M, Kanaya SJB (1999a) Identification of the genes encoding Mn2+-dependent RNase HII and Mg2+-dependent RNase HIII from *Bacillus subtilis*: classification of RNases H into three families. 38: 605-618

Ohtani N, Haruki M, Morikawa M, Kanaya S (1999b) Molecular diversities of RNases H. *J Biosci Bioeng* 88: 12-19

Oviedo-Bocanegra LM, Hinrichs R, Rotter DAO, Dersch S, Graumann PL (2021) Single molecule/particle tracking analysis program SMTracker 2.0 reveals different dynamics of proteins within the RNA degradosome complex in *Bacillus subtilis*. *Nucleic Acids Research* 49: e112-e112

Paintdakhi A, Parry B, Campos M, Irnov I, Elf J, Surovtsev I, Jacobs-Wagner C (2016) Oufti: an integrated software package for high-accuracy, high-throughput quantitative microscopy analysis. *Mol Microbiol* 99: 767-777

Patlán AG, Ayala-García VM, Valenzuela-García LI, Meneses-Plascencia J, Vargas-Arias PL, Barraza-Salas M, Setlow P, Brieba LG, Pedraza-Reyes MJPo (2019) YwqL (EndoV), ExoA and PolA act in a novel alternative excision pathway to repair deaminated DNA bases in *Bacillus subtilis*. 14: e0211653

Pediaditakis M, Kaufenstein M, Graumann PL (2012) *Bacillus subtilis* hlpB Encodes a Conserved Stand-Alone HNH Nuclease-Like Protein That Is Essential for Viability Unless

the hlpB Deletion Is Accompanied by the Deletion of Genes Encoding the AddAB DNA Repair Complex. *Journal of Bacteriology* 194: 6184-6194

Randall JR, Hirst WG, Simmons LA (2018) Substrate Specificity for Bacterial RNases HII and HIII Is Influenced by Metal Availability. *Journal of Bacteriology* 200: e00401-00417

Randall JR, Nye TM, Wozniak KJ, Simmons LA (2019) RNase HIII Is Important for Okazaki Fragment Processing in *Bacillus subtilis*. *Journal of Bacteriology* 201: e00686-00618

Rotter DAO, Heger C, Oviedo-Bocanegra LM, Graumann PL (2021) Transcription-dependent confined diffusion of enzymes within subcellular spaces of the bacterial cytoplasm. *Bmc Biology* 19: 1-30

Sanders GM, Dallmann HG, McHenry CS (2010) Reconstitution of the *B. subtilis* replisome with 13 proteins including two distinct replicases. *Mol Cell* 37: 273-281

Schindelin J, Arganda-Carreras I, Frise E, Kaynig V, Longair M, Pietzsch T, Preibisch S, Rueden C, Saalfeld S, Schmid B *et al* (2012) Fiji: an open-source platform for biological-image analysis. *Nat Methods* 9: 676-682

Schroeder JW, Randall JR, Hirst WG, O'Donnell ME, Simmons LA (2017) Mutagenic cost of ribonucleotides in bacterial DNA. *Proc Natl Acad Sci U S A* 114: 11733-11738

Seco EM, Ayora S (2017) *Bacillus subtilis* DNA polymerases, PolC and DnaE, are required for both leading and lagging strand synthesis in SPP1 origin-dependent DNA replication. *Nucleic Acids Res* 45: 8302-8313

Shaner NC, Lambert GG, Chammas A, Ni Y, Cranfill PJ, Baird MA, Sell BR, Allen JR, Day RN, Israelsson M *et al* (2013) A bright monomeric green fluorescent protein derived from Branchiostoma lanceolatum. *Nat Methods* 10: 407-409

Stracy M, Schweizer J, Sherratt DJ, Kapanidis AN, Uphoff S, Lesterlin C (2021) Transient non-specific DNA binding dominates the target search of bacterial DNA-binding proteins. *Mol Cell* 81: 1499–1514

Su'etsugu M, Errington J (2011) The replicase sliding clamp dynamically accumulates behind progressing replication forks in *Bacillus subtilis* cells. *Mol Cell* 41: 720-732

Thomaides HB, Davison EJ, Burston L, Johnson H, Brown DR, Hunt AC, Errington J, Czaplewski LJJob (2007) Essential bacterial functions encoded by gene pairs. 189: 591-602

Williams JS, Kunkel TA (2014) Ribonucleotides in DNA: origins, repair and consequences. *DNA Repair (Amst)* 19: 27-37

Yao NY, Schroeder JW, Yurieva O, Simmons LA, O'Donnell ME (2013) Cost of rNTP/dNTP pool imbalance at the replication fork. *Proceedings of the National Academy of Sciences of the United States of America* 110: 12942-12947

3. Unpublished results

3.1. 3D SIM reveals more pronounced membrane-localization for components of the Y-complex

As shown in the manuscript (article II) using SMT and postulated by previous work, the Y-complex proteins have been localized in different ways in the cell (Hinrichs, Pozhydaieva *et al*. 2022; DeLoughery, Lalanne *et al.* 2018). Furthermore, structural analysis of the Y-complex proteins showed that different combinations of individual components are possible *in vitro* (see chapter 1.6.) (Adusei-Danso, Khaja *et al*. 2019).

In order to characterize possible different localization patterns *in vivo*, 3D structure illumination microscopy was applied (3D-SIM) (Images were taken by Maximilian Greger).

First, the Y-complex proteins were fused to the N-terminus of a mNeonGreen fluorophore and mNeptune fluorophore (data not shown) (see chapter 5.2.4.). The genes encoding the Y- proteins were expressed from their native locus under original promotor conditions. To analyse the expression of the full-length fusion proteins, western blotting was performed using α-mNeonGreen antiserum as well as a fluorescence blot (Fig. S1 A, B). It is important to note that the proteins had a faster running behavior in the SDS-PAGE than expected from their size (57.97 kDa for YaaT-mNeo, 43.67 kDa for YlbF-mNeo, 42,92 kDa for YmcA-mNeo).

The 3D images are displayed as a reconstruction using an overlay of a z-stack of 14 slices. Green signal shows the localization of the mNeonGreen fusions (see chapter 5.2.7) (Fig. 3.1.). SIM shows that in comparison to the other Y-complex proteins, it might be clear that the highest signal could be achieved for the protein YmcA. This indication is confirmed by the fluorescence blot (loading control is not shown) (Fig. S1 B).

YaaT was found preferentially at the membrane but also in the cytoplasm. The distribution of the membrane signal is very uniform, whereas the cytosolic part was more punctual, with a tendency towards the septum.

The YlbF-mNeo fusion showed a higher amount of the signal in the cytosol, and only low signals are located on the membrane. Interestingly, the cytosolic fraction is mostly homogeneous.

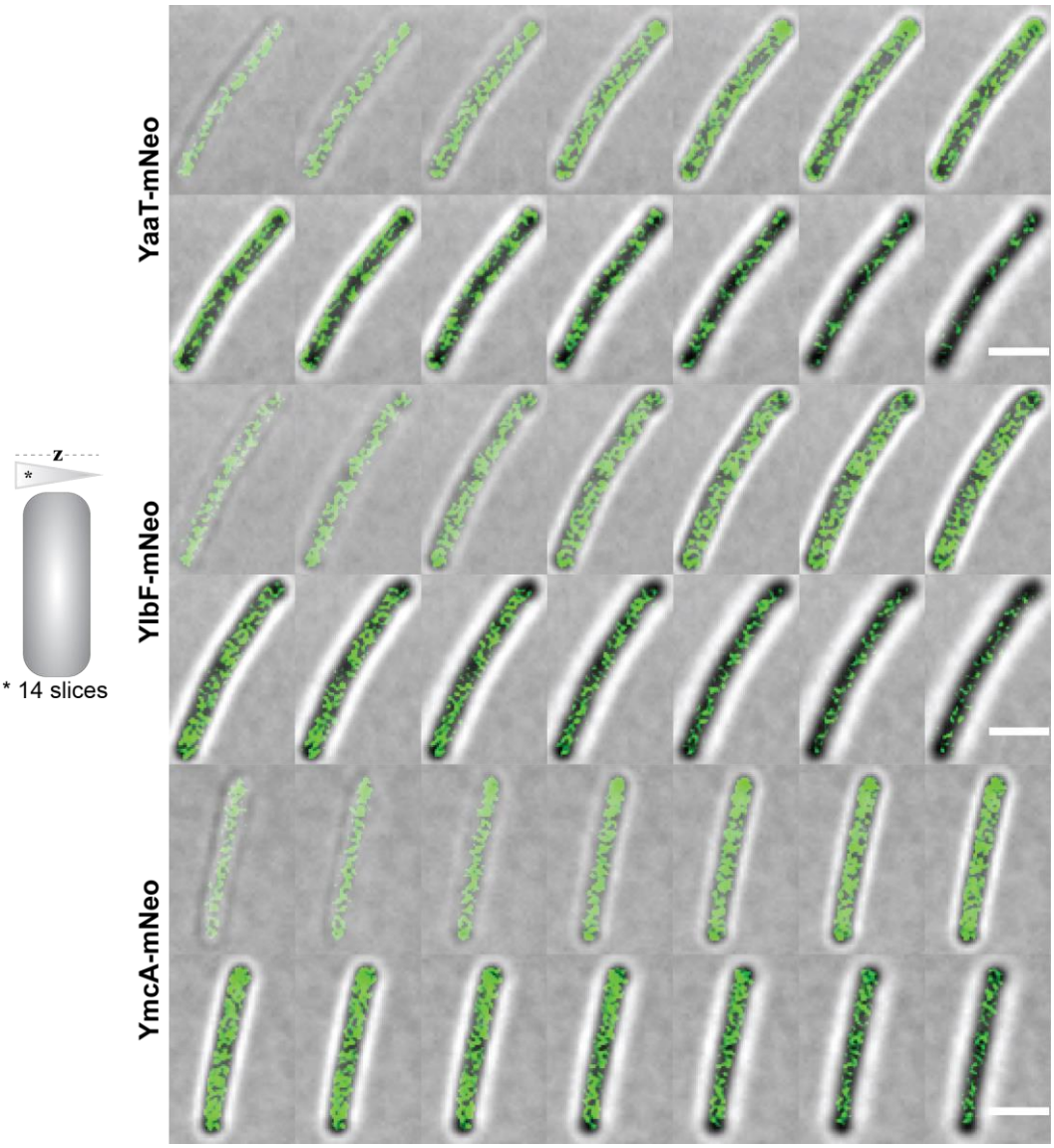

Figure 3.1: *Localization of the Y-complex mNeongreen fusion proteins expressed from native locus by structured illumination microscopy (SIM) in Bacillus subtilis (BG214).* A z-stack of 14 slices is shown. YaaT-mNeo localized at the membrane and in the cytosol. YlbF-mNeo shows signal at the membrane and the cytosol. YmcA shows the most signal in the cytosol.

In contrast, the localization of the YmcA-mNeo fusion behaved differently. There was a clear cytosolic pattern. The attachment to the membrane did not seem to be clearly present and the distribution of the signal in the cell was punctate but more uniform than that of the other two Y-complex proteins (Fig. 3.1.). These experiments support the idea that the Y-complex does not have a defined stoichiometry and its members confer somewhat different functions, in agreement to Hinrichs et al., 2022.

3.2. BiFC reveals direct interaction of RNase Y to Y-complex proteins

Using bacterial two-hybrid studies, it has been shown that YlbF and YaaT interact with the membrane protein RNase Y *in vivo*. For YmcA, it was not possible to show a direct interaction by using this method (DeLoughery, Lalanne *et al*. 2018). Similarly, pulldown assays have not detected interaction of the entire complex with RNase Y (Carabetta, Tanner *et al.* 2013).

Bimolecular fluorescence complementation (BiFC) was used as an alternative to studying protein-protein interaction. In BiFC, a signal is formed when both proteins of interest localize at the same position in the cell for a certain period of time (complementation of the fluorophore) (see chapter 5.2.4) (Defeu Soufo *and* Graumann 2006). The maturation of the fluorescent, irreversibly linked complex is reported to have a half-time of about 50 min (Kerppola 2008).

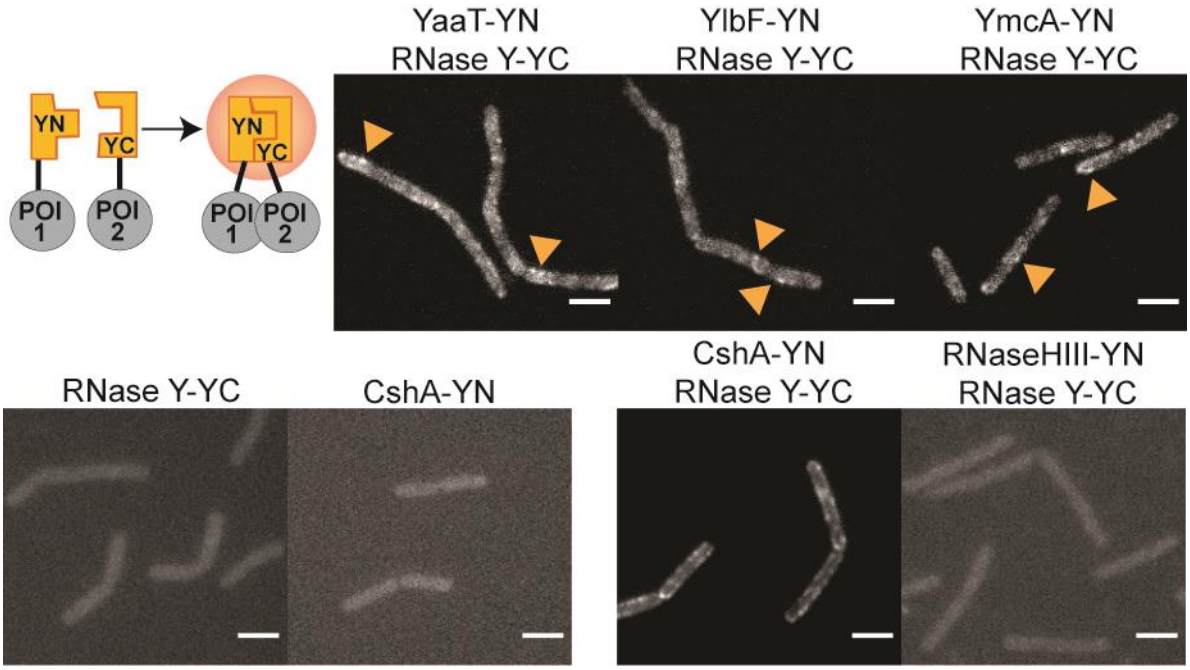

Figure 3.2: *Bimolecular fluorescence complementation (BiFC) of Y-complex proteins and* RNase Y*.* The Y-complex proteins (YN) show distinct foci at the membrane (orange arrows) after induction of RNase Y-YC (0.5 mM IPTG). The fluorophore control (RNase Y-YC), the C-terminal fluorophore fusion, and N-terminal fusion (RNase HIII-YN RNase Y-YC) show no signal. The positive control strain (CshA-YN RNase Y-YC) shows signal at the membrane. Scale bar 2 µm.

For the experiments, the fusion gene *rny-YC* was ectopically integrated at the *amy* locus and transcription and following protein synthesis were induced using 0.5 mM IPTG. RNase Y carried the first 154 amino acids of the split mVenus fluorophore (YN). The other part of the fluorophore (YC) was expressed from the original locus under the control of a native

promoter. Both parts of the split fluorophore were in each case C-terminally fused to proteins of interest. Both fusions were integrated into one strain (*Bacillus subtilis*, BG214). To test the fusions of the split mVenus fluorophore, a N-terminal GFP antibody was used with a binding specificity of AA 1-100 (N-term), as well as a C-terminal antibody which has a binding specificity at the C-terminus of the fluorophore (Fig. S3).

Initially, cultivation was performed without the addition of IPTG to an OD_{600} of ~ 0.4 (early exponential growth). After the addition of 0.5 mM IPTG, the cells were cultured for one hour. To exclude artifacts and background, both the N-terminal part and the C-terminal were induced separately. No signal was detectable under these control conditions. The positive control performed with CshA showed a signal along the membrane as expected (Fig. 3.2., lower part) (Cascante-Estepa, Gunka *et al.* 2016). RNase HIII was used as a negative control. This is an endoribonuclease involved in endonucleolytic cleavage of RNA in RNA-DNA hybrid molecules, processing of R-loops, and maturation of Okazaki fragments in *B. subtilis* (Randall, Nye *et al*. 2019). It is important to note, that the antibody with the binding specifity at the N-terminus was unable to detect a signal for RNase HIII. Integration was checked by Integration-PCR (data not shown).

Using BiFC, I was able to show that distinct signals are present at the membrane for all Y-complex proteins (Fig. 3.2., orange triangle). The protein-protein interaction *in vivo* of the entire Y-complex (YaaT, YlbF, YmcA) with the endoribonuclease RNase Y was thus confirmed.

3.3. *In silico* analysis via AlphaFold v 2.0 reveals possible connection between YlbF-YmcA and YaaT

A recognized method for the prediction of three-dimensional protein structures, as well as the prediction of whole complexes, is the computer method AlphaFold v 2.0. This method had a median backbone accuracy of 0.96 Å r.m.s.d.95 (Cα root-mean-square deviation at 95% residue coverage) (95% confidence interval = 0.85–1.16 Å), which describes the highest possible accuracy in this sector up to now (Jumper, Evans *et al.* 2021).

AlphaFold v 2.0 was used to predict the connection of YlbF-YmcA and the YaaT (Jumper, Evans *et al.* 2021). The viewer ChimeraX (Pettersen, Goddard *et al*. 2021) was used to perform the application of Alphafold v 2.0 via ColabFold (Mirdita, Schütze *et al.* 2022). Obtained parameters like the confidence of the prediction are shown in Figure S. 5.

Previously published data could be shown the connection between YlbF and YmcA by means of crystal structures, but no crystal structure could be generated for the entire complex (Adusei-Danso, Khaja *et al.* 2019).

The prediction was used to identify a possible heterotrimer (1:1:1) stoichiometric of the Y-complex, with the YaaT shown in red, YlbF in green, and YmcA in blue (Fig. 3.3.).

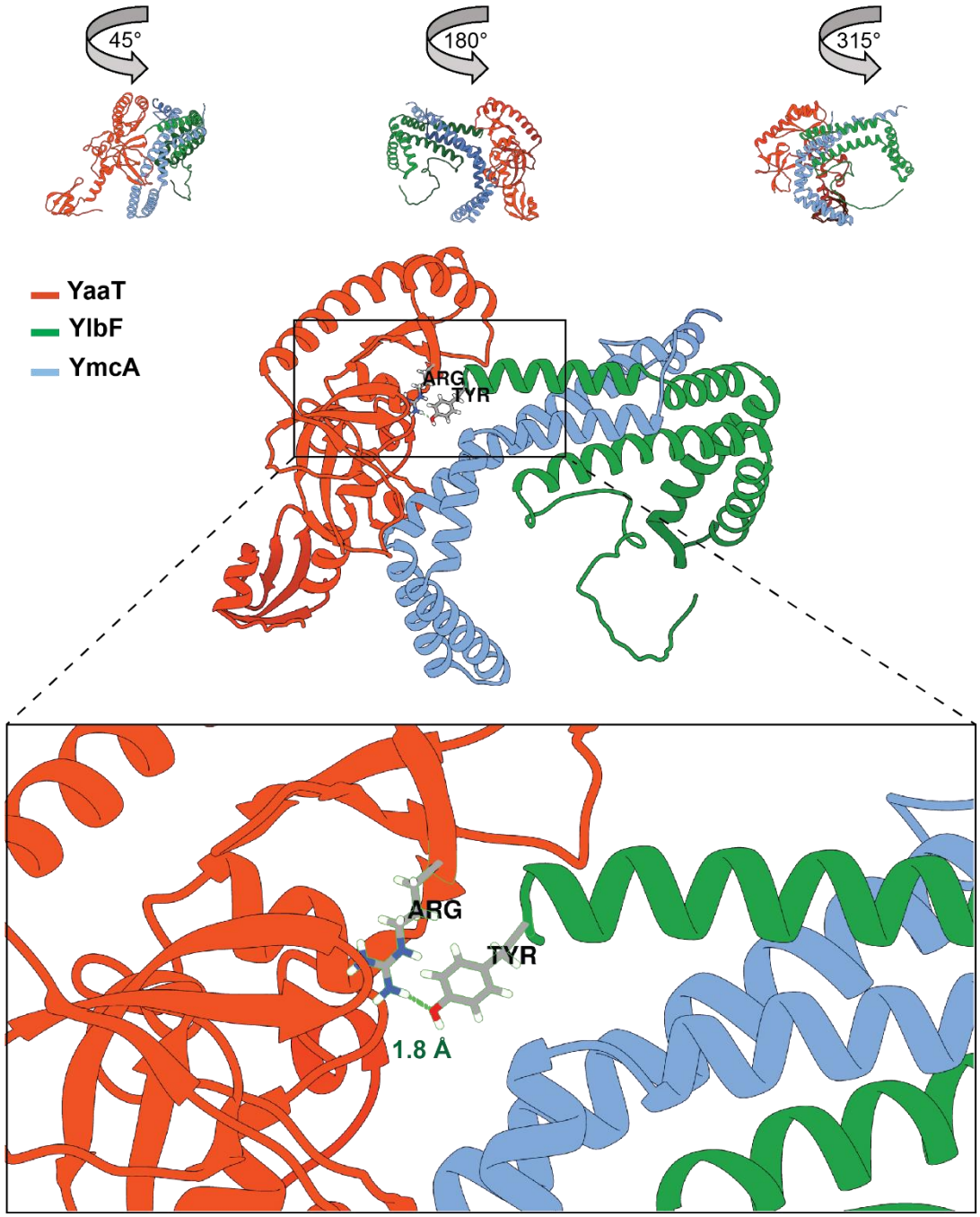

Figure 3.3: *AlphaFold v 2.0 prediction of the Y-complex proteins with potential bindings inside of the complex.* The structure of YaaT is illustrated in red, YlbF in green and YmcA in green. The side chains are displayed as sticks and colored heteroatoms. The amino acids

of binding are labeled with name and the distance between are specified in Ångström (Å). The structure is presented at different angles (0°, 45°, 180°, 315°).

A possible connection via hydrogen bonds between the oxygen of tyrosine (position 2) in YlbF and the nitrogen of arginine (position 144) in YaaT was found with a predicted distance of 1.8 Å. This corresponds to a typical bond length of hydrogen bonds in an aqueous solution of 0.18 nm (Jiang and Lai 2002). No further connections were predicted between YaaT and YlbF, likewise, no connections were found between YaaT and YlbF. The confidence of the prediction is described by means of colour code in an additional representation (Fig. S5 B).

3.4. A “clean” RNase Y fusion at the original locus shows localization solely to the membrane

We postulated that RNase Y had a large cytosolic fraction in a fusion with mVenus *via* single crossover (pSG1164) in *B. subtilis* BG214 (Oviedo-Bocanegra, Hinrichs *et al.* 2021). To further investigate this observation, we received a strain, generated by the laboratory of Prof. Dr. Harald Putzer, which was based on a different type of cloning (markerless allelic replacement with pMAD). SSB2048 (*rny*-sfGFP) described *in vivo* data in which it showed RNase Y to be a pure membrane protein (Hamouche, Billaudeau *et al*. 2020). Epifluorescence images have been shown the expression of RNase Y-sfGFP in the exponential growth phase as described with signal at the membrane (Fig. 3.4. A).

In the western blot performed (antibody against GFP), in contrast to the fractionation of the RNase Y-mVenus strain (Fig. S5 A), the RNase Y-sfGFP was present solely in the membrane fraction (Fig. 3.4. B, Fig S5 A). Interestingly, there was a difference in the running behaviour of the different fusions in the specific antibody (α-*ymdA/ α-gfp-tag*). To further visualize the localization of RNase Y, structure illumination microscopy (SIM) montages were prepared. This was a z-stack of 9 slices, which includes an overlay of brightfield and fluorescence (Fig. 3.4. C). In the reconstruction, a distinct pattern can be seen solely at the membrane.

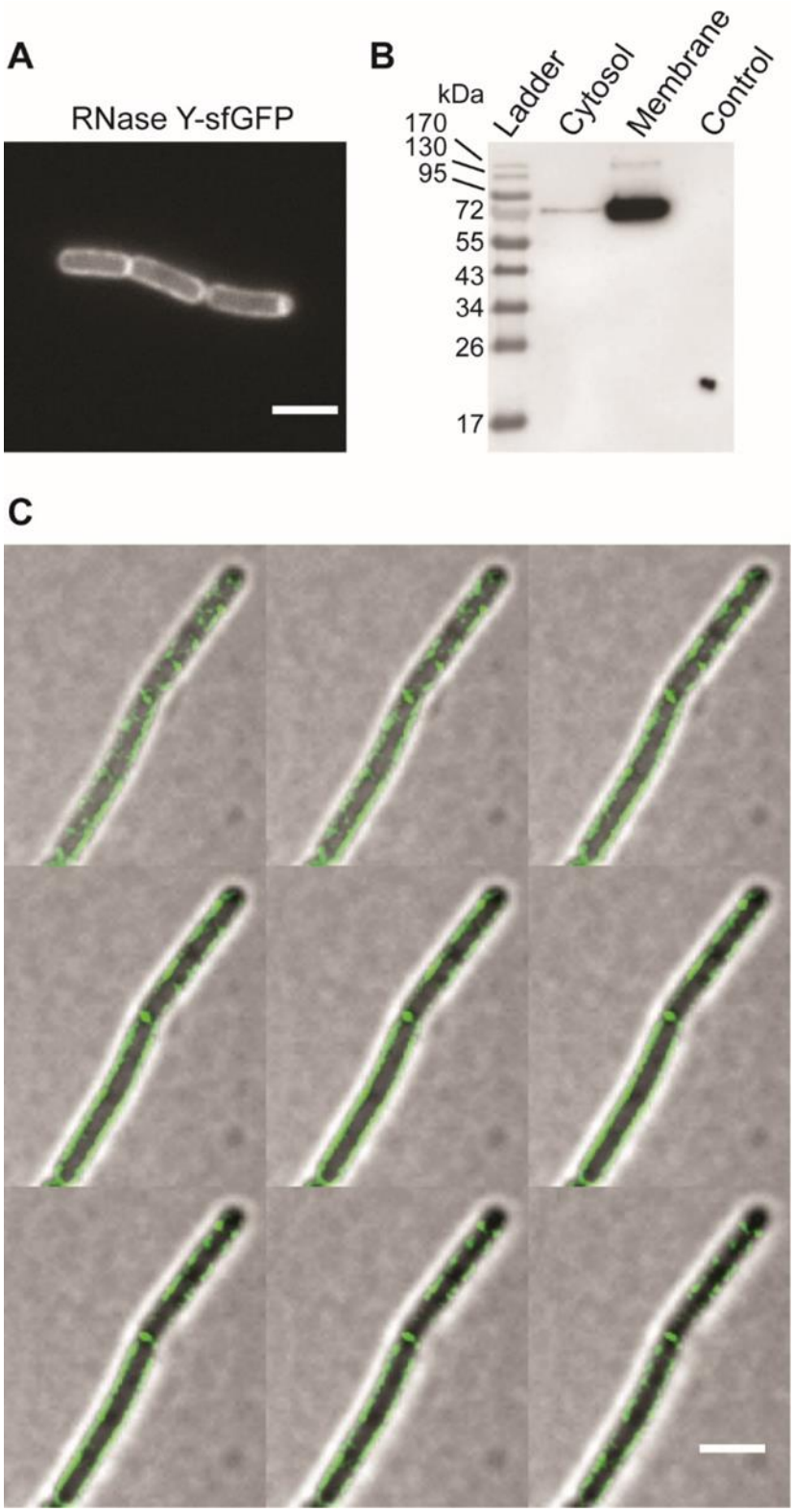

Figure 3.4: *Imaging of* RNase Y*-sfGFP in B. subtilis.* (A) Epifluorescence image of RNase Y-mV localization expressed from native locus. (B) Western blots of the fusion protein showing cell fractionation. Total cell extracts from exponentially growing cultures (LB) were used. The fusion (85.65 kDa) contains the sfGFP (~ 27 kDa). The Protein was detected via GFP-antiserum. The fractionation was carried out by ultracentrifugation (100,000 x g). The shown fractions are supernatant (Cytosol) and pellet (Membrane). "Control" BG214 wild type cells without sfGFP fusion. (C) Structured illumination microscopy

(SIM) of RNase Y-sfGFP. Shown is a z-stack (9 slices). The signal was located at the membrane of the cell. Scale bars 2 µm.

3.5. RNase Y becomes more diffusive after transcriptional arrest

We were able to show that RNase Y, fused with mVenus, exhibited a significant increase of diffusion constant after treatment with rifampicin, resulting in transcriptional stop (Oviedo-Bocanegra, Hinrichs *et al.* 2021). Based on divergent localization, we repeated the single molecule analysis (SMT) with an RNase Y-sfGFP fusion (SSB2048) (an example video for the method over 1000 frames is shown in the link (https://hessenbox.uni-marburg.de/getlink/fiQjxCQokQAAByLekZDEjK3x/)).

Confined tracks were used to localize positions in the cell where the protein likely arrests for an extended time. In this case, a minimum step length of 7 was selected in a confinement radius of 120 nm. The confined tracks were projected in a standardized *B. subtilis* cell and displayed in form of a heat map. The frequency of the tracks was indicated by a colour code (red = high, blue = 0) RNase Y-sfGFP showed localization along the membrane, the septum as well as low in the cytosol. Interestingly, the intensity of the confined tracks seemed to be highest at the poles. After treatment with rifampicin (25 µg/ml) to obtain a transcriptional stop, confined tracks appeared more in the cytosol of the cell and less at the membrane. Remarkably, the localization at the septum remained after the rifampicin treatment (Fig. 3.5. A).

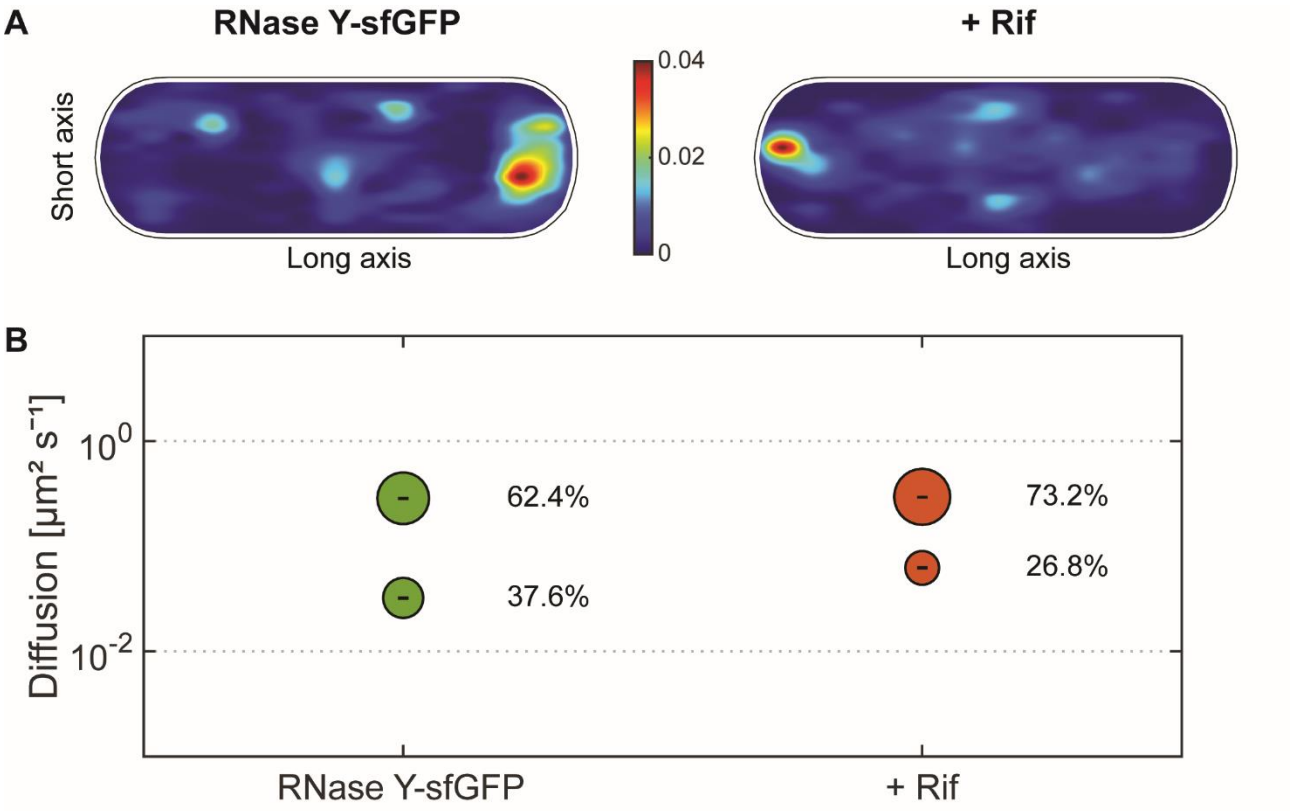

C

	Rnase Y-sfGFP	+ Rif
D1 (static) $\mu m^2 s^{-1}$	0.03	0.06
D2 (mobile) $\mu m^2 s^{-1}$	0.29	0.29
Static %	37.6	26.8
Mobile %	62.4	73.2
R^2	0.988	0.999

Figure 3.5: *Single molecule analyses of* RNase Y-*sfGFP*. (A) Heat maps of confined tracks of RNase Y-sfGFP proteins in a medium-size *Bacillus subtilis* cell with and without rifampicin. The distribution of tracks is indicated by a color shift from blue (low probability) to red (highest probability). (B) Bubble blots show diffusion constants of RNase Y-sfGFP without and with treatment of Rifampicin and fractions sizes for mobile and static molecules. (C) Diffusion constants and percentages of static and mobile molecule fractions. Values were fitted using non-linear least-square fitting, R^2 values for each condition are stated.

One method to determine the dynamics of the protein is the square displacement analysis (SQD). SQD analysis can be used to determine the diffusion constant, as well as the population size of the protein *in vivo*. In this case, a two-population fit was used (Fig. 3.5. B) (Rösch, Oviedo-Bocanegra *et al.* 2018; Oviedo-Bocanegra, Hinrichs *et al*. 2021). RNase Y was divided into a static population with a size of 37.6% and a diffusion constant of 0.03 $\mu m^2 s^{-1}$, and a mobile population with a size of 62.4% and a diffusion constant of

0.29 $\mu m^2 s^{-1}$. In comparison, RNase Y showed up during a transcriptional stop, with a lower static population (26.8%) and a diffusion constant doubled to 0.06 $\mu m^2 s^{-1}$. It was interesting to note that the diffusion constant of the mobile fraction remains stable at 0.29 $\mu m^2 s^{-1}$ with a fraction size of 73.2% (Fig. 3.5. C).

3.6. *In silico* analysis via AlphaFold v 2.0 shows a possible dimer of RNase Y

The endonuclease RNase Y is composed of a N-terminal transmembrane region (residue 1-24), a subsequent catalytic domain (residue 210-280), as well as a HD motif (330-430) the C-terminal part is functionally unknown (Grishin 2001; Aravind and Koonin 1998).

It has not been possible to obtain a structure of the full-length RNase Y.

A structure of a truncated version of the N-terminus was shown (6F7T PDB) which seems to exist as a dimer. Also, only a few activity assays of truncated versions could be shown (Shahbabian, Jamalli *et al.* 2009; Hardouin, Velours *et al.* 2018).

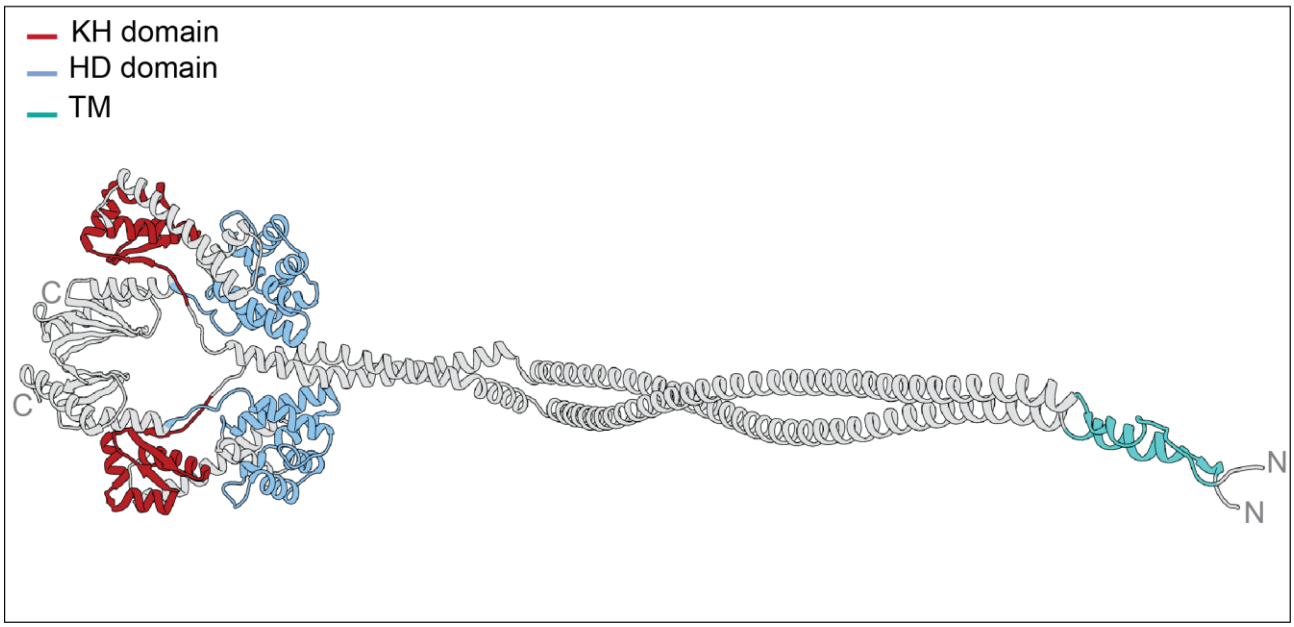

Figure 3.6: *Schematic illustration of AlphaFold v 2.0 prediction of dimerized RNase Y.* The dimerized full-length protein of RNase Y is shown with coloured motives (KH-domain in red and HD-domain in blue). The transmembrane domain is coloured in turquoise. The C and N-termini are described.

To get an impression of the full-length protein structure of RNase Y in *B. subtills* and obtain a hint for a purification scheme of the full-length protein, a prediction with AlphaFold v 2.0

was created (Jumper, Evans *et al*. 2021). The confidence of the prediction was described by a colour code (Fig. S5 A).

RNase Y is shown as a dimer (grey), known domains such as the HD domain (blue) and the KH domain (red) are shown in colours. Likewise, the predicted transmembrane domains (N-terminus) are shown in turquoise. The prediction showed high confidence with a pLDDT of around 90 or higher, in the known motifs (HD, KH) as well as in the range of alpha helices (Ser 81 -Glu 120) (Figure S4 A). The position of long α-helices (Ser 26- Cys 200) indicates a possible area of dimerization, due to intermolecular contacts.

3.7. Purification of $_{B.s.}$RNase Y-His$_6$ and Mass photometry analyses

For heterologous expression and purification of RNase Y in full-length, an overexpression plasmid was generated based on pET24+ (strain DH5a pAL172 *rny-his*$_6$) containing an RNase Y with a C-terminal fusion tag a 6xHis-tag (Fig. 3.7. A). Overexpression was performed in *E. coli* BL21 C41 (DE3). The strain C41(DE3) was based on BL21(DE3). This strain had at least one mutation that prevents cell death associated with the expression of many recombinant toxic and membrane proteins (Dumon-Seignovert, Cariot *et al.* 2004; Zhang, Kuipers *et al.* 2015). Since RNase Y is a membrane protein, the necessary solubilization of the protein was initially performed with Lauryl Maltose Neopentyl Glycol (LMNG). During purification, the protein was kept in micelles (0.05% LMNG) (see chapter 5.3.1.).

An IPTG concentration of 0.25 mM was used for overexpression. Overnight expression at 20°C was performed. The samples collected during the Ni-NTA affinity purification showed the flow rate and washing steps (three times) as well as the three-step elution and the concentrated elution. For the control, a western blot was performed in parallel (α-His-serum) (Fig. 3.7.B). The expected size of RNase Y was around 59 kDa. In the SDS-PAGE of the wash, fractions showed little loss of the expressed protein and the elutions showed only minor contaminations. Please note, that the strong contaminants seen in the western blot were due to the increasing effect of a western blot. The purified protein was determined by mass spectrometry (https://hessenbox.uni-marburg.de/getlink/fiQjxCQokQAAByLekZDEjK3x/). The concentrated elution fraction was applied to size exclusion chromatography (SEC) via 10/300 GL Superdex 200 column. The SEC purification resulted in two main peaks which

directly follow each other (Fig. 3.7. D). In the SDS-PAGE of the resulting fractions, RNase Y was mainly found in the first peak and the concentration in the second peak decreased, whereas contaminations increased (Fig. 3.7 C). Work was continued with the protein of the first peak. In mass photometry (Fig. 3.7 E.)(Mass photometry was taken by Franziska Sendker), it was useful to measure the membrane protein under the critical micelle concentration (cmc) to avoid artifacts, since there should be no empty micelles in the sample (Olerinyova, Sonn-Segev *et al.* 2021). For this purpose, a dilution below the critical micelle concentration (cmc) (0.001%/ 0.1 mM in H_2O) of LMNG was used during the measurement (Chaptal, Delolme *et al.* 2017). To exclude possible artifacts, the buffer was measured with LMNG without protein (Fig. 13 E, orange, 59 kDa). The result of the measurement showed a single peak corresponding to 101 kDa for RNase Y (Fig. 13E, grey). Since LMNG is a very stable micelle, it can be assumed that the peak was the monomeric RNase Y within a micelle (see chapter 5.3.3.).

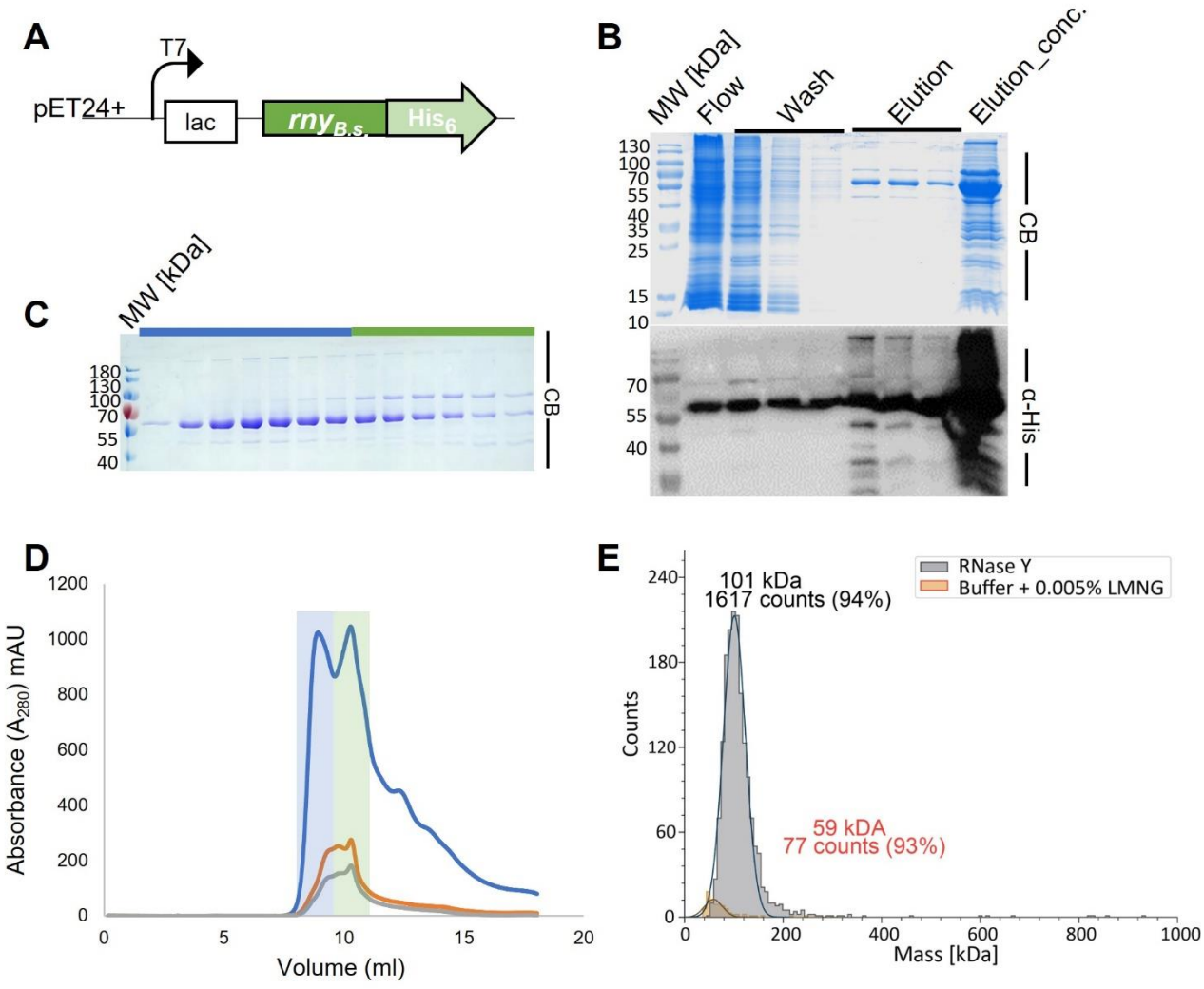

Figure 3.7: *Purification of full length His_6-RNase Y from B. subtilis via IMAC and SEC.* (A) Scheme of *rny* gene fused to 6xHis tag (C-term.) under control of T7-system in pET24+. (B) SDS-PAGE, Coomassie staining (CB) and western blot (α-His) using a His-tag antibody) of samples collected during Ni-NTA affinity purification of RNase Y-His_6 from soluble *E. coli* BL21 (DE3, C41). (C) Characterization of peak fractions via SDS-PAGE and Coomassie staining. Molecular weight of ~60 kDa was expected. (D) Size exclusion chromatography of RNase Y-His_6. The blue line displays the absorbance of 215 mAU, the orange line of 255 mAU, and the grey line of 280 mAU. The first peak was coloured in blue and the second peak in green. (E) Results of Mass photometry analysis of purified RNase Y-His_6 (peak 1). As a control (orange) the buffer was measured.

3.8. Purification of $_{Geo}$RNase Y-His_6, Mass photometry analysis and negative staining

As explained in chapter 1.5., the active form of RNase Y appears to be the dimer (Shahbabian, Jamalli *et al.* 2009). Since it was not possible to obtain a stable dimerized RNase Y in the full-length purification of RNase Y from *Bacillus subtilis*, a new construct was created.

The homolog of the RNase Y from the thermostable organism *Geobacillus thermodenitrificans NG-80* was used. Due to the thermostable properties of the organism, it was suitable as a donor of the gene sequence and subsequently a purification of the homolog protein (Schuhmacher, Rossmann *et al.* 2015). Similarly, *G. thermodenitrificans* showed a similarity of 86.97% for the RNase Y match to *Bacillus subtilis* (www.ncbi.nlm.nih.gov).

Please note that a point mutation was found in the genome of *G. thermodenitrificans*, which leads to an exchange of amino acids (*rny* G^{287E}). In comparison to the gene sequence of the homologs *Bacillus subtilis* and *Staphylococcus aureus* the point mutation resulted in the same amino acid, so we ignored this mutation (Fig. S6).

Furthermore, a MISTIC (*mstX*) tag was attached to N-terminus of RNase Y to provide an improvement in purification (Weiland and Altegoer 2021). The integral membrane protein is able to fold itself into the membrane by acting as a targeting signal. In the case of overexpression of integral membrane proteins, the MISTIC-tag is helpful to bring them into their native conformation (Roosild *et al*., 2005).

To enable the removal of the MISTIC, a TEV site was added (Figure 14A). In micelles, MISTIC becomes stabilizing through hydrophobic and polar interactions with detergents

(Frotscher, Krainer *et al.* 2018). This property is supposed to support the purification of the $_{GEO}$RNase Y.

The construct was made with the plasmid pPB179 (received from Dr. Patricia Bedrunka) which ensures expression *via* the T7-system. At the N-terminal is a 10xHIS tag, which is followed by a MISTIC and a TEV site (Fig. 3.8. A).

The expression was performed in TB-media overnight at 30°C, 150 rpm without the addition of IPTG in *E. coli* BL21 C41(DE3) expression strain (Zhang, Kuipers *et al*. 2015). The solubilization was carried out with Dodecyl-β-D-maltose (DDM) and a concentration of 0.01%. DDM was used with a CMC of (H2O) ~ 0.17 mM (0.0087%) (VanAken, Foxall-Van Aken *et al.* 1986) and a molecular weight of the micelle of 72 kDa (Strop and Brunger 2005).

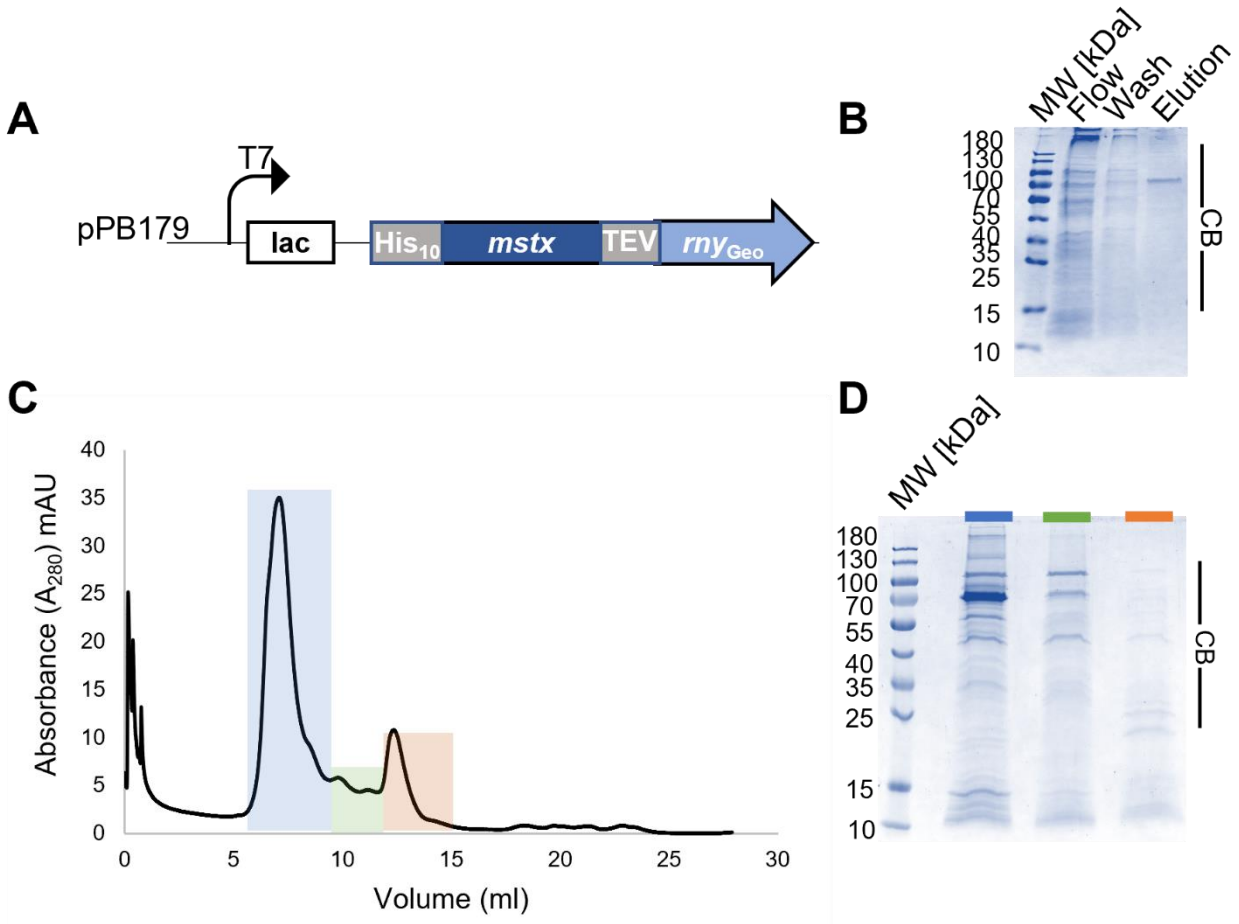

Figure 3.8: *Purification of full length His$_{10}$-MISTIC*-RNase Y *from G. thermodenitrificans via IMAC and SEC.* (B) SDS-PAGE and Coomassie staining (CB) of samples collected during Ni-NTA affinity purification of His$_{10}$-MISTIC-RNase Y from soluble *E. coli* BL21 (DE3, C41). (C) SDS-PAGE and Coomassie staining of peak fractions. A molecular weight of ~70 kDa was expected. (C) Size exclusion chromatography of His$_{10}$-MISTIC-RNase Y. The first peak

was coloured in blue, the second peak in green, and the third peak in orange. (D) Concentrated peak fractions of SEC.

Ni-NTA affinity purification showed minor amounts of the protein were detected in the flow through as well as in the wash. The elution clearly showed the protein with an expected molecular weight of approximately 70 kDa (Fig. 3.8. B). The expressed protein was determined by mass spectrometry (https://hessenbox.uni-marburg.de/getlink/fiQjxCQokQAAByLekZDEjK3x/). The concentrated elution was then separated by SEC to remove contaminants. Three distinct peaks appeared in the SEC (blue, green, orange).

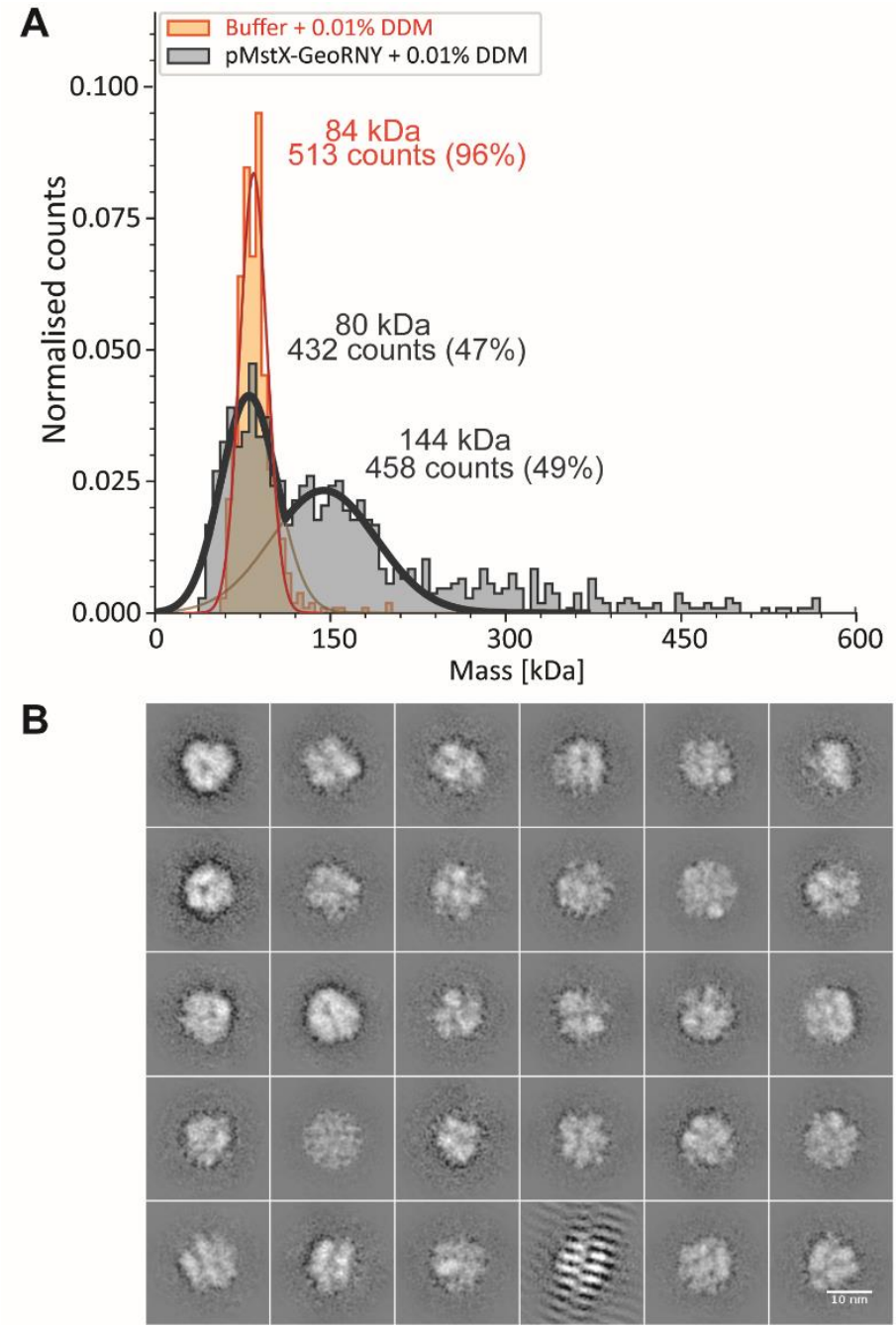

Figure 3.9: *Mass photometry and 2D class averages (electron microscopy) of His$_{10}$-MISTIC-*RNase Y. (A) Results of Mass photometry analysis of purified His$_{10}$-MISTIC-RNase Y

(peak 1). As a control (orange) the buffer was measured. (B) Representative single-particle class averages visualization by negative staining and EM of His_{10}-MISTIC-RNase Y. Scale bar 10 nm. The experiment was performed by Dr. Thomas Heimerl.

To determine the RNase Y, the peaks were concentrated and detected by SDS-PAGE. The first peak contained the most RNase Y and was therefore used for further analysis (Fig. 3.8. D).

Mass photometry was used to analyse the concentrated protein from peak 1. The protein was measured with a DDM concentration of 0.01%. The TRIS buffer used with the corresponding DDM concentration (0.01%) was measured as a reference. The reference showed a molecular weight of 84 kDa with a count of 96% (Fig. 3.9. 15A, orange).

The protein was visualized in two peaks. One peak showed a size of 80 kDa with a count of 47% and the second peak a size of 144 kDa with a count of 49% (Fig. 3.9.A, grey). The sizes correspond to the expected sizes for a monomer (~ 70 kDa) and dimer (~140 kDa) of the RNase Y.

Similarly, the protein from peak 1 was analyzed by negative staining to identify a possible structure of the protein. It shows a regular, circular shape with six subunits (Fig. 3.9. B).

4. General Discussion

4.1. *In vivo* analysis of the localization of Y-complex proteins

It was assumed that the Y-complex act as a specificity factor for the RNase Y (DeLoughery, Lalanne *et al*. 2018). It has been shown that the Y-complex, as well as the RNase Y, are involved in functions such as specific RNA maturation, various riboswitches, and biofilm formation (Hosoya, Asai *et al*. 2002; Tortosa, Albano *et al.* 2000).

In vitro experiments have shown that the Y-complex may exist in different formations. It was shown that the Y-complex not only appears to be present as a heterotrimer (1:1:1) but also that YmcA can be present as a homodimer and YmcA-YlbF as a heterodimer *in vitro* (Adusei-Danso, Khaja *et al.* 2019).

Using single molecule tracking (SMT), it could be shown that these different forms seem to exist *in vivo* as well. We have shown that the Y-complex is not only localized at the membrane but was also found in the cytosol (Article II, Fig. 6). Similarly, we showed that the Y-complex proteins had different populations with different diffusion constants (Article II, Fig. 4 and 7) and that they behaved differently during transcriptional arrest or loss of Y complex proteins.

Interestingly, using SMT YmcA and YlbF showed different behaviors in a deletion background. YmcA showed a loss of membrane association in the absence of YaaT (*ΔyaaT*), whereas the localization did not change significantly in the absence of YlbF (*ΔylbF*). The deletion of YlbF (*ΔylbF*) appeared to have less influence on the localization of YmcA than YaaT(*ΔyaaT*), but it seemed that YlbF and YaaT did affect the amount of expression (Article II, Fig. S7). The heatmaps of the confined tracks showed a higher appearance of YmcA under the deletions condition (*ΔylbF/ ΔyaaT*) compared to wild type cells (Article II, Fig. 6).

Remarkably, YlbF seemed to behave in the opposite way with regard to the loss of YmcA (*ΔymcA*). It seemed as if the deletion background (*ΔyaaT* and *ΔymcA*) lead to a lower expression of YlbF (Article II, Fig S7). Also, there might be a lower tendency to localize at the membrane compared to the wild type. To verify this observation, the expression level was determined under different conditions and visualized with a western blot (Article II, Fig. S7). Therefore the assumption that the deletions have different influences on the proteins and their expression levels was confirmed. The different localization of the

proteins was also clearly shown by SIM microscopy. Here, the YaaT was found to localize mostly at the membrane, consistent with fractionation and previous research (Hinrichs, Pozhydaieva *et al.* 2022; DeLoughery, Lalanne *et al.* 2018). The YlbF and YmcA were found to be cytosolic parts of the complex (Fig. 3.1.).

This different behaviour supported the hypothesis that different forms of the Y-complex are present *in vivo* and possibly perform different functions. Thus, it seems most likely that the heterotrimeric complex (1:1:1) is involved in mRNA degradation and maturation, which is why all three proteins showed similar behaviour during the transcriptional arrest (Article II, Fig. 6, S6).

The different localizations of the Y-complex proteins suggest that not all of the three proteins interact equally with membrane-anchored RNase Y *in vivo*. To verify this, colocalization strains were first generated (Fig. S2). It was found that colocalization from YaaT-mNeo and YmcA-mNeptune was not possible. A possible reason could be the fluorophores, which were C-terminally fused in both cases and could lead to an inhibition of complex formation. However, it was interesting to see that the organism (*B. subtilis*, BG214) solely rejected the plasmid of YmcA-mNeptune and at no time that of YaaT-mNeo. Since both used plasmids integrate to the original locus and thus only the fusions of the respective proteins would exist in the cell, it can be speculated that the YaaT is more necessary for the organism, since it seems that the YmcA can rather be dispensed with. In contrast to the colocalization between YaaT and YmcA, colocalization between YaaT and YlbF was limited. A fresh transformation allowed SIM microscopy and visualization of the colocalization, but the double fusion was not stable enough to detect the expression of both fusions by western blot (Fig. S1B) The fact that in the double fusion of YaaT to YlbF and YmcA, only the YaaT remained fused at the original locus and, correspondingly, the loss of YlbF or YmcA may indicate that YaaT gives the most important part of the three Y-complex proteins.

Four cysteines of YaaT with the motif Cys-X4-Cys-X31-Cys-X4-Cys bind directly to one of the two $[4Fe\text{-}4S]^{2+}$ clusters (Adusei-Danso, Khaja *et al*. 2019). One possible reason for the stability of YaaT relative to YlbF and YmcA could be that the YaaT carries solely one of the $[4Fe\text{-}4S]^{2+}$ clusters present in the Y-complex and these form an important role in the function of the Y-complex (Tanner, Carabetta *et al*. 2017; Adusei-Danso, Khaja *et al.* 2019). This may support the hypothesis that the processes catalyzed by Y-complex are dependent on the redox state of the cell (Tanner, Carabetta *et al.* 2017). Interestingly, mutations in the cysteine residues, have been shown to mimic a *yaaT* deletion in terms of mRNA maturation

phenotype (DeLoughery, Lalanne *et al*. 2018; Adusei-Danso, Khaja *et al.* 2019). Overall, these observations suggest that YaaT may play a greater role in the organism than YlbF and YmcA. This confirms the result that YaaT coordinates the clusters and is essential for the functionality of the complex (Adusei-Danso, Khaja *et al.* 2019).

In previous work, it was found that the protein amounts in the cell of YaaT, YlbF, and YmcA are not stoichiometric. YaaT is the most abundant, followed by YmcA and then YlbF (100:5:1) protein in the cell (Adusei-Danso, Khaja *et al.* 2019). Based on this knowledge, it can be expected that the analysis using BiFC would reflect this stoichiometry. In BiFC, the protein-protein interaction of the Y-complex proteins to the membrane-anchored RNase Y should be demonstrated. An expected result would be a different intensity of signal along the membrane concerning the known amount in the cell (100:5:1) (Adusei-Danso, Khaja *et al.* 2019). However, remarkably, no significant differences were found. All proteins showed a clear interaction with RNase Y at the membrane. But it should be noted that the RNase Y-YC fusion is ectopically expressed in this experiment and is not present at the native level, which may lead to overexpression artifacts (Fig. 3.2.).

This is confirmed by the idea that the individual proteins have additional functions independent of the Y-complex (Dubnau, Carabetta *et al*. 2016; DeLoughery, Lalanne *et al.* 2018). As it would be expected that in a three-protein complex, equal amounts of the proteins would localize at the membrane and interact with the RNase Y. However, we were able to show by SMT and also SIM that the three proteins showed up differently at the membrane and thus further functions can be assumed to be independent of the membrane, and thus of the membrane protein RNase Y.

In order to understand the role of the individual proteins of the Y-complex, it would be helpful to solve the structure of the Y-complex. Since this was not successful so far, a prediction was carried out with the help of AlphaFold v 2.0 (Jumper, Evans *et al.* 2021). In this case, the structural composition of the complex could indicate the different localization in the cell *in vivo* (Fig. 3.1).

The AlphaFold prediction, in addition to the known structure of YlbF-YmcA being present as a dimer (Adusei-Danso, Khaja *et al.* 2019), it was shown that the YaaT is in direct contact with YlbF, and YmcA is present in the complex only through the YlbF (Fig S5 C). Prediction showed clear hydrogen bonding in the residues of arginine 144 of YaaT to the residue of tyrosine 2 of YlbF. Further connection could not be determined through AlphaFold. Interestingly, no direct connections to YmcA were found. The contact between YlbF and

YmcA appeared to be very strong since dimerization occurs through intermolecular contacts between helices forming an antiparallel helix core bundle (Adusei-Danso, Khaja *et al*. 2019).

This prediction supports the *in vivo* data because such low binding between YaaT and the YlbF/ YmcA reflects the different behaviors of each protein and makes different forms possible. The low linkage of YaaT within the complex explains the results of the fractionation, as well as the microscopic observations. The fractionation showed equally clear that there appeared to be only direct binding from the YaaT to RNase Y, as only the YaaT was present in the membrane fraction. YlbF and YmcA did not show presence in the membrane fraction (Article II, Fig. 8). This also indicates no direct binding to RNase Y, but also a low binding to YaaT (Hinrichs, Pozhydaieva *et al*. 2022).

Taken together, all data showed that different forms of the Y-complex, with possibly different functions, are present in the cell. It seems that in addition to the membrane-associated functions together with RNase Y, other functions are present in the cytosol for which there are different conformations of the complex. It is conceivable that the Y complex could act as an adapter between nucleoid-associated mRNA synthesis, membrane-associated processing, and degradation. Therefore, different cytosolic forms of the complex would be conceivable (Fig. 4.1.).

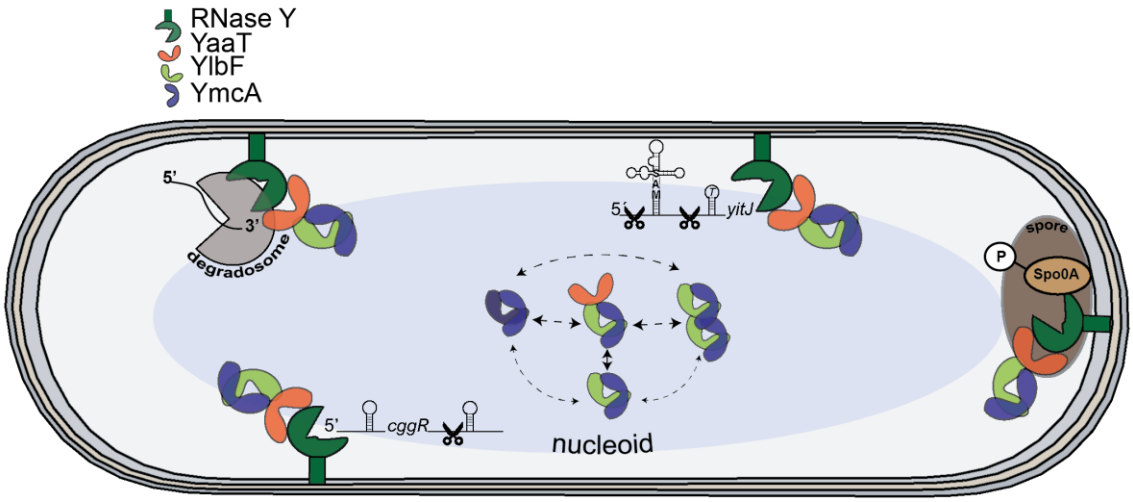

Figure 4.1: *Model for possible forms of the Y-complex in vivo.*

4.2. RNase Y showed change in the dynamic after transcriptional arrest

The Y-complex is described as a direct interaction partner to the membrane-anchored endoribonuclease RNase Y (Tortosa, Albano *et al*. 2000; DeLoughery, Dengler *et al.* 2016; DeLoughery, Lalanne *et al.* 2018). The 5'endoribunuclease is involved in the degradation and maturation of mRNA, as well as the initiator of the RNA degradosome, which associates the degradosome to the membrane through its transmembrane domain (Trinquier, Durand *et al*. 2020; Durand and Condon 2018).

We published that our RNase Y-mVenus fusion, which is expressed from the original locus, was cytosolic to a large amount *in vivo* (Article I, Fig.3.) as well as *in vitro* (Fig. S4 A) data.

We reviewed this finding because it is in contrast to the known data in which microscopic analyses showed that RNase Y localized solely to the membrane (Hamouche, Billaudeau *et al*. 2020). Similarly, the membrane domain in the structure of RNase Y indicated that membrane binding was most likely (Shahbabian, Jamalli *et al.* 2009).

For this study, we obtained a RNase Y-sfGFP fusion strain (SSB2048, Hamouche, Billaudeau *et al.* 2020) characterized by its cloning with constructed by markerless allelic replacement using the thermoexcisable plasmid pMAD (Arnaud, Chastanet *et al.* 2004). In contrast to the single crossover method that we used in the study before (Article I, Construction of strain). There, we used the pSG1164, which integrates not only the fluorophore but also the entire vector backbone at the original locus (Lewis and Marston 1999) (Article I, Construction of strain).

We were able to show using single molecule tracking, that, in addition to the general present cytosolic part, the RNase Y-mVenus became more dynamic and lost its membrane association after the addition of rifampicin, therefore during transcriptional arrest (Article I, Fig 2, 3). In order to investigate the membrane integration of both fusions, fractionation was performed. Interestingly the western blot against the fluorophore(*α-gfp-tag*-serum) showed that about one-third (not quantified) of the mVenus fusion was located in the cytosolic fraction, whereas the sfGFP fusion was almost solely located in the membrane fraction (Fig. S4 A). Both strains showed a similar running behaviour of more than 80 kDa (87 kDa expected). This difference in behavior can be explained by the different integration methods.

The western blot with a specific antibody against RNase Y (*α-ymdA*) showed a large deviation (Fig. S4 B). This showed that the cytosolic part of the mVenus fusion was not detectable and the membrane fraction showed a lower running behaviour. The sfGFP fusion showed localization solely in the membrane, which is consistent with previous data for the fusion (Hamouche, Billaudeau *et al*. 2020). Interestingly, the wild type showed the same bands, whereas the deletion control had no bands. Only one band due to nonspecific binding (~53 kDa) was equally present in all samples, except in the membrane fraction of sfGFP, for which no explanation has yet been found.

This experiment suggests that the fusion strain at the original locus contains tagged (87 kDa), as well as untagged RNase Y (58.7 kDa), and that the mVenus fused RNase Y was present at such a low ratio that it was not detectable with the specific antibody (expected at 87 kDa). Against this thesis argues that the antibody against the fluorophore showed no significant difference in the amount of the protein. The cytosolic behaviour of RNase Y-mVenus may also argue for a N-terminally truncated form of RNase Y. Since a truncation *in vivo* did not lead to major problems for the organism (Lehnik-Habrink, Newman *et al.* 2011). It also suggests that there was a full-length fusion of RNase Y-mVenus, as the epifluorescence data showed membrane localization in addition to cytosolic (Article I, Fig. S1).

The fusion RNase Y-sfGFP was shown not only in the western blot of fractionation solely membrane-bound but also in epifluorescence microscopy, as well as SIM showed a clear localization along the membrane (Fig. 3.4.). Comparing the dynamics of both fusions by SMT, we saw parallels. During the transcription arrest, the RNase Y-sfGFP also displayed higher dynamics and a significant increase in the size of the mobile fraction in comparison to the RNase Y-mVenus fusion. It was also remarkable to see that the static fraction doubles its diffusion constant (from 0.03 to 0.06 $\mu m^2\ s^{-1}$) (Fig. 3.5. B, C). However, in contrast to RNase Y-mVenus, for RNase Y-sfGFP, there was no loss of membrane binding in the heat maps of the confined tracks (Fig. 3.5. A). Comparing the two fusions (RNase Y-sfGFP /RNase Y-mV), fusion by single crossover to the original locus appeared to have resulted in incorrect RNase Y-mVenus. Possibly, the single crossover method, and thus the integration of a vector backbone to the original locus, in this case, lead to N-terminal truncated versions of RNase Y, which would have an explanation for the cytosolic fractions.

The SMT data obtained are consistent with published data for the RNase Y-sfGFP strain (SSB2048) (Hamouche, Billaudeau *et al*. 2020). They found that after the addition of

rifampicin, the static foci along the membrane decreased and the absolute amount of RNase Y increased by around 40%. Overall, they were able to show that RNase Y is very dynamic in the membrane and that this is substrate-specific (RNA), but also interaction partner (Y-complex) dependent. Similarly, they postulated that higher forms of RNase Y ("very static foci with high intensity") may be an inactive form of RNase Y and the constrained mobile form may be an active, substrate-interacting form (Hamouche, Billaudeau *et al*. 2020).

Considering all the results, it can be assumed that the RNase Y-mVenus strain has several forms of RNase Y. A fused form in full-length, a N-terminal truncated form, and an untagged form. However, the question remains whether the N-terminal truncated form is functional, as it has been shown that RNase Y is active as a dimer and both monomeric and higher forms are inactive forms of the RNase Y (Hamouche, Billaudeau *et al.* 2020; Shahbabian, Jamalli *et al*. 2009).

Whether the possible truncations influence the functionality of RNase Y can be explained by the prediction of RNase Y (dimer) (Fig. 3.6.). If the first N-terminal 25 amino acids (Fig. 3.6., coulored in turquoise) are truncated, a loss of function cannot be assumed, since it has been shown that membrane anchoring is not essential (Lehnik-Habrink, Newman *et al.* 2011). If, on the other hand, there is a truncation by the entire coiled-coil domain (30-150 amino acids), a loss of function was assumed, because the domain is supposable for a dimer or multimer of RNase Y.

4.3. The membrane-anchored endonuclease RNase Y

Previously, it was not possible to solve the structure of a full-length RNase Y from *Bacillus subtilis*. To get a structure for the full length of RNase Y and to analyze the influence of the transmembrane domain on the functionality, also to possible interaction partners or binding to the substrate, in this work it was the aim to purify the RNase Y and solve the structure *via* negative staining (EM) and cryo-EM.

Membrane proteins position themselves through hydrophobic interactions between the hydrocarbon chains of lipids and the hydrophobic domains of proteins. Detergents can interrupt these interactions. They are classified into "mild" and "hard" categories depending on the denaturing effect on proteins. Mild detergents are known to be uncharged and have larger head groups and longer hydrophobic tails. Also, non-ionic detergents are known to

induce not any change in the secondary structure of proteins (Abeyrathne and Grigorieff 2017; Yang, Wang *et al*. 2014). LMNG and DDM are non-ionic detergents (Seddon, Curnow *et al*. 2004).

The purification of membrane proteins is quite difficult because without detergents they are not soluble (Lin and Guidotti 2009). To get a soluble RNase Y the purification was done with LMNG. The workflow was adapted to the previous work of Weiland and Altegoer 2021. The RNase Y from *B. subtilis* was fused to a C-terminal His_6-tag and was expressed under a T7-system in BL21 C41 (DE3) *E. coli* cells (Fig. 3.7.). In SDS-PAGE, as well as in western blot (*α-His*-serum), the expression of RNase Y (~ 60 kDa) could be visualized as expected. Mass spectrometry was performed to ensure that the largest amount was RNase Y, which was confirmed (https://hessenbox.uni-marburg.de/getlink/fiQjxCQokQAAByLekZDEjK3x/). However, the concentrated protein, which was eluated by Ni-NTA-chromatography, showed high contamination (Fig. 3.7. B). Size exclusion chromatography (SEC) was performed to separate the protein of interest from the contaminants (SuperdexTM 200 increase 10/300 GL). The SDS page of the two peaks showed that RNase Y was present in the first peak, which was therefore used for the study by mass photometry (Fig. 3.7. C). Mass photometry should be used to determine whether RNase Y was present as an active form (dimer) or an inactive form (monomer) (Hamouche, Billaudeau *et al.* 2020; Shahbabian, Jamalli *et al.* 2009).

The data showed that it is exclusively the monomer of RNase Y because only a peak with a size of about 101 kDa could be shown (Fig. 3.7. E) The fact that this was a monomer can be based on the measurement of empty micelles (buffer + 0.0005% LMNG) since previous work has shown that LMNG micelles are measured at a size of about 60 kDa. Together with the RNase Y, which had a size of about 60 kDa, a monomer can be assumed (Breyton, Javed *et al.* 2019). Also showed that only a very small amount of RNase Y was present after separation by SEC (data not shown). The fact of low yield and the sole presence of the monomeric form of RNase Y led to the conclusion to continue the purification from the homologous thermostable organism *G. thermodenitrificans* in order to minimize problems with the following analytical methods (Schuhmacher, Rossmann *et al.* 2015). Likewise, alternative detergency should be considered, since a reduced dynamic of proteins was described due to the strong binding of LMNG to the protein, to exclude a negative effect on RNase Y (Breyton, Javed *et al*. 2019). Furthermore, a so-called MISTIC membrane anchor was used for the new construct, which was expected to

have a positive, stabilizing effect on the purification of membrane proteins, and was expected to help achieve a stable dimer of RNase Y and thus a functional RNase Y (Frotscher, Krainer *et al.* 2018). The alternative construct consists of a N-terminal His_{10} tag, the MISTIC, and a TEV cleavage site to remove the tags from the full-length RNase Y from *G. thermodenitrificans* for further experiments (Dougherty, Cary *et al*. 1989) (Fig. 3.8. A). The expression was also performed in BL21 C41 (DE3) *E. coli* cells without the addition of IPTG and the purification was carried out with n-dodecyl-β-D-maltoside (DDM) (Knol, Sjollema *et al.* 1998).

In SDS PAGE, the expression, as well as the elution of MISTIC-RNase Y could be verified. The assumption was supported by mass spectrometry (https://hessenbox.uni-marburg.de/getlink/fiQjxCQokQAAByLekZDEjK3x/) (Fig. 3.8. B). In order to separate contaminants, a SEC-analyses was performed with the addition of 0.01% DDM in the buffer. This resulted in three main peaks. The first and largest peak showed RNase Y as well as small amounts of contaminants or degradation products which can be seen in the SDS-PAGE of the concentrated protein peaks (Fig. 3.8. C, D). Since the following mass spectrometry analysis takes place under a dilution of 20-40-fold the contamination can be ignored as it was marginal concerning RNase Y. The protein quantity determination resulted in a total amount of 1 ml with a concentration of 65,3 µM.

Interestingly, mass photometry revealed a possible monomeric 80 kDa as well as a dimeric form of the MISTIC-RNase Y 144 kDa in micelles (Fig. 3.9. A). The buffer with empty micelles was measured as a reference. The measurement within the micelles corresponds to the experiments shown (Olerinyova, Sonn-Segev *et al.* 2021). Thus, by using RNase Y from *G. thermodenitrificans* with the MISTIC tag and DDM, a structurally functional RNase Y could be purified which, at the time of measurement, formed a monomer to dimer ratio of rounded 50/50 (Fig. 3.9. A).

As a preliminary experiment, negative staining of RNase Y was prepared (Dr. Thomas Heimerl, Philipps-Universität-Marburg). The negative staining of MISTIC-RNase Y showed a monodisperse distribution in the representative single-particle class averages (Fig. 3.9. B). The results of negative staining did not make clear whether RNase Y is in micelles or it is the well-known image graining from empty micelles (Ohi, Li *et al.* 2004). To improve this, attention should be focused on the fact that DDM has a relatively large micelle size (~ 60 kDa) and membrane proteins (<100 kDa) can be covered in their hydrophobic region.

So, minimizing the micelle size or removing the micelles with for example Bio-beads would be helpful (Rigaud, Mosser *et al*. 1997; Abeyrathne and Grigorieff 2017).

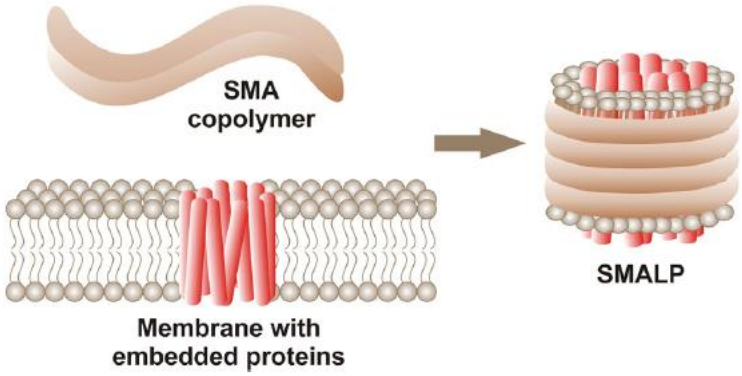

Figure 4.2: *Schematic illustration of SMALP*. SMALP consists of the copolymer (SMA, brown) which surrounds the native membrane (grey) surrounding the membrane protein (red) (Prabudiansyah, Kusters *et al*. 2015).

Another alternative could be the use of lipid-nano discs like SMALP. Lipid nano discs offer the advantage of providing cmc independent stability and a bilayer-like environment (Parmar, Rawson *et al*. 2018). Styrene-maleic acid lipid particles (SMALP) provide the advantage of incorporating the native membrane into the system, thus creating optimal conditions for the membrane protein. The scaffold protein (SMA) determines the size of the alternative membrane environment and is therefore individually adaptable (Fig. 4.2.) (Prabudiansyah, Kusters *et al.* 2015; Knowles, Finka *et al.* 2009).

Overall, the preliminary results showed that the purification of RNase Y in the active form (dimer) seems to be possible. In addition to the use of the homolog from *G. thermodenitrificans*, further optimizations should be made, such as the use of nanodiscs. In this work, important basic principles for the purification of the full-length RNase Y were demonstrated.

4.4. Four enzymes with RNase activity are at the replication forks in *Bacillus subtilis*

In eukaryotic cells, the two ribonucleases RNase H1 and RNase H2 are described to be responsible for processing RNA/DNA hybrids (Cartalas, Coudray *et al*. 2022). In contrast in prokaryotes exhibit three RNases, there are RNase HI, RNase HII, and RNase HIII. In *E. coli*, the presence of RNase HI and HII is described, whereas in *B. subtilis* RNase HII and HIII are present (Frank, Braunshofer-Reiter *et al*. 1998).

Previous *in vitro* work has been shown that, in addition to RNase HIII, the DNA polymerase PolA with its exonuclease function, as well as ExoR, are involved in the removal of Okazaki fragments during DNA replication in *B. subtilis*. Similarly, RNase HII was shown to be responsible for the removal of individual rNMPs that are incorporated into DNA by DNA polymerase during DNA replication (Randall, Nye *et al*. 2019).

SMT analyses were able to show, that four enzymes with RNase activity are involved at the DNA replication in *B. subtilis* (https://hessenbox.uni-marburg.de/getlink/fiQjxCQokQAAByLekZDEjK3x/).

As previous *in vitro* studies showed (Randall, Nye *et al*. 2019), RNase HIII was closely associated with DNA polymerase. Thus, RNase HIII showed a higher frequency at the replication fork (DnaX-CFP), in comparison with all other tested proteins (ExoR, PolA, RNase HII) after induction of DNA damage by UV. Whereas PolA was the only protein to showed an increase in static population after UV damage. This suggests that the proteins (RNase HIII and PolA) are involved in the removal and repair of cyclobutane-thymine dimers produced by UV damage (Selby & Sancar, 2006).

However, ExoR, PolA, RNase HII, and RNase HIII were clearly shown to localize at the replication fork, like the helicase DnaC, which served as a reference (Article III, Fig 3, 4). It was also clearly shown that RNase HIII is the most diffusive RNase of the four shown RNases. The in *vivo data* thus confirmed the assumptions shown *in vitro* (Schroeder, Randall *et al*. 2017; Randall, Nye *et al*. 2019) that RNase HIII, PolA, ExoR, and also RNase HII are involved in replication in *B. subtilis*.

So with the *in vivo* analyses, we come up with a current model (Article III, Fig 7). During DNA replication, the leading strand (5' to 3') is continuously replicated. On the lagging strand (3' to 5'), RNA primers are required on which Okazaki fragments are generated. To remove the RNA/DNA hybrids and thus promote Okazaki fragment maturation, four main enzymes with RNase activity are involved. The ribonuclease RNase HIII works in support of the DNA polymerase PolA and the magnesium-dependent 5'->3' exonuclease ExoR and removes this RNA. Likewise, RNase HII removes individual ribonucleoside mono-phosphates (rNMPs) that were incorporated during DNA replication. In response to repair of UV DNA damage and involvement of repair of double-strand breaks, incorporation of single or multiple rNMPs, PolA as well as RNase HIII appear to be present and otherwise not ExoR (Hernandez-Tamayo, Oviedo-Bocanegra *et al.* 2019).

5. General Material and Methods

5.1 Material and methods

5.1.1. Kits and chemicals

In this work the chemicals were purchased from AppliChem GmbH (Darmstadt, Germany), Carl Roth GmbH & Co. KG (Karlsruhe, Germany), Sigma-Aldrich Chemie GmbH/ Merck KGaA (Taufkirchen/ Darmstadt, Germany) and GE HealthCare GmbH (Frankfurt am Main, Germany). Enzymes, DNA polymerases, and reagents for Gibson assembly (molecular cloning), also DNA and protein standards were acquired by New England Biolabs GmbH (Frankfurt am Main, Germany). The plasmid extraction was performed with the Monarch Plasmid Miniprep kit by New England Biolabs GmbH (Frankfurt am Main, Germany) and the extraction of genomic DNA with innuPREP DNA extraction kit by Analytic Jena GmbH (Jena, Germany). Kits for PCR purification and gel extraction were supplied by Qiagen GmbH (Hilden, Germany).

5.1.2. Antibiotics/ supplements

Table S1 Antibiotics and supplements that were used in this study

Name	**Final concentration**
Ampicillin	100 µg/ ml
Chloramphenicol	5 µg/ ml
Kanamycin	50 µg/ ml
Spectinomycin	100 µg/ ml
D-Xylose	up to 0.5% (w/v)
IPTG	0.25 mM
Rifampicin	25µg/ ml

5.1.3. Vectors

Plasmids used in this work are listed in the following table:

Table S2

Name	Application	Resistance	Backbone
pSG1164-mVenus	c-term integration original locus	Ampicillin/ Chloramphenicol	pSG1164-YFP
pSG1164-mNeo	c-term integration original locus	Ampicillin/ Chloramphenicol	pSG1164-YFP
pSG1164-mNeptune	c-term integration original locus	Ampicillin/ Chloramphenicol	pSG1164-YFP
pDR111-YC	c-term integration *amy*-site	Ampicillin/ Spectinomycin	pDR111
pSG1164-YN	c-term integration original locus	Ampicillin/ Chloramphenicol	pSG1164-YFP
pAL172	overexpression	Kanamycin	pET24d (gift from Dr. Patricia Bedrunka)
pPB179	overexpression	Ampicillin	pET24d (gift from Dr. Patricia Bedrunka)

5.1.4. List of Oligonucleotides and strains

Table S3 Oligonucleotides used in this study

Primer	Sequence 5´→ 3´
YaaT-mNeo fw	CCTAGGATGGGTACCGAATTCCGTTTGATCGCAATAAAGT
YaaT-mNeo rev	AGGCCAGATAGGCCGGGCCCATCTGTGGTTTGTGCGG
YaaT-mNeo Integration fw	AAGAAAGTGATTGAGCATGG
YlbF-mNeo fw	CTAGGATGGGTACCGAATTCATGTATGCGACGATGGAATC
YlbF-mNeo rev	AGGCCAGATAGGCCGGGCCCGGACACTTTACATCCGC
YlbF-mNeo Integration fw	CATGCGGTCATAAGGTTTTG
YmcA-mNeo fw	CTAGGATGGGTACCGAATTCGAAAATCCAGCAAGCGAAAA

YmcA-mNeo rev	AGGCCAGATAGGCCGGGCCCGAGAGAACAGCTGTTAT
YmcA-mNeo Integration fw	AAGGAAGCCATCGGCAAAAT
mNeo Integration reverse	CTTGTACAGCTCGTCCATGC
B.S.RNase Y_fw	TTAAGGTCTCCCATGGGCACCCCAATTATGATGGTTCTC
PB179fw_GeoRNY	TTAAGGTCTCCCATGGGCGGTTCGATCATCATCTC
PB179rev_GeoRNY	TTAAGGTCTCCTCGAGTTATTTCGCATATTCGACCGC

Table S4 Strains used in this study

Name	**strain**	**organism**	**reference**
PG4190	BiFC_pSG1164 YN (aa 1-154 mVenus)	*E. coli* (DH5α)	this work
PG4191	BiFC_pDR111_YC (aa 155-end mVenus)	*E. coli* (DH5α)	This work
PG4339	*yaaT*-mNeonGreen (cat)	*B.subtilis* BG214	This work
PG4340	*ylbF*-mNeonGreen (cat)	*B. subtilis* BG214	This work
PG4341	*ymcA*-mNeonGreen (cat)	*B. subtilis* BG214	This work
PG4342	*ylbF*-mNeptune (cat)	*B. subtilis* BG214	This work
PG4343	*ymcA*-mNeptune (cat)	*B. subtilis* BG214	This work
PG4344	*yaaT*-mNeonGreen (tet) *ylbF*-mNeptune (cat)	*B. subtilis* BG214	This work
PG4063	*rny*-sfGFP	*B. subtilis* BG214	SSB2048 (*rny*-sfGFP), gift from Harald Putzer
PG4345	*yaaT*-YC_pSG1164_BiFC	*B. subtilis* BG214	This work
PG4346	*ylbF*-YC_pSG1164_BiFC	*B. subtilis* BG214	This work

PG4347	*ymcA*-YC_pSG1164_BiFC	*B. subtilis* BG214	This work
PG4348	*rnhC*-YC_pSG1164_BiFC	*B. subtilis* BG214	This work
PG4349	*rny*-YN_pSG1164_BiFC	*B. subtilis* BG214	This work
PG4350	P_{IPTG}-$_{B.s.}$*rny-His*$_6$	*E. coli* (DH5α)	This work
PG4351	P_{IPTG}-*mstX-His*$_{10}$-$_{GEO}$*rny*	*E. coli* (DH5α)	This work

5.2. Microbiological and cell biological methods

5.2.1. Isolation of chromosomal DNA

In order to isolate genomic DNA (gDNA) or plasmid DNA for polymerase chain reactions, transformations, sequencing, or similar, it must be possible to separate these from the other cell components. For this purpose, the bacterial cells are treated according to the manufacturer's instructions for the kit used (InnuPREP Bacteria DNA Kit from analytikjena (Analytic Jena GmbH (Jena, Germany)) for gDNA and GenElute HP Plasmid Miniprep Kit from sigma for plasmid DNA) (Sigma-Aldrich Chemie GmbH/ Merck KGaA (Taufkirchen/ Darmstadt, Germany)). First, the bacterial cell wall is lysed by lysozyme, which cleaves the β-1,4-glycosidic bond between N-acetylmuramic acid and N-acetylglucosamic acid residues in the peptidoglycan cell wall of bacteria by hydrolysis. In addition, RNA present is degraded by the addition of RNAse, and proteins present are degraded by the addition of proteinase K. The undissolved cell components are then separated and the DNA is applied to a filter column using a "Binding Solution". There, further washing steps are carried out, after which the DNA is eluted in the final step by adding an elution buffer. Deviating from the manufacturer's instructions, RNase was added to the lysis step and eluted in the elution step with an elution volume of 30 - 40 µL.

5.2.2. Polymerase chain reaction (PCR)

The polymerase chain reaction (PCR) is a method that allows DNA segments to be specifically amplified *in vitro*. The PCR process consists of several cycles that take place in a thermal cycler. Each cycle consists of three different steps. In the first step, the double-stranded DNA is denatured at 98°C. This results in the separation of the hydrogen bonds between the bases. The second step involves hybridization of the oligonucleotides, which serve as start sequences for the DNA polymerase and delimit the region to be amplified. Subsequently, the temperature is set to a determined level for 30 s. The temperature is set to the desired level. The temperature is determined by the length and GC content and is usually between 55°C - 65°C. In step three, elongation takes place, during which the DNA is amplified by the polymerases. The elongation time is adjusted via the length of the fragment (1000 bp/1 min).

Step	Temperature [°C]	Time [Minute]	Repeats
Initial denaturation	98	5	1
Denaturation	98	0,5	
Annealing	x_1	0,5	30x
Extension	72	x_2	
Final extention	72	8	1
Hold	4	∞	-

X_1: Temperature is determined by the length and GC content of the fragments. X_2 The duration is determined by the length 1000bp/ min.

5.2.3. Growth conditions

To culture the cells of *E. coli* and *B. subtilis* in liquid medium, the desired cells were taken up in LB medium. The LB medium was mixed with the antibiotic required for the appropriate selection (Tab. S1). Incubation of the liquid culture was then performed at 200rpm and a temperature of 37°C for *E. coli* and 30°C for *B. subtilis* until the desired OD was reached. Cultivation on growth plates was also performed at a temperature of 37°C/ 30°C. In this process, Petri dishes were cast with LB agar mixture in which the desired antibiotic was added.

5.2.4. Strain construction

General strain construction

All of used vectors were produced in *Escherichia coli* DH5*α* (Tab. S2). For cloning the Gibson assembly by New England Biolabs GmbH (Frankfurt am Main, Germany) was used. For the cloning at the original locus, the pSG1164 plasmids (ECE155, Lewis P. J. and A. L. Marston, 1999) was used. The last 500 base pairs from the gene of interest were amplified without the stop codon with a polymerase chain reaction (PCR) under usage of restriction sites *Apa*I and *Eco*RI, which were included in the primer (Tab. S3) and fused at the linker with a length of twelve amino acid to the fluorophore. The pSG1164 integrated at the original locus under the native promotor. The correct integration was verified with full length primer (Table S3).

Strain construction bimolecular fluorescence complementation (BiFC)

For cloning the BiFC, N-terminal the first 154 amino acids of the mVenus were used (pSG1164-YN). The c-terminal fusion was generated with the 2nd half of the fluorophore (pDR111-YC). In both cases, an 8 amino acids long linker was used.

Strain construction overexpression $_{GEO}$RNase Y/$_{B.S.}$RNase Y

For the production of the overexpression strains, the sequences from *Bacillus subtilis* as well as *Geobacillus thermodenitrificans* were used in full gene length (www.ncbi.nlm.nih.gov.). All strains used are listed in Table S4.

5.2.5. Preparation of chemical competent cells

To ensure chemical competence for the desired transformation into *E. coli* DH5*α* cells and the resulting uptake of a plasmid, *E. coli* DH5α cells were cultured in 400 mL LB media, at a temperature of 37°C. The aim of incubation was to achieve exponential growth (OD_{600} 0.6 - 0.8). After entering the exponential phase, cells were incubated on ice for 30 minutes. This was followed by incubation at 4°C, 5000rpm for 10 minutes. The resulting supernatant was discarded and the cell pellet was resuspended in 5 mL of competent buffer (0.1 M CaCl2, 15% Glycerol). For storage, cells were aliquoted into 1.5 mL Eppendorf tubes (150 µL each). Competent cells were snap frozen using liquid nitrogen and stored in a -80°C cabinet.

5.2.6. Transformation of plasmid DNA into chemically competent *E. coli* DH5*α* cells

For plasmid DNA transformation, 100 µL of competent *E. coli* DH5α cells were thawed on ice. At a reach of 4°C, 2 µL of plasmid DNA was then added. The batch was then incubated on ice for 20 minutes. This was followed by heat shock at 42°C for 2 minutes in a heating block. This procedure increases the efficiency of the transformation. The mixture was incubated again for 10 minutes on ice. Then 1 mL of LB medium was added and incubated for one hour at 37°C and 200rpm. The heat leads to the opening of the pores in the membrane and thus a passage to the inside is created for the DNA. After incubation, a smear was made on LB+Amp. Plates with a 10% concentration, as well as a 90% concentration (achieved by centrifugation). The plates were incubated overnight at 37°C.

5.2.7. 3D structure illumination microscopy (SIM)

High resolution microscopy was performed with the ZEISS ELYRA microscope PS.1 system. Using the wavelength 488 nm and a 10% laser intensity and a gain of 50 with 20 ms. The images(z-stacks) were taken from 3 angles. The setup also consists of an EMCCD camera (ANDOR Solis EMCCD). The reconstructions were processed by the ZEISS Zen-Black. The assembly shown was done with the help of Fiji (Schindelin, Arganda-Carreras *et al*. 2012) The measurement was made by Maximilian Greger.

5.3. Biochemical methods

5.3.1. Protein purification (Ni-NTA)

Protein purification was performed according to a modification of known protocols. (Weiland and Altegoer 2021) For protein purification, the *E. coli* BL21 C41 (DE3) with the plasmid pAL172_RNase Y-His^6 and pPB179_His_{10}-MISTIC-$_{GEO}$RNase Y were used and cultured to an OD_{600} of 0.4 (37°C, 200 rpm). Expression was then induced with 0.25 mM IPTG (the expression of pPB179_His_{10}-MISTIC-$_{GEO}$RNase Y was without adding IPTG and 30°C). Cultivation was carried out overnight at 20°C and TB medium was used for cultivation.

Terrific Broth (TB)

900 ml TB medium	tryptone	1.20%	
	yeast extract	2.40%	
	glycerol	0.50%	
100 ml 10x TB salts		89 mM	0.17 M KH2PO4
			0.72 M K2HPO4

After harvesting the pellets, they were taken up in W buffer (buffers are described in table below) and disrupted by microfluidizer. This is followed by low spin centrifugation at 8000 g for 25 minutes. The resulting supernatant are transferred into 26.3 mL, Polycarbonate Bottle (Quick seal, Beckman) and Type 70 Ti Fixed-Angle Titanium Rotor is then centrifuged by ultracentrifuge (Beckman Optima XE) at 115,000 g for 1 hour in Type 70 Ti Fixed-Angle Titanium Rotor. For solubilization, the resulting pellet is taken up in W buffer with 1% detergent (LMNG for pAL172_RNase Y-His^6 and DDM for pPB179_His_{10}-MISTIC-$_{GEO}$RNase Y) and an incubation under rotation for 3h at 4°C. The solubilized protein is centrifuged again by ultracentrifuge (115,000 g/ 1 h). The resulting supernatant is then mixed with Ni-NTA (HisPur™ Ni-NTA Resin, Thermo Scientific™) beats and incubated at 4°C overnight. The purification was performed using empty gravity flow columns without applying pressure. Three washing steps and elution steps were used.

Buffer W (Lyse)	
NaCl	500mM
Tris pH 8	50mM
Glycerol	5%
Imidazole	40mM
$MgCl_2$	20 mM
Elution Buffer	
NaCl	500mM
Tris pH 8	50mM
Glycerol	5%
Imidazole	500mM
Detergent (optional)	0.01%

5.3.2. Size exclusion chromatography (SEC)

The size exlucion chromatography was performed on the ÄKTA pure purification system with a SuperdexTM 200 increase 10/300 GL column and a fraction collector F9-C. The SEC buffer used had a pH value of 8. The protein from the elution (Ni-NTA) was concentrated at 1 ml (using Amicon, Millipore, 30 kDa) and injected into a 500µl loop. The collected fractions were collected and detected by SDS-PAGE. The protein was then concentrated. Protein concentrations were determined using spectrophotometer (NanoDrop Lite, Thermo Fisher Scientific) or Pierce™ BCA Protein Assay Kit (Thermo Scientific™).

SEC Buffer	
NaCl	500mM
Tris pH 8	50mM
Glycerol	5%
Detergent (optional)	0.01%

5.3.3. Mass photometry

Mass photometry was described after (Young, Hundt *et al.* 2018). They explain that the amount of scattered light when a molecule touches the surface of a glass slide is directly linearly correlated with the molecular weight of the molecule. Analysis was performed using DiscoverMP software (Refeyn, v 2.2.0) according to the manufacturer's protocol. For this, data were acquired with a OneMP mass photometer (Refeyn, Oxford, UK) using AcquireMP software (Refeyn, v 2.3.0) for detection. Data were acquired for 60 s at 100 frames per second using AcquireMP.

The measurement was taken in 20µl volume. Reusable silicone gasket (CultureWellTM, CW-50R-1.0, 50-3mm diameter x 1 mm depth) were set up on a cleaned microscopic cover slip (1.5 H, 24 x 60 mm, Carl Roth) and mounted on the stage of the mass photometer using immersion oil (IMMOIL-F30CC, Olympus). The gasket was filled with 19 µl buffer (PBS or 20 mM Tris, 200 mM NaCl pH 7.5) to focus the instrument. Then, 1 µl of prediluted protein solution (1 µM) was added to the buffer droplet and mixed thoroughly. The dilution was between 1:10 and 1:20. The measurement was made by Franziska Sendker (AG Hochberg, MPI Marburg).

5.4. Software

To get DNA and amino acid sequences of *Bacillus subtilis*, SubtiWiki was used (http://subtiwiki.uni-goettingen.de/). The SnapGene® Viewer 6.0.2. was used to create primers and to modify the plasmids *in silico* (https://www.snapgene.com/snapgene-viewer). Plasmid DNA sequences were obtained from addgene (http://www.addgene.org/) or the Bacillus genetic stock center (BGSC) (https://bgsc.org/). The structure and topologies of the Protein domains were analysed using SMART (http://www.smart.embl-heidelberg.de), NCBI (http://www.ncbi.nlm.gov), UniProt (http://www.uniprot.org/) and Pfam (http://www.sanger.ac.uk). The protein predictions were generated AlphaFold v 2.0 (Jumper, Evans *et al.* 2021). The viewer ChimeraX (Pettersen, Goddard *et al.* 2021) was used to perform the application of Alphafold v 2.0 via ColabFold (Mirdita, Schütze *et al*. 2022). The data of protein purification obtained during SEC were analysed with UNICORN™ software (ÄKTA™ pure; Cytiva). Single molecule analyses using Oufti (Paintdakhi *et al*., 2016), MATLAB R2016a, and SMTracker 2.0 (Oviedo-Bocanegra, Hinrichs *et al.* 2021). The microscope images were analysed using Fiji ImageJ, MetaMorph 6.3-Software (Meta Imaging Software), VisiView® (Visitron Systems), and Zen Black Software 2012 (Carl Zeiss). The visualisation of the western blots using Image Lab (Version 6.1.0 build 7; 2020© BioRad Laboratories, Inc). The figures were made with Adope® Illustrator® CS6 and for the statistical analysis and to visualize experimental data, Microsoft® Excel® LTSC was used.

6. References

Abeyrathne, P. D., & Grigorieff, N. (2017). Expression, purification, and contaminant detection for structural studies of Ralstonia metallidurance ClC protein rm1. *PLoS One*, 12(7), e0180163.

Adusei-Danso, F., Khaja, F. T., DeSantis, M., Jeffrey, P. D., Dubnau, E., Demeler, B., *et al*. (2019). Structure-Function Studies of the *Bacillus subtilis* Ric Proteins Identify the Fe-S Cluster-Ligating Residues and Their Roles in Development and RNA Processing. *mBio*, 10(5).

Al-Hinai, M. A., Jones, S. W., & Papoutsakis, E. T. (2015). The Clostridium sporulation programs: diversity and preservation of endospore differentiation. *Microbiol Mol Biol Rev*, 79(1), 19-37.

Andrade, J. M., Pobre, V., Silva, I. J., Domingues, S., & Arraiano, C. M. (2009). The role of 3′–5′ exoribonucleases in RNA degradation. *Progress in Molecular Biology and Translational Science, Academic Press, 85*,187-229.

Aravind, L., & Koonin, E. V. (1998). The HD domain defines a new superfamily of metal-dependent phosphohydrolases. *Trends Biochem Sci*, 23(12), 469-472.

Arnaud, M., Chastanet, A., & Debarbouille, M. (2004). New vector for efficient allelic replacement in naturally nontransformable, low-GC-content, gram-positive bacteria. *Appl Environ Microbiol*, 70(11), 6887-6891.

Bechhofer, D. H., & Deutscher, M. P. (2019). Bacterial ribonucleases and their roles in RNA metabolism. *Critical Reviews in Biochemistry and Molecular Biology*, 54(3), 242-300.

Benda, M., Woelfel, S., Fasshauer, P., Gunka, K., Klumpp, S., Poehlein, A., *et al*. (2021). Quasi-essentiality of RNase Y in *Bacillus subtilis* is caused by its critical role in the control of mRNA homeostasis*. Nucleic Acids Research*, 49(12), 7088-7102.

Brantl, S., & Licht, A. (2010). Characterisation of *Bacillus subtilis* transcriptional regulators involved in metabolic processes. *Curr Protein Pept Sci*, 11(4), 274-291.

Breyton, C., Javed, W., Vermot, A., Arnaud, C. A., Hajjar, C., Dupuy, J., *et al*. (2019). Assemblies of lauryl maltose neopentyl glycol (LMNG) and LMNG-solubilized membrane proteins. *Biochim Biophys Acta Biomembr*, 1861(5), 939-957.

Carabetta, V. J., Tanner, A. W., Greco, T. M., Defrancesco, M., Cristea, I. M., & Dubnau, D. (2013). A complex of YlbF, YmcA and YaaT regulates sporulation, competence and biofilm formation by accelerating the phosphorylation of Spo0A. *Mol Microbiol*, 88(2), 283-300.

Cardenas, P. P., Carrasco, B., Sanchez, H., Deikus, G., Bechhofer, D. H., & Alonso, J. C. J. N. a. r. (2009). *Bacillus subtilis* polynucleotide phosphorylase 3′-to-5′ DNase activity is involved in DNA repair. *Nucleic Acids Research,* 37(12), 4157-4169.

Cartalas, J., Coudray, L., & Gobert, A. (2022). How RNases Shape Mitochondrial Transcriptomes. *International Journal of Molecular Sciences*, 23(11), 6141.

Cascante-Estepa, N., Gunka, K., & Stulke, J. (2016). Localization of Components of the RNA-Degrading Machine in *Bacillus subtilis*. *Front Microbiol*, 7, 1492.

Cerritelli, S. M., & Crouch, R. J. (2009). Ribonuclease H: the enzymes in eukaryotes. *FEBS J*, 276(6), 1494-1505.

Chaptal, V., Delolme, F., Kilburg, A., Magnard, S., Montigny, C., Picard, M., *et al*. (2017). Quantification of Detergents Complexed with Membrane Proteins. *Sci Rep*, 7(1), 41751.

Commichau, F. M., Rothe, F. M., Herzberg, C., Wagner, E., Hellwig, D., Lehnik-Habrink, M., *et al*. (2009). Novel activities of glycolytic enzymes in *Bacillus subtilis*: interactions with essential proteins involved in mRNA processing. *Mol Cell Proteomics*, 8(6), 1350-1360.

Condon, C. (2003). RNA processing and degradation in *Bacillus subtilis*. *Microbiol Mol Biol Rev*, 67(2), 157-174, table of contents.

Crooke, S. T. (1999). Molecular mechanisms of action of antisense drugs. *Biochim Biophys Acta*, 1489(1), 31-44.

Crouch, R., & Dirksen, M. (1985). Nucleases. Linn SM & Roberts RJ: *Cold Spring Harbor Laboratory Press*, 211-241.

Crouch, R. J. (1990). Ribonuclease H: from discovery to 3D structure. *New Biol*, 2(9), 771-777.

Defeu Soufo, H. J., & Graumann, P. L. (2006). Dynamic localization and interaction with other *Bacillus subtilis* actin-like proteins are important for the function of MreB. *Mol Microbiol*, 62(5), 1340-1356.

DeLoughery, A., Dengler, V., Chai, Y., & Losick, R. J. M. m. (2016). Biofilm formation by *Bacillus subtilis* requires an endoribonuclease-containing multisubunit complex that controls mRNA levels for the matrix gene repressor SinR. *Mol Microbiol*, 99(2), 425-437.

DeLoughery, A., Lalanne, J. B., Losick, R., & Li, G. W. (2018). Maturation of polycistronic mRNAs by the endoribonuclease RNase Y and its associated Y-complex in *Bacillus subtilis*. *Proc Natl Acad Sci U S A*, 115(24), E5585-E5594.

Diethmaier, C., Pietack, N., Gunka, K., Wrede, C., Lehnik-Habrink, M., Herzberg, C., *et al*. (2011). A novel factor controlling bistability in *Bacillus subtilis*: the YmdB protein affects flagellin expression and biofilm formation. *J Bacteriol*, 193(21), 5997-6007.

Doan, T., & Aymerich, S. (2003). Regulation of the central glycolytic genes in *Bacillus subtilis*: binding of the repressor CggR to its single DNA target sequence is modulated by fructose-1, 6-bisphosphate. *Mol Microbiol*, 47(6), 1709-1721.

Dos Santos, R. F., Quendera, A. P., Boavida, S., Seixas, A. F., Arraiano, C. M., Andrade, J. M., *et al*. (2018). Major 3′–5′ exoribonucleases in the metabolism of coding and non-coding RNA. *Progress in Molecular Biology and Translational Science*, 159, 101-155.

Dougherty, W. G., Cary, S. M., & Parks, T. D. (1989). Molecular genetic analysis of a plant virus polyprotein cleavage site: a model. *Virology*, 171(2), 356-364.

Dubnau, E. J., Carabetta, V. J., Tanner, A. W., Miras, M., Diethmaier, C., & Dubnau, D. (2016). A protein complex supports the production of Spo0A-P and plays additional roles for biofilms and the K-state in *Bacillus subtilis*. *Mol Microbiol*, 101(4), 606-624.

Duigou, S., Ehrlich, S. D., Noirot, P., & Noirot-Gros, M. F. (2005). DNA polymerase I acts in translesion synthesis mediated by the Y-polymerases in *Bacillus subtilis*. *Mol Microbiol*, 57(3), 678-690.

Dumon-Seignovert, L., Cariot, G., & Vuillard, L. (2004). The toxicity of recombinant proteins in *Escherichia coli*: a comparison of overexpression in BL21(DE3), C41(DE3), and C43(DE3). *Protein Expr Purif*, 37(1), 203-206.

Durand, S., & Condon, C. (2018). RNases and Helicases in Gram-Positive Bacteria. *Microbiol Spectr*, 6(2), 6.2. 16.

Frank, P., Braunshofer-Reiter, C., Wintersberger, U., Grimm, R., & Busen, W. (1998). Cloning of the cDNA encoding the large subunit of human RNase HI, a homologue of the prokaryotic RNase HII. *Proc Natl Acad Sci U S A*, 95(22), 12872-12877.

Frotscher, E., Krainer, G., Hartmann, A., Schlierf, M., & Keller, S. (2018). Conformational Dynamics Govern the Free-Energy Landscape of a Membrane-Interacting Protein. *ACS Omega*, 3(9), 12026-12032.

Georg, J., & Hess, W. R. (2011). cis-Antisense RNA, Another Level of Gene Regulation in Bacteria. *Microbiology and Molecular Biology Reviews*, 75(2), 286.

Grishin, N. V. (2001). KH domain: one motif, two folds. *Nucleic Acids Res*, 29(3), 638-643.

Hamouche, L., Billaudeau, C., Rocca, A., Chastanet, A., Ngo, S., Laalami, S., *et al*. (2020). Dynamic Membrane Localization of RNase Y in *Bacillus subtilis*. *mBio*, 11(1), e03337-03319.

Hardouin, P., Velours, C., Bou-Nader, C., Assrir, N., Laalami, S., Putzer, H., *et al*. (2018). Dissociation of the Dimer of the Intrinsically Disordered Domain of RNase Y upon Antibody Binding. *Biophysical Journal*, 115(11), 2102-2113.

Haruki, M., Tsunaka, Y., Morikawa, M., & Kanaya, S. (2002). Cleavage of a DNA-RNA-DNA/DNA chimeric substrate containing a single ribonucleotide at the DNA-RNA junction with prokaryotic RNases HII. *Febs Letters*, 531(2), 204-208.

Hernandez-Tamayo, R., Oviedo-Bocanegra, L. M., Fritz, G., & Graumann, P. L. (2019). Symmetric activity of DNA polymerases at and recruitment of exonuclease ExoR and of PolA to the *Bacillus subtilis* replication forks. *Nucleic Acids Res*, 47(16), 8521-8536.

Hinrichs, R., Pozhydaieva, N., Hofer, K., & Graumann, P. L. (2022). Y-Complex Proteins Show RNA-Dependent Binding Events at the Cell Membrane and Distinct Single-Molecule Dynamics. *Cells*, 11(6), 933.

Hosoya, S., Asai, K., Ogasawara, N., Takeuchi, M., & Sato, T. (2002). Mutation in yaaT leads to significant inhibition of phosphorelay during sporulation in *Bacillus subtilis*. *J Bacteriol*, 184(20), 5545-5553.

Huen, J., Lin, C. L., Golzarroshan, B., Yi, W. L., Yang, W. Z., & Yuan, H. S. (2017). Structural Insights into a Unique Dimeric DEAD-Box Helicase CshA that Promotes RNA Decay. *Structure*, 25(3), 469-481.

Jiang, L., & Lai, L. (2002). CH··· O Hydrogen Bonds at Protein-Protein Interfaces* 210. *Journal of Biological Chemistry,* 277(40), 37732-37740.

Jumper, J., Evans, R., Pritzel, A., Green, T., Figurnov, M., Ronneberger, O., *et al*. (2021). Highly accurate protein structure prediction with AlphaFold. *Nature*, 596(7873), 583-589.

Kearns, D. B., Chu, F., Branda, S. S., Kolter, R., & Losick, R. (2005). A master regulator for biofilm formation by *Bacillus subtilis*. *Mol Microbiol*, 55(3), 739-749.

Kerppola, T. K. (2008). Bimolecular fluorescence complementation (BiFC) analysis as a probe of protein interactions in living cells. *Annual review of biophysics,* 37, 465-487

Knol, J., Sjollema, K., & Poolman, B. (1998). Detergent-mediated reconstitution of membrane proteins. *Biochemistry*, 37(46), 16410-16415.

Knowles, T. J., Finka, R., Smith, C., Lin, Y. P., Dafforn, T., & Overduin, M. (2009). Membrane proteins solubilized intact in lipid containing nanoparticles bounded by styrene maleic acid copolymer. *J Am Chem Soc*, 131(22), 7484-7485.

Laalami, S., Cavaiuolo, M., Roque, S., Chagneau, C., & Putzer, H. (2021). *Escherichia coli* RNase E can efficiently replace RNase Y in *Bacillus subtilis*. *Nucleic Acids Research*, 49(8), 4643-4654.

Lebreton, A., Tomecki, R., Dziembowski, A., & Seraphin, B. (2008). Endonucleolytic RNA cleavage by a eukaryotic exosome. *Nature*, 456(7224), 993-996.

Lehnik-Habrink, M., Lewis, R. J., Mader, U., & Stulke, J. (2012). RNA degradation in *Bacillus subtilis*: an interplay of essential endo- and exoribonucleases. *Mol Microbiol*, 84(6), 1005-1017.

Lehnik-Habrink, M., Newman, J., Rothe, F. M., Solovyova, A. S., Rodrigues, C., Herzberg, C., *et al*. (2011a). RNase Y in *Bacillus subtilis*: a Natively disordered protein that is the functional equivalent of RNase E from *Escherichia coli*. *J Bacteriol*, 193(19), 5431-5441.

Lehnik-Habrink, M., Newman, J., Rothe, F. M., Solovyova, A. S., Rodrigues, C., Herzberg, C., *et al*. (2011b). RNase Y in *Bacillus subtilis*: a Natively Disordered Protein That Is the Functional Equivalent of RNase E from *Escherichia coli*. *Journal of Bacteriology*, 193(19), 5431-5441.

Lehnik-Habrink, M., Schaffer, M., Mader, U., Diethmaier, C., Herzberg, C., & Stulke, J. (2011). RNA processing in *Bacillus subtilis*: identification of targets of the essential RNase Y. *Mol Microbiol*, 81(6), 1459-1473.

Lehnik-Habrink, M., Pförtner, H., Rempeters, L., Pietack, N., Herzberg, C., & Stülke, J. J. M. m. (2010). The RNA degradosome in *Bacillus subtilis*: identification of CshA as the major RNA helicase in the multiprotein complex. *Mol Microbiol*, 77(4), 958-971.

Letunic, I., Khedkar, S., & Bork, P. (2020). SMART: recent updates, new developments and status in 2020. *Nucleic Acids Research*, 49(D1), D458-D460.

Lewis, P. J., & Marston, A. L. (1999). GFP vectors for controlled expression and dual labelling of protein fusions in *Bacillus subtilis*. *Gene*, 227(1), 101-110.

Lin, S. H., & Guidotti, G. (2009). Purification of membrane proteins. *Methods Enzymol*, 463, 619-629.

Ludwig, H., Homuth, G., Schmalisch, M., Dyka, F. M., Hecker, M., & Stulke, J. (2001). Transcription of glycolytic genes and operons in *Bacillus subtilis*: evidence for the presence of multiple levels of control of the gapA operon. *Mol Microbiol*, 41(2), 409-422.

Mahendran, G., Jayasinghe, O. T., Thavakumaran, D., Arachchilage, G. M., & Silva, G. N. (2022). Key players in regulatory RNA realm of bacteria. *Biochem Biophys Rep*, 30, 101276.

Mars, R. A., Nicolas, P., Denham, E. L., & van Dijl, J. M. (2016). Regulatory RNAs in *Bacillus subtilis*: a Gram-Positive Perspective on Bacterial RNA-Mediated Regulation of Gene Expression. *Microbiol Mol Biol Rev*, 80(4), 1029-1057.

Mathy, N., Benard, L., Pellegrini, O., Daou, R., Wen, T., & Condon, C. (2007). 5'-to-3' exoribonuclease activity in bacteria: role of RNase J1 in rRNA maturation and 5' stability of mRNA. *Cell*, 129(4), 681-692.

Mathy, N., Hebert, A., Mervelet, P., Benard, L., Dorleans, A., Li de la Sierra-Gallay, I., *et al*. (2010). *Bacillus subtilis* ribonucleases J1 and J2 form a complex with altered enzyme behaviour. *Mol Microbiol*, 75(2), 489-498.

McCown, P. J., Corbino, K. A., Stav, S., Sherlock, M. E., & Breaker, R. R. (2017). Riboswitch diversity and distribution. *RNA*, 23(7), 995-1011.

Meinken, C., Blencke, H. M., Ludwig, H., & Stulke, J. (2003). Expression of the glycolytic *gapA* operon in *Bacillus subtilis*: differential syntheses of proteins encoded by the operon. *Microbiology*, 149(3), 751-761.

Mirdita, M., Schutze, K., Moriwaki, Y., Heo, L., Ovchinnikov, S., & Steinegger, M. (2022). ColabFold: making protein folding accessible to all. *Nature Methods*, 19(6), 679.

Mohanty, B. K., & Kushner, S. R. (2016). Regulation of mRNA Decay in Bacteria. *Annu Rev Microbiol*, 70, 25-44.

Nava, G. M., Grasso, L., Sertic, S., Pellicioli, A., Falconi, M. M., & Lazzaro, F. (2020). One, No One, and One Hundred Thousand: The Many Forms of Ribonucleotides in DNA. *International Journal of Molecular Sciences*, 21(5), 1706.

Newbury, S. F., Smith, N. H., & Higgins, C. F. J. C. (1987). Differential mRNA stability controls relative gene expression within a polycistronic operon. *Cell*, 51(6), 1131-1143.

Nick McElhinny, S. A., Watts, B. E., Kumar, D., Watt, D. L., Lundström, E.-B., Burgers, P. M., *et al*. (2010). Abundant ribonucleotide incorporation into DNA by yeast replicative polymerases. *PNAS*, 107(11), 4949-4954.

Ogawa, T., & Okazaki, T. (1984). Function of RNase H in DNA replication revealed by RNase H defective mutants of *Escherichia coli. Mol Gen Genet*, 193(2), 231-237.

Ohi, M., Li, Y., Cheng, Y., & Walz, T. (2004). Negative staining and image classification—powerful tools in modern electron microscopy. *Biol. Proced. Online,* 6(1), 23-34.

Olerinyova, A., Sonn-Segev, A., Gault, J., Eichmann, C., Schimpf, J., Kopf, A. H., *et al*. (2021). Mass Photometry of Membrane Proteins. *Chem*, 7(1), 224-236.

Overduin, M., Trieber, C., Prosser, R. S., Picard, L. P., & Sheff, J. G. (2021). Structures and Dynamics of Native-State Transmembrane Protein Targets and Bound Lipids. *Membranes (Basel)*, 11(6), 451.

Oviedo-Bocanegra, L. M., Hinrichs, R., Rotter, D. A. O., Dersch, S., & Graumann, P. L. (2021). Single molecule/particle tracking analysis program SMTracker 2.0 reveals different dynamics of proteins within the RNA degradosome complex in *Bacillus subtilis*. *Nucleic Acids Research*, 49(19), e112-e112.

Papenfort, K., & Vogel, J. (2010). Regulatory RNA in bacterial pathogens. *Cell Host Microbe*, 8(1), 116-127.

Parmar, M., Rawson, S., Scarff, C. A., Goldman, A., Dafforn, T. R., Muench, S. P., *et al*. (2018). Using a SMALP platform to determine a sub-nm single particle cryo-EM membrane protein structure. *Biochimica Et Biophysica Acta-Biomembranes*, 1860(2), 378-383.

Pettersen, E. F., Goddard, T. D., Huang, C. C., Meng, E. C., Couch, G. S., Croll, T. I., *et al*. (2021). UCSF ChimeraX: Structure visualization for researchers, educators, and developers. *Protein Sci*, 30(1), 70-82.

Piggot, P. J., & Hilbert, D. W. (2004). Sporulation of *Bacillus subtilis*. *Curr Opin Microbiol*, 7(6), 579-586.

Prabudiansyah, I., Kusters, I., Caforio, A., & Driessen, A. J. (2015). Characterization of the annular lipid shell of the Sec translocon. *Biochim Biophys Acta*, 1848(10), 2050-2056.

Randall, J. R., Nye, T. M., Wozniak, K. J., & Simmons, L. A. (2019). RNase HIII Is Important for Okazaki Fragment Processing in *Bacillus subtilis*. *Journal of Bacteriology*, 201(7), e00686-00618.

Rigaud, J. L., Mosser, G., Lacapere, J. J., Olofsson, A., Levy, D., & Ranck, J. L. (1997). Bio-Beads: an efficient strategy for two-dimensional crystallization of membrane proteins. *J Struct Biol*, 118(3), 226-235.

Roosild, T. P., Greenwald, J., Vega, M., Castronovo, S., Riek, R., & Choe, S. (2005). NMR structure of Mistic, a membrane-integrating protein for membrane protein expression. *Science, 307*(5713), 1317-1321.

Rösch, T. C., Oviedo-Bocanegra, L. M., Fritz, G., & Graumann, P. L. (2018). SMTracker: a tool for quantitative analysis, exploration and visualization of single-molecule tracking data reveals highly dynamic binding of *B. subtilis* global repressor AbrB throughout the genome. *Sci Rep,* 8(1), 1-12.

Santos-Pereira, J. M., & Aguilera, A. (2015). R loops: new modulators of genome dynamics and function. *Nat Rev Genet*, 16(10), 583-597.

Schindelin, J., Arganda-Carreras, I., Frise, E., Kaynig, V., Longair, M., Pietzsch, T., *et al*. (2012). Fiji: an open-source platform for biological-image analysis. *Nat Methods*, 9(7), 676-682.

Schroeder, J. W., Randall, J. R., Hirst, W. G., O'Donnell, M. E., & Simmons, L. A. (2017). Mutagenic cost of ribonucleotides in bacterial DNA. *Proc Natl Acad Sci U S A*, 114(44), 11733-11738.

Schroeder, R., Barta, A., & Semrad, K. (2004). Strategies for RNA folding and assembly. *Nat Rev Mol Cell Biol*, 5(11), 908-919.

Schuhmacher, J. S., Rossmann, F., Dempwolff, F., Knauer, C., Altegoer, F., Steinchen, W., *et al*. (2015). MinD-like ATPase FlhG effects location and number of bacterial flagella during C-ring assembly. *Proc Natl Acad Sci U S A*, 112(10), 3092-3097.

Seddon, A. M., Curnow, P., & Booth, P. J. (2004). Membrane proteins, lipids and detergents: not just a soap opera. *Biochimica et Biophysica Acta (BBA) – Biomembranes* (1666), 105-117.

Selby, C. P., & Sancar, A. (2006). A cryptochrome/photolyase class of enzymes with single-stranded DNA-specific photolyase activity. *Proc Natl Acad Sci U S A*, 103(47), 17696-17700.

Shahbabian, K., Jamalli, A., Zig, L., & Putzer, H. (2009). RNase Y, a novel endoribonuclease, initiates riboswitch turnover in *Bacillus subtilis*. *EMBO J*, 28(22), 3523-3533.

Siranosian, K. J., & Grossman, A. D. (1994). Activation of spo0A transcription by sigma H is necessary for sporulation but not for competence in *Bacillus subtilis*. *Journal of Bacteriology*, 176(12), 3812-3815.

Strop, P., & Brunger, A. T. (2005). Refractive index-based determination of detergent concentration and its application to the study of membrane proteins. *Protein Sci*, 14(8), 2207-2211.

Szklarczyk, D., Gable, A. L., Nastou, K. C., Lyon, D., Kirsch, R., Pyysalo, S., *et al*. (2021). The STRING database in 2021: customizable protein–protein networks, and functional characterization of user-uploaded gene/measurement sets. *Nucleic Acids Research* (49), D605-D612.

Tanner, A. W., Carabetta, V. J., Martinie, R. J., Mashruwala, A. A., Boyd, J. M., Krebs, C., *et al*. (2017). The RicAFT (YmcA-YlbF-YaaT) complex carries two [4Fe-4S] 2+ clusters and may respond to redox changes. *Mol Microbiol,* 104(5), 837-850.

Tortosa, P., Albano, M., & Dubnau, D. (2000). Characterization of ylbF, a new gene involved in competence development and sporulation in *Bacillus subtilis*. *Mol Microbiol*, 35(5), 1110-1119.

Trinquier, A., Durand, S., Braun, F., & Condon, C. (2020). Regulation of RNA processing and degradation in bacteria. *Biochim Biophys Acta Gene Regul Mech*, 1863(5), 194505.

Valverde, R., Edwards, L., & Regan, L. (2008). Structure and function of KH domains. *FEBS J*, 275(11), 2712-2726.

VanAken, T., Foxall-VanAken, S., Castleman, S., & Ferguson-Miller, S. (1986). Alkyl glycoside detergents: Synthesis and applications to the study of membrane proteins. *Methods in enzymology* (125), 27-35.

Waters, L. S., & Storz, G. (2009). Regulatory RNAs in bacteria. *Cell*, 136(4), 615-628.

Weiland, P., & Altegoer, F. (2021). Identification and Characterization of Two Transmembrane Proteins Required for Virulence of Ustilago maydis. *Front Plant Sci*, 12, 669835.

Yamamoto, J., Chumsakul, O., Toya, Y., Morimoto, T., Liu, S., Masuda, K., *et al*. (2022). Constitutive expression of the global regulator AbrB restores the growth defect of a genome-reduced *Bacillus subtilis* strain and improves its metabolite production. *DNA Res*, 29(3), dsac015.

Yang, Z. R., Wang, C., Zhou, Q. X., An, J. L., Hildebrandt, E., Aleksandrov, L. A., *et al*. (2014). Membrane protein stability can be compromised by detergent interactions with the extramembranous soluble domains. *Protein Science*, 23(6), 769-789.

Yao, N. Y., Schroeder, J. W., Yurieva, O., Simmons, L. A., & O'Donnell, M. E. (2013). Cost of rNTP/dNTP pool imbalance at the replication fork. *Proceedings of the National Academy of Sciences of the United States of America*, 110(32), 12942-12947.

Young, G., Hundt, N., Cole, D., Fineberg, A., Andrecka, J., Tyler, A., *et al*. (2018). Quantitative mass imaging of single biological macromolecules. *Science*, 360(6387), 423-427.

Zhang, Z., Kuipers, G., Niemiec, L., Baumgarten, T., Slotboom, D. J., de Gier, J. W., *et al*. (2015). High-level production of membrane proteins in *E. coli* BL21(DE3) by omitting the inducer IPTG. *Microb Cell Fact*, 14(1), 142.

7. Supplement

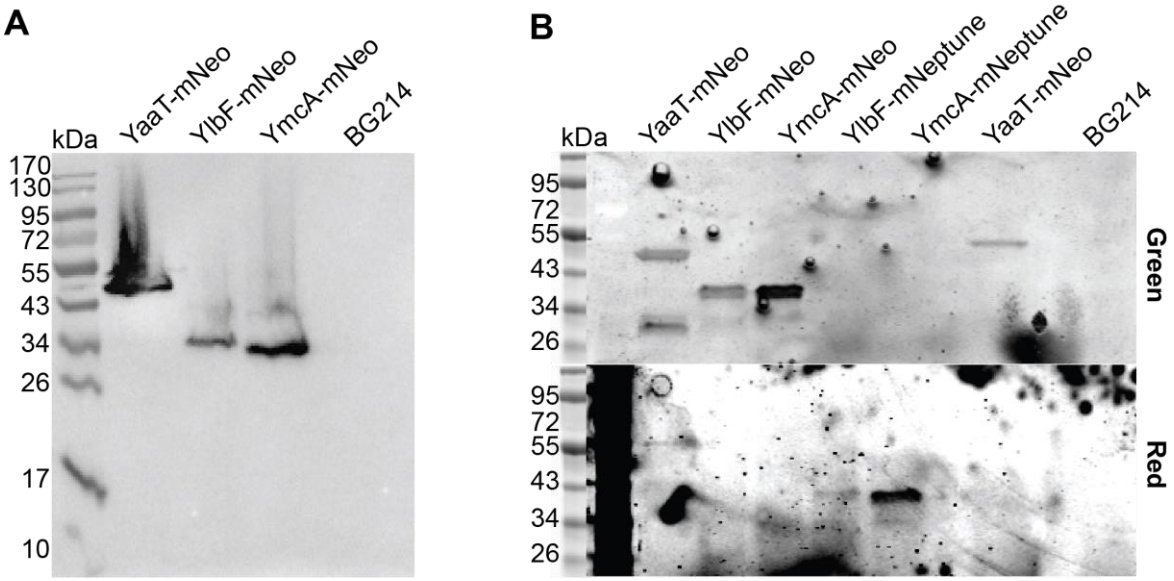

Figure S1 (A) *Western blots showing mNeo fusion expressed from native locus*. Total cell extracts from exponentially growing cultures (LB) were used. The YaaT-mNeo fusion (57.9 kDa), YlbF-mNeo (43.7 kDa), YmcA-mNeo (42.9 kDa) contains the mNeongreen polypeptide (26.9 kDa). Note that YlbF and YmcA runs erroneously low, possibly because samples have not been heated before loading to the gel, which yields clearer bands. All strains were detected via mNeongreen-antiserum. (B) Fluorescence blots showing mNeo fusion and mNeptune fusion from native locus. Cells are harvested from the exponential growth phase. Showing are the green (mNeonGreen) and the red channel (mNeptune) to show the excitation of the corresponding fluorophores.

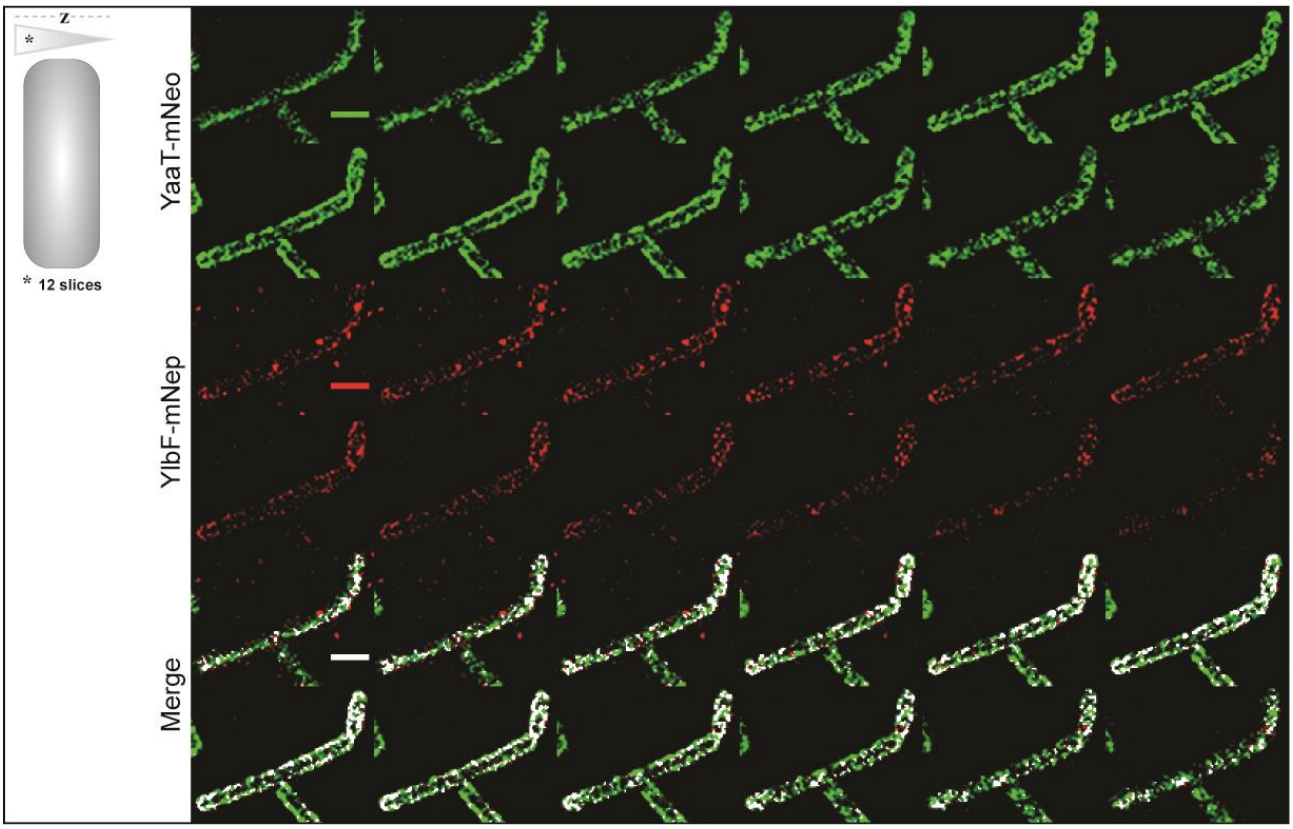

Figure S2 *Structured illumination microscopy (SIM) of colocalization by YaaT-mNeo and YlbF-mNeptune.* The montage of the stack is divided into 12 slices. YaaT-mNeo is coloured in green, YlbF-mNeptune in red. The areas of the overlay show up as a white signal (merge).

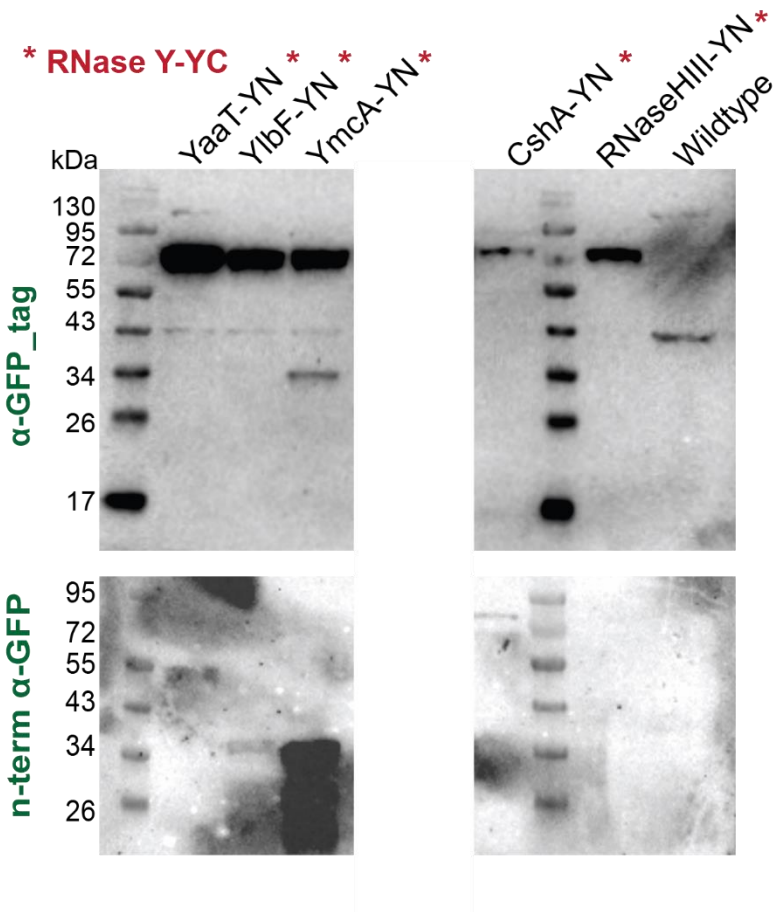

Figure S3 *Western blot of BiFC strains.* The western blot shows on the one hand the C-terminal signal (α-GFP_tag c-term) and on the other hand the N-terminal part of the mVenus split strain (α-GFP n-term). As a negative control, the wildtype is shown.

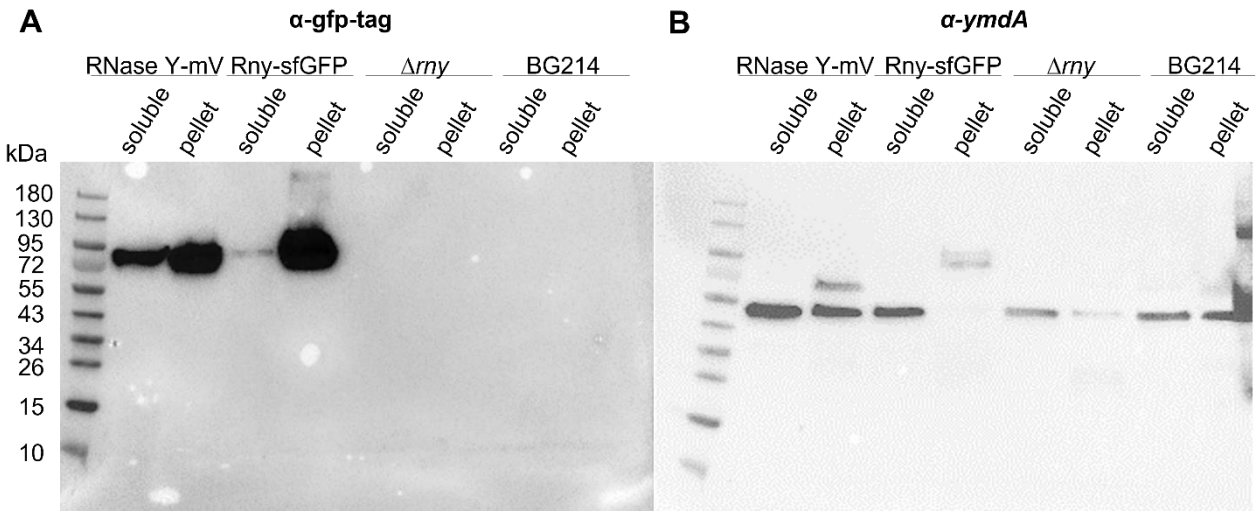

Figure S4 *Western blots of fractionation of* RNase Y*-mVenus compared with* RNase Y*-sfGFP.* As a control, the *Δrny* strain and wildtype strain (BG214) are shown. (A) Western blot against α-gfp-tag. (B) Western blot against α-*ymdA*.

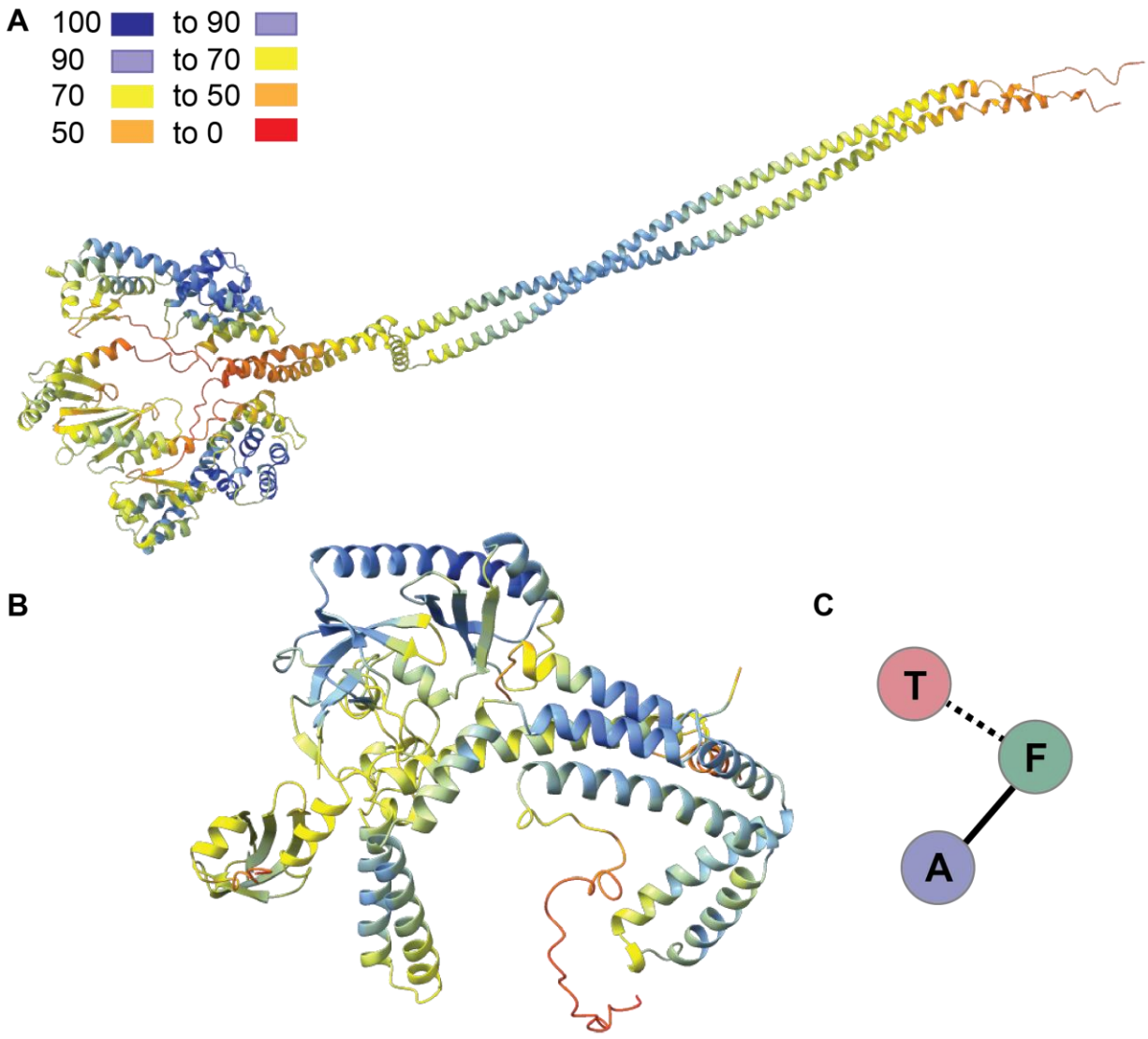

Figure S5 *Alpha fold prediction of* RNase Y *(A) and the Y-complex (B).* The color codes give information about the confidence of the prediction. (C) Chain contact diagram (T= YaaT, F= YlbF, A= YmcA). The solid line shows already secured connections. Dotted line a predicted possible connection

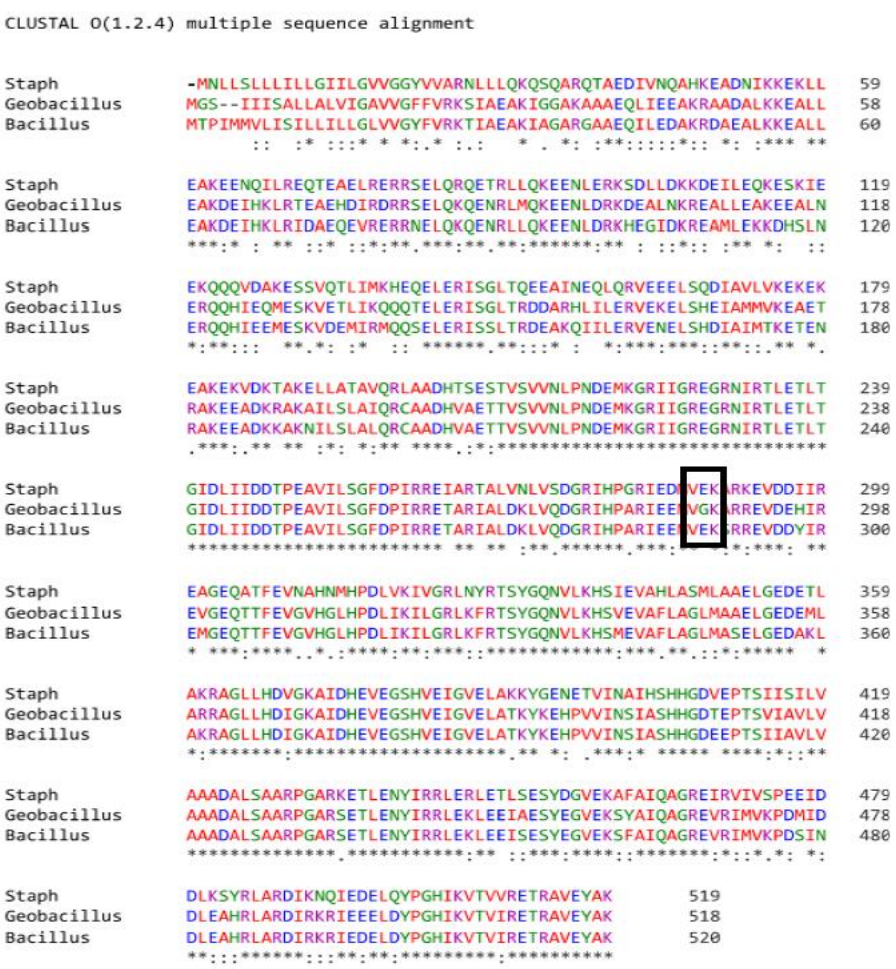

Figure S6 *Multiple sequence alignment of rny in different organism.* The amino acid sequence of *rny* in *Staphylococcus aureus* (Staph), *Geobacillus thermodenitrificans* (*Geobacillus*) and *Bacillus subtilis* were aligned with the online tool Clustal omega. The sequences of the organism were used by www.ncbi.nlm.nih.gov.